Direct Photon and Neutral Meson Production at High Transverse Momentum by Negative 515 GeV/c Pions and 530 GeV/c Protons Incident upon Hydrogen, Beryllium, and Copper Targets

by

George B. Osborne III

Submitted in Partial Fulfillment

of the

Requirements for the Degree

DOCTOR OF PHILOSOPHY

Supervised by: Professor Frederick Lobkowicz

Department of Physics and Astronomy

The College

Arts and Sciences

University of Rochester

Rochester, New York

1996

Curriculum Vitae

George B. Osborne III

The author was born on December 4, 1967 in Rochester, New York. Beginning in 1985, his senior year in high school, George attended Roberts Wesleyan College. There, under the guidance of Professor Philip Ogden, he began his formal study of physics. During his undergraduate years, George received a National Merit Scholarship and a Scholastic All-American Collegiate Award and was an American Physical Society Summer Intern. In the spring of 1989, he earned his Bachelor of Science in Physics and Mathematics, graduating Summa Cum Laude.

The following fall, the author began his graduate education at the University of Rochester where he was supported and advised by Professors Frederick Lobkowicz and Paul Slattery. The summer of 1990 found George working on detector electronics at Brookhaven National Laboratory. George earned his Masters of Arts in the spring of 1991. Shortly thereafter, he moved to Illinois, just in time to assist in the 1991 data acquisition for E706 at Fermilab, during which he had primary responsibility for the forward calorimeter. Since that time, George became involved in the data analysis, with primary responsibilities involving the determination of muon content in the beam, the removal of coherent pedestal effects in the EMLAC, and the analysis of the 1991 trigger efficiencies.

Acknowledgements

In these few words of thanks, I must begin where I began, and thank my parents, George and Betsy Osborne. Through many dangers, toils, and snares, they were always available for strength, wisdom, guidance, and every sort of support to the end of their means, from day one until today. You two are the absolute best.

Fast-forwarding, then, to the present, let me express my gratitude to my loving wife and the wonderful mother of my children. Not only has Richelle been supportive of me in my every endeavor, she has also found the enduring strength to administer the health, wholeness, and education of our three precious children. Richelle, David, Courtney, and Betsy, the four of you bring true joy to my life.

In the years between the beginning and the present, there we find Becky and Dave. I appreciate you two, not just because of your love, support, and encouragement as my brother and sister, but also for those same qualities as aunt and uncle and as sister-in-law and brother-in-law. Thanks, guys – you know I love you.

The value of our families to us is inestimable. From our littlest niece to our eldest grandparent, they have provided a network of support and stability. To single out any is surely an injustice to the rest, but special thanks is due to Rich and Linda for their continuous support in so many ways over the years, to Jeff and Trish for their generosity and very special friendship (all those 2-hour phone calls and the trips in a full-to-the-brim family wagon!), to Ann, Tom, Ben, and Will for their love and for our Wisconsin refuge (a home away from home), and to Mark and Jane and Doug and Jean for their support when times were lean. I

also wish to thank my grandparents especially for their loving prayers, support, and encouragement. To the Osborne Tribe (and associates), the Balentine's, the Koehn's and the Chase's – you are all so very much loved and appreciated.

I would also like to express my gratitude to several members of the RWC faculty – to Dr. Ogden, for his excellent counsel, teaching, and encouragement and for giving me a solid start in physics, the Coisman's for their friendship (and all those rides!), Dr. Brown for his excitement for learning, and Dr. Chamberlain for all her investments in me.

Many thanks to Dr. John Toner, for being a mentor and a friend. Not only did my work at EK make it possible for me to support my family and continue my education, it also let me taste all the joys of scientific research from design to publication – thanks for letting me be a part of it all.

I would also like to thank the University of Rochester support staff. Life would have been vastly more difficult without the help of Mary Kraus, Barbara Warren, Betty Cook, Connie Jones, Sue Brightman, Judy Mack, and Betty Bauer. Thank you all for making it possible for me to get through the University's tangled bureaucracies and graduate life in general.

Here at E706, I owe much to many. Many thanks to Professors Fred Lobkowicz and Paul Slattery for their advice and support, in many instances over-and-above the call of duty. I am very grateful to George Ginther for always having the time to teach, to think, and to discuss; during my time as a graduate student, George's contributions to my general education and my understanding of experimental science are probably more significant than those of any other person. Thanks, too, to Marek Zielinski for his willingness to very thoughtfully answer so many questions (sometimes repeatedly!). Lee Sorrell also deserves much credit for his

patient tutelage of the 1991 trigger group. I am grateful to Michael Begel for his help in many ways, especially during the preparation of this thesis. I much appreciate Dan Ruggiero for his substantial contributions to E706 and to me personally – from system administration to all those rides to work when the car was in the shop. Thanks, John and Sarah Mansour and Nikos and Maria Varelas, for the cookouts, and for letting us enjoy your families. I really enjoyed being part of the team with Lenny Apanasevich, Vishnu Zutshi, Rob Roser, Dave Striley, Dane Skow, Paul Madsen, Andre Maul, Chris Lirakis, Jan Ftacnik, John Kuehler, Paoti Chang, Woo-Hyun Chung, John Bacigalupi, Jim Dunlea, Wieslaw Dlugosz, Casey Hartman, Steve Blusk, Carlos Yosef, Bill DeSoi, George Fanourakis, Dave Brown, Ed Pothier, Vijay Kapoor, and Lucy deBarbaro. Thanks, guys for all your help and hard work – many of you have been willing on numerous occasions to give me a one-on-one explanation of your work or to help me on a personal level, and I want you to know that you are appreciated. I also appreciate for the investments of the many professors involved with E706; special thanks to Tom Ferbel, Gene Engels, and Carl Bromberg for their contributions of both style and substance to this group. It has truly been a pleasure to work with all the members of the E706 group, from Alverson to Zutshi – it is only through all your superhuman efforts that this experiment was possible. You all have my sincere gratitude.

This work has been supported by grants from the National Science Foundation and the Department of Energy.

Abstract

This thesis presents analyses of π^0, η, and direct photon production by 515 GeV/c negative pion and 530 GeV/c proton beams incident upon hydrogen, beryllium, and copper targets. The data upon which these analyses are based were collected by experiment E706 at Fermi National Accelerator Laboratory during the 1990 and 1991 data acquisition periods using a finely segmented liquid argon electromagnetic calorimeter for photon detection. A description is given of the experimental apparatus and of the techniques used in data acquisition, reconstruction, and analysis. Inclusive differential π^0, η, and direct photon cross sections are presented as functions of transverse momentum and center-of-mass rapidity in the ranges $p_T > 3$ GeV/c and $-0.75 < Y_{CM} < 0.75$. Measurements of the η/π ratio and a ratio of cross sections from the two beam types are presented. The nuclear dependence of these measurements is also reported. These results are compared with corresponding measurements by other experiments and with theoretical calculations.

Table of Contents

Curriculum Vitae — ii

Acknowledgements — iii

Abstract — vi

Chapter 1 Introduction — 1

1.1 The Standard Model and Quantum Chromodynamics ... 1

1.2 Motivations ... 5

1.2.1 Direct Photons ... 5

1.2.2 Neutral Mesons ... 6

1.2.3 Nuclear Dependence ... 7

1.3 Direct Photon Experiments ... 8

1.4 Thesis Overview ... 10

Chapter 2 The Spectrometer — 11

2.1 Beamline and Target ... 13

2.1.1 Meson West Beamline ... 13

2.1.2 The *Čerenkov* Detector ... 15

2.1.3 The Beam and Interaction Counters ... 16

2.1.4 The Targets ... 18

2.2 The Tracking System ... 18

2.2.1 The Silicon Strip Detectors ... 21

2.2.2 The Analysis Magnet ... 22

2.2.3 The Proportional Wire Chambers ... 22

2.2.4 The Straw Tubes ... 23

2.3 Calorimetry ... 25

2.3.1 The Liquid Argon Calorimeter ... 26

2.3.2 The Forward Calorimeter ... 35

Chapter 3 The Event Selection and Data Acquisition Systems — 37

3.1 The Trigger 37

3.1.1 Beam and Interaction Definitions 37

3.1.2 The Pretrigger 38

3.1.3 Triggers 40

3.2 The Data Acquisition System 45

Chapter 4 Data Reconstruction — 47

4.1 PLREC – PLanes REConstruction 48

4.1.1 Beam Tracking 48

4.1.2 Downstream Tracking (PWC and STRAW Tracks) 49

4.1.3 Upstream Tracking and Linking 51

4.1.4 Vertex Finding and Relinking 52

4.2 EMREC – ElectroMagnetic REConstruction 53

4.2.1 Unpacking 53

4.2.2 FREDPED 54

4.2.3 Group and Peak Finding 60

4.2.4 Gamma Reconstruction 61

4.2.5 Gamma Correlation and Photon Reconstruction 64

4.2.6 Photon Timing Information 65

Chapter 5 Analysis — 66

5.1 The Data Sample 66

5.2 The EMLAC Energy Scale 66

5.3 Trigger Efficiency Measurement 74

5.3.1 Event-wise Trigger p_T Reconstruction: General Methods 75

5.3.2 Image Charge and other Trigger Challenges 79

5.3.3 The Local Triggers 81

5.3.4 The Global Triggers 82

5.4 The Monte Carlo 85

5.4.1 The Monte Carlo: Event Generation and Reconstruction 86

5.4.2 Comparisons of Monte Carlo and Data 88

5.5 Analysis Methods 89

5.5.1 Vertex Requirements and Related Corrections 90

5.5.2 Muon Bremsstrahlung Rejection 95

5.5.3 Energy Asymmetry Cut 101

5.5.4 Longitudinal Shower Development Cut 102

5.5.5 The Fiducial Cut and the Geometric Acceptance Correction ... 103

5.5.6 The Corrections for Photon Conversion and Beam Absorption . 106

5.5.7 The Reconstruction Efficiency 108

5.5.8 Selection of Valid Trigger Ranges 112

5.5.9 The Beam Contamination Correction 114

5.5.10 The Pointing-Track Cut 114

5.5.11 Normalization 115

5.5.12 Meson Signal Definition 117

5.5.13 Direct Photon Signal Definition 121

5.5.14 Cross Section Calculation 123

5.5.15 Combining 1990 and 1991 π^- Beam Results 124

Chapter 6 Neutral Meson and Direct Photon Results _____ 130

6.1 Invariant Cross Sections 130

6.2 The η/π^0 Ratio 141

6.3 Beam Particle Dependence 141

6.4 Nuclear Dependence 145

6.5 Cross Section Comparisons to other Experiments 158

6.6 Comparison of Cross Sections to NLL QCD Calculations 163

6.7 Systematic Uncertainties 177

6.7.1 Uncertainties in the Cross Sections 177

6.7.2 Uncertainties in Various Cross-Section Ratios 179

6.8 Conclusions 180

References ____ **183**

Appendix: Measured Cross Sections ____ **188**

List of Tables

1.1 Fundamental fermions and gauge bosons. 2

1.2 Selected direct photon experiments [11]. 9

2.1 Target materials, positions, and dimensions in the 1990 and 1991 configurations. Note that the thickness of the hydrogen target is defined by a fiducial cut which excludes regions compromised by the proximity of the container material. See discussion in Section 5.5. 19

2.2 The size and locations of the PWC modules. The size given is both the height and the width of the module and the z position given is an average of the four planes' positions. 23

5.1 Number and types of events recorded by E706. 67

5.2 Comparison of the PDG [5] value to the masses of the π^0 and η mesons obtained after all corrections were applied. 74

5.3 Average weight for beam absorption and photon conversion for the various materials in the 1990 and 1991 target configurations. .. 108

5.4 Signal and sideband mass ranges for π^0 and η meson analysis. . 121

5.5 Corrections applied to the meson and direct photon cross sections. Ranges or values of the corrections are given, along with the variables upon which the corrections depend most strongly. References are given to corrections tabulated or displayed elsewhere. 126

6.1 The nuclear-dependence parameter $\alpha_{Be/Cu}$ measured for π^0, η, and direct photon production by π^- and p beams. (Statistical uncertainties only.) 146

6.2 Combined systematic uncertainty contributions (added in quadrature) for the direct photon, π^0, and η inclusive cross sections. . 178

6.3 Invariant differential cross sections per nucleon as functions of p_T for inclusive π^0 production in the range $-0.75 < Y_{CM} < 0.75$ by 515 GeV/c π^- beam incident upon hydrogen, beryllium, and copper targets. 189

6.4 Invariant differential cross sections per nucleon as functions of p_T for inclusive π^0 production in the range $-0.75 < Y_{CM} < 0.75$ by 530 GeV/c p beam incident upon hydrogen, beryllium, and copper targets. 190

6.5 Invariant differential cross sections per nucleon as functions of p_T for inclusive η production in the range $-0.75 < Y_{CM} < 0.75$ by 515 GeV/c π^- beam incident upon hydrogen, beryllium, and copper targets. 191

6.6 Invariant differential cross sections per nucleon as functions of p_T for inclusive η production in the range $-0.75 < Y_{CM} < 0.75$ by 530 GeV/c p beam incident upon hydrogen, beryllium, and copper targets. 192

6.7 Invariant differential cross sections per nucleon as functions of p_T for inclusive γ production in the range $-0.75 < Y_{CM} < 0.75$ by 515 GeV/c π^- beam incident upon hydrogen, beryllium, and copper targets. 193

6.8 Invariant differential cross sections per nucleon as functions of p_T for inclusive γ production in the range $-0.75 < Y_{CM} < 0.75$ by 530 GeV/c p beam incident upon hydrogen, beryllium, and copper targets. 194

6.9 For several p_T bins, the invariant differential cross sections per nucleon as functions Y_{CM} for inclusive direct photon, π^0, and η production by 515 GeV/c π^- beam incident upon beryllium. .. 195

6.10 For several p_T bins, the invariant differential cross sections per nucleon as functions Y_{CM} for inclusive direct photon, π^0, and η production by 530 GeV/c proton beam incident upon beryllium. 196

List of Figures

1.1 The leading-order diagrams for the production of direct photons. 7

2.1 A schematic drawing of the Meson West Spectrometer in the 1991 configuration. 12

2.2 A schematic drawing of the beamline Čerenkov counter. The numbers label the individual photomultiplier tubes, with 6 phototubes arrayed in each of the proton, kaon, and pion rings. 16

2.3 The positions of the targets and SSD wafers in the 1990 configuration. 20

2.4 The positions of the targets and SSD wafers in the 1991 configuration. 21

2.5 The proportional wire chambers, showing the relative orientations of the X, Y, U, and V planes. Also note that the beam and diffractive regions of the cathode planes were electrically independent from each other and from the main regions, allowing the desensitization of the beam region and preventing the high-intensity beam region from causing inefficiency in the main regions of the PWC's. 24

2.6 A cross-sectional view of a straw tube bundle. 25

2.7 A cut-away schematic view of the gantry and the LAC. 27

2.8 The electromagnetic calorimeter, with a quadrant with splayed layers to show an r–board and a ϕ–board. 29

2.9 A block diagram of the LAC amplifiers. 32

2.10 The pad structure of the HALAC. 33

2.11 An exploded view of part of one cookie. 34

2.12 The forward calorimeter. 36

3.1 p_T summing for the local and global triggers. A local trigger fired if in any octant, any one of the 31 overlapping 16-strip LOCAL's contained a p_T deposition over threshold for that trigger. A global trigger utilized the cutoff-reduced global p_T sum over the entire octant. 41

3.2 A block diagram of the trigger system. The LACAMPs' fast outputs are paired, summed, and attenuated to form 2-strip p_T measurements. Combining four of these produced each of the 32 sums-of-eight. These sum-of-eight p_T's were summed in various ways to provide the basis for the PRETRIGGER and the local and global trigger decisions. 42

3.3 A block diagram of the E706 data acquisition system, showing the pathway of the information from various spectrometer elements through FASTBUS and the PDP's to the 8 mm tape on a MicroVAX. 46

4.1 The time dependence of reconstructed π^0 and η masses (in ratio to accepted values [5]) during the 1990 and 1991 running periods. The open triangles represent the energy detected by the EMLAC for 50 GeV/c incident electron test beam. It should be noted that the time values on the abscissa were only incremented during periods in which beam was present and the EMLAC high-voltage was on. 55

4.2 One quadrant of a raw event with significant pedestal shifts, before application of FREDPED. (Energies in GeV). Note ramp in the Left R View, offset in Right R View, and step in Outer ϕ View. The FREDPED-corrected event is shown in Figure 4.3. 58

4.3 The raw data from the same quadrant for the same event shown in Figure 4.2, but after FREDPED had been invoked, correcting for the ramp and shifts in the pedestals. (Energies in GeV.) 59

5.1 The systematic uncertainty in the cross section for 0.5%, 1.0%, and 2.0% systematic uncertainties in the calibration of the EMLAC energy scale, as measured for inclusive π^0 production by 515 GeV/c π^- beam incident on beryllium. 68

5.2 The average energy lost by photon (solid line) and electron (dashed line) showers in the material in front of the active region of the EMLAC, as determined from the Monte Carlo. 70

5.3 The radial dependence of the EMLAC energy response is demonstrated here by plotting the ratio of reconstructed masses to the nominal values given by the Particle Data Group (PDG) [5] for the 1991 data. Corroborating evidence is supplied by overlaying the radial dependence of E/P (the ratio of the EMLAC energy to the tracking system momentum measurement) for a sample of ZMP electrons. 71

5.4 Observed radial dependence of the reconstructed π^0 mass shown for various BEFORE/AFTER gate settings. The BEFORE/AFTER gate defined the charge-integration time. 72

5.5 The $\gamma\gamma$ mass distributions in the π^0 and η signal regions and the $\pi^0\gamma$ mass distribution in the ω signal region, along with fitted central values and widths. 73

5.6 The mass of the η in the 1991 sample (relative to the PDG value) after the final energy scale calibration versus energy (top) and versus p_T (bottom). 75

5.7 The number distribution of π^0's prior to trigger corrections. In regions of p_T overlap between two triggers, trigger corrections can allow for the use of the higher-threshold trigger, along with its higher statistics. 76

5.8 SINGLE LOCAL LOW (top) and SINGLE LOCAL HIGH (bottom) turnons for selected inner and outer LOCAL's as a function of trigger p_T. The error bars above the turnon region are intended to provide an estimate of the statistical uncertainty of the measurement, and should not be taken to imply that the efficiency could exceed 100%. 83

5.9 Selected inner (left) and outer (right) PRETRIGGER turnons for few (solid) and many (dashed) sums-of-eight. 85

5.10 A comparison of the shapes of data and Monte Carlo π^0 asymmetry distributions. π^0's contributing to this plot were those in the 1990 data sample and the associated Monte Carlo sample with $3.5 < p_T < 4.0$ GeV/c. 89

5.11 A comparison of the shapes of data (histogram) and Monte Carlo (points) $\gamma\gamma$ mass distributions in the π^0 and η signal regions. .. 90

5.12 A comparison of the shapes of data (histogram) and Monte Carlo (points) photon E_{front}/E_{total} distributions in six photon energy bins. 91

5.13 The weighted longitudinal distribution of reconstructed vertices for 1990 (top) and 1991 (bottom) spectrometer configurations. The events contributing to these plots were selected by requiring a $\gamma\gamma$ pair with $p_T > 4.0$ GeV/c with a mass in the π^0 signal region. 93

5.14 The effects of the muon bremsstrahlung rejection cuts on the 1990 $\gamma\gamma$ mass distribution in the vicinity of the π^0 peak for $\gamma\gamma$ p_T in the range 7 to 9 GeV/c in two rapidity bins. The top plots have no muon rejection criteria, the middle satisfy the offline Veto Wall cut, and the bottom plots additionally satisfy the directionality, balanced-p_T, and χ^2/E requirements. 97

5.15 Comparisons of muon and photon distributions of directionality, χ^2/E, and balanced-p_T. The muon sample was selected by requiring veto wall hits, and the photon selection for each cut utilized a combination of the other cuts. 99

5.16 The $\gamma\gamma$ mass distribution before (solid) and after (dashed) an asymmetry cut of 0.75 from the 1991 data. The signal-to-noise ratio is significantly enhanced. 102

5.17 The E_{front}/E_{total} distribution for showers associated with all tracks (top) and electrons only (bottom). A shower with large E_{front}/E_{total} is likely to be of electromagnetic origin. 104

5.18 The fiducial volume of the EMLAC. Plotted here are the positions of photons from π^0's which satisfy the fiducial requirement. ... 105

5.19 The geometric acceptance for single photons (thick histogram) and π^0 and η mesons at high and low p_T (thin solid and dashed histograms, respectively). The abscissa is the center-of-mass rapidity, and the dotted lines at $Y_{CM} = \pm 0.75$ delimit the rapidity region used in this analysis. 107

5.20 The untriggered π^0 reconstruction efficiency (and unsmearing correction) for the proton beam data as a function of transverse momentum and rapidity. Note the suppressed zero. 110

5.21 The SINGLE LOCAL HIGH trigger π^0 reconstruction (and unsmearing correction) efficiency for the proton beam data as a function of transverse momentum and rapidity. Note the suppressed zero. 111

5.22 The SINGLE LOCAL LOW trigger single photon reconstruction efficiency (and unsmearing correction) for the proton beam data as a function of transverse momentum and rapidity. Note the suppressed zero. 113

5.23 The distribution of ΔR^2, the square of the distance (at the face of the EMLAC) between a photon shower and the projected position of the nearest charged track. 116

5.24 For the 1990 π^- beam data, the $\gamma\gamma$ mass distribution for two p_T ranges in the π^0 and η meson signal regions. The full set of cross-section weights have been applied to the events entered into these plots. Note that these plots are not background subtracted. ... 118

5.25 For the 1991 π^- beam data, the $\gamma\gamma$ mass distribution for two p_T ranges in the π^0 and η meson signal regions. The full set of cross-section weights have been applied to the events entered into these plots. Note that these plots are not background subtracted. ... 119

5.26 For the 1991 530 GeV/c proton beam data, the $\gamma\gamma$ mass distribution for two p_T ranges in the π^0 and η meson signal regions. The full set of cross-section weights have been applied to the events entered into these plots. Note that these plots are not background subtracted. 120

5.27 For the 515 GeV/c π^- beam incident on beryllium, the unsubtracted γ/π along with the corresponding γ_{fake}/π computed from the Monte Carlo. 124

5.28 For the 530 GeV/c proton beam incident on beryllium, the unsubtracted γ/π along with the corresponding γ_{fake}/π computed from the Monte Carlo. 125

5.29 Ratios of direct photon (top) and π^0 (bottom) cross sections obtained from the 1991 (numerator) and 1990 (denominator) π^- beam incident upon beryllium, showing very good agreement between these independent measurements. Error bars represent statistical uncertainties only. 129

6.1 The invariant differential inclusive π^0 cross sections per nucleus as functions of the π^0 transverse momentum for 515 GeV/c π^- beam on copper, beryllium, and hydrogen targets. 132

6.2 The invariant differential inclusive π^0 cross sections per nucleus as functions of the π^0 transverse momentum for 530 GeV/c p beam on copper, beryllium, and hydrogen targets. 133

6.3 The invariant differential inclusive η cross sections per nucleus as functions of the η transverse momentum for 515 GeV/c π^- beam on copper, beryllium, and hydrogen targets. 134

6.4 The invariant differential inclusive η cross sections per nucleus as functions of the η transverse momentum for 530 GeV/c p beam on copper, beryllium, and hydrogen targets. 135

6.5 The invariant differential inclusive direct photon cross sections per nucleus as functions of the direct photon transverse momentum for 515 GeV/c π^- beam on copper, beryllium, and hydrogen targets. 136

6.6 The invariant differential inclusive direct photon cross sections per nucleus as functions of the direct photon transverse momentum for 530 GeV/c p beam on copper, beryllium, and hydrogen targets. 137

6.7 The invariant inclusive π^0 cross section per nucleon for 515 GeV/c π^- (left) and 530 GeV/c proton (right) beams incident on beryllium, as a function of Y_{CM} for several p_T intervals. 138

6.8 The invariant inclusive η cross section per nucleon for 515 GeV/c π^- (left) and 530 GeV/c proton (right) beams incident on beryllium, as a function of Y_{CM} for several p_T intervals. 139

6.9 The invariant inclusive direct photon cross section per nucleon for 515 GeV/c π^- (left) and 530 GeV/c proton (right) beams incident on beryllium, as a function of Y_{CM} for several p_T intervals. 140

6.10 The ratio as a function of p_T of the η and π^0 cross sections for 515 GeV/c π^- beam (top) and for 530 GeV/c proton beam (bottom) on the beryllium target. The ratio is essentially independent of p_T; the dashed line indicates the measured ratio. 142

6.11 The η/π^0 ratio versus mean $x_T = 2p_T/\sqrt{s}$ for measurements made by various experiments. The overall trend is relatively flat and the E706 points are quite consistent with other measurements in our x_T region. 143

6.12 The ratio of the cross section from 515 GeV/c π^- beam and 530 GeV/c proton beam on beryllium for direct photons (top) and π^0's (bottom). 144

6.13 The nuclear-dependence parameter $\alpha_{Be/Cu}$ as a function of p_T and rapidity for π^0 production by 515 GeV/c π^- beam. The dashed lines represent the mean value over the range indicated. (See Table 6.1.) 148

6.14 The nuclear-dependence parameter $\alpha_{Be/Cu}$ as a function of p_T and rapidity for π^0 production by 530 GeV/c proton beam. The dashed lines represent the mean value over the range indicated. (See Table 6.1.) 149

6.15 The nuclear-dependence parameter $\alpha_{Be/Cu}$ as a function of p_T and rapidity for η production by 515 GeV/c π^- beam. The dashed lines represent the mean value over the range indicated. (See Table 6.1.) 150

6.16 The nuclear-dependence parameter $\alpha_{Be/Cu}$ as a function of p_T and rapidity for η production by 530 GeV/c proton beam. The dashed lines represent the mean value over the range indicated. (See Table 6.1.) 151

6.17 The nuclear-dependence parameter $\alpha_{Be/Cu}$ as a function of p_T and rapidity for direct photon production by 515 GeV/c π^- beam. The dashed lines represent the mean value over the range indicated. (See Table 6.1.) 152

6.18 The nuclear-dependence parameter $\alpha_{Be/Cu}$ as a function of p_T and rapidity for direct photon production by 530 GeV/c proton beam. The dashed lines represent the mean value over the range indicated. (See Table 6.1.) 153

6.19 A comparison of the nuclear-dependence parameter α measured for π^0 production by a 515 GeV/c π^- beam and for charged pion production by 200 GeV/c π^- beam. The 515 GeV/c results are those measured in this thesis with additional low-p_T points from the low-bias trigger analysis by Kuehler [35], and the 200 GeV/c results were measured by Frisch *et al.* [9]. 154

6.20 $\alpha_{Be/Cu}$ measured for direct-photon production by 515 GeV/c π^- beam (top) and by 530 GeV/c proton beam (bottom), compared to theoretical expectations [10]. 155

6.21 The hydrogen-, beryllium-, and copper-target cross sections per nucleon for π^0 and direct-photon production by 515 GeV/c π^- beam averaged over $-0.75 < Y_{CM} < 0.75$ and $p_T > 4$ GeV/c. The dashed lines are fits to the copper and beryllium data; the slope of the line is $\alpha_{Be/Cu} - 1$. 156

6.22 The hydrogen-, beryllium-, and copper-target cross sections per nucleon for π^0 and direct-photon production by 530 GeV/c proton beam averaged over $-0.75 < Y_{CM} < 0.75$ and $p_T > 4$ GeV/c. The dashed line are fits to the copper and beryllium data; the slope of the line is $\alpha_{Be/Cu} - 1$. 157

6.23 π^0 production by π^- beams at various values of $\sqrt{s}$. Cross sections measured by NA24 [36], WA70 [37], E111 [38], and NA3 [39] are compared to the E706 results. The uncertainties shown are statistical only, and nuclear dependence (where applicable) has been taken into account, using the α measured in this analysis. 159

6.24 Pion production by proton beams at nearby values of $\sqrt{s}$. Cross sections measured by R806 [40], CCRS [41], CCOR [42], and CP [43] are compared to the E706 results. The uncertainties shown are statistical only; in the case of the Chicago-Princeton result, the uncertainties shown are the spread in the $\pi^\pm$ results. Nuclear dependence has been taken into account for the E706 data. ... 160

6.25 Direct-photon production by π^- beams at various values of $\sqrt{s}$. Cross sections measured by NA24 [44], NA3 [45], and WA70 [46] are compared to the E706 results. The uncertainties shown are statistical only, and nuclear dependence (where applicable) has been taken into account, using the α measured in this analysis. 161

6.26 Direct-photon production by proton beams at various values of $\sqrt{s}$. Cross sections measured by R110 [47], R806 [48], R108 [49], UA6 [50], NA24 [44], WA70 [51], NA3 [45], and E629 [52] are compared to the E706 results (including preliminary 800 GeV/c results). The uncertainties shown are statistical only, and an adjustment for nuclear dependence (where applicable) has been made. 162

6.27 The fractional difference between π^0 cross-section calculations, illustrating the calculations' sensitivity to choice of fragmentation scale (top), factorization and renormalization scales (middle), and choices of a few recent PDF's (bottom). 167

6.28 The fractional difference between direct photon cross-section calculations, illustrating the calculations' sensitivity to choice of factorization scale (top), renormalization scale (middle), and choices of a few recent PDF's (bottom). 168

6.29 Comparison of the invariant π^0 cross section for 515 GeV/c π^- beam on beryllium to calculations employing BKK (dashed) and CGGRW (dotted) fragmentation functions. Both calculations were performed with ABFOW/ABFKW parton distribution functions and with $Q = p_T/2$, and both were corrected for the observed nuclear dependence. 169

6.30 Comparison of the invariant π^0 cross section for 530 GeV/c proton beam on beryllium to calculations employing BKK (dashed) and CGGRW (dotted) fragmentation functions. Both calculations were performed with ABFOW parton distribution functions and with $Q = p_T/2$, and both were corrected for the observed nuclear dependence. 170

6.31 QCD calculations with $Q^2 = \frac{1}{2}p_T$ compared to the measured η cross section for 515 GeV/c π^- beam incident on beryllium. The CGGRW [62] fragmentation function depends on the parameter δ, which corresponds to a cone size used in assigning final state η's to fragmenting partons. 171

6.32 QCD calculations with $Q^2 = \frac{1}{2}p_T$ compared to the measured η cross section for 530 GeV/c proton beam incident on beryllium. The CGGRW [62] fragmentation function depends on the parameter δ, which corresponds to a cone size used in assigning final state η's to fragmenting partons. 172

6.33 Comparison of the invariant direct photon cross section for 515 GeV/c π^- beam on beryllium to calculations employing ABFOW/ABFKW parton distribution functions with $Q = p_T$ (dotted) and $Q = p_T/2$ (dashed). 173

6.34 Comparison of the invariant direct photon cross section for 530 GeV/c proton beam on beryllium to calculations employing the ABFOW parton distribution function with $Q = p_T$ (dotted) and $Q = p_T/2$ (dashed). 174

6.35 The π^0 and direct photon cross sections for 515 GeV/c π^- beam on beryllium compared to calculations which included k_T's of 1.0 (dashed) and 1.4 GeV/c (dotted). 175

6.36 The π^0 and direct photon cross sections for 530 GeV/c proton beam on beryllium compared to calculations which included k_T's of 1.0 (dashed) and 1.4 GeV/c (dotted). 176

Chapter 1 Introduction

This thesis presents results obtained from data taken during the 1990-1991 fixed-target run of experiment E706 at the Fermi National Accelerator Laboratory (Fermilab). E706 is a second-generation experiment proposed to study direct photons, and the apparatus designed for this purpose was built according to specifications based on experience gained from the earlier experiments. The centerpiece of the E706 spectrometer, a finely-segmented Liquid Argon Calorimeter (LAC), provided good energy and excellent position resolution for direct photons and their backgrounds. The 1988 fixed-target run, E706's initial run, provided an opportunity to evaluate the performance of various components of the spectrometer, and a number of important improvements were made prior to the 1990-1991 run. The results from the 1988 data, available via Refs. [1, 2, 3, 4], provide a preview of the much larger and richer 1990-1991 samples.

The following sections contain a brief discussion of the relevant theoretical framework, in addition to a discussion of the motivations for studying direct-photon production.

1.1 The Standard Model and Quantum Chromodynamics

The Standard Model has been relatively successful in describing three of the four basic forces in nature, namely the electromagnetic, the weak, and the strong forces, leaving only gravitation yet to be assimilated. In the standard model, there are two families of fundamental spin-$\frac{1}{2}$ particles, namely leptons and quarks. As shown in Table 1.1, each family of fermions contains six particles[1] categorized into three generations. Each leptonic generation consists of a charged lepton

[1] The corresponding antiparticles are implied.

Leptons			Charge
ν_e	ν_μ	ν_τ	0
e	μ	τ	-1

Quarks			Charge
u	c	t	$+\frac{2}{3}$
d	s	b	$-\frac{1}{3}$

Interaction	Mediating Bosons	Source
Electromagnetism	γ	Electric Charge
Weak Force	$W^{\pm}, Z^0$	Weak Charge
Strong Force	g (8 varieties)	Color
Gravitation	graviton	Mass

Table 1.1 Fundamental fermions and gauge bosons.

and a corresponding electrically neutral neutrino. Similarly, each of the three generations of quarks consists of a $+\frac{2}{3}$-charged quark paired with a quark with electric charge of $-\frac{1}{3}$ for a total of six quark flavors. Interactions among these particles are mediated by the various gauge bosons, also shown in Table 1.1.

Quantum ChromoDynamics (QCD), the theory which describes the strong interaction, derives its name from the designation of the strong charge as *color*. Color is a characteristic of a subset of the standard model fundamental particles, specifically the quarks and gluons, which collectively are referred to as partons. Hadrons, or particles composed of partons, are the bound states of two or more "valence" quarks; the binding force is mediated by gluons and thus the interior of the hadron is awash in gluons and gluon-produced virtual $q\bar{q}$ pairs (the "sea"

of quarks). Hadrons are observed to be colorless. Mesons are hadrons composed of a valence quark and a valence antiquark with opposite color charge. Baryons contain three valence quarks, with each of the color varieties represented, again producing a color singlet state. The hypothesis that a free, colored state cannot be produced is referred to as *confinement*.

Exact calculations of cross sections for processes mediated by the strong interaction using QCD have not been accomplished. Instead, approximations to the cross sections are obtained using perturbation theory, with expansions in the strong coupling constant, α_s. To leading $\log^2$ in Q^2,

$$\alpha_s(Q^2) = \frac{12\pi}{(11n_c - 2n_f)\ln(Q^2/\Lambda^2)} \tag{1.1}$$

where Q^2 is the momentum transfer, Λ is a scale parameter used in the expansion,[3] n_c is the number of QCD colors, and n_f is the number of quark flavors. This equation illustrates the concept of *asymptotic freedom*, i.e. that as $Q^2 \to \infty$, $\alpha_s \to 0$. Asymptotic freedom justifies the use of perturbative calculations of parton-level cross sections in the high-Q^2 regime, and provides motivation for the investigation of interactions which produce particles with large transverse momentum (high p_T).

Outside the realm of the parton-level hard scatter, the perturbative calculations break down: when Q^2 is small, α_s is of order unity or larger. For this reason, the non-perturbative regimes before and after the hard scatter

---

[2] "Leading log" refers to the procedure in which an expansion is summed to all orders, retaining only terms containing the leading-order logarithm.

[3] If it were possible to sum all terms in the expansion, α_s would be independent of Λ. Since this is not the case, $\Lambda = 234 \pm 26 \pm 50$ has been determined experimentally [5].

are separated out of the calculation in a process termed *factorization*. The probability of finding within hadron I a parton i with a fraction x_i of the hadron's momentum is given by a Parton Distribution Function (PDF), which is designated by $G_{i|I}(x_i, Q^2)$. The process of *hadronization*, or the dressing of outgoing partons to produce hadrons, defines the fragmentation function: the probability that an outgoing parton i will produce a hadron I with a fraction z of the original parton momentum is designated by $D_{I|i}(z, Q^2)$. In factorization, fragmentation functions and parton distribution functions are assumed to be independent of the details of the interaction being investigated.[4] Using measurements from a variety of experiments, these functions can be constrained and our understanding of perturbative QCD can be advanced.

Within the above framework, the inclusive cross section for initial particles A and B scattering to produce final particle C is given by

$$E_C \frac{d\sigma}{d^3p_C}(AB \to CX) = \sum_{abcd} \int dx_a dx_b dz_c G_{a|A}(x_a, Q^2) G_{b|B}(x_b, Q^2)$$
$$\times D_{C|c}(z_c, Q^2) \frac{\hat{s}}{z_c^2 \pi} \frac{d\sigma}{d\hat{t}}(ab \to cd) \delta(\hat{s} + \hat{t} + \hat{u}) \qquad (1.2)$$

where the assumption has been made that the interacting partons are colinear [6]. Here, $\hat{s}$,$\hat{t}$,and $\hat{u}$ are the Mandelstam variables defined by

$$\hat{s} = (p_a + p_b)^2 \qquad (1.3)$$

$$\hat{t} = (p_a - p_c)^2 \qquad (1.4)$$

$$\hat{u} = (p_a - p_d)^2 \qquad (1.5)$$

and $\frac{d\sigma}{d\hat{t}}$ is the parton-level cross section. The lower-case indices label the partons and summation over all possible parton combinations is implied. X represents all products of the interaction except C.

[4] To first order, even the Q^2 dependence of the PDF's and fragmentation functions is small, and these functions are said to *scale*. Higher order effects do, however, produce a dependence on Q^2, i.e. scaling violation.

1.2 Motivations

The term *direct photon* refers to photons which are produced *directly* in the hard scattering interaction, as opposed to those which result from the decay of other particles produced in an interaction. Since high-p_T photons from neutral-meson decay mimic direct photons, detailed knowledge of neutral-meson production is an essential part of the careful study of direct photons. The following sections present some of the motivations for the study of direct-photon, π^0, and η production.

1.2.1 Direct Photons

The study of QCD processes in which quarks and gluons are the primary products of the hard scatter is complicated by the fragmentation of these colored particles. Experimentally, analysis of such data is sensitive to the details of the jet-finding algorithm; in general, it is not possible to define an algorithm that includes all products of a single parton's fragmentation while simultaneously excluding products of the other hard-scatter or spectator partons.[5] In the case of direct photons, such an algorithm is unnecessary. The direct photon is the entire "jet" and an isolated photon provides a reasonably well-defined experimental signature. In addition, calculations concerning inclusive direct-photon production avoid the uncertainties and complexities associated with fragmentation, and since QED is well understood, the parton-level reaction kinematics are simpler and less uncertain.

Experimental and calculational considerations would be meaningless if direct photons did not provide interesting constraints on the current understanding

[5] In fact, this very concept contradicts the color-neutralizing function of fragmentation.

of QCD. However, direct-photon measurements should in fact provide such constraints. Figure 1.1 shows diagrams of the two first-order processes contributing to direct-photon production; the Compton diagrams are sensitive to the gluon PDF while the annihilation diagrams involve the fragmentation of the emerging gluon. Thus, studies of direct photons may provide valuable insight into gluon behavior in QCD.[6]

While the motivations for the study of direct photons are clear, there remain some experimental challenges. The chief among these is distinguishing the direct-photon signal from the background due to electromagnetic decays of neutral mesons (in particular, π^0's, but also η's, ω's, etc.). These neutral mesons are products of the fragmentation of quarks and gluons and are produced at rates of $\approx$100 times that of direct photons. However, the fragmentation process distributes the outgoing parton's transverse momentum among several particles; thus, the signal-to-background ratio for direct photons increases rapidly with p_T. In addition, the use of a finely-segmented calorimeter makes possible the reconstruction of many such mesons and therefore allows the rejection of much of the background from associated decay photons.

1.2.2 Neutral Mesons

Although meson studies are of primary importance in the rejection of the direct-photon background, it should be noted that such studies are also useful in their own right. The π^0 and η cross section measurements can be used either to test QCD or to constrain fragmentation functions. Neutral meson measurements using the E706 data set are quite interesting due both to their precision and large (and, in the case of the π^- beam, unique) kinematic range.

---

[6] This is particularly true if these fundamental parton-level diagrams can be studied individually by using various incident beam particle types with different quark content; such a study is in progress [7].

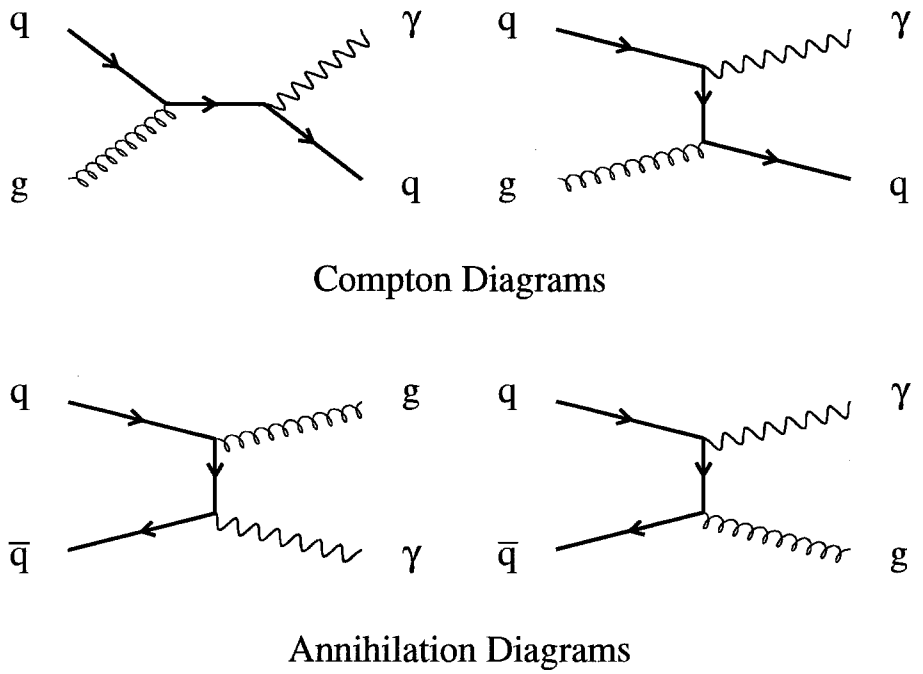

Figure 1.1 The leading-order diagrams for the production of direct photons.

1.2.3 Nuclear Dependence

The dependence of particle production on the target material can be parametrized in the form

$$\sigma_i = \sigma_0 A_i^{\alpha} \tag{1.6}$$

where σ_i is the cross section per nucleus i of atomic mass A_i, σ_0 is the nominal cross section for a free nucleon, and the parameter α may depend on transverse momentum and rapidity. In fact, at low p_T, one might expect $\alpha \approx \frac{2}{3}$ since the cross section should be proportional to the cross-sectional area of the nucleus. At higher p_T's, individual nucleons are probed, leading to an expectation of $\alpha \approx 1$. Several experiments [8, 9] have measured values of α for meson production exceeding unity. One explanation for this observed effect is multiple scattering (within the nucleus) of the partons involved in or produced by the hard scatter. E706 is a unique direct-photon experiment in that it has targets of several different materials; therefore the E706 data can be used to measure α for direct-photon production and also can test the multiple-scattering hypothesis. Since it is unlikely that direct photons would rescatter, only the incoming parton might be affected, and thus one might expect that the measured α for direct-photon production would be closer to unity than the corresponding α's measured for neutral-meson production at high p_T. Calculations of α have been recently published [10], and will be compared to the E706 measurement.

1.3 Direct Photon Experiments

Table 1.2 presents a selection of the other direct photon experiments which have measured results comparable to those contained in this thesis. The six experiments listed in the top portion of the table are fixed-target experiments; the remainder employ colliding beams. E706 and E629 were performed at Fermilab;

Experiment	$\sqrt{s}$ (GeV)	Beam	Target(s)	x_T Range
E629	19.4	$\pi^{\pm}$, p	C	0.22 – 0.52
NA3	19.4	$\pi^{\pm}$, p	C	0.26 – 0.62
WA70	23.0	$\pi^{\pm}$, p	H	0.35 – 0.61
NA24	23.7	$\pi^{\pm}$, p	H	0.23 – 0.59
UA6	24.3	p, $\overline{p}$	H	0.28 – 0.58
E706	**31.1,31.6,38.8**	$\pi^{\pm}$, **p**	**H,Be,Cu**	**0.21 – 0.77**
R108	62	p	p	0.17 – 0.42
R110	63	p	p	0.14 – 0.29
R806	31,45,53,63	p	p	0.12 – 0.38

Table 1.2 Selected direct photon experiments [11].

the remainder were performed at CERN. It should be noted that there are a number of other direct-photon experiments, including several using very high $\sqrt{s}$ $\overline{p}p$ collisions to probe regions of very small x_T.

1.4 Thesis Overview

This thesis will provide a description of the spectrometer, data selection and acquisition systems, event reconstruction methods, and analysis techniques used to study π^0, η, and direct-photon production. For the E706 515 GeV π^- and 530 GeV proton beams incident on the beryllium, copper, and hydrogen targets, measured cross sections, cross section ratios, and nuclear dependences will be presented and compared to data from other experiments and recent phenomenological calculations.

Chapter 2 The Spectrometer

The various elements of the E706 spectrometer can be partitioned by function into three divisions. The first division, the beam transport system and target region, was designed to direct beams of various particles and energies onto a number of nuclear targets. The second, the tracking system, provided information concerning the trajectories of the charged particles emerging from interactions. The third division consisted of a series of calorimeters, which measured the positions and energies of neutral particles, which is vital information for the study of direct photons. For reference, Figure 2.1 displays the elements of the apparatus housed within the experimental hall, including spectrometer elements used primarily by E672. (Fermilab E672, which accumulated data concurrently with E706, employed a high-mass dimuon trigger to study J/ψ production in hadronic interactions.)

The following sections will describe the three divisions, beginning with the production of the beam, and proceeding through the various subsystems of the apparatus roughly following the direction of the beam propagation, i.e. *downstream*. Within the experimental hall, the coordinate system chosen to describe the spectrometer has its origin in the vicinity of the targets. The nominal beam direction defines the z axis, with the beam travelling in the positive z direction. The y axis is in the vertical direction ("up" is positive), and the x axis is then determined by the right-hand rule.

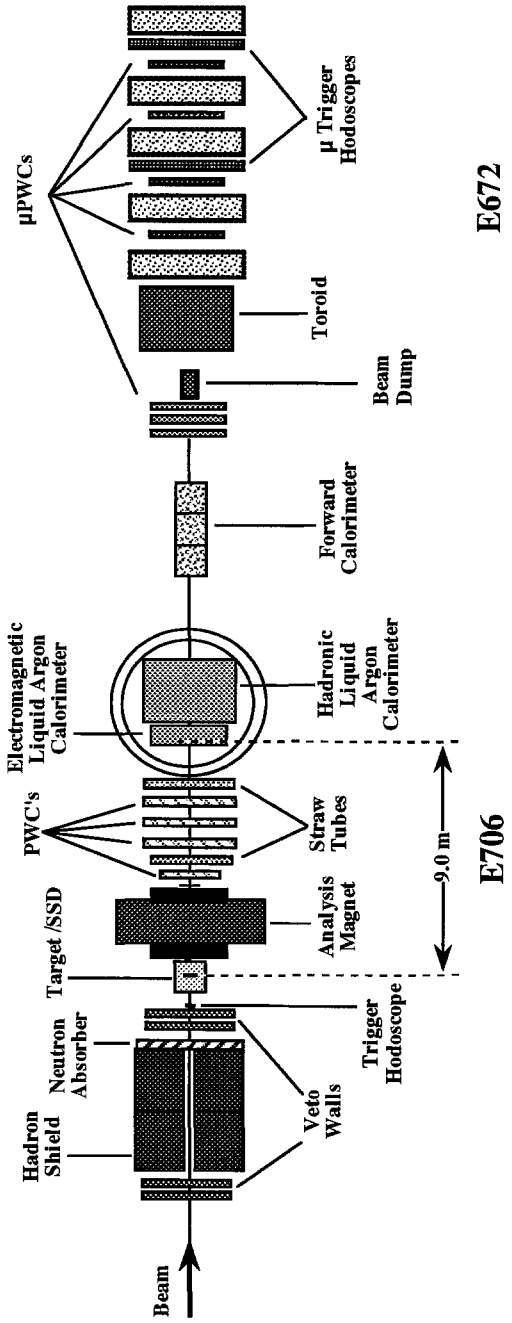

Figure 2.1 A schematic drawing of the Meson West Spectrometer in the 1991 configuration.

2.1 Beamline and Target

2.1.1 Meson West Beamline

During the 1990/91 fixed-target run, the Tevatron accelerated $\approx 10^{13}$ protons per 58-second cycle. The acceleration of the protons to 800 GeV/c occurred during the first 35 seconds. During the 23-second slow extraction period, or *spill*, these protons were extracted from the Tevatron and split among the three FNAL fixed-target experimental areas, namely Meson, Proton, and Neutrino. The beam was distributed among the various experiments housed in these areas. Due to the RF structure of the Tevatron, beam protons were clustered in $\approx$1 ns buckets separated by 19.1 ns.

The Meson West beamline transported beam from the main switchyard to MW9, the building which housed the E706 spectrometer. Three main types of beam[1] were transported to MW9 during the 1990/91 run, namely 800 GeV/c primary protons and positive and negative polarity secondary beams at $\approx$500 GeV/c. The secondary beams were produced by 800 GeV/c primary protons incident on a beryllium target[2] which was housed in MW6. The beam momentum was selected by the optics of the secondary beamline between the primary target and MW9. The positive protons in the secondary beam had a mean momentum of 530 GeV/c; the mean momentum of the pions in the negative beam was 515 GeV/c. Each secondary beam had a non-negligible momentum "bite" with the RMS half-width $\frac{\Delta p}{p} \approx 6\%$. To generate the desired secondary

---

[1] For a summary of the data taken by E706 with the various beam types, see Table 5.1.

[2] This primary target was 1.14 interaction lengths in 1990 and 0.75 interaction lengths in 1991.

beam rate[3] of $\approx 2 \times 10^8$ particles per spill required $\approx 2 \times 10^{12}$ primary protons per spill for positive polarity beam and $\approx 6 \times 10^{12}$ primary protons per spill for negatives.[4] Radiation safety concerns and the instability in the extraction of very low intensity primary beam forced the use of higher intensity primary beam ($\approx 5 \times 10^{11}$ protons per spill) and pin-hole collimators to achieve the desired beam intensities of $\approx 2 \times 10^8$ for incident 800 GeV/c beam.

Associated with the production and transport of the secondary beams were hadronic particles which travelled parallel to the beamline at some distance from the beamline, forming what is referred to as the *beam halo*. Since halo particles impinging on the electromagnetic calorimeter mimicked high-p_T showers, their ubiquitous presence could dominate a trigger designed to detect the relatively rare genuine high-p_T events unless steps were taken to reduce their frequency. To remove these beam halo particles, five spoiler magnets were installed in the secondary beamline. Each of these beamline elements generated a magnetic field which deflected halo particles away from the beamline while leaving the trajectory of central beam particles unchanged. In addition, a 900-ton steel hadron shield was placed just inside MW9. Measuring 3.7 m high by 4.3 m wide by 4.7 m long, the hadron shield had a beam hole through its center and a removable vertical stack of steel positioned above the beamhole so that the beam could be pitched up or down for calibration purposes. Immediately downstream of the hadron shield was a large tank of distilled water to moderate neutrons coming from the hadron absorber. Despite the spoiler magnets, a small number of muons survived to impinge upon the spectrometer. To detect these occurrences, large scintillation

---

[3] Based on limits imposed by the data acquisition speed.

[4] Radiation safety issues limited the primary intensity to $2 - 3 \times 10^{12}$ for a fair fraction of the 1990 run (negative beam).

counters, termed *veto walls*, were positioned to sandwich the hadron shield. In 1990, there were two veto walls placed downstream of the hadron shield and one upstream of it. Before the 1991 run, an additional upstream veto wall was added. Each veto wall consisted of four quadrants, and a coincidence between hits in corresponding quadrants of an upstream and a downstream wall was sufficient to reject an event. Veto wall information was also used later in the analysis to remove additional suspect apparently high-p_T events. (See Section 5.5.)

2.1.2 The Čerenkov Detector

Since the secondary beams were composed of pions, kaons, and protons (or antiprotons), a differential Čerenkov detector (Figure 2.2) was placed in the beamline to tag the incident beam particle species. This detector, a 43-m long helium-filled cylinder, was placed in MW8, a region of the beamline designed to have minimal angular divergence of the beam. As a particle traverses a gas with sufficiently high velocity, it emits Čerenkov radiation at an angle which depends on the particle's mass and velocity and the index of refraction of the medium. In the E706 Čerenkov detector, the index of refraction could be adjusted by increasing or decreasing the helium pressure. At the optimal operating pressure, the angular separation of light from the three particle species is sufficiently large that, through the use of a spherical mirror on the downstream end of the detector and a sophisticated array of optics, light from each species impinged on its own circular array of photomultiplier tubes, effectively simultaneously tagging the incident beam particle species. Using the Čerenkov detector, the negative beam was found to consist of 97% π^-'s, 2.9% K^-'s, and 0.1% $\bar{p}$'s. The particle fractions for the positive beam were 96.7% (proton), 2.8% (pion), and 0.5% (kaon) [7].

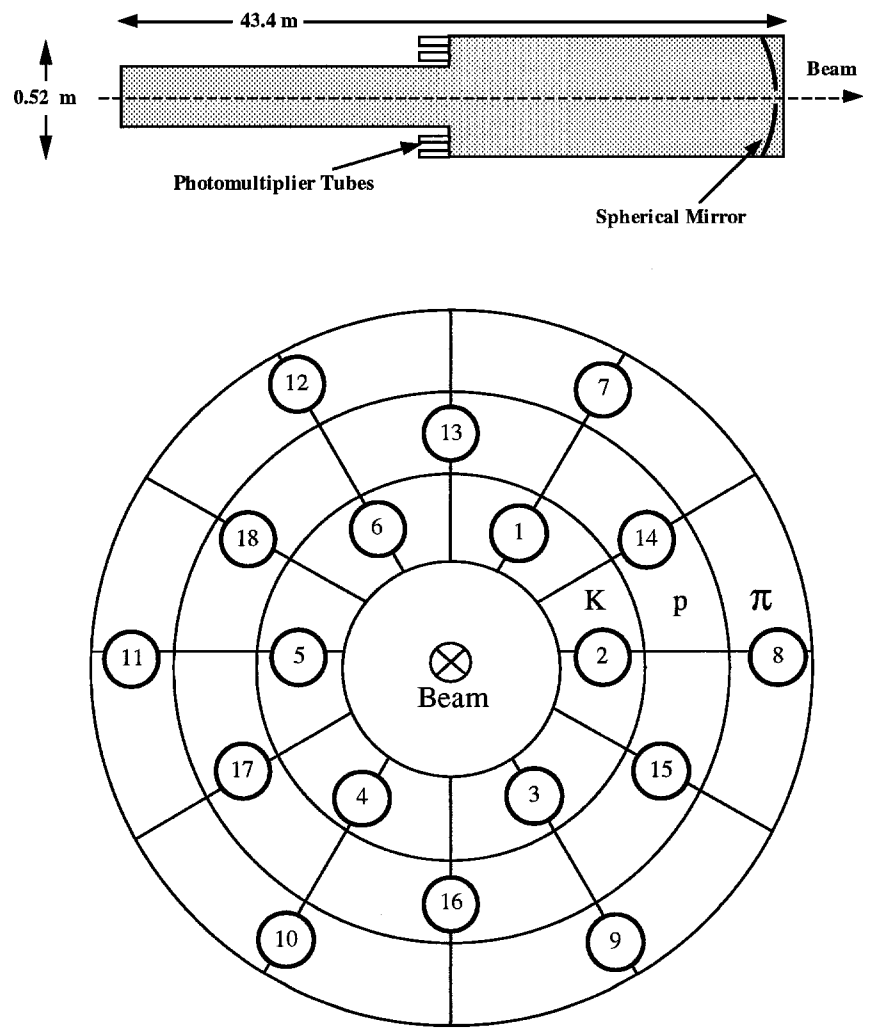

Figure 2.2 A schematic drawing of the beamline Čerenkov counter. The numbers label the individual photomultiplier tubes, with 6 phototubes arrayed in each of the proton, kaon, and pion rings.

2.1.3 The Beam and Interaction Counters

The hodoscope, placed immediately downstream of the veto walls, was designed to detect beam particles incident upon the target region. The hodoscope consisted of three planes of scintillating counters, each of which was 2 mm thick and 35 mm long and consisted of 12 transverse elements. The eight central elements of each hodoscope plane were 1 mm wide to identify buckets containing more than one incident beam particle and to avoid detector rate limitations. Since the beam was considerably less intense near the edges of each plane, wider elements were employed near the planes' extremities. The elements adjacent to the central eight were 2 mm in width, and the edge elements were 5 mm wide. The three planes, labelled X, Y, and U, were oriented such that the Y plane was rotated by 90° with respect to the X plane and the U plane was rotated by 45° relative to the others.

The beamhole counter was a scintillating counter with a small hole cut in the beam region. This counter was used to define the transverse beam size to match the beam silicon strip detector acceptance and to veto events with multiple incident beam particles for which at least one particle was outside the hodoscope. In 1990, the beam hole counter was a single plane with a 1 cm hole in its center. In 1991, this single counter was replaced with four counters, each covering a quadrant. The interior corner of each of the four was removed such that when taken as a unit, the four planes formed a single beam hole with a diameter of 1.2 cm.

Two pairs of scintillating counters were employed to identify interactions. The first pair of interaction counters was downstream of the targets, between the silicon strip detectors and the magnet. Each of these planes was 7.6×15.2 cm^2

and each had a semicircular beamhole of diameter 1.9 cm to avoid detection of non-interacting beam particles. The second pair of planes, located downstream of the magnet, were 10.2×20.4 cm^2 with beam hole diameters of 3.8 cm.

These various scintillation counters were used in the definition of a trigger (see Section 3.1.1). The individual scintillation elements of the hodoscope, beam hole counter, and interaction counters were read out for the 15 buckets roughly centered on the in-time, or triggering, bucket. In addition, numerous quantities based on the status of various scintillators and other trigger elements were sent to scalers and recorded. For example, BEAM and BEAM1 (defined in Section 3.1.1) were scaled, along with quantities such as LIVE_BEAM1, which required BEAM1 in conjunction with a computer-ready signal. These and other scaled quantities were used in the cross section calculations.

2.1.4 The Targets

During 1990, four targets were used; two cylinders of beryllium were downstream of the two thin copper targets. In 1991, the two similar thin copper targets were used and a liquid hydrogen target was installed between two beryllium targets. The sizes and locations of the targets in both configurations are tabulated in Table 2.1.

2.2 The Tracking System

The E706 charged-particle tracking system consisted of the Silicon Strip Detectors (SSD's), the analysis magnet, the Proportional Wire Chambers (PWC's), and the Straw Tube Drift Chambers (STRAW's). By identifying charged particles and measuring their momenta, the tracking system provided vital information for a variety of purposes. One such purpose was the

Data Run	Material	$Z_{UPSTREAM}$ (cm)	Diameter (cm)	Length (cm)
1990	Cu	-15.54	2.54	0.0780 ± 0.0005
	Cu	-15.22	2.54	0.0781 ± 0.0005
	Be	-14.65	2.08	3.7092 ± 0.0005
	Be	-9.92	2.06	1.1201 ± 0.0005
1991	Cu	-30.44	2.54	0.0780 ± 0.0005
	Cu	-29.95	2.54	0.0781 ± 0.0005
	Be	-28.36	8.1	0.249 ± 0.001
	H_2	-26.9	6.35	15.3
	Be	-10.52	9.9	0.282 ± 0.001
	Be	-10.8	2.54	2.5397 ± 0.0005

Table 2.1 Target materials, positions, and dimensions in the 1990 and 1991 configurations. Note that the thickness of the hydrogen target is defined by a fiducial cut which excludes regions compromised by the proximity of the container material. See discussion in Section 5.5.

reconstruction of primary and secondary vertices. A vertex is defined as a point from which multiple tracks are observed to diverge. The primary vertex results from the interaction of the incident beam with the target; the determination of the location of the primary vertex was necessary to calculate the kinematics of the resulting particles and to determine in which of the nuclear targets this initial interaction occurred. Secondary vertices, which are due to particle decays or interactions involving the products of the primary interaction, occur farther downstream. Another very significant use of this tracking information was in

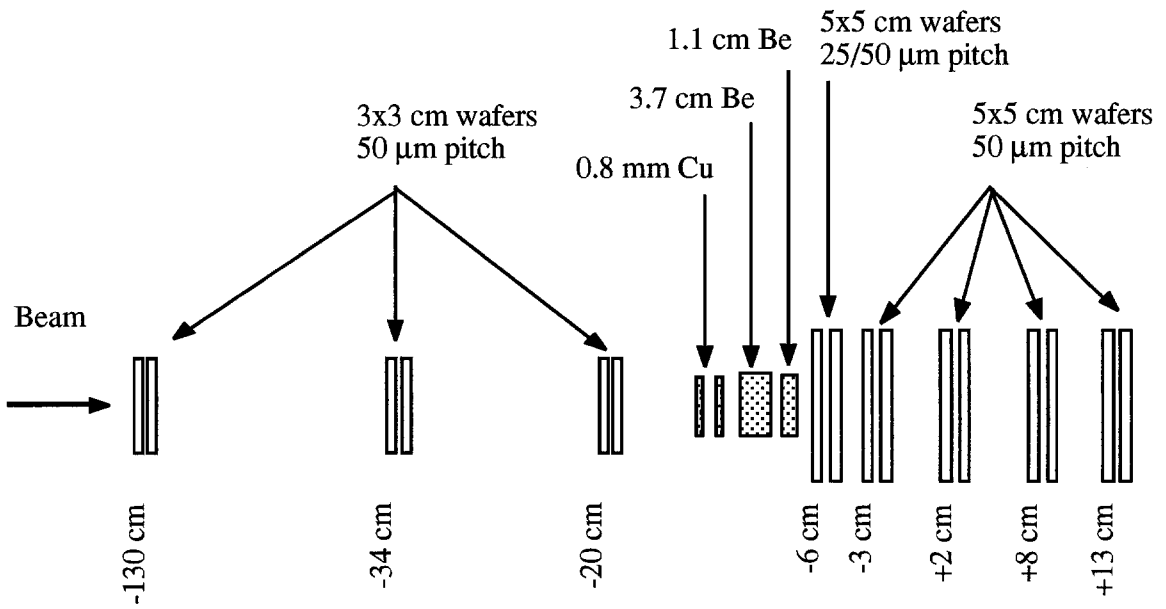

Figure 2.3 The positions of the targets and SSD wafers in the 1990 configuration.

the calibration of the EMLAC energy scale. Since electrons' momenta can be independently determined by the tracking system, electrons were used in the initial stages of energy calibration. The final energy scale was confirmed by using the tracking system to reconstruct Zero-Mass Pairs (ZMP's) produced when one or both photons from π^0 decay converted in the target into e^+e^- pairs, and comparing the peak in the reconstructed γe^+e^- or $e^+e^-e^+e^-$ mass to the known π^0 mass. Yet another important use of the tracking information was to identify and measure away-side jets. Although the analysis in this thesis does not directly incorporate the jet information, a number of other studies [4, 12, 13] have made use of the jet data.

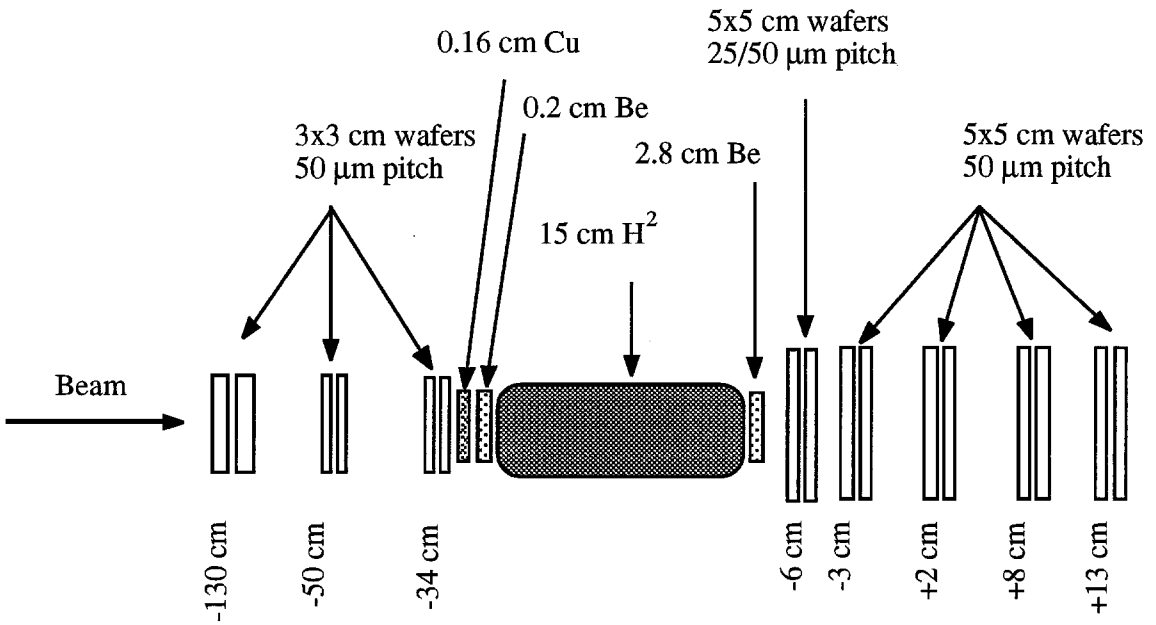

Figure 2.4 The positions of the targets and SSD wafers in the 1991 configuration.

2.2.1 The Silicon Strip Detectors

Silicon Strip Detectors (or SSD's) detect the passage of a charged particle by collecting the charge induced upon strips etched into silicon wafers. Eight pairs of silicon strip detectors were positioned along the beam axis near to the target region (see Figures 2.3 and 2.4). Three pairs upstream of the targets provided beam-track information; these SSD's were 3×3 cm^2 in area. The remaining five downstream SSD pairs were 5×5 cm^2 in area and were essential in vertex reconstruction. Each of these pairs consisted of an SSD with its strips etched parallel to the y axis and an SSD with its strips etched parallel to the x axis. The spacing

between strip centers, or *pitch*, was 50 μm for all SSD pairs except the first one downstream of the target; this pair had a pitch of 25 μm near the beam axis and 50 μm at larger angles. All 16 SSD's, their front-end electronics, and the targets were contained in an aluminum box which provided both electronic shielding and physical protection. Further details on the construction and performance of the E706 SSD system may be found in Refs. [14] and [15].

2.2.2 The Analysis Magnet

Positioned 2 m downstream of the target, MW9AN was a rectangular analysis magnet which provided charged particles with a momentum impulse of 450 MeV/c in the x-z plane. The magnet aperture was 35.6×25.4 cm^2 on the upstream end and increased to 137.2×124.5 cm^2 on the downstream end. The entire aperture was filled with a helium bag to minimize interactions in this region. Mirror plates were positioned upstream and downstream of the magnet to reduce the fringe field. This served both to reduce interference with the beam and interaction counters' photomultiplier tubes and also to simplify track reconstruction.

2.2.3 The Proportional Wire Chambers

Sixteen planes of proportional wire chambers [16], directly downstream of the magnet, were grouped into four modules. Each module contained an X, Y, U, and V plane, where the U planes were at an angle of $+37^\circ$ and the V planes were at an angle of -53° with respect to the y axis (see Figure 2.5). The sizes and positions of the PWC modules are given in Table 2.2. The sense wires were made of gold-plated tungsten, and had a diameter of 20 μm and a pitch of 2.54 mm. The graphite-coated mylar cathode was segmented into pads which allowed for independent control of the high voltage; this was particularly useful in desensitizing the beam region during high-intensity running. The active medium was a gaseous mixture

Module Number	Height(m)	Width (m)	Z Position (cm)
1	1.219	1.626	382
2	2.032	2.032	475
3	2.032	2.032	570
4	2.438	2.438	663

Table 2.2 The size and locations of the PWC modules. The size given is both the height and the width of the module and the z position given is an average of the four planes' positions.

of 18% isobutane, 1.1% isopropyl alcohol, 0.1% freon, and 79.7% argon. The signals, from a total of 13440 channels, were amplified, latched, and read out using Nanometrics[5] electronics.

2.2.4 The Straw Tubes

To improve the resolution of the downstream tracking system, a straw tube drift chamber module was placed between PWC modules one and two, and another was placed downstream of the fourth PWC module [17]. Each of the two straw tube modules contained four X and four Y planes. To minimize the left-right ambiguity of the drift timing information (see below), the four planes in X (or Y) were offset relative to each other. As Figure 2.6 indicates, the second, third, and fourth planes were offset by $\frac{1}{2}$, $\frac{1}{4}$, and $\frac{3}{4}$ tube diameters, respectively, relative to the first plane. 20 μm gold-plated tungsten anode wires were threaded through the aluminized mylar tubes, which served as the cathodes. The tubes had diameters of 1.0 cm for the upstream module and 1.6 cm for the downstream

[5] Nanometric Systems, Inc., Oak Park Illinois

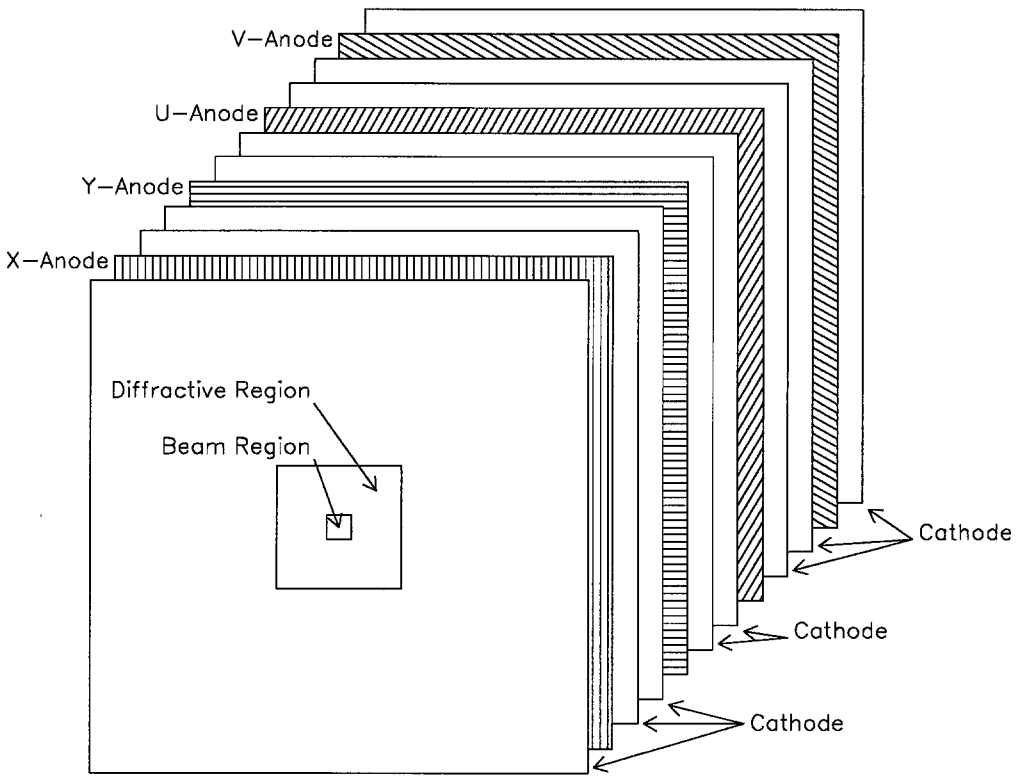

Figure 2.5 The proportional wire chambers, showing the relative orientations of the X, Y, U, and V planes. Also note that the beam and diffractive regions of the cathode planes were electrically independent from each other and from the main regions, allowing the desensitization of the beam region and preventing the high-intensity beam region from causing inefficiency in the main regions of the PWC's.

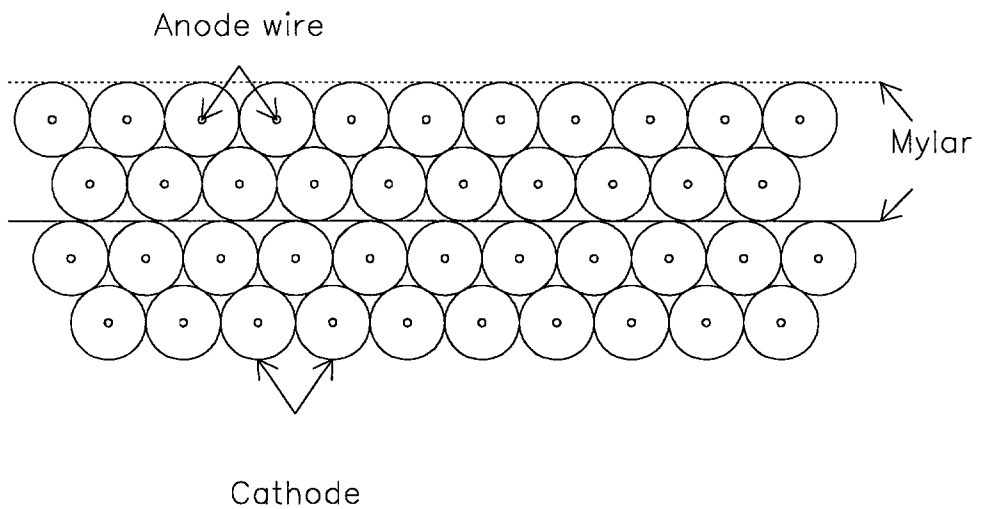

Figure 2.6 A cross-sectional view of a straw tube bundle.

module. The active medium was an argon-ethane gas mixture. The STRAW signals were amplified and discriminated using Nanometrics cards and were then fed into time-to-digital converters. This timing information was translated into the (unsigned) distance between the track and the wire, providing significant resolution improvements over the PWC's, albeit with an ambiguity due to the fact that a track passing the same distance from the wire but on the other side would elicit identical STRAW output. This ambiguity was overcome by using PWC space tracks to "seed" the STRAW tracking algorithm (see Section 4.1.2).

2.3 Calorimetry

The E706 spectrometer contained three calorimeters, the ElectroMagnetic Liquid Argon Calorimeter (EMLAC), the HAdronic Liquid Argon Calorimeter (HALAC), and the Forward CALorimeter (FCAL). All three of these calorimeters

measured energies of showers by sampling. In sampling calorimetry, layers of an active medium are interleaved between layers of an absorbing material. Much of the energy of a shower in a sampling calorimeter is deposited in the absorber, and a fraction of the shower's energy is measured by the active medium. Although sampling in this way reduces the maximum possible energy resolution of the calorimeter, it provides significant gains in terms of shower containment or detector size and economic feasibility.

2.3.1 The Liquid Argon Calorimeter

The EMLAC and the HALAC, together referred to as the Liquid Argon Calorimeter (LAC), were both contained within a cryostat, and this entire unit was suspended from the gantry (Figure 2.7). The gantry was capable of motion transverse to the beam for calibration purposes. Within the cryostat, the components of the detector were immersed in liquid argon, the temperature of which was controlled by regulating the temperature of liquid nitrogen flowing through refrigeration coils. To exclude liquid argon from the region inside the cryostat in front of the EMLAC, a "filler vessel" was inserted in this region. Constructed of Rohacell foam coated with fiberglass and epoxy and encased in a thin steel skin, the filler vessel significantly reduced the energy lost in material in front of the active regions of the LAC.

The EMLAC and the HALAC both used this liquid argon as their active media, with lead and steel, respectively, for absorber. As electrons and other charged particles passed through the argon gaps, they ionized the argon, producing electron-ion pairs. High voltage maintained across the argon gaps caused these electrons to drift toward the anode. The integrated electronic charge collected on the anode comprised the sampled signal; one may calibrate the detector by comparing the values of a known energy deposition and the resultant signal.

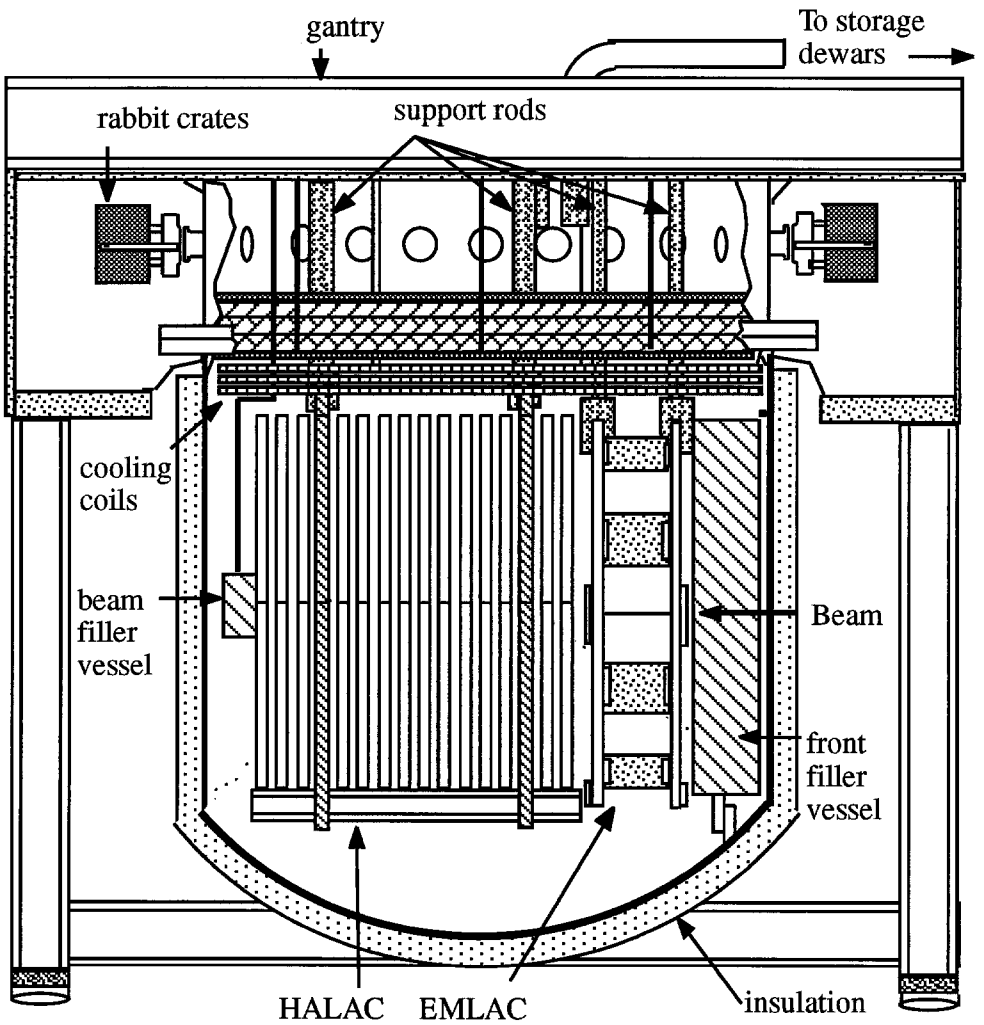

Figure 2.7 A cut-away schematic view of the gantry and the LAC.

The Electromagnetic Liquid Argon Calorimeter

The outer dimensions of the ElectroMagnetic Liquid Argon Calorimeter described a cylinder 160 cm in radius and 71 cm in length. A concentric cylinder of radius 20 cm defined the EMLAC's beam hole, which contained a second filler vessel to minimize interactions in this region. The beam filler vessel was constructed of stainless steel and contained gaseous helium. The EMLAC, as shown in Figure 2.8, was subdivided into four quadrants, each of which comprised 33 composite layers in depth. Each of these layers contained, from front to back, a radial board (*r–board*), a lead sheet, an azimuthal board (*ϕ–board*), and another lead sheet, with 0.25 cm liquid argon gaps between each component. The EMLAC as a whole comprised $\approx$30 radiation lengths.

The r– and ϕ–boards were the octant-sized anodes, each of which was a sheet of G10 clad on both sides with copper. The r–boards were segmented into arcs of fixed distance from the beam axis, with 256 channels per r–board. A front-most r–board had strips of width .5466 cm, and the strips on each succeeding r–board had the appropriate width and position such that a ray projecting from the target would impinge on the same-numbered strip on all r–boards. Due to this focussed geometry of the r–strips and to the physical boundaries of the EMLAC, not all r–boards had the same angular coverage; downstream r–boards did not have strips which corresponded to the outer strips of upstream r–boards, and inner strips on the downstream r–boards did not have corresponding counterparts in the upstream r–boards.

Each ϕ–board was divided into an inner and an outer section; this design allowed for sufficiently fine resolution in the outermost portions of the EMLAC without overly-narrow strips in the innermost portions and also simplified the

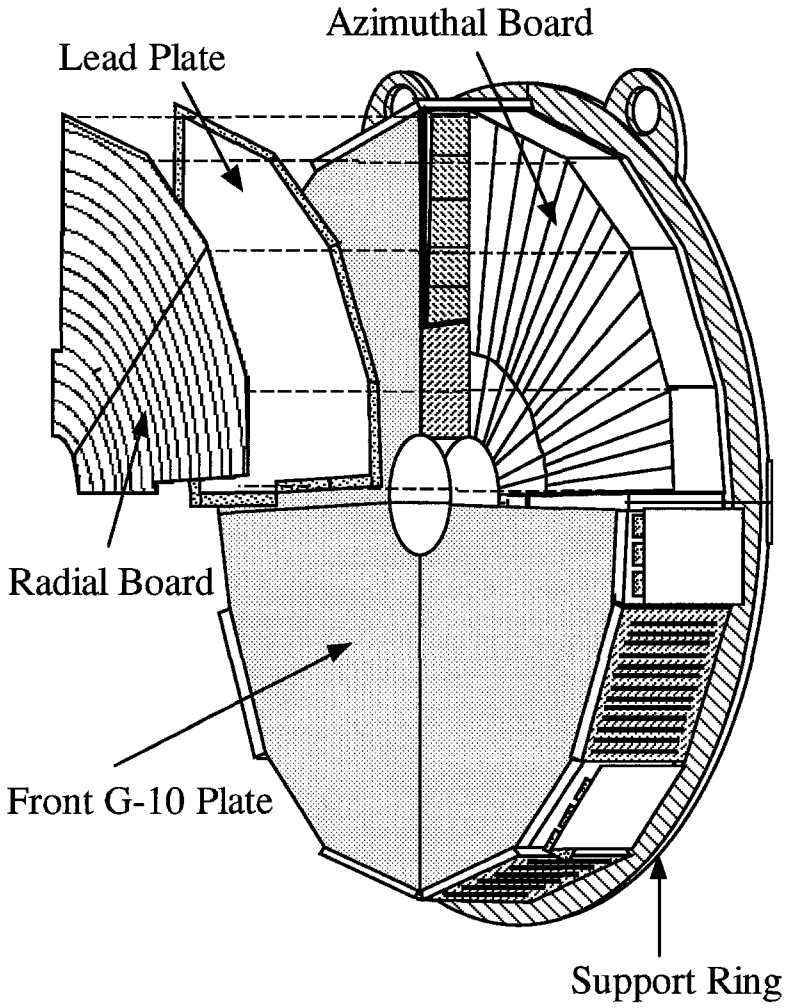

Figure 2.8 The electromagnetic calorimeter, with a quadrant with splayed layers to show an r–board and a ϕ–board.

correlation between r and ϕ energy depositions. The inner/outer boundary, which was focussed on the target in a similar fashion to the strips on r–boards, was at 40.2 cm for the first ϕ–board, the radius that roughly corresponds to 90^0 in the center of mass reference frame for beams near 500 GeV/c. The inner-ϕ strips subtended an angle of $\pi/192$ radians, and the outer-ϕ strips subtended an angle of $\pi/384$ radians.

Readout of all strips of all layers independently would not have been feasible in terms of electronic noise, readout time, and/or cost. Nevertheless, some longitudinal segmentation is useful for a number of purposes:

- Hadron rejection: hadronic shower maxima tend to be closer to the back of the detector than are electromagnetic shower maxima, providing discrimination.
- Muon rejection: Since the angle of incidence with the face of the EMLAC is different between halo particles and particles coming from the target, discrimination against muons is possible if the shower position is measured as a function of longitudinal position within the EMLAC.
- R-ϕ Correlation: Matching of the longitudinal development of the shower in the R– and ϕ views provided a constraint in the correlation routines.

Therefore, readout of the EMLAC was performed in two longitudinal segments (or "sections") for each octant. The front section contained 11 of the composite layers described above, and the back section contained 22. In each of these sections, all corresponding strips were connected together using wire braids called connector strings. For the r–boards, this "ganging" occurred along the quadrant

boundaries; for the ϕ–boards, the braids were channeled along the inner and outer edges of the quadrant. The front- and back-section connector strings were attached to readout boards upstream and downstream, respectively, of the EMLAC. From the readout boards, low-impedance cables transported the signals through the cap of the cryostat to the LAC amplifier cards [18], or LACAMP's. LACAMP's (see Figure 2.9) were RABBIT [19] cards designed to provide three types of output: a fast energy measurement to be used for the trigger, a (longer-timescale) precision energy measurement, and a measurement of shower time-of-arrival via the Time-to-Voltage Converters (TVC's). These electronics were housed in a Faraday room mounted on the top of the gantry. Constructed of galvanized sheet metal walls, the Faraday room was designed to isolate the readout electronics from external electronic signals. Signals to or from the outside were communicated via optical cables or using pulse transformers, and power was supplied to the Faraday room electronics via transformers.

The Hadronic Liquid Argon Calorimeter

The HAdronic Liquid Argon Calorimeter (HALAC), positioned immediately downstream of the EMLAC, measured 4 m in diameter and had a beam hole with a diameter of approximately 45 cm. This sampling calorimeter had 52 octagonal composite layers each of which consisted of a 2.5 cm stainless steel plate and a sampling unit called a "cookie" which contained 7 planes of G10 and liquid argon gaps. The front section contained 13 full layers (plus an additional cookie appended to the very front of the HALAC) and the back contained the remaining 39. The HALAC as a whole comprised $\approx$8 interaction lengths.

Since hadronic showers typically are broader than electromagnetic showers, the design specifications for spatial resolution of the HALAC were not as stringent as for the EMLAC; for this reason, the HALAC charge collection utilized a pad

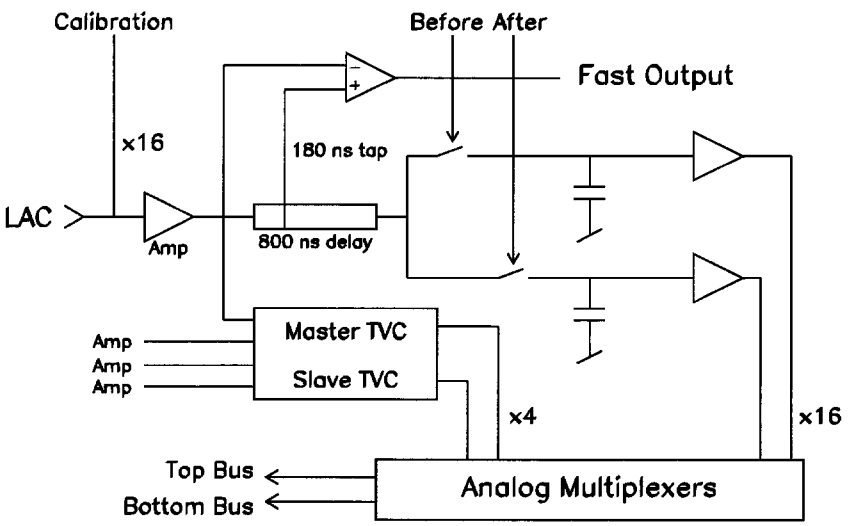

Figure 2.9 A block diagram of the LAC amplifiers.

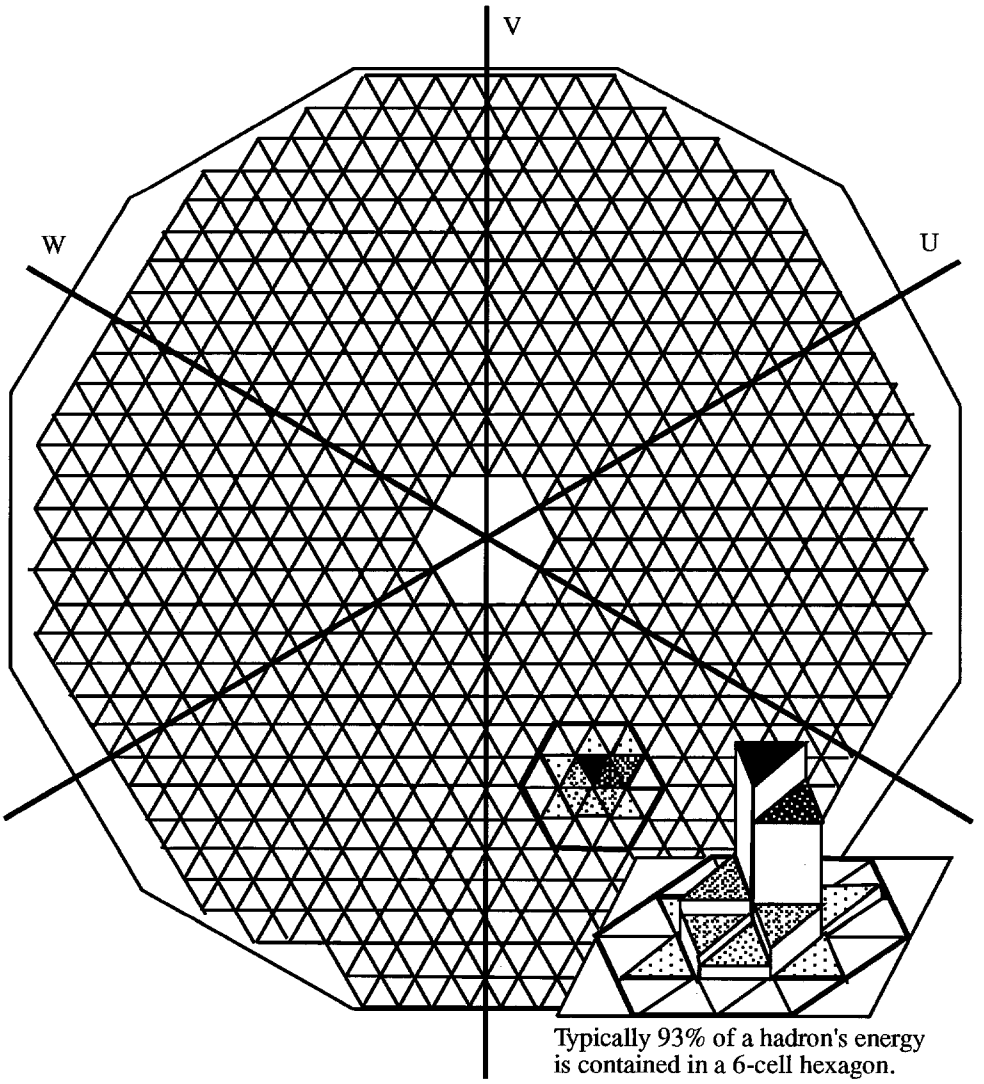

Figure 2.10 The pad structure of the HALAC.

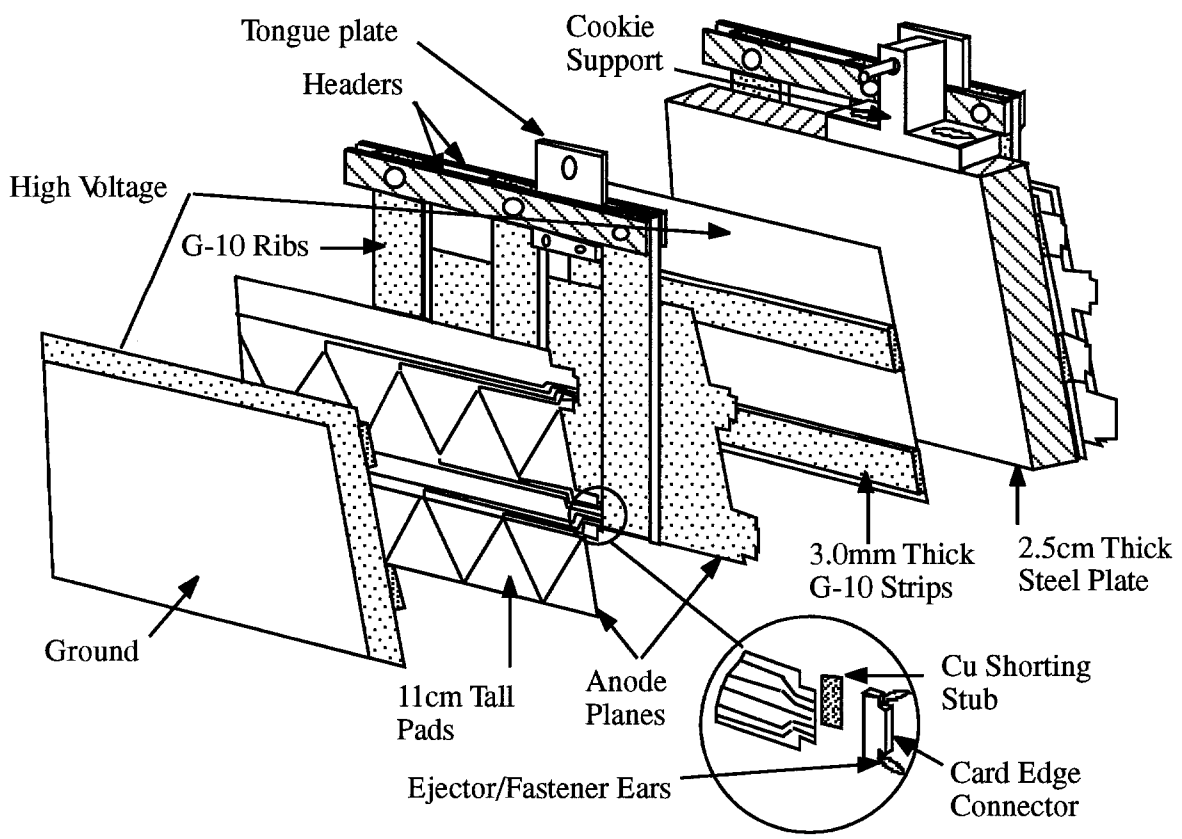

Figure 2.11 An exploded view of part of one cookie.

structure, as opposed to the finely-segmented r–ϕ structure of the EMLAC. This design removes the reconstruction complexity inherent in the correlation required by an r–ϕ or x–y geometry. The HALAC's pads were equilateral triangles (see Figure 2.10) and, being focussed on the target, the pads ranged in height from 10.9 cm in the front to 13.3 cm in the back. As is shown in Figure 2.11, the charge-collecting pads were cut into two single-sided copper-clad G10 boards which were positioned back-to-back in the center of the cookie, separated only by G10 ribs

which provided structural rigidity. On each of these anodes, horizontal rows of triangular pads alternated with uninstrumented horizontal rows, leaving space for signal traces running to readout boards at the edge of the detector. The two back-to-back anodes were vertically offset by the height of one horizontal row so that each cookie instrumented its entire physical coverage. The uninstrumented rows were covered by G10 strips which not only inhibited charge collection directly onto the signal traces, but also acted as spacers for the 3 mm argon gaps. Across these argon gaps were double-sided copper-clad G10 boards, with the side near the argon gap providing the high voltage and the other side held at ground.

2.3.2 The Forward Calorimeter

The Forward Calorimeter was designed to extend calorimetric coverage into the rapidity region left uninstrumented by the beamhole in the LAC, and thereby measure the energy of jets from spectator partons. Positioned 15 m from the target, the cylindrical FCAL had an outer diameter of 114 cm and a beamhole of diameter 3.2 cm, providing an additional $\approx$2.5 units of rapidity coverage.

The FCAL consisted of three distinct but very similar modules, each of which was positioned along the beam axis (Figure 2.12). Each module was composed of interleaved plates of steel absorber (1.9 cm thick) and acrylic scintillator (4.8 mm thick). The upstream module contained 28 steel plates and 29 scintillator sheets, as did the middle module; the downstream module contained 32 layers of steel and 33 of scintillator. When taken together, the three modules constituted 10.5 interaction lengths, sufficient to contain more than 98% of the energy due to an hadronic shower.

On a grid with 11.4 cm spacing across the face of each module, 76 holes were drilled parallel to the beam direction. These holes provided space for acrylic rods

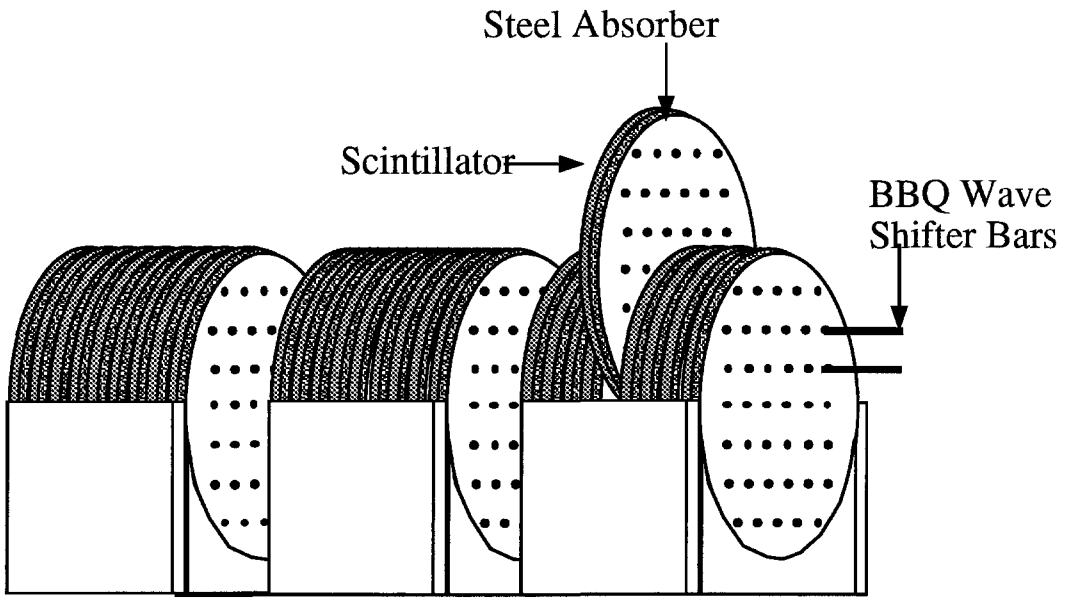

Figure 2.12 The forward calorimeter.

which redirected the photons generated in the scintillator to the front and back of the module to be read out by photomultiplier tubes (PMT's). The passage of charged particles through the scintillator produced blue light, but since the PMT efficiency was higher for green light, the acrylic rods were doped with an organic dye (BBQ) which shifted the blue light to green. The BBQ rods were also doped to absorb UV light, thereby reducing signals due to particles passing through the rods themselves. For the downstream module, the BBQ rods were read out by flash ADC's connected to PMT's on its downstream end; the other two modules' BBQ rods were read out on both ends.

Chapter 3 The Event Selection and Data Acquisition Systems

3.1 The Trigger

E706 was designed to study events containing high-p_T photons. Since particle production rates decrease rapidly with increasing p_T, and since the data acquisition system was limited to several hundreds of events per spill, it was essential to discriminate against events with low p_T. To this end, a trigger system was built which rejected nearly five orders of magnitude more events than it selected. The following sections briefly describe the E706 trigger system.[1] Section 5.3 describes the methods used to measure the efficiency of triggers in the turnon[2] region.

3.1.1 Beam and Interaction Definitions

At a most fundamental level, the first requirement of the trigger system was that there exist an interaction in the target associated with beam from the beamline. This information was acquired using the beam and interaction scintillating counters. To be assured of beam entering the target region (a condition labeled BEAM), two of the three hodoscope planes were required to have registered one or more hits in the same 19-ns bucket. To guard against multiple beam particles within the same bucket, BEAM1 required BEAM and not more than one plane registering multiple clusters of hits.[3] By allowing a single plane to have more than one cluster, this definition avoided vetoing on a noise hit

---

[1] For further details, consult Refs. [20, 21].

[2] The "turnon region" is the transition p_T range in which the a trigger efficiency changes from zero to one.

[3] A cluster is defined as one or more adjacent hodoscope elements containing a hit.

in a single hodoscope plane. To assure that beam particles passed through the target region, a hit in the beamhole counter (BH) was used as a veto. The INT signal was generated when two or more of the four interaction counters fired in the same bucket, in coincidence with BEAM.

Temporal isolation of the interaction signal was required both to allow the PRETRIGGER electronics time to reset in the case when no trigger was satisfied and also to ensure that the recorded tracking information was associated with the triggering event. To this end, a requirement (CLEANINT) was imposed that there be no interaction signals within ± 3 buckets of the triggering interaction. Before further calculations involving EMLAC information were made, a potential event was required to satisfy

$$\text{BEAM1} \bullet \overline{\text{BH}} \bullet \text{INT} \bullet \text{CLEANINT}$$

where the $\bullet$ symbol is the logical AND, and a correlation in time is implied.

3.1.2 The Pretrigger

The PRETRIGGER was based on a fast estimate of observed LAC p_T. The PRETRIGGER rejected a large fraction of the very low-p_T events quickly without adding undue deadtime associated with the computation required to check the status of the other triggers. In addition, the PRETRIGGER provided timing information for the LAC signals.

The trigger p_T value was computed using the fast outputs of the LACAMP's of the r-view strips. These strip energies, obtained using only the leading $\approx$180 ns of the energy deposition, were not as accurately measured as the values obtained by the longer integration time used to get final photon energies. They were, however, sufficiently precise for the purpose of rejecting low-p_T events. The fast-output strip

energies from pairs of neighboring channels were summed together. To acquire a p_T measurement, these strip-pair energies were then fed into p_T attenuator cards which weighted the energy by a factor proportional to $\sin\theta$, where θ is the angle of the ray from the target to the strip pair relative to the beam axis. Summing over four of these weighted pairs produced a sum-of-eight; there were 32 sums-of-eight for each octant. These sums-of-eight were sent to the biased p_T adder cards and the local discriminator cards.

The biased p_T adder cards were designed to compute the total p_T in each half-octant. The resulting p_T measurement was designated the "global[4] p_T" for that half-octant. Blindly adding all appropriate sums-of-eight would have exposed the half-octant global p_T sums to the effects of coherent noise and image charge. "Image charge" refers to an effect in which a signal in one region of an octant causes shifts in the apparent pedestal level in another region, with the direction of the shift dependent on the relative timing of the two signals. To minimize sensitivity to image charge effects, the biased p_T adder cards subtracted a small threshold (of a few hundred MeV) from each sum-of-eight and summed the resulting value only if it were larger than zero. The outputs of the adder cards were then sent to zero-crossing discriminators. These discriminators processed the global signal to provide a timing reference for the LAC signals which was relatively insensitive to nearby interactions and independent of the magnitude of the energy. The zero-crossing time was then compared to the timing of the signal from the scintillation counters.

The PRETRIGGER logic imposed several vetoes on the event. SCRKILL vetoed PRETRIGGERS in coincidence with Faraday Room power supply noise spikes. An

[4] Thus, "global" refers to the method of summing p_T's within an octant, and does not indicate that the measurement was made using information from the entire EMLAC.

early-p_T veto was imposed by requiring the absence of significant global p_T (in the PRETRIGGER octant) $\approx$350 ns prior to the event. This was necessary in order to avoid signal pileup and image charge effects from previous showers in the LAC. Another requirement imposed by the PRETRIGGER used information from the veto wall quadrants associated with a potential PRETRIGGER octant. The veto logic used for each quadrant was

$$(\mathrm{VW1} + \mathrm{VW2}) \bullet (\mathrm{VW3} + \mathrm{VW4})$$

where $\bullet$ and $+$ designate the logical AND and OR, respectively, and VW1 indicates that the first veto wall was fired, VW2 indicates a hit in the second veto wall, etc. Note that correlation in time is assumed and that VW4 was installed after completion of the 1990 run. In the absence of these vetoing conditions, the PRETRIGGER logic compared the global half-octant p_T sums to thresholds in order to determine whether to complete the full trigger calculation. In 1990, these thresholds were $\approx$2 GeV/c p_T and in 1991 they were slightly higher. When the PRETRIGGER was satisfied, signals were sent to latch the data in all systems.

3.1.3 Triggers

Due to the rapid falloff of particle production with p_T, the vast majority of events selected by a trigger are very near that trigger's p_T threshold. Thus, to obtain significant reach in p_T, it was necessary to employ several triggers with different thresholds. Of course, in order that the lower-threshold trigger not completely dominate the higher-threshold triggers, the low triggers needed to be prescaled. In addition to multiple thresholds, E706 employed multiple trigger types each of which was optimized for specific topologies and situations. Figure 3.1 pictorially demonstrates the essential differences between a local and a global trigger. Figure 3.2 shows the flow of information from the fast-outs to the discriminators. Discussion of the various trigger types follows.

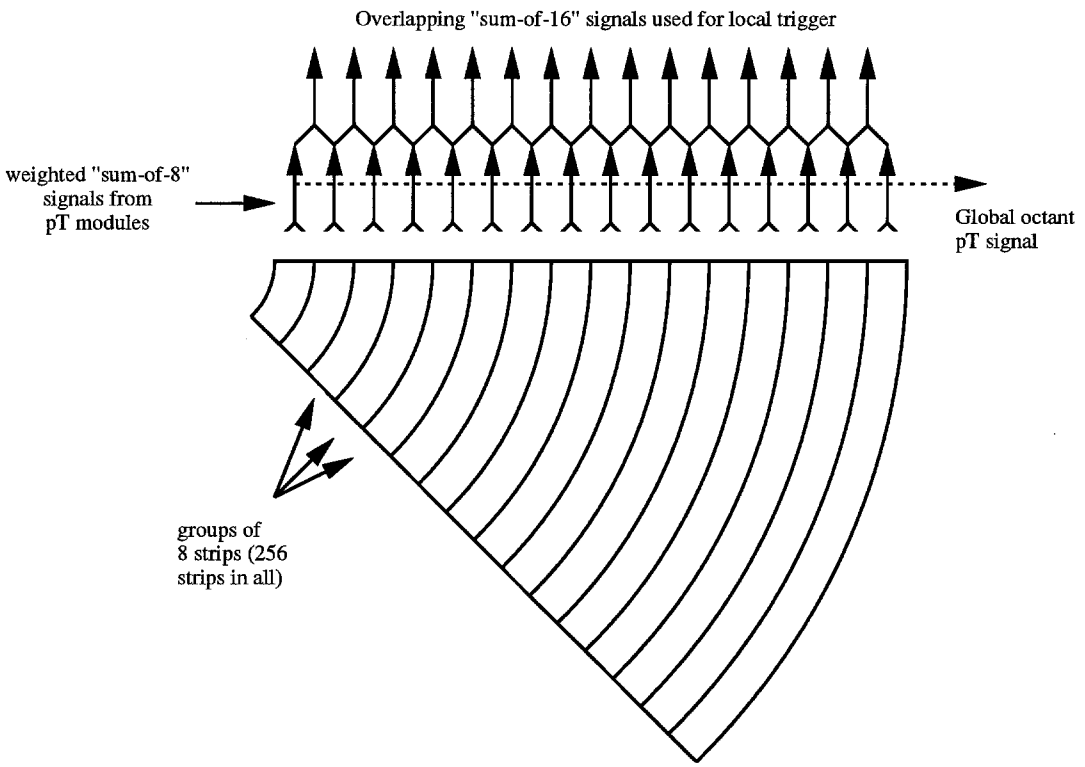

Figure 3.1 p_T summing for the local and global triggers. A local trigger fired if in any octant, any one of the 31 overlapping 16-strip LOCAL's contained a p_T deposition over threshold for that trigger. A global trigger utilized the cutoff-reduced global p_T sum over the entire octant.

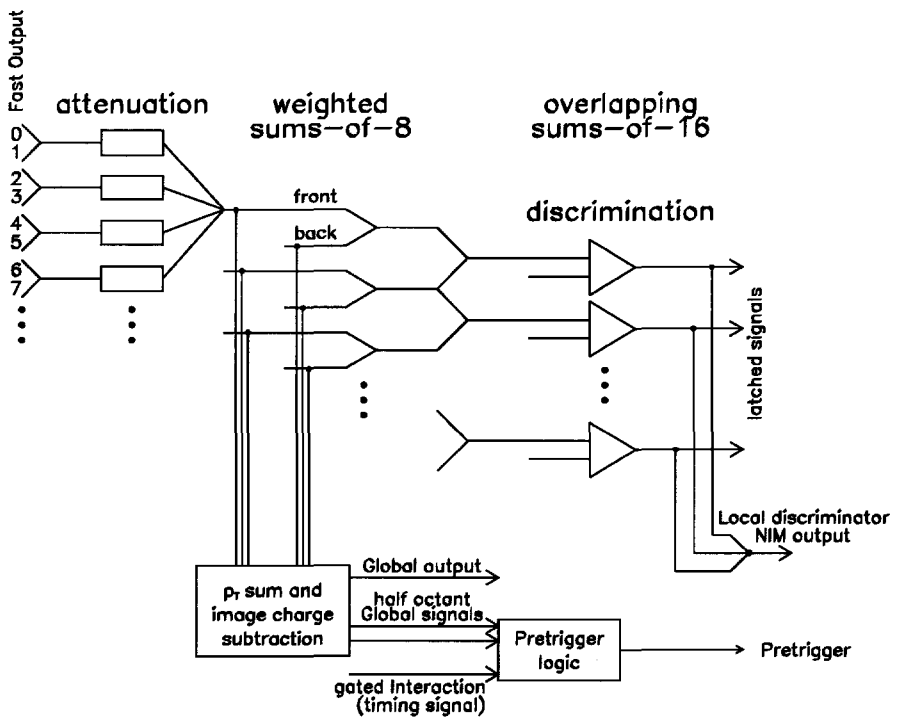

Figure 3.2 A block diagram of the trigger system. The LACAMPs' fast outputs are paired, summed, and attenuated to form 2-strip p_T measurements. Combining four of these produced each of the 32 sums-of-eight. These sum-of-eight p_T's were summed in various ways to provide the basis for the PRETRIGGER and the local and global trigger decisions.

Three heavily prescaled triggers were recorded to study the lowest p_T regions and to enable studies of the performance of the other triggers. Collectively known as the "Prescaled Triggers",[5] the PRESCALED BEAM, INTERACTION, and PRETRIGGER constituted between 4% and 10% of the triggers written to tape. The PRESCALED BEAM required BEAM with early/late bucket cleaning similar to the high triggers. The PRESCALED INTERACTION was the same as the PRESCALED BEAM except for the additional INT requirement. Neither of the preceding low-bias triggers used LAC information, which made them useful in studies of the LAC triggers. The prescaled PRETRIGGER provided access to the p_T range between the low-bias triggers and the low threshold triggers discussed below.

Local triggers were designed to efficiently detect photons and high-energy π^0's, which are associated with showers of relatively limited spatial extent. Each "LOCAL" within a local trigger consisted of a pair of adjacent sums-of-eight, and the p_T of this pair was compared to a threshold. Since there were 32 sums-of-eight in each octant, there were 31 overlapping LOCAL's per octant, and the local trigger was satisfied if any octant contained any LOCAL with a signal above threshold. Due to the restricted number of channels contributing to each LOCAL, the local triggers were less likely to be sensitive to noise or image charge elsewhere in the octant. In addition, since fewer strips contribute, the turnon of a local is rather narrow, resulting in a smaller p_T range over which the events are unusable or difficult to correct. The effective SINGLE LOCAL HIGH threshold (i.e. the 50%-point) was $\approx$4 GeV/c. All triggers exhibited order $\pm$10% variations as a function of radius (the outer r typically turned on at higher p_T) and time (1991 triggers had somewhat higher thresholds). The SINGLE LOCAL LOW was introduced at

[5] Of course, the other low threshold triggers were also prescaled, just not as much.

run 9183 during the 1990 run; it turned on at $\approx$2.75 GeV/c, and was prescaled by a factor of 40 in the 1990 run and by a factor between 200 and 280 for the 1991 run.

Global triggers were designed for better sensitivity to more diffuse topographies. η's, ω's, and low-energy π^0's, depending on the decay orientation and energy asymmetry, may deposit significant energy beyond the limits of any given 16-strip LOCAL. The p_T input into the global triggers' discriminators was the analog sum of the inner and outer global trigger p_T's for the corresponding half-octants which were used for the PRETRIGGER, viz. the sum of cutoff-suppressed fast-out p_T's greater than zero. An additional requirement of at least one LOCAL above the lower local threshold ensured that the event contained a minimum of one significant shower and rejected events containing only noise or image charge. In 1990, the LOCAL GLOBAL LOW, prescaled by a factor ranging between 10 and 40, had a threshold of $\approx$2.75 GeV/c. The 1991 LOCAL GLOBAL LOW threshold was slightly above 3 GeV/c; the corresponding prescale factor was between 20 and 70. The effective LOCAL GLOBAL HIGH threshold was slightly larger than 4 GeV/c.

The TWO GAMMA trigger was designed to select event topologies with two back-to-back p_T depositions (e.g. parton-level diphoton events). To focus on these sorts of topologies, the TWO GAMMA required p_T depositions in two octants of the EMLAC, and further required that there be a minimum of two intervening octants between the two trigger octants (i.e. that the trigger octants are opposite each other or nearly so). The p_T threshold used in the TWO GAMMA was the same as for the SINGLE LOCAL LOW, but due to the topological requirements, no prescaling was necessary.

3.2 The Data Acquisition System

Once the trigger was satisfied, signals were sent to each of four data acquisition subsystems to begin their readout. At the top end of three of these subsystems were PDP-11 computers attached to the experiments' CAMAC electronics. Two separate PDP's read out information from the FCAL and the E672 spectrometer. The third read out the data provided by several important systems. Trigger-related data, termed Discrete Logic information, read out by this PDP-11 included the status of the triggers and numerous trigger components by octant and time histories of the various scintillation counters. PWC and SSD hits and Čerenkov information was also read out by the same PDP. The fourth subsystem, based on FASTBUS electronics, read out and buffered the STRAW and LAC information. In addition, the FASTBUS system monitored and calibrated the RABBIT system between spills, performing checks on cable continuity, amplifier gains and pedestals, amplifier crate temperatures and voltages, and RABBIT card inventory [22]. After all four of the subsystems had completed their respective readout tasks, a COMPUTER READY signal was sent to the trigger, receipt of which was necessary before the trigger electronics would once again be "Live", i.e. ready to evaluate other interactions as trigger candidates. Output from the four data acquisition subsystems was coordinated by a μVAX running VAXONLINE [23], a FNAL data acquisition software package, which examined various headers to ensure that the four inputs were from the same event. Fully concatenated events were then written to a pair of 8mm tape drives. A schematic of the data acquisition system is shown in Figure 3.3, and a complete description of the data acquisition system can be found in Refs. [22], [24], and [25].

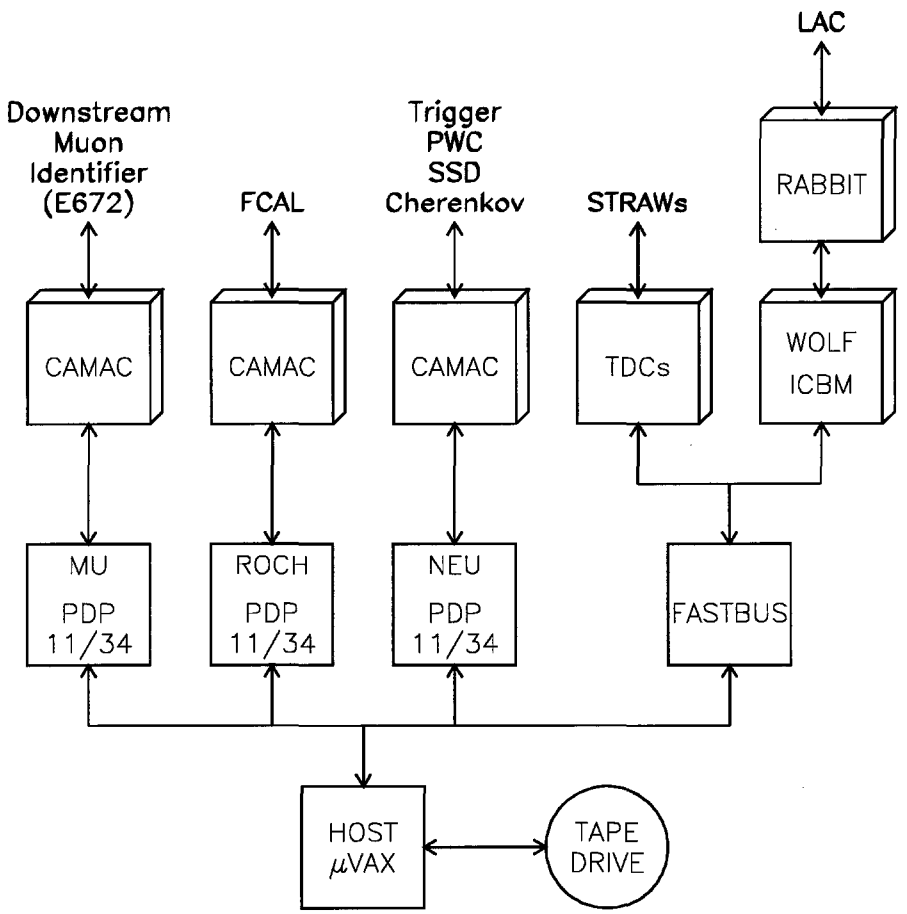

Figure 3.3 A block diagram of the E706 data acquisition system, showing the pathway of the information from various spectrometer elements through FASTBUS and the PDP's to the 8 mm tape on a MicroVAX.

Chapter 4 Data Reconstruction

The reconstruction of the E706 data sample was accomplished by a large software package organized around a program called MAGIC. MAGIC, in response to user inputs, sequenced the various parts of the reconstruction and provided numerous "hook" routines to allow users to access the data at various stages of reconstruction. The reconstruction itself was split into a number of subpackages. The EMLAC, the HALAC, the tracking spectrometer, the FCAL, and the trigger and Čerenkov information were independently handled by EMREC, HCREC, PLREC, FCREC, and DLREC, respectively. DLREC was responsible for decoding the discrete logic information which included data from the various scintillation counters, the status of various trigger logic units, and the outputs of the Čerenkov detector. DLREC output information on readout failures and compared information from different units, performing consistency checks. Further details on DLREC [20], FCREC [26], and HCREC [27] are provided in the references. The salient features of the reconstructors most relevant to this analysis are discussed in the ensuing sections.

The large amounts of computing resources required to reconstruct the 1990-1991 data samples were provided by several FNAL SGI[1] farms. Each of these farms consisted of a single I/O node and numerous "worker" nodes, and the reconstruction proceeded in a parallel fashion. The I/O node read events from raw data tapes, distributed these raw events individually to worker nodes, later received the reconstructed results from the worker nodes, and wrote the results to Data Summary Tapes (DST's). Within a farm, each worker node processed only one event at a time, albeit in parallel with $\approx$8 other similar nodes.

---

[1] Silicon Graphics, Inc.

4.1 PLREC – PLanes REConstruction

PLREC (the PLanes REConstruction package) was designed to use information from the SSD's, the PWC's, and the STRAW tubes to reconstruct the trajectories of charged particles produced in interactions in the target. The SSD information was used to reconstruct the location of the primary vertex (i.e. the point at which the beam interacted.) The degree to which a particle was observed to bend as it passed through the analysis magnet was used to determine the momentum and sign of the associated charged particle; this information was used in analysis of the charged-particle component of jets, in calibration of the EMLAC, and to tag depositions in the EMLAC due to charged particles.

The first step in reconstruction of the tracking information was to translate the planes' strip or wire hits to spatial coordinate hits. To accomplish this, it was necessary to determine the positions and orientations of the various elements in the tracking system to very fine accuracy. After this alignment, tracks were reconstructed in each subsystem. PLREC then "linked" the tracks from each subsystem to reconstruct the full trajectory of charged particles. The following sections give a general description of the methods used in tracking reconstruction; further details are available in Ref. [28].

4.1.1 Beam Tracking

The three X and three Y planes of beam SSD's were designed to measure the direction of the incident beam particle as it entered the target region. View tracks (i.e. tracks found in only one view) were reconstructed first by least-squares fitting of three-hit tracks. These three-hit tracks were located by selecting candidate pairs of hits in the first and third beam SSD chambers, and searching for a hit in the second chamber within 75 μm of the hypothesized track. After removing

all hits associated with a three-hit track, two-hit tracking was implemented, thus accounting for inefficiencies in the planes. To minimize the inclusion of spurious two-hit tracks due to noise, a two-hit track was accepted only if its slope was small (less than 2 milliradians). Approximately 20% of the beam tracks were two-hit tracks. Beam tracks were used in vertex reconstruction and in the identification of downstream tracks from non-interacting beam particles.

4.1.2 Downstream Tracking (PWC and STRAW Tracks)

As can be seen in Figure 2.1, the downstream PWC system consisted of four modules. Each module contained four planes, corresponding to X, Y, U, and V views. Reconstruction of the PWC tracks occurred in three iterations, and each iteration consisted of two phases, namely view track reconstruction and space track reconstruction.

To find 4-hit view tracks, hits in modules 1 and 4 were hypothesized to form tracks and modules 2 and 3 were searched for hits within ± 1 wire spacing of the supposed track. If four hits were found, a fit was performed; a 4-hit track was saved if the χ^2 per degree of freedom (χ^2_{DOF}) was below the accepted cut and if the tracks did not share too many hits with other 4-hit tracks. To find 3-hit tracks, hits in modules 1 and 3 (and later, modules 2 and 4) were hypothesized to form tracks and the remaining two views were searched for corroborating hits (within ± 1 wire spacing). 3-hit tracks with reasonable χ^2_{DOF} were also saved if they shared no more than one hit with a 4-hit track. 3-hit tracking reduced the effects of local inefficiencies on the track-finding efficiency. 2-hit tracking was performed using the first two modules in the X- and Y-views only. No sharing of hits was allowed in the 2-hit tracks, and in addition, the 2-hit X-view tracks were required to be outside the acceptance of modules 3 and 4 and the 2-hit Y-view tracks were required to point toward the target region.

The second phase of PWC track reconstruction began with the hypothesized pairing of each X-view track and each Y-view track. The U and V planes were then searched for hits within 1.5 wire spacings of this postulated space track. Then the XY/UV roles were reversed: hypothesized UV space tracks were projected onto the X and Y planes in search of confirming hits. A final space track was one which did not share too many hits with competing tracks and which passed cuts based on number of hits and the fit's χ^2 per degree of freedom (χ^2_{DOF}).

During the first iteration, space tracks with overall hit multiplicities of 14, 15, and 16 and $\chi^2_{\mathrm{DOF}} < 3$ were retained. PLREC also saved 13-hit tracks with $\chi^2_{\mathrm{DOF}} < 2$. The second iteration was performed excluding the hits used in tracks found in the first iteration. 10-hit tracks which passed outside the acceptance of either the first or the last module and 11- and 12-hit tracks were retained if $\chi^2_{\mathrm{DOF}} < 1.5$. After excluding all hits from accepted space tracks found in the first two iterations, the final iteration accepted tracks with as few as 6 hits with the following three stringent requirements: $\chi^2_{\mathrm{DOF}} < 1.5$, the projection of the track missed both of the two downstream modules, and that the track pointed back to the target in the Y-view. Approximately a third of the PWC space tracks had 16 hits, and another third had 15 hits. Of the remainder, only $\approx$3% had fewer than 13 hits. These numbers are consistent with an average PWC plane efficiency of $\approx$94%.

Since the STRAW chambers were built with X and Y views only, it was impossible to reconstruct space tracks solely based on STRAW information. Therefore, existing PWC tracks were used to correlate X and Y view STRAW information. In order to associate the straw hits with PWC tracks, it was necessary to overcome both the PWC projection errors and the inherent left-right ambiguity of the STRAW hits. (Since a STRAW's time-to-distance relation

provides only the distance between the central wire and the charged particle track, it is impossible to know *a priori* on which side of the wire the particle passed.) To resolve these ambiguities, an algorithm processed the hits in the following steps:

1) Project the PWC track into both STRAW chambers searching for STRAW hits within a certain window, not allowing STRAW-hit sharing.
2) For tracks with a sufficiently large number of associated STRAW hits in each view, refit the track using all PWC and STRAW hits, choosing the left/right STRAW hits which minimized the χ^2.
3) Iterate the two previous steps with a smaller search window to refine the track parameters.
4) After removing STRAW hits associated with previously-found STRAW tracks, iterate the previous three steps with less stringent requirements on the number of associated STRAW hits.

A track which was refit using STRAW information was called a STRAW track; approximately 75–80% of the final downstream tracks were STRAW tracks. The spatial resolution of STRAW tracks was improved by a factor of 2.5 relative to tracks which used only PWC information.

4.1.3 Upstream Tracking and Linking

To reconstruct downstream SSD view tracks, each pair of hits from different planes in the same view was postulated to form a track. Projecting these postulated tracks into the other three planes in that view, a search was performed for corroborating hits within 75 μm. Hits associated with four- and five-hit view tracks reconstructed in this fashion were excluded and three-hit tracks were then identified using the same procedure. Since the five planes of SSD's downstream

of the target had only X and Y views, it was impossible to reconstruct space tracks from SSD information only. To correlate the X and Y view tracks, SSD view tracks were linked to PWC and STRAW space tracks by requiring a spatial match at the center of the magnet, where a match is defined via a window, the size of which depended on momentum and whether the linking track was a PWC track or a STRAW track. In cases in which more than one SSD track matched with a PWC/STRAW track, the closest match was termed the "best-linked" SSD track.

4.1.4 Vertex Finding and Relinking

The SSD tracks were used to reconstruct vertices, first in the X and Y views, and then using information from both views together to get the spatial position of the vertices. At least three SSD tracks were required for a vertex to be found in a view. All best-linked tracks with three, four, or five hit were used. If necessary, extra links and unlinked tracks, were included; however, if three SSD tracks were still unavailable, no vertex was found. The position of the vertex was determined by minimizing

$$\chi^2 = \sum_i \frac{b_i^2}{\sigma_i^2} \tag{4.1}$$

where σ_i is the projection uncertainty of track i and b_i is the impact parameter of track i with respect to the hypothesized vertex location. If the resulting χ^2 was large, the worst track was excluded and the vertex was refit. Consequently, tracks associated with a secondary vertex would be excluded from the calculation of the primary vertex position. If a pointing beam track was found, it was included in the vertex position fit. Having located the X and Y vertices, the Z position was determined as the weighted average of the positions calculated in the two views. Having located one vertex, a second iteration was performed after excluding all

SSD tracks associated with the first vertex. If more than one vertex was found, the one further upstream was assumed to be the primary vertex.

In a procedure designated "relinking", the SSD track's impact parameter relative to the primary vertex was used as an additional constraint. This procedure improved the linking and therefore also improved the resolution of the tracking momentum measurement. Using the full detector simulation in the Monte Carlo (see Section 5.4), the momentum resolution was determined to be

$$\sigma_{\mathrm{p}}/\mathrm{p} \approx 0.0076 + 0.00026\mathrm{p} \tag{4.2}$$

where p is the momentum in units of GeV/c.

4.2 EMREC – ElectroMagnetic REConstruction

4.2.1 Unpacking

The electromagnetic reconstruction began with the unpacking of the ADC counts for each R and ϕ strip in the detector, and the rearrangement of these counts into orderly arrays based on quadrant, view,[2] strip, and section.

The next task of the unpacker was to convert from ADC counts to energy units. The first step in this process was the subtraction of the measured pedestal for each strip. A pedestal for a given channel is the value that is read out for that channel in the absence of an energy deposition. At intervals of approximately 8 hours during the data aquisition, a special LAC calibration task was performed. This task, performed between spills, read each amplifier channel 128 times; the initial pedestal value was computed as an average of these readings. Upon investigation

[2] There were four views per quadrant, namely an r-view associated with each octant, and the inner and outer ϕ-views common to both octants.

of the data taken under normal running conditions, minor offsets in the pedestals were observed; therefore the pedestal values were further refined by examination of beam triggers. In this analysis, channels containing energy from showers were ignored, and the remaining strips contributed to a measurement of the average pedestal values [25].

After subtraction of the pedestal value, a number of multiplicative corrections were applied. One factor was a correction for variations among the gains of various channels. Another factor accounted for the observed time-dependent energy response of the EMLAC illustrated in Figure 4.1. Finally, a global factor for the conversion of ADC counts to energy in GeV was applied. It should be noted that these factors did not provide the final energy calibration, but did correct for the majority of the variations in the energy response of the EMLAC.

4.2.2 FREDPED

Although the pedestal tasks described above were necessary to remove uncorrelated strip-to-strip variations, they were not sufficient to correct correlations among the pedestals on an event-by-event basis. Events were observed to contain ramps or steps in the apparent pedestal values. The frequency and size of these occurrences were correlated with the severity of extreme variations in the instantaneous intensity of the primary beam. At its worst, this *spill structure* wreaked havoc with the entire spectrometer, and caused significant pileup in the LAC which translated to severe pedestal and LAC trigger complications.

To remove the underlying structures in the pedestals, a package of routines called FREDPED was called after the unpacker and before the photon reconstruction. FREDPED used an iterative procedure in which each succeeding

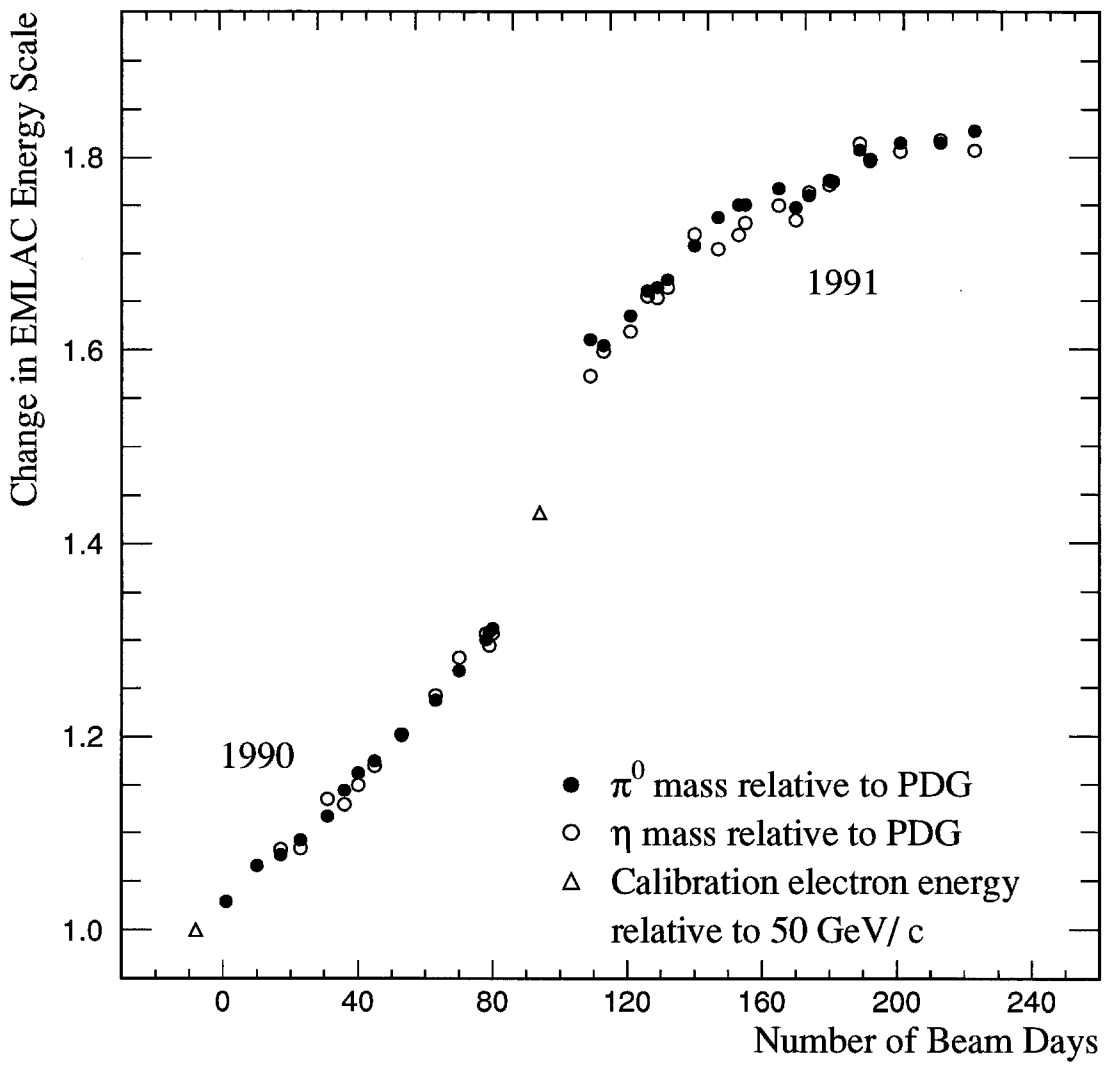

Figure 4.1 The time dependence of reconstructed π^0 and η masses (in ratio to accepted values [5]) during the 1990 and 1991 running periods. The open triangles represent the energy detected by the EMLAC for 50 GeV/c incident electron test beam. It should be noted that the time values on the abscissa were only incremented during periods in which beam was present and the EMLAC high-voltage was on.

cycle refined the determination of the pedestal values. Each iteration consisted of the following steps:

1) Locate and remove *groups*, or ranges of strips associated with energy depositions.
2) Perform a linear fit to the remaining strips, i.e. the pedestal strips.
3) Correct the data by subtracting the fit from it.

In R views, the first iteration identified groups by calculating the difference between adjacent strips. A large difference corresponded to significant energy deposition, whereas the noise in the pedestals produced smaller differences. In subsequent iterations, groups were identified by requiring the existence of a number of strips above threshold, a minimum summed group energy, and a minimum peak strip energy. Early iterations utilized relatively high group thresholds and later iterations refined the measurement of the pedestal level through the use of progressively lower thresholds. This iterative process was required because, prior to correction, worst-case pedestals could have very large differences or offsets from zero. The difference-based group-finding process was performed first since it showed the least sensitivity to large differences or offsets. Although some energy from the tails of showers influenced the fit in this iteration, a majority of a large ramp or offset was removed in this iteration. By then using the threshold-based group-finding with decreasing thresholds, each successive iteration was less sensitive to energy from showers' tails influencing the determination of the pedestal level. The final fits were performed on pedestal strips determined with a threshold just above the level of pedestal noise, thereby minimizing the effects of shower tails on the fit.

The outer ϕ view of each quadrant was split into two parts at the octant boundary since the pedestal effects were clearly distinct in the two halves. For

each half, a special preprocessor was invoked that used the information from the corresponding r-view to acquire a zeroth-order correction. This preprocessor first calculated the total energy correction to the outer portion of the corresponding R view. It then applied a level-offset correction to the outer ϕ half-view strips in proportion to the total R view correction. (The constant of proportionality was determined by measuring the mean of the distribution of the ratio of the total energy correction in the corresponding outer R and ϕ strips when the offsets were large and well-measured.) By so doing, a majority of a large offset in the outer ϕ was removed. The refinement of the outer ϕ view correction, including a determination of the slope of the pedestals, was accomplished through several iterations of the threshold-based group-finding process described above.

Part of the reason for the preprocessor in the outer ϕ view was the fact that the measurement of the R view correction, based on a total of $\approx$256 strips, was frequently more robust than the outer ϕ correction which was based on $\approx$96 strips for each half-view. (Of course, the presence of showers in a view subtracts significantly from the number of strips available for pedestal determination.) This problem is most acute, however, in the inner ϕ half-views each of which contains only $\approx$48 strips and frequently contains several showers in the busier events. Thus, in the inner ϕ, frequently very few strips could be of use in the pedestal fitting, making the fitting procedures an unreliable means of determining the pedestal level. A better result was obtained by using the approach similar to the outer ϕ preprocessor. Since the inner ϕ views rarely had significant slopes, the level offset provided by the preprocessor was used as the final correction.

Figure 4.2 shows an example of an event with significant pedestal level complications, most notably the ramp in the "left R view" and the step in the "outer ϕ view", although there is clearly an offset also in the "right R

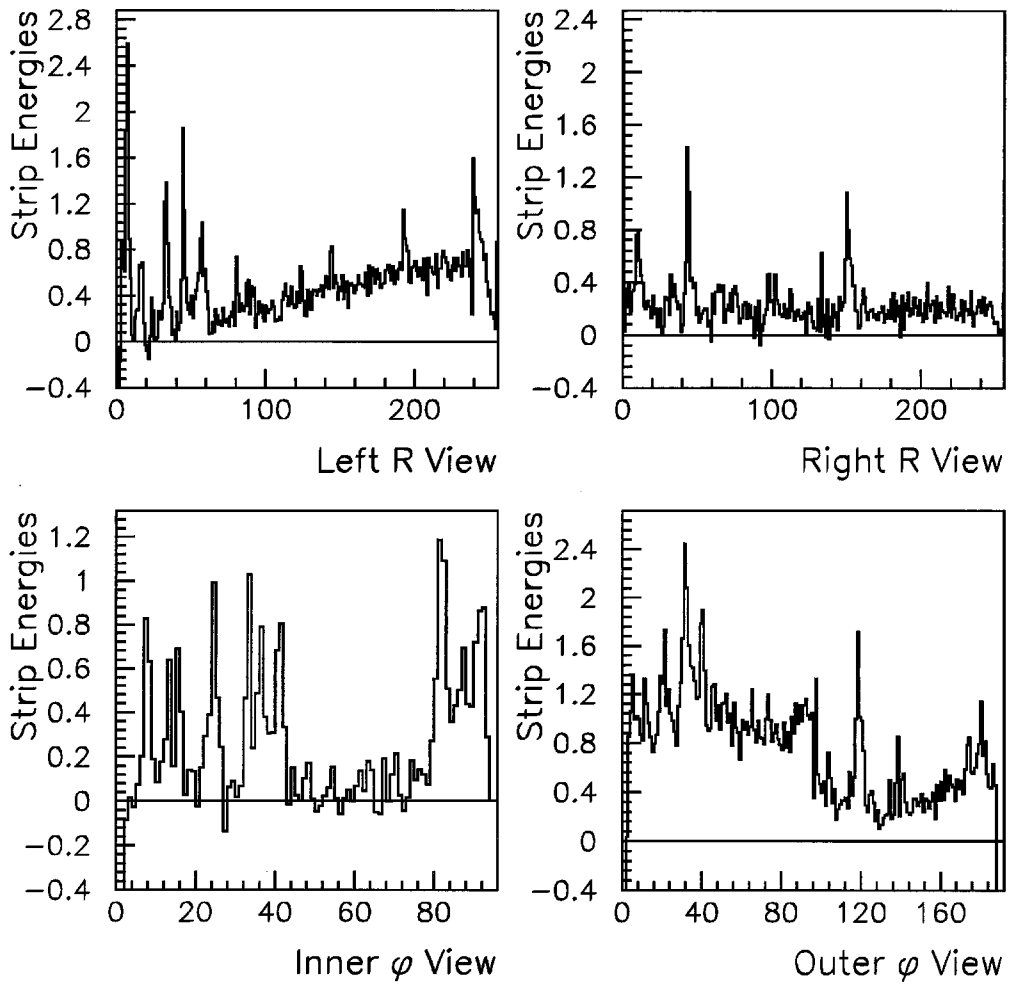

Figure 4.2 One quadrant of a raw event with significant pedestal shifts, before application of FREDPED. (Energies in GeV). Note ramp in the Left R View, offset in Right R View, and step in Outer ϕ View. The FREDPED-corrected event is shown in Figure 4.3.

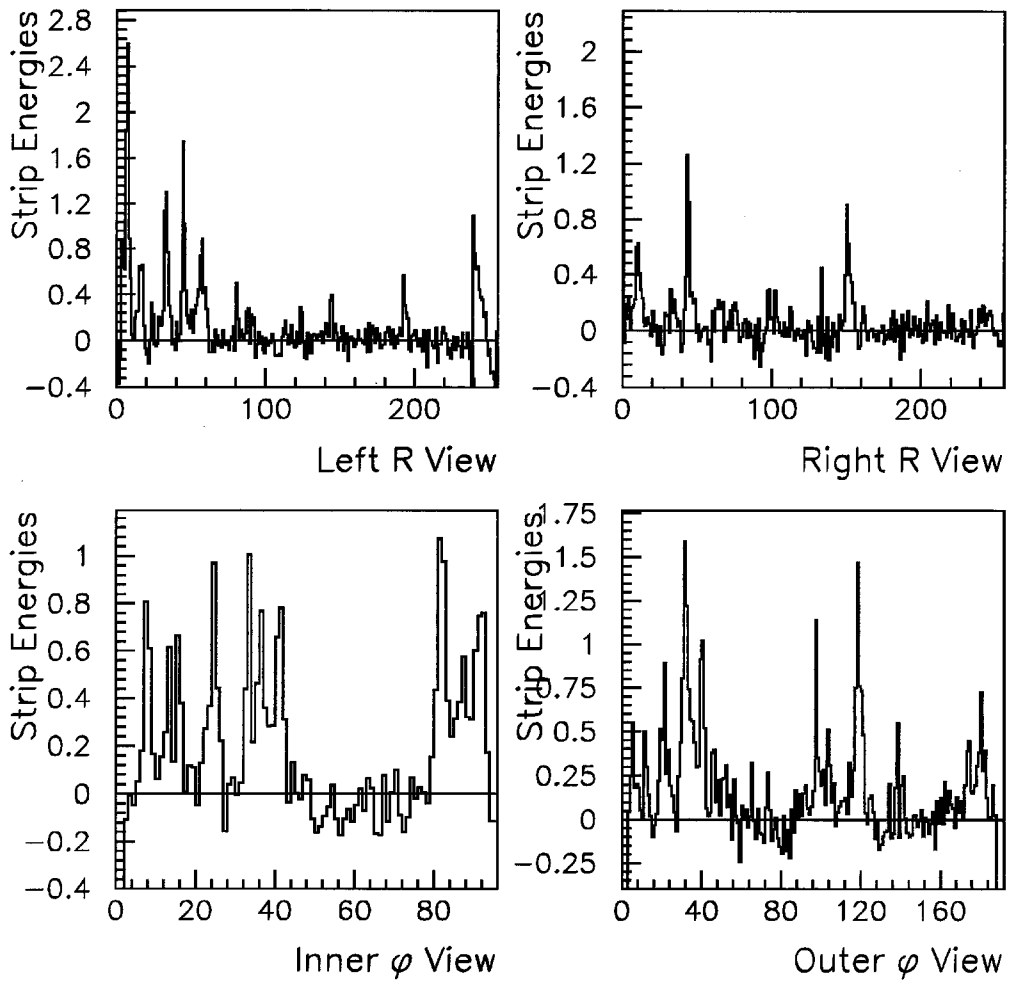

Figure 4.3 The raw data from the same quadrant for the same event shown in Figure 4.2, but after FREDPED had been invoked, correcting for the ramp and shifts in the pedestals. (Energies in GeV.)

view". Figure 4.3 shows this same event after FREDPED corrections. Although this event dump demonstrates the effectiveness of the FREDPED package on a single event, it does not reflect the size of the typical FREDPED corrections. Typical events required much smaller corrections. The average value of the FREDPED corrections depended on octant, section (front/back), and view (r/ϕ), but generally was less than or of order 20 MeV per strip.

4.2.3 Group and Peak Finding

The first step in electromagnetic shower reconstruction was the identification of groups in each view. This process was similar to the FREDPED threshold-based group finding. Each group was required to satisfy the following criteria:

- 3 or more strips with energy greater than 80 MeV (2 or more strips with energy greater than 95 MeV for outer ϕ groups since the strips are wider)
- total energy of at least 600 MeV
- at least one strip with energy greater than 300 MeV (350 MeV for outer ϕ)

Having found all groups in a view, EMREC then located *peaks*, or local maxima, within the groups. By comparing the height of the peak to that of the surrounding valleys (defined as the minimum between peaks or the end strip of the group), a quality factor was computed to determine whether a local maximum was a significant peak or merely an energy fluctuation. This process of peak finding was repeated in the front and back sections in order to split peaks that coalesced in the sum section. In such a case, the peak energy in the sum section was split in proportion to the energies of the observed peaks.

This peak-finding technique was frequently insufficient to locate a low energy shower which impinged on the EMLAC very near to a high energy shower. Since the asymmetric decay of a high energy π^0 presents precisely this scenario, special routines were developed to detect these low energy peaks, or *shoulders*. For groups containing a single peak with energy greater than 25 GeV, a shoulder was located by observing a change in the sign of the logarithmic derivative of the strip energies. These shoulder peaks were then subjected to peak-significance criteria to avoid the inclusion of energy fluctuations as peaks.

After locating the peaks, preliminary estimates of the energy and position were calculated for each one. The energy was computed as the sum of the strip energies between the peak's minima. The position was estimated as the energy-weighted average position of the peak strip and the strips on either side of the peak strip.

4.2.4 Gamma Reconstruction

Single-view photons, or *gammas*, were formed by fitting a parametrized shower shape to the peaks. This shower shape was determined by measuring the fractional energy deposition as a function of the distance from the center of the shower for well-isolated Monte Carlo photons. The shower shape was parametrized independently in both the front and the back, since the energy deposition in the back section was considerably wider than in the front. The sum-section shower shape parametrization was formed using the formula

$$E_{sum} = 0.7E_{front} + 0.3E_{back} \tag{4.3}$$

based on the observed typical E_{front}/E_{sum} ratio. In the sum section, the shower shape was observed to be nearly energy-independent. Comparison of these shower shapes to those obtained by examining well-isolated photons in data demonstrated

consistency between the Monte Carlo and data shapes. Of course, the shower shape was less suitable for accurate measurement of showers due to particles other than photons. "Gammas" due to electrons required a separate energy scale correction and the energy measured for an hadronic "gamma" frequently depended on the shower shape only for a small tail-energy correction, as described below.

The fitting procedure minimized the χ^2, computed as

$$\chi^2 = \sum_i \frac{1}{\sigma_i^2}(e_i - E\, z_i)^2 \tag{4.4}$$

The index i labels all strips in the central portion of the peak; to avoid the fluctuations in these low energy tails, a strip near an edge of the peak was included only if its energy was greater than twice the group energy threshold. For strip i, e_i is the observed energy deposition, z_i is the fraction of the shower's energy as predicted by the shower shape, and σ_i^2 is a parametrization of the estimated LAC energy resolution, given by

$$\sigma^2(E) = (0.22)^2 + (0.16)^2\, E + (0.01)^2\, E^2 \tag{4.5}$$

where E is in GeV and σ^2 is in GeV^2. In this formula, the first coefficient is the noise term, the second is the "sampling" or resolution term, and the third is the "constant" or gains term.

Since the shower shape was parametrized as a function of the distance from the center of the shower, the fitting of a peak in the ϕ view required some estimate of the radial position of the shower. This estimate was obtained by making use of the correlation between the observed width of the shower and the radial position of the ϕ peak. After correlation of gammas in the r- and ϕ-views, the ϕ gammas were refit using the radial position of the corresponding r-view gamma.

The first step in the fitting process used the estimated peak energy and computed the χ^2 for shower positions in the vicinity of the estimated peak position. Using the position associated with minimum χ^2, the next step fit for the energy of the gamma. For multiple-peak fitting, a χ^2 definition (similar to Equation (4.4)) was used which compared the strip energies to the sum of N shower shapes (for N peaks), and the minimization was performed with respect to the energies and positions of all peaks.

In the case of hadronic showers, which are often significantly wider than the photon showers for which the shower shape was measured, the χ^2 of the fit was frequently larger than 5. Therefore, for "gammas" (in this case, hadronic showers) with $\chi^2 > 5$, an estimate of the energy was made by summing the energy in the peak strips and then adding the fit's estimated energy contribution due to tails:

$$E_{tail} = E_{fit}\left\{1 - \sum_i z_i\right\} \tag{4.6}$$

When the gamma was close to a fiducial boundary, a correction was made for the energy outside the acceptance of the EMLAC. Similarly, if the tails of a gamma crossed an internal boundary (i.e. the inner/outer ϕ boundary or the left/right r boundary), and if the tail of the shower was not reconstructed as second gamma on the other side of the boundary, a correction based on the fit was applied to the gamma energy. Since this fitting process was performed in the front and back sections as well as the sum section, a calculation of the angle of incidence of the showering particle provided discrimination against muons travelling parallel to the beam at large radius.[3]

---

[3] See discussion of *directionality* in the Section 5.5.2.

4.2.5 Gamma Correlation and Photon Reconstruction

To reconstruct the full energy and position of photons in the EMLAC, correlation of the r- and ϕ-view gammas was necessary. Although correlation was performed quadrant by quadrant, the geometry of the views reduced the gamma combinatorics. For example, an r-view gamma with r > 40 cm would correlate only with a gamma in the outer-ϕ view. Along with this constraint, the correlation routines were guided by matching of the total gamma energies ($\frac{E_r - E_\phi}{\sigma^2}$) and the longitudinal shower development ($\frac{E_{front}}{E_{total}}$). Photon correlation was an iterative process in which the correlation window (i.e. the amount correlated gammas were allowed to disagree) was expanded for each successive iteration.

Special routines were developed in order to deal with each of the diverse configurations of gammas to be correlated. The simplest case corresponds to one r-gamma and one ϕ-gamma, termed a 1-1 correlation. For 1-1 correlations, EMREC merely checked that the two gammas could have come from the same subquadrant and that their energies and $\frac{E_{front}}{E_{total}}$ were consistent within the current iteration's limits. If these constraints were satisfied, the ϕ gamma was refit using the newly determined radial position, the two gammas were considered correlated and were excluded from further consideration. A more complicated configuration occurred when two photons had very nearly the same radial position, which is frequently the case for a low-asymmetry decay of a high-energy π^0. In this case, called 1-2 correlation, two ϕ gammas were required to match with one r-gamma. When this correlation type occurred, the r-gamma was refit assuming two gammas with energies matching the ϕ-gammas' energies. Similarly, when two distinct r-gammas were associated with a single ϕ-gamma, the 2-1 correlation routines split the observed ϕ-gamma, and resulted in two fully correlated photons. A similar situation occurred when a photon was incident near an internal boundary. For

example, if a photon hit the inner/outer ϕ boundary, gammas from both the inner ϕ and the outer ϕ were correlated with a single r-gamma. Yet higher levels of complexity were required for the rarer multiple-photon cases of 1-3, 3-1, 2-2, 1-4, and 4-1 correlations. These correlation types were attempted only after the simpler correlations failed to locate additional gamma pairs which matched according to the current iteration's criteria. When, possibly after several iterations, all gammas had been correlated or only gammas with highly disparate energies remained, the first correlation pass was complete. Since the fit energy of a ϕ-gamma depends on the radial position used, the ϕ-gamma fit energies were known to better precision after the first correlation pass. A second correlation pass was performed using the improved ϕ-gamma energies.

4.2.6 Photon Timing Information

Time-of-arrival information for photons was acquired through the use of Time-to-Voltage Converters, or *TVC's*. Four EMLAC strips fed into each TVC channel. In order to avoid firing on noise, an energy of at least 4 GeV was required to engage the timing circuit. To assign a time to a photon or gamma, the times derived from TVC channels associated with the energy deposition were sorted into $\approx$21 ns bins. The best time was calculated as the energy-weighted average of the TVC values in the bin with highest population. In the case of two bins with identical number of TVC channels, the bin with the highest energy was chosen, since the TVC resolution improved with energy. The efficiency likewise was energy dependent, with efficiencies around 50% at 16 GeV and at 100% by 50 GeV. Because low energy depositions in the outer portion of the detector have higher p_T's than similar deposition in the inner portion of the detector, the energy-dependence of the TVC's makes their use in cross section measurements difficult. Nevertheless, the photon timing information was very useful in trigger studies (where timing plays a significant role) as well as in the understanding of muon rejection cuts.

Chapter 5 Analysis

5.1 The Data Sample

Table 5.1 provides an inventory of the events written to tape for E706 during the 1988, 1990, and 1991 data acquisition periods, and furnishes an estimate of the corresponding sensitivity. The analysis presented in this thesis utilizes the 1990 data from π^- on beryllium and copper targets and the 1991 data from 515 GeV/c π^- and 530 GeV/c p beams incident on beryllium, copper, and hydrogen targets.

5.2 The EMLAC Energy Scale

The setting of the "energy scale" is the task of constructing a set of photon energy corrections so that the final *reconstructed* photon energy is an accurate reflection of the energy of the *real* photon incident on the EMLAC.[1] Minimization of energy scale uncertainty is extremely important: as Figure 5.1 illustrates, the fractional uncertainty in the cross section measurement as a function of p_T is roughly an order of magnitude larger than the fractional systematic energy scale uncertainty because of the rapid change in the cross section versus p_T.

The energy scale calibration relied heavily on the $\gamma\gamma$ mass peaks from π^0 and η decays. A number of additional checks were performed, including examination of the ω mass in the $\pi^0\gamma$ mode and the π^0 mass in the $\pi^0 \rightarrow \gamma\gamma$ mode, where one of the photons converts into an e^+e^- pair and the ZMP[2] information was evaluated using the tracking system. The following paragraphs indicate the

---

[1] Smearing due to nonzero energy resolution is not dealt with by the "energy scale." See Section 5.5.7.

[2] A ZMP (Zero Mass Pair) is a low-mass e^+e^- pair, i.e. a converted photon.

Run	Interaction	Beam Momentum (GeV/c)	Number of Events (millions)	Sensitivity (events/pb)
1988	π^-Be	500	2	0.5
	π^-Cu			0.1
	(p,π^+)Be		3	0.75
	(p,π^+)Cu			0.1
1990	π^-Be	515	30	8.6
	π^-Cu			1.4
1991	pBe	800	23	7.3
	pCu			1.8
	pH			1.5
	(p,π^+)Be	530	14	6.4
	(p,π^+)Cu			1.6
	(p,π^+)H			1.3
	π^-Be	515	4	1.4
	π^-Cu			0.3
	π^-H			0.3

Table 5.1 Number and types of events recorded by E706.

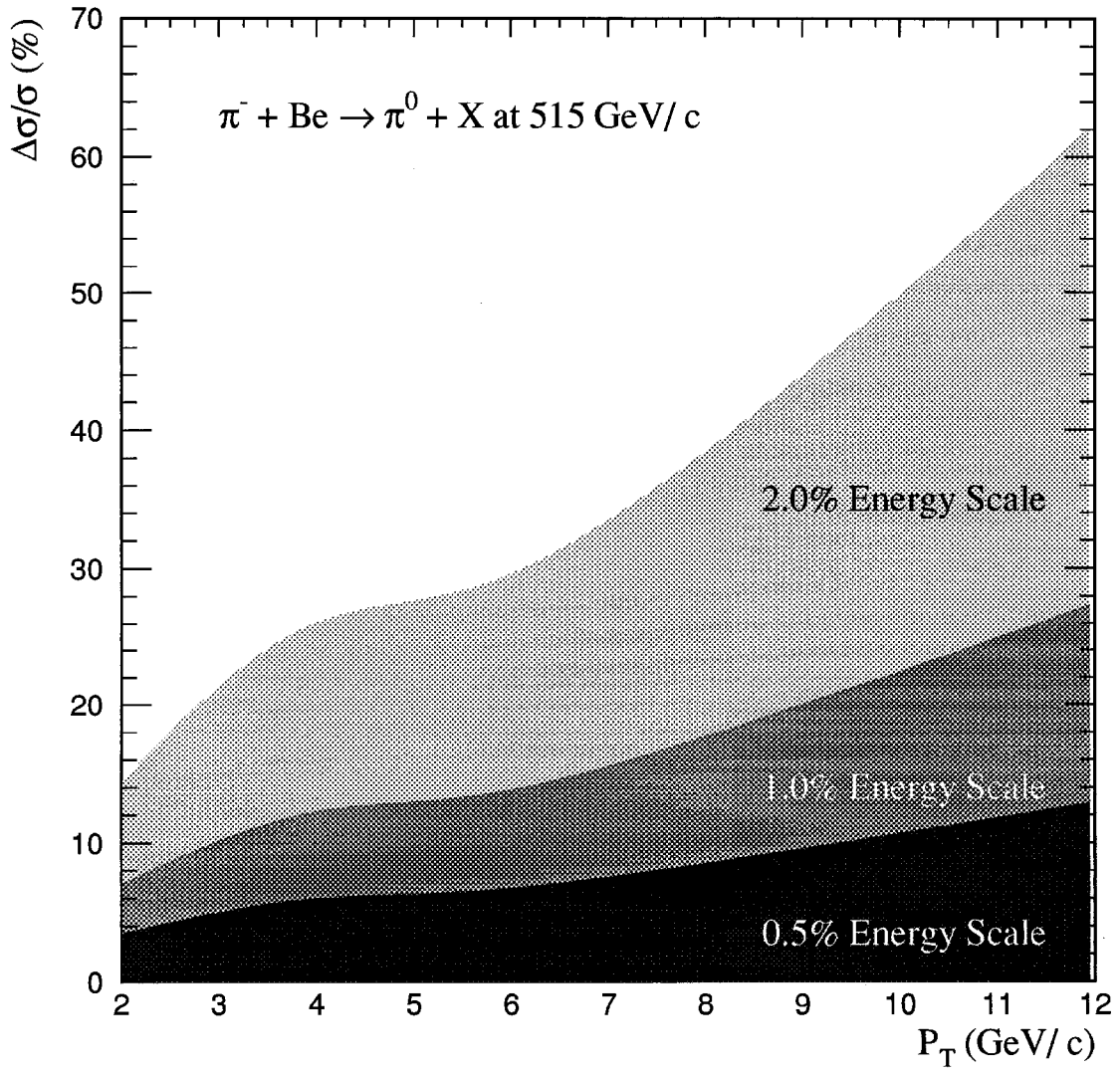

Figure 5.1 The systematic uncertainty in the cross section for 0.5%, 1.0%, and 2.0% systematic uncertainties in the calibration of the EMLAC energy scale, as measured for inclusive π^0 production by 515 GeV/c π^- beam incident on beryllium.

general procedure used in calibrating the energy scale; the details of this algorithm are available elsewhere [25, 29, 30].

The first step in the determination of the energy scale was a correction for the observed time-dependence of the EMLAC energy response, as discussed previously (see Figure 4.1). The π^0 and η samples used in the evaluation of the remaining corrections were defined by the following cuts:

- Both photons must be within the fiducial volume of the same octant.
- $\frac{E_{front}}{E_{total}} > 0.2$ for each photon.
- Neither photon has a charged track within 1 cm.
- $A < 0.5$, i.e. requiring a low energy asymmetry of the decay. (The energy asymmetry is defined as $A = \frac{|E_1 - E_2|}{E_1 + E_2}$).

The following steps were then performed:

1) Using low-p_T π^0's (1991) or η's (1990), correct for the average octant-to-octant variations.
2) Use $E = 2E_R$ (rather than $E = E_R + E_\phi$) for photons within 5 cm of the inner-outer ϕ boundary, since the ϕ energies of these photons were compromised due to the proximity of the boundary.
3) Correct for the mean energy lost due to showering in the material before the active region of the EMLAC. This correction, shown in Figure 5.2, was determined as a function of the reconstructed energy using a Monte Carlo simulation of the EMLAC response.
4) Use π^0's (with $p_T > 2$ GeV/c for 1990, and $p_T > 3$ GeV for 1991) to parametrize and correct for the dependence of the measured photon energy on radius for each octant independently. Figure 5.3 illustrates the magnitude of this correction, averaged over all octants, for the

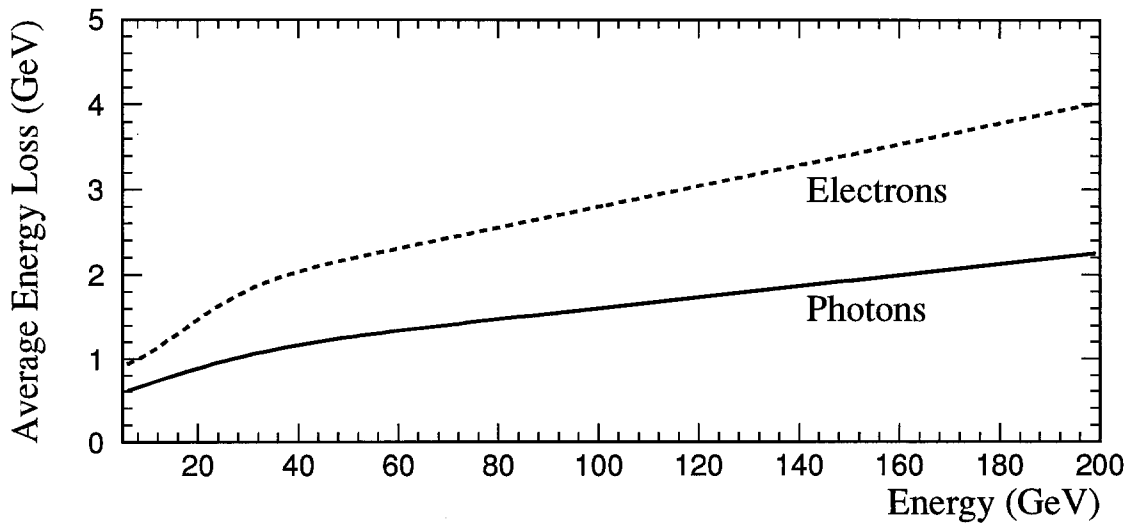

Figure 5.2 The average energy lost by photon (solid line) and electron (dashed line) showers in the material in front of the active region of the EMLAC, as determined from the Monte Carlo.

full sample of 1991 data. The radial dependence of the EMLAC energy response was attributed to differences in shape between the data signals and the gains-calibration pulses [31]. Figure 5.4 shows the shape of the radial dependence for the various E706 data samples, demonstrating a correlation between the radial energy-dependence and the choice of charge-integration times [29, 31].

5) Correct for residual octant-to-octant variations to establish the final scale.

Figure 5.5 shows the final mass distributions in the signal regions of the π^0 and η (in the $\gamma\gamma$ mode) and of the ω (in the $\pi^0\gamma$ mode) for the full 1991 data sample after completion of the energy scale calibration. The final fit values of

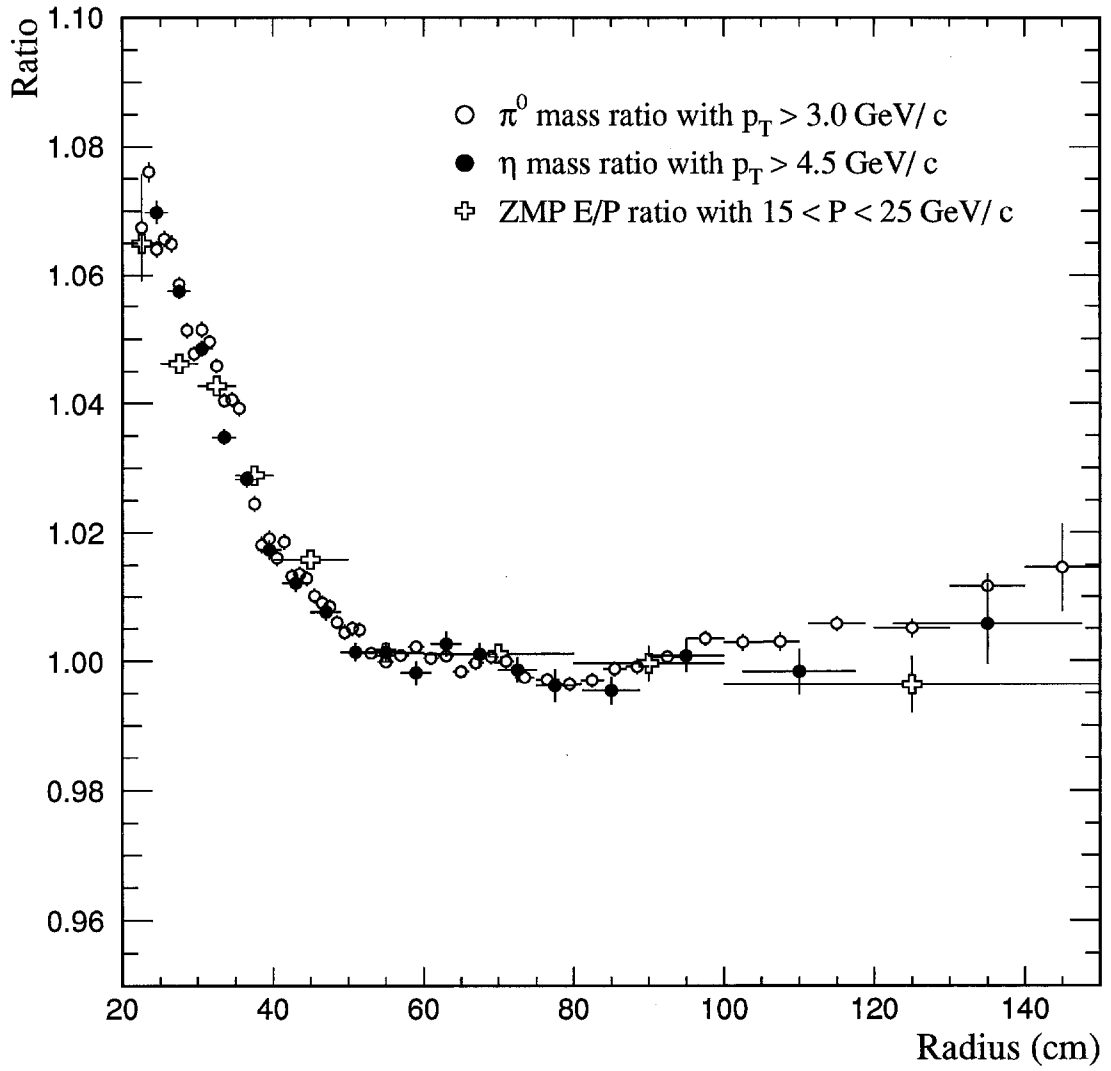

Figure 5.3 The radial dependence of the EMLAC energy response is demonstrated here by plotting the ratio of reconstructed masses to the nominal values given by the Particle Data Group (PDG) [5] for the 1991 data. Corroborating evidence is supplied by overlaying the radial dependence of E/P (the ratio of the EMLAC energy to the tracking system momentum measurement) for a sample of ZMP electrons.

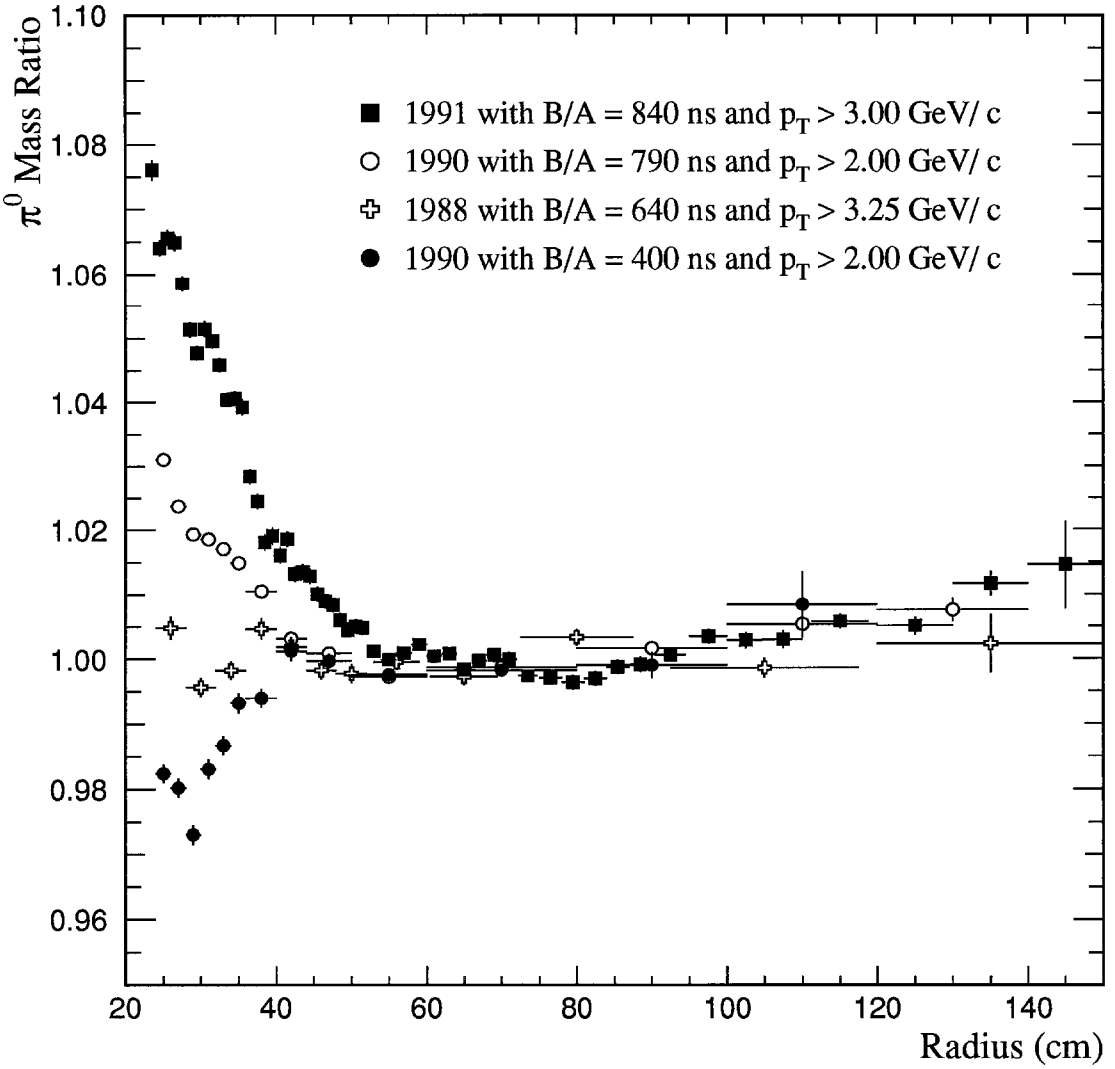

Figure 5.4 Observed radial dependence of the reconstructed π^0 mass shown for various BEFORE/AFTER gate settings. The BEFORE/AFTER gate defined the charge-integration time.

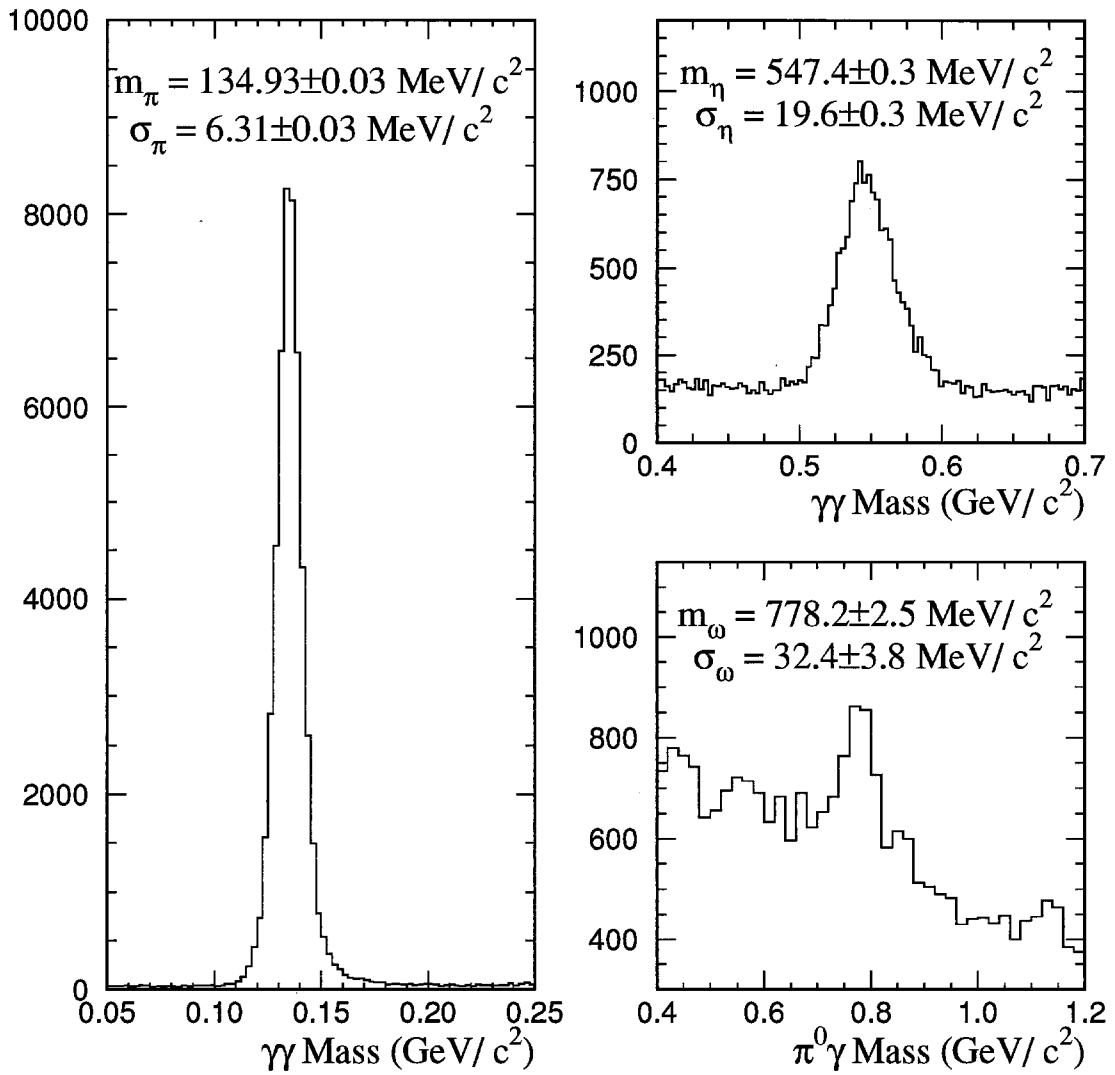

Figure 5.5 The $\gamma\gamma$ mass distributions in the π^0 and η signal regions and the $\pi^0\gamma$ mass distribution in the ω signal region, along with fitted central values and widths.

Meson	Sources (Masses given in MeV/c^2)		
	PDG Value	1990 Data	1991 Data
π^0	134.976 ± 0.001	135.15 ± 0.02	134.93 ± 0.03
η	547.45 ± 0.19	547.5 ± 0.2	547.4 ± 0.3
ω	781.94 ± 0.12	781.3 ± 2.8	778.2 ± 2.5

Table 5.2 Comparison of the PDG [5] value to the masses of the π^0 and η mesons obtained after all corrections were applied.

the three meson masses for both 1990 and 1991 are given in Table 5.2; these measured values are consistent with the values published by the PDG when the quoted energy scale uncertainty of 0.5% is taken into consideration. The linearity of the calibrated energy response is illustrated in Figure 5.6; the mass of the η is quite flat versus both energy and p_T.

5.3 Trigger Efficiency Measurement

Due to sharply falling production spectra, the majority of events selected by a trigger have transverse momenta relatively close to the trigger threshold. Figure 5.7 demonstrates this fact by overlaying π^0 number distributions before trigger corrections were applied for events selected by various triggers. In the interest of maintaining high statistics, it is therefore necessary to investigate the performance of the trigger near its threshold. Since the author had primary responsibility for the 1991 trigger analysis, the following sections relate some of the details of the methods used.

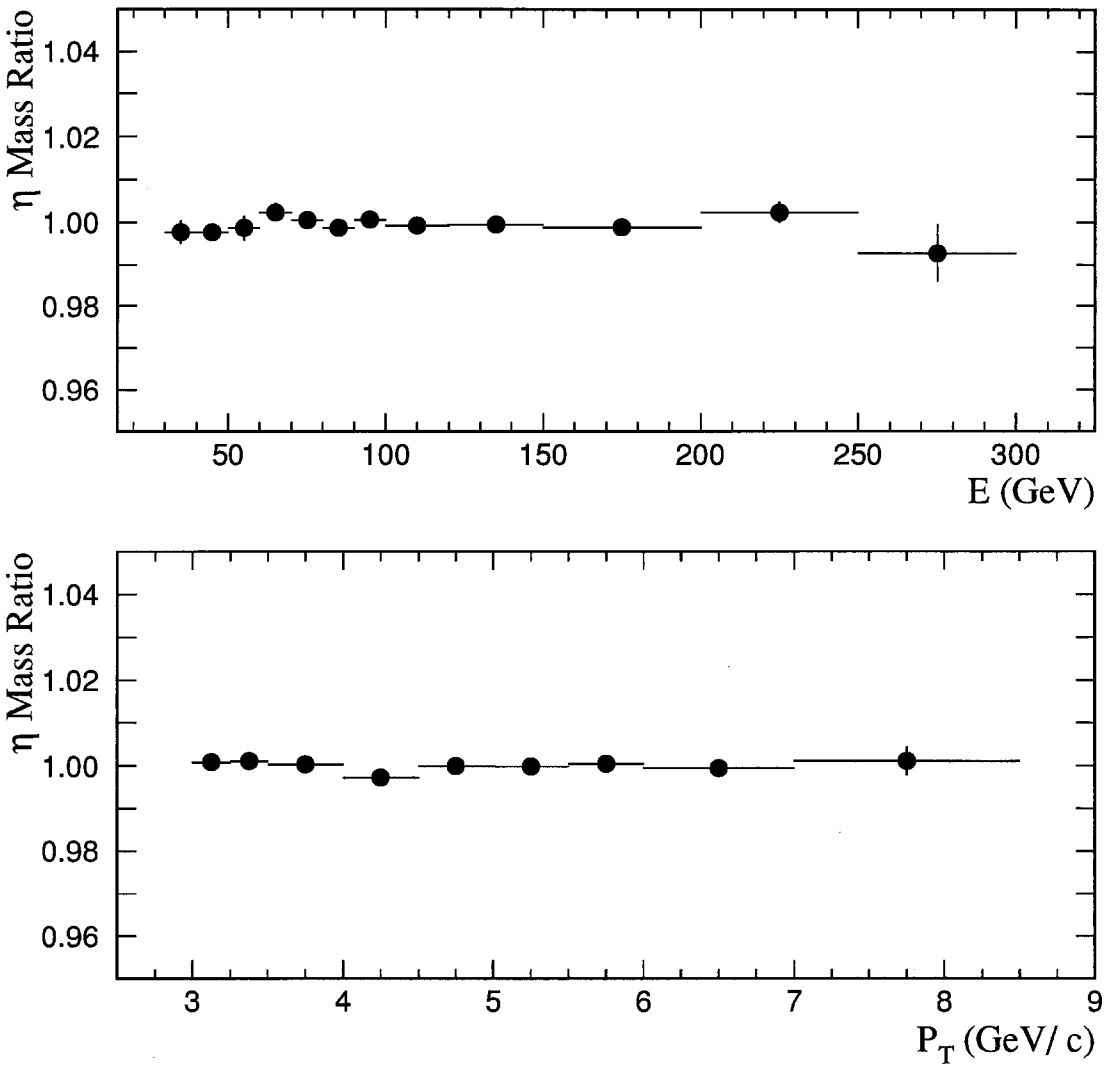

Figure 5.6 The mass of the η in the 1991 sample (relative to the PDG value) after the final energy scale calibration versus energy (top) and versus p_T (bottom).

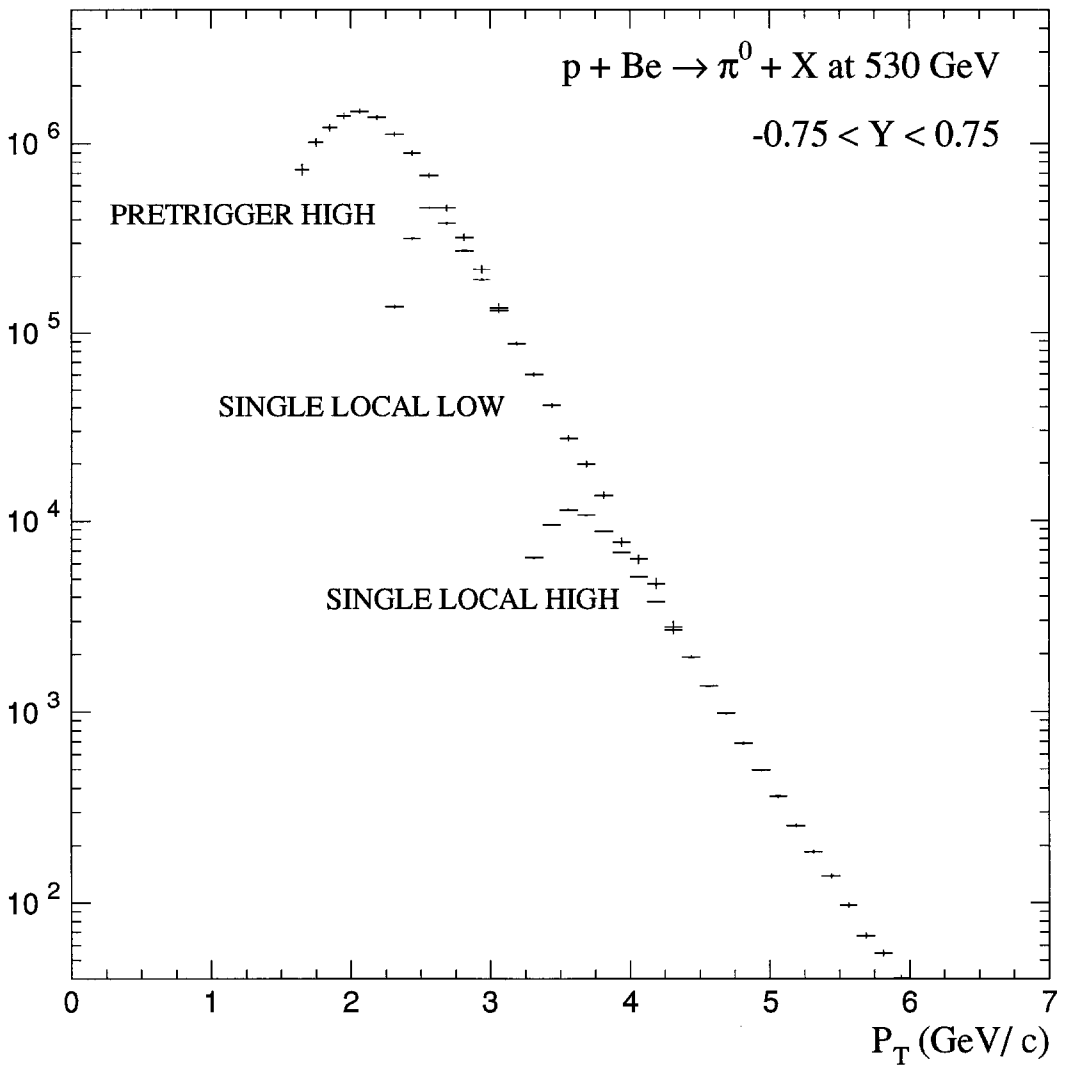

Figure 5.7 The number distribution of π^0's prior to trigger corrections. In regions of p_T overlap between two triggers, trigger corrections can allow for the use of the higher-threshold trigger, along with its higher statistics.

5.3.1 Event-wise Trigger p_T Reconstruction: General Methods

The method chosen to evaluate the E706 trigger efficiencies was based on our event-by-event reconstruction of the trigger p_T. Since this method is independent of the final physics analysis, trigger studies need not be repeated for each new topic or method (e.g. different particle type, different cross-section binning, etc.). The "trigger p_T" used for the functional dependence of the efficiency evaluation was reconstructed by summing the LACAMPs' 800 ns outputs over the appropriate number of strips, with the signal from each strip[3] weighted by an appropriate trigger gain. Significant effort was expended to, as closely as possible, match the reconstructed trigger p_T with the online trigger p_T since significant variations between these variables increase possible bias in calculated trigger efficiency.

The general procedure employed in the evaluation of the efficiencies of all E706 triggers is given below. Of course, vagaries of specific triggers required special handling for certain data samples, some of which will be discussed in the following section.

1) Identify a sample of events with an appropriate p_T range which is unbiased with respect to the trigger being analyzed. For high[4] triggers, events selected by the corresponding low trigger in the same octant were employed in this manner, since the low trigger was typically fully efficient in the turnon region of the high trigger. For the low

---

[3] The strip energies were uncorrected for the EMLAC time-dependent energy response. This is important because the online trigger thresholds did not scale continuously with the EMLAC energy, and using corrected strip energies would have caused spurious time-dependence in the trigger.

[4] A "high trigger is one with a relatively high threshold, typically around 5 GeV/c. "Low" triggers' thresholds were around 3 GeV or so.

triggers, a special "opposite octant" sample was used to avoid trigger bias. For each high-triggered octant, the octant of the remaining seven which contained the largest amount of p_T was designated an "opposite octant." In fact, these octants often contained showers from the recoil jet, and were therefore frequently directly opposite to the triggering octant.

2) Apply the same vetoes and requirements as the online trigger (e.g. veto wall, early p_T, and SCRKILL for the pretrigger analysis).
3) Divide the data sample into "trigger sets," or regions in which the trigger's response was constant. Changes in thresholds or vetoes, replacement of electronic modules, or other relevant alterations in the experimental apparatus constitute reasonable locations and times to insert a "trigger break."
4) Select the event sample corresponding to each individual trigger discriminator (e.g. an octant or a LOCAL), histogram the trigger p_T distribution for all events (denominator) and the trigger p_T distribution for events satisfying the trigger (numerator), and take the ratio to calculate the efficiency as a function of trigger p_T. Parametrize the efficiency by fitting to an error function.

Once the appropriate efficiencies have been evaluated as outlined above, given an octant selected by the trigger in question and given the associated trigger p_T, one may query the appropriate error function(s) to calculate the *a priori* probability of having fired the trigger. The inverse of this probability can be used as a weight to account for events at that particular trigger p_T which were not selected by the trigger. Since a local trigger status in an octant depends on the status of all LOCAL's in that octant, the calculation of the trigger weight must

in principle query error functions associated with each of the 31 LOCAL's. The probability P for firing a local trigger is

$$P = 1 - \prod_{i=1}^{31}(1 - p_i) \tag{5.1}$$

where p_i is the probability that LOCAL i fired.

5.3.2 Image Charge and other Trigger Challenges

There are a number of challenges associated with the evaluation of trigger performance near threshold for the E706 triggers. Since the online trigger used strip energies measured by the LACAMP fast-outs and the reconstructed trigger p_T was based on the 800 ns outputs, any effect which was dependent on signal timing could broaden the measured turnon curves or otherwise compromise the analysis if the sample selected was inappropriate. Of particular consequence was the effect denoted "image charge" in the E706 parlance. Image charge effects were due to the propensity for a signal in one region of the detector to capacitively induce "image" signals in other regions. During the time of signal collection, this generally had the effect of reducing the apparent pedestal values across the octant. Approximately 300 ns later, however, the apparent pedestal values[5] were above zero due to "overshooting" as the high voltage recovered from the induced signal. Thus, depending on the relative timing of two signals, one signal could increase or decrease the apparent size of another. Indeed, image charge was the reason for global cutoffs and for the early-p_T veto, as mentioned in Section 3.1.2. Nevertheless, since this effect was very sensitive to signal timing and integration length, it represented a significant challenge in the analysis of the trigger.

---

[5] It should be noted that the correlated pedestal shifts (which FREDPED was designed to remove) were likely due, at least in part, to image charge effects from out-of-time events.

Several pieces of information relating to the timing of energy depositions (or potential energy depositions) were available for studies and cuts in the trigger analysis. The beam and interaction counters provided such information for ≈100 ns before and after the interaction of interest. Photon TVC values provided another valuable source of such information. Finally, for all of 1991, and the later portions of 1990, the early-p_T veto status was latched for all octants, furnishing some information concerning the status of the detector several hundred nanoseconds prior to the "in-time" event. Each of these sources of timing information was used to study the various triggers, and with special attention paid to avoiding topological bias when using the TVC's, timing cuts were imposed to reduce the dependence of the trigger analysis on out-of-time p_T depositions. The local triggers, with more limited spatial extent, were somewhat less susceptible to image charge effects than were the globals, and thus the local analyses were simpler in that regard.

Another complexity in the analysis of E706 triggers was due to the difficulty in determining the trigger gains which weighted the strip energies to compute the trigger p_T. Of course, improper variations of these gains would broaden the trigger turnon and bias the efficiency measurements. Periodically, gains calibration data were taken when the experiment was not receiving beam; a pulse was generated in the LACAMP's and measurements were made of the observed reconstructed trigger p_T and the adder cards' analog output (for the global triggers) and the threshold location for an applied threshold voltage (for the local triggers). Although this data provided an estimate of the gains at the time of calibration, the trigger gains were susceptible both to changes in the electronics over time and to differences between the conditions during gains measurements and the conditions during data acquisition. The methods used in addressing these residual gains variations depended somewhat on trigger type, and are therefore discussed below.

5.3.3 The Local Triggers

As discussed previously, each EMLAC octant contained 31 overlapping 16-strip LOCAL's. The online local triggers for an octant were satisfied if any of the 31 LOCAL's contained p_T in excess of its threshold. For each LOCAL, a discriminator status bit was recorded to provide the capability to calculate a turnon for each LOCAL, and local trigger p_T was calculated from the front and back energies of the 16 strips corresponding to a given LOCAL. Careful analysis of the 1991 local turnons revealed that residual gains corrections were necessary to optimize the efficiency measurements. To accomplish this task, four turnons were computed for each LOCAL: one turnon from events dominated by trigger p_T in the front of the innermost 8 strips, a second corresponding to the front outermost 8 strips, a third for the back inner, and the fourth for the back outer. By iteratively correcting the trigger p_T contributions to these four regions so that the corresponding turnons occurred at the same location in trigger p_T, the effective average gains were corrected. Another difficulty was due to the fact that the online local trigger discriminators were subtly different than the latched status bits because the acceptance of the two sets of discriminators depended differently on the relative signal timing. This challenge was met by judicious application of timing cuts on the sample used to measure the turnons, as discussed above.

The SINGLE LOCAL HIGH efficiency analysis utilized events selected by the SINGLE LOCAL LOW and the TWO GAMMA triggers as the unbiased (with respect to the SINGLE LOCAL HIGH) sample, with the following exceptions. In 1990, the SINGLE LOCAL LOW trigger was not installed until late in the run, so the TWO GAMMA was used exclusively, and during the early portion of the 1991 run, the TWO GAMMA was particularly susceptible to noise-type events (due to the extracted spill structure during that part of the run) and thus was not used until

after run 13598. The SINGLE LOCAL LOW turnons were computed using opposite octants. Figure 5.8 shows some typical turnons for the 1991 local triggers.

5.3.4 The Global Triggers

By definition, the trigger p_T input to global trigger discriminators is directly dependent upon information from many more strips than the corresponding signals for local triggers. Thus, by their very nature, global triggers are even more susceptible both to gains variations and to image charge effects than are the local triggers. Tuning of the zero-cross discriminators' timing and the installation of the global p_T cutoffs reduced the sensitivity of the online global triggers to image charge. However, these steps generated additional challenges in the offline analysis of these triggers.

Image charge in the offline analysis was, to a large extent, controlled by the application of various signal/timing cuts to the event sample accepted for analysis; however, these cuts reduced the efficacy of the trigger correction by effectively decreasing the resolution of the trigger p_T calculation. The high-p_T biases of these effects could be removed only by means degrading the corrections at lower p_T's. This trade-off was, of course, most properly accepted, since lower-threshold triggers provided coverage in regions for which the higher trigger became significantly biased.

The global p_T cutoffs presented a challenge due to the fact that although the voltages associated with these cutoffs were measured, the conversion factor between the units of the voltage measurements and the units of trigger p_T (i.e. the "cutoff scale") was difficult to determine precisely. By plotting the adder card output (in ADC counts) versus the reconstructed trigger p_T for the gains calibration data, and then extrapolating a linear fit of the high-p_T data to the

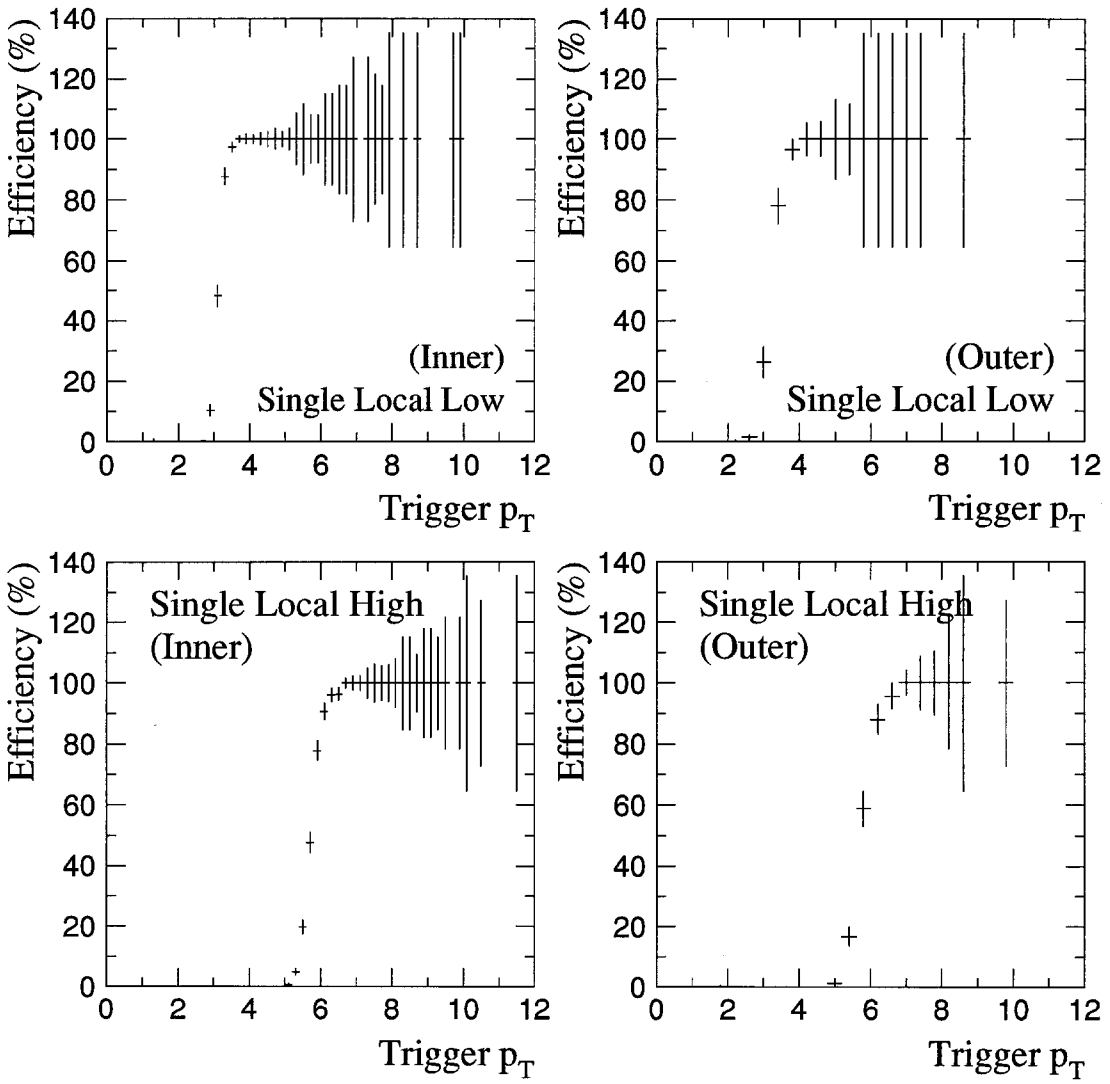

Figure 5.8 SINGLE LOCAL LOW (top) and SINGLE LOCAL HIGH (bottom) turnons for selected inner and outer LOCAL's as a function of trigger p_T. The error bars above the turnon region are intended to provide an estimate of the statistical uncertainty of the measurement, and should not be taken to imply that the efficiency could exceed 100%.

ADC axis, an estimate of the cutoffs was made. In 1990, this method of analysis produced reasonable estimates for the cutoff scale; difficulties arose in certain regions where electronic modules were changed during the course of the run. For these regions, the cutoff scale was determined by comparing the turnons in which few sums-of-eight contributed to turnons in which many sums-of-eight contributed. For cutoff scales much smaller (larger) than appropriate, all calculated trigger p_T's would be too large (small), but the "many-groups" trigger p_T would be affected the most. By requiring correspondence between the two turnons, a data-derived estimate of the cutoff scale was determined; for regions of overlap, the two methods agreed within errors. Due to its efficacy and to its ease of use, the latter method was used exclusively in the 1991 analysis.

For 1990, the LOCAL GLOBAL HIGH trigger corrections were analyzed using an event sample selected by the LOCAL GLOBAL LOW, and the LOCAL GLOBAL LOW analysis used the "opposite octants." To date, corrections have not been evaluated for either of these triggers in the 1991 sample. The 1990 and 1991 PRETRIGGER correction analysis also made use of the opposite octants. For all the global triggers, the turnons were found to be somewhat dependent on event topology. For this reason, turnons were fit for each octant as a function of the number of sums-of-eight (front and/or back) contributing to the turnon. In addition, the PRETRIGGER analyzed separately for the inner and outer half of each octant due to observed differences in the turnons between the two half octants. Figure 5.9 contains typical turnons for the 1991 pretrigger. The 1990 PRETRIGGER analysis was hampered by the unavailability of the early p_T veto status for much of the run. The effect of this veto, however, was determined to be p_T-independent. Thus, the turnons were fit to an error function with a floating normalization and then the function was scaled so that the high-p_T efficiency was 100%.

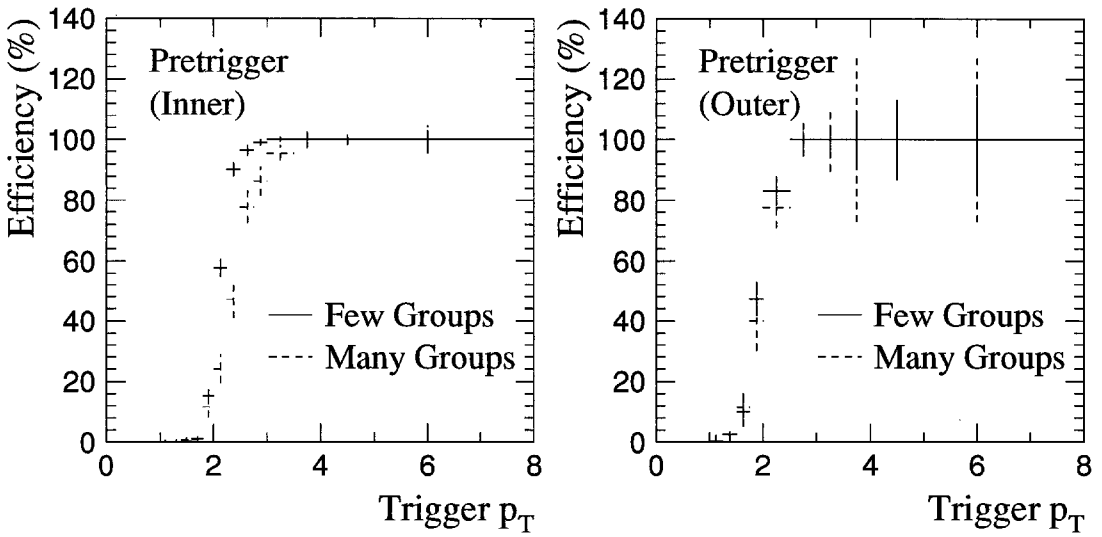

Figure 5.9 Selected inner (left) and outer (right) PRETRIGGER turnons for few (solid) and many (dashed) sums-of-eight.

5.4 The Monte Carlo

A Monte Carlo simulation of events in our detector furnished corrections for several effects in the data. Subsequent sections in this chapter discuss the role of the Monte Carlo simulation in the calculation of the various reconstruction efficiencies and in the correction for direct photon backgrounds. This section provides an overview of the Monte Carlo package and a comparison of the Monte Carlo results with data.

5.4.1 The Monte Carlo: Event Generation and Reconstruction

The event generator selected for our Monte Carlo simulation was HERWIG [32]. HERWIG was chosen primarily because, among the generators available to us, it compared most favorably with our data in terms of both charged and neutral multiplicities. HERWIG was used to generate separate samples dominated by π^0's, η's, and direct photons. To evenly populate the entire range of transverse momentum, event samples were generated with various minimum-p_T thresholds. To reduce biases due to these generated-p_T thresholds, events with reconstructed p_T's less than 0.5 GeV/c above the generation threshold were not used in the evaluation of corrections. The Monte Carlo events were weighted as a function of p_T and rapidity to match the inclusive neutral meson and direct photon distributions measured in the data.

Events generated by HERWIG were propagated through a simulation of our detector using the GEANT [33] package. Certain GEANT routines allow for the definition of "volumes" or physically homogeneous and spatially contiguous elements of a detector; other routines simulate the propagation of particles through the volumes of the spectrometer and the interaction of particles with the material in each volume. Using GEANT and the specifications of the various components

of the spectrometer, a virtual E706 spectrometer was constructed, tuned, and tested. Then, in order to reduce the amount of time necessary to produce Monte Carlo events, certain approximations were tested; approximations determined to be inconsequential to the final results were implemented in the final Monte Carlo code. For example, by reducing the number of volumes, the computational time could be reduced; therefore, instead of using copper-clad G10 readout boards in the EMLAC, homogeneous "G10" boards with greater density and width were substituted, significantly reducing the number of distinct volumes. A substantial reduction in computing time was also obtained by raising the threshold below which GEANT stopped tracking individual particles. This threshold was increased from 1 MeV to 10 MeV and a simpler routine was used to deposit the remaining energy.

The simulation in GEANT was "perfect" in the sense that the detector was idealized; for example, inefficiencies and time dependences in the various spectrometer components were not included in the simulation. A separate package, the "preprocessor", added such effects and introduced real-world complexities to the Monte Carlo simulation. (The imposition of these effects on the Monte Carlo in the preprocessor stage allowed tuning of the preprocessor parameters without necessitating the repetition of the time-consuming process of generating the Monte Carlo events.) After this preprocessor was invoked, Monte Carlo events followed the data stream through MAGIC and DST production, with the exception that, since the effects necessitating the use of FREDPED were not introduced into the Monte Carlo, FREDPED was not invoked on the Monte Carlo events during reconstruction.

The generation and reconstruction schemes outlined above were twice performed in full: once using a simulated incident 530 GeV/c π^- beam and

spectrometer parameters matching the 1990 configurations, and once with an 800 GeV/c proton beam with the 1991 spectrometer's parameters. To acquire Monte Carlo coverage for the 1991 secondary beam samples, the events generated at 530 GeV/c for the 1990 samples were re-reconstructed using the simulation of the 1991 spectrometer. By doing this, substantial time was saved in the generation of completely new samples; since all Monte Carlo events are weighted in transverse momentum and rapidity bins so that the Monte Carlo cross sections match those in the data, these Monte Carlo samples behave properly with respect to the corresponding data. Small additional samples of Monte Carlo for the 1991 secondary beams were generated and reconstructed to study and account for any residual bias due to these approximations.

5.4.2 Comparisons of Monte Carlo and Data

Verification that the Monte Carlo provides an adequate representation of the data is important for building the confidence necessary to use the Monte Carlo for corrections of the data. The major sources of direct photon background are π^0's (and to a lesser degree, η's, ω's, etc.) for which only one of the decay photons is reconstructed and coalesced π^0's (i.e. π^0's whose decay photons were reconstructed as a single photon). Figure 5.10 is a comparison of the shape of data and Monte Carlo energy asymmetry[6] distributions, demonstrating reasonable consistency between the Monte Carlo and data results and providing assurance that the reconstruction program had a similar level of difficulty in reconstructing high-asymmetry coalescence-prone π^0's for the Monte Carlo as for data. Figure 5.11 shows comparisons of the shapes of the π^0 and η signal regions and backgrounds in the data and Monte Carlo, demonstrating that the

[6] See Section 5.5.3 for discussion of asymmetry distributions in the data.

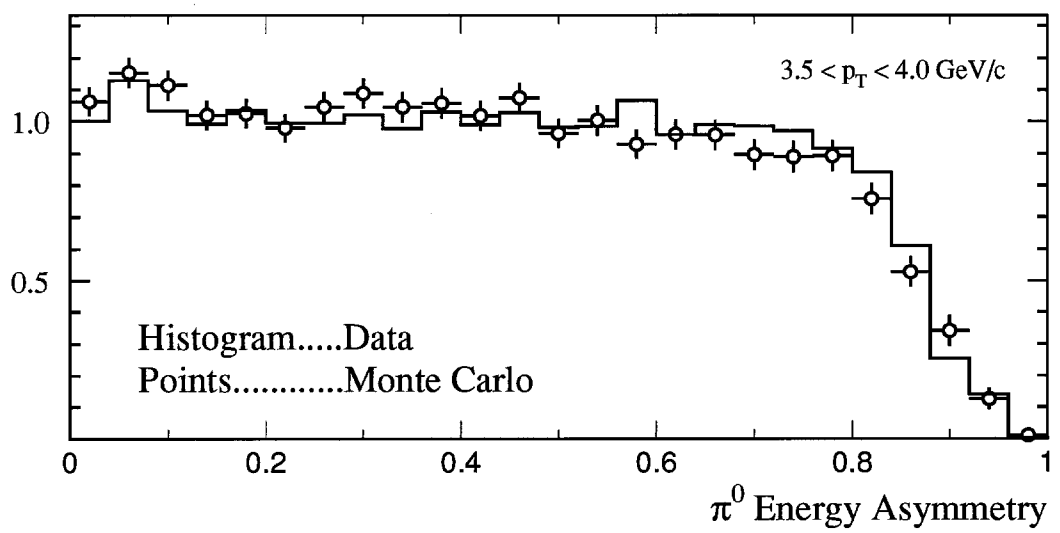

Figure 5.10 A comparison of the shapes of data and Monte Carlo π^0 asymmetry distributions. π^0's contributing to this plot were those in the 1990 data sample and the associated Monte Carlo sample with $3.5 < p_T < 4.0$ GeV/c.

significant features of the EMLAC are well modelled. Finally, Figure 5.12 shows the longitudinal development of photon showers in data and Monte Carlo events; the agreement here not only builds confidence in the Monte Carlo simulation as a whole, but also demonstrates the reliability of the Monte Carlo correction for the E_{front}/E_{total} requirement on the data.

5.5 Analysis Methods

The following sections describe the various requirements, corrections, and methods used to determined the π^0, η, and direct photon cross sections, nuclear dependences, and cross-section ratios.

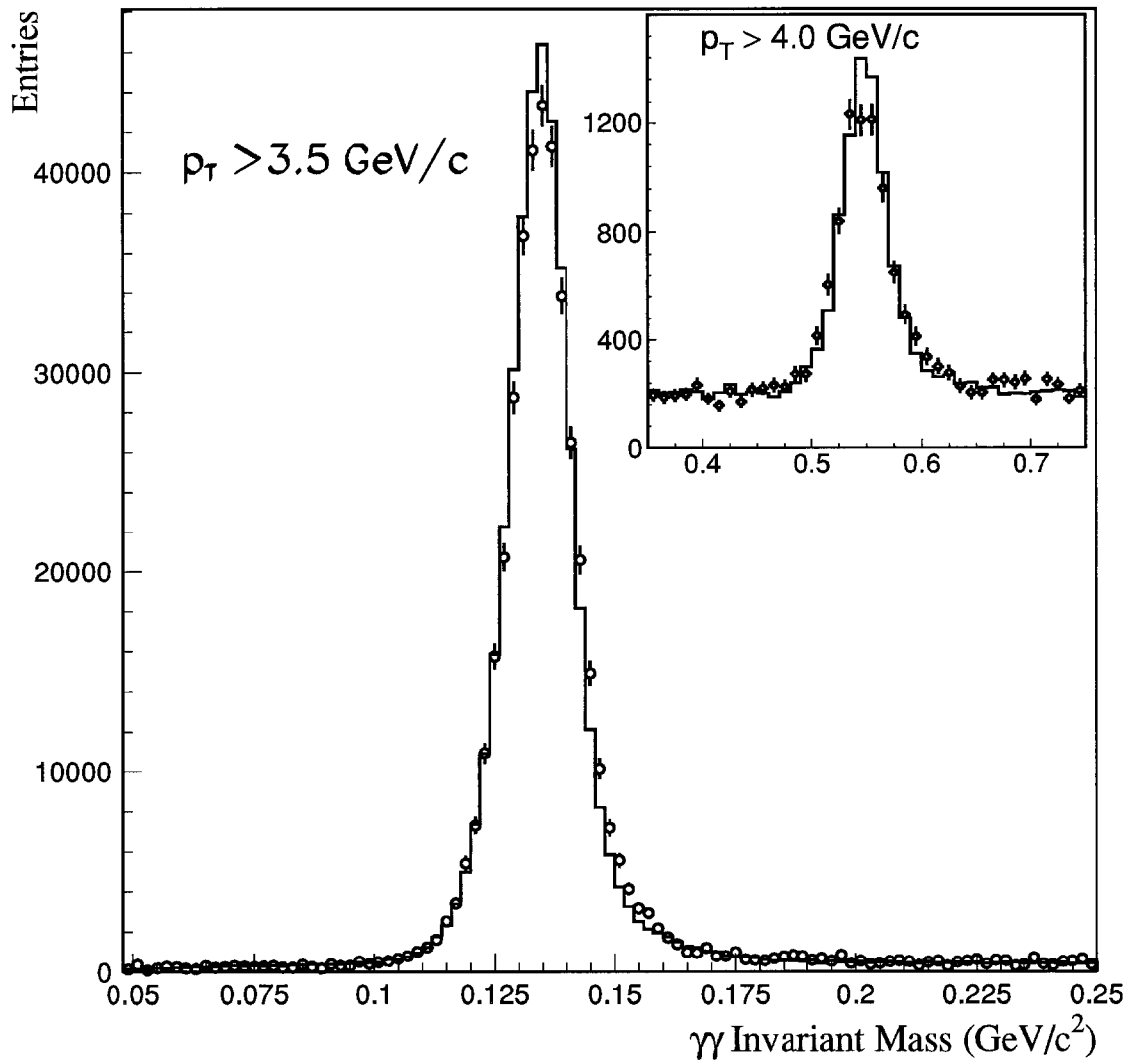

Figure 5.11 A comparison of the shapes of data (histogram) and Monte Carlo (points) $\gamma\gamma$ mass distributions in the π^0 and η signal regions.

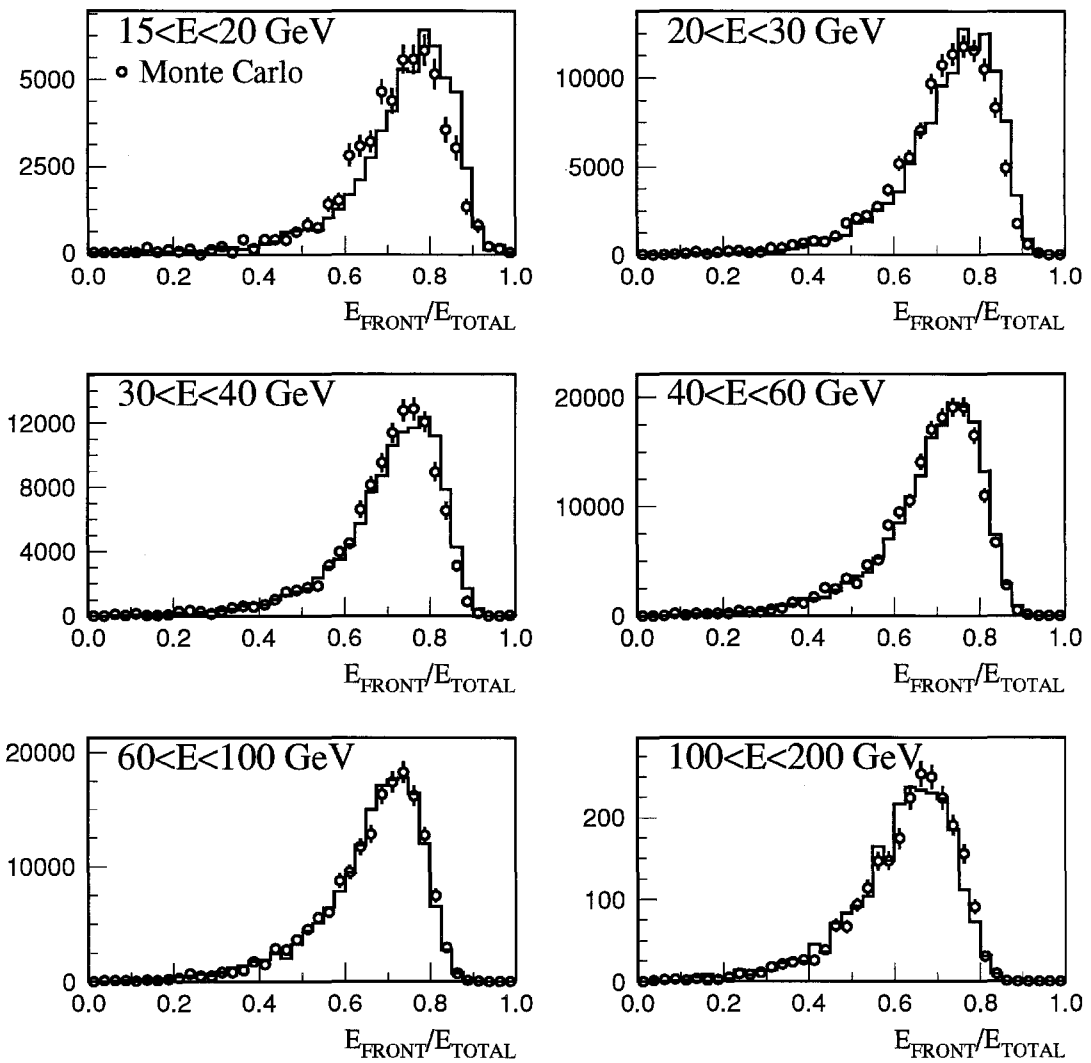

Figure 5.12 A comparison of the shapes of data (histogram) and Monte Carlo (points) photon E_{front}/E_{total} distributions in six photon energy bins.

5.5.1 Vertex Requirements and Related Corrections

A reconstructed vertex in the target region was required in each event which was to contribute to the cross-section measurements. Figure 5.13 shows the longitudinal vertex position distribution for the 1990 and 1991 target configurations for events containing a high-p_T diphoton mass in the π^0 signal region. To make these plots, weights[7] were applied to account for beam absorption by targets and other materials upstream of the reconstructed vertex and for photon conversion in materials downstream of the reconstructed vertex. The various targets and the SSD wafers are clearly visible, and from plots such as these, appropriate longitudinal-position cuts were determined to distinguish among events from different target materials. The hydrogen target, for example, required fiducial cuts to exclude the peaks near each end. (These peaks are due primarily to the beryllium windows which were part of the structure containing the hydrogen target and its peripherals.)

A transverse target fiducial requirement was imposed on the reconstructed vertex position. A correction was then made for the beam outside of this fiducial volume. This cut and correction avoided bias in the normalization of the measurements due to the counting of beam which did not impinge on the target. The correction was made by counting vertices in the upstream set of beam SSD's inside and outside of the transverse target fiducial region and adjusting the beam count accordingly. For 1990, the size of this correction, which was computed as a function of run number, was $\approx$1.35; in 1991, this correction was close to unity.

Additional corrections were necessary to account for inefficiency in vertex-finding and to account for vertices reconstructed in locations outside of the

[7] See Section 5.5.6 for a description of these corrections.

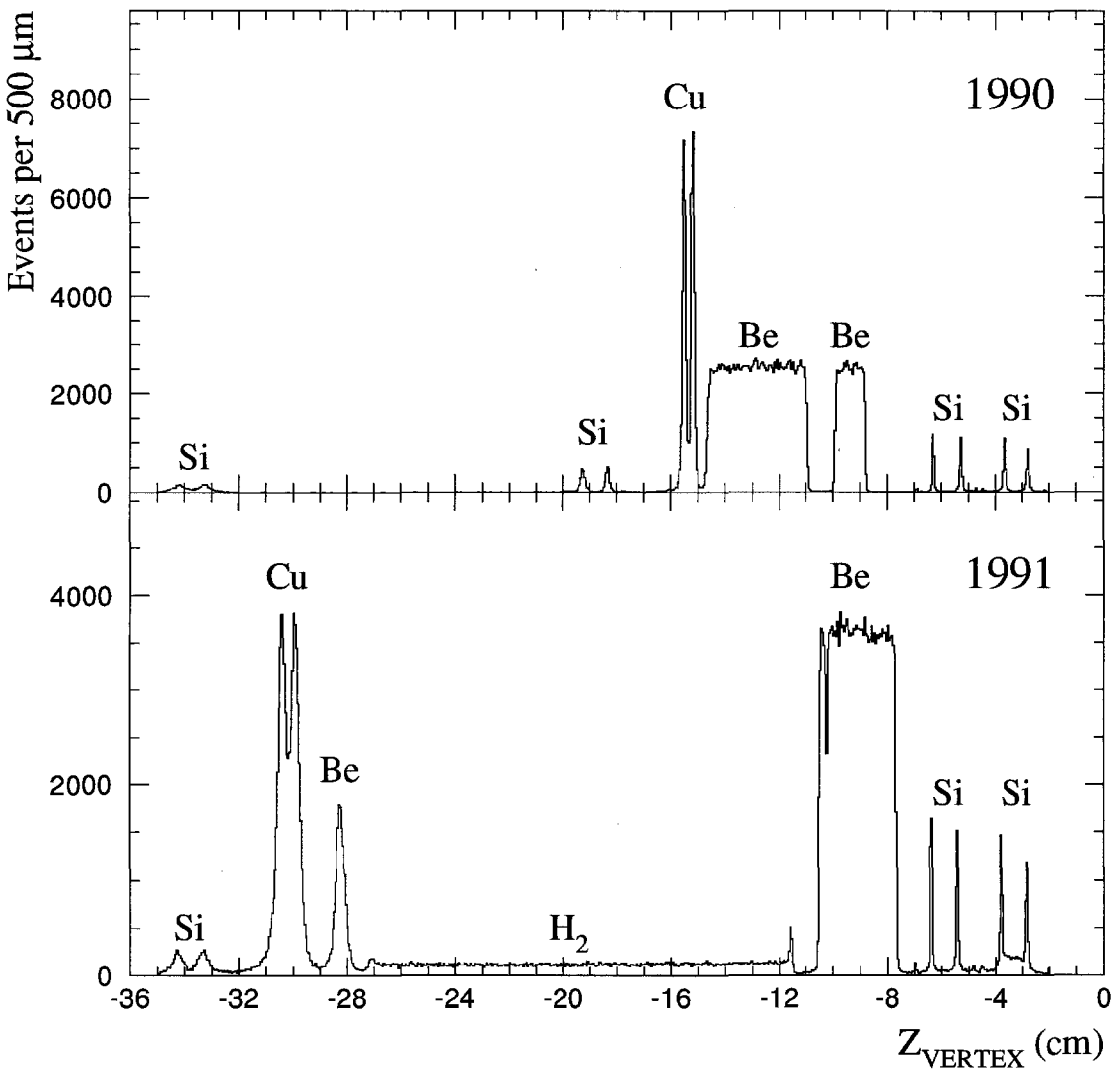

Figure 5.13 The weighted longitudinal distribution of reconstructed vertices for 1990 (top) and 1991 (bottom) spectrometer configurations. The events contributing to these plots were selected by requiring a $\gamma\gamma$ pair with $p_T > 4.0$ GeV/c with a mass in the π^0 signal region.

longitudinal fiducial regions associated with the target in which the interaction actually occurred. The latter correction, the "tail correction," actually had two partially cancelling terms: the correction for losses due to tails outside of the longitudinal target fiducial cuts and the correction to remove contributions from the tails associated with nearby targets. The longitudinal extent of the target region in the 1990 configuration was relatively small; in this case, the vertex reconstruction efficiency was very high and the resolution was relatively good as well, resulting in small corrections for both effects. Using the HERWIG Monte Carlo (see Section 5.4), the vertex reconstruction efficiency in 1990 was found to be 99.6%. The tails corrections, which were estimated by fitting and extrapolating visible tails in the data, were 1.01 for copper and 0.998 for beryllium. In 1991, the copper targets and the upstream beryllium target were both significantly farther upstream than the 1990 targets. In this case, the tail corrections for these targets were estimated at 1.025; the efficiency, as measured by the ratio of cross sections calculated from the upstream and downstream beryllium targets, was 94.5%. The reconstruction efficiency use for the 1991 downstream beryllium targets was 99.6%; tail losses and gains were negligible. The combined tail correction and efficiency for the hydrogen target was 0.945.

The above cuts and corrections were sufficient to provide relatively small vertex-related systematics in the measurement of cross sections. However, the systematics associated with the measurement of nuclear dependence (see Section 6.7.2) are dominated by vertex-related uncertainties. For this reason, a number of additional cuts were imposed in the nuclear dependence analysis which reduced the potential for confusion in the vertex reconstruction. A cut was imposed on the timing information from the interaction counters; this cut removed events containing out-of-time interactions which occurred within the timing window of the tracking system. The beam hodoscope information was used

to further reduce the incidence of events in which more than one beam particle impinged on the target. (Of course, the BEAM1 requirement imposed by the trigger helped in this regard; however, the definition used for the cut in the nuclear dependence measurement rejected events in which the hodoscope had even some small indication of multiple beam particles.) An additional cut, which rejected very few events, required that the data acquisition system performed adequately for both the trigger-related scintillation detectors and the tracking system. None of these cuts depend on the target material associated with the vertex; since the nuclear dependence measurement depends on cross-section ratios between targets, no correction was necessary.

5.5.2 Muon Bremsstrahlung Rejection

As discussed in Chapter 2, some halo muons produced upstream of the spectrometer were incident upon the EMLAC. Spoiler magnets were placed in the beamline to steer many of the muons away from our spectrometer, and veto wall scintillation counters were installed to veto potential triggers associated with the remaining muons. Due to inefficiencies in these counters, some halo muons still generated triggers by producing showers in the EMLAC via the process of bremsstrahlung. Although this occurred rarely, these muon-induced showers at large radii simulated high-p_T photon showers, which also occur relatively rarely. To avoid large backgrounds in the π^0 and photon cross-section measurements, several cuts were imposed to identify and remove muon-triggered events from the data set.

Offline Veto Wall Cut

The online veto wall inefficiency was due in part to the tight timing employed in the online veto coupled with the challenge of timing the many veto wall elements

precisely. The veto wall status was latched for offline investigation; it contained useful information for removing additional muons. The same logic was applied, namely

$$(\mathrm{VW1} + \mathrm{VW2}) \bullet (\mathrm{VW3} + \mathrm{VW4}) \tag{5.2}$$

where $\bullet$ and $+$ designate the logical AND and OR, respectively. (In the 1990 data, the fourth veto wall did not exist, but the logic was otherwise unchanged.) In the offline analysis, the normal bucket-wise timing correlation requirement was replace with a ± 1 bucket requirement which allowed for timing variations among the signals. In addition, only buckets 4 through 12 were used in the offline veto because hits in the buckets outside this range did not correlate with energy depositions in the LAC. Figure 5.14 demonstrates that while this cut is effective, significant muonic background remains at high p_T, making the additional muon-rejection tools discussed below valuable in further reducing the remaining background.

Directionality Cut

The comparison of the reconstructed shower positions in the front and back section of the detector provides some information concerning the angle of incidence of the showering particle. Since the halo muons do not emanate from the target, but impinge on the EMLAC approximately perpendicular to its face, information regarding the angle of incidence can be used to reject showers associated with these muons. To this end, directionality is defined as

$$D = r_{\mathrm{front}} - \frac{z_{\mathrm{front}}}{z_{\mathrm{back}}} r_{\mathrm{back}} \tag{5.3}$$

where r_{front} and r_{back} are the reconstructed radial positions and z_{front} and z_{back} are the z positions of the first layers of the front and back sections of the EMLAC.

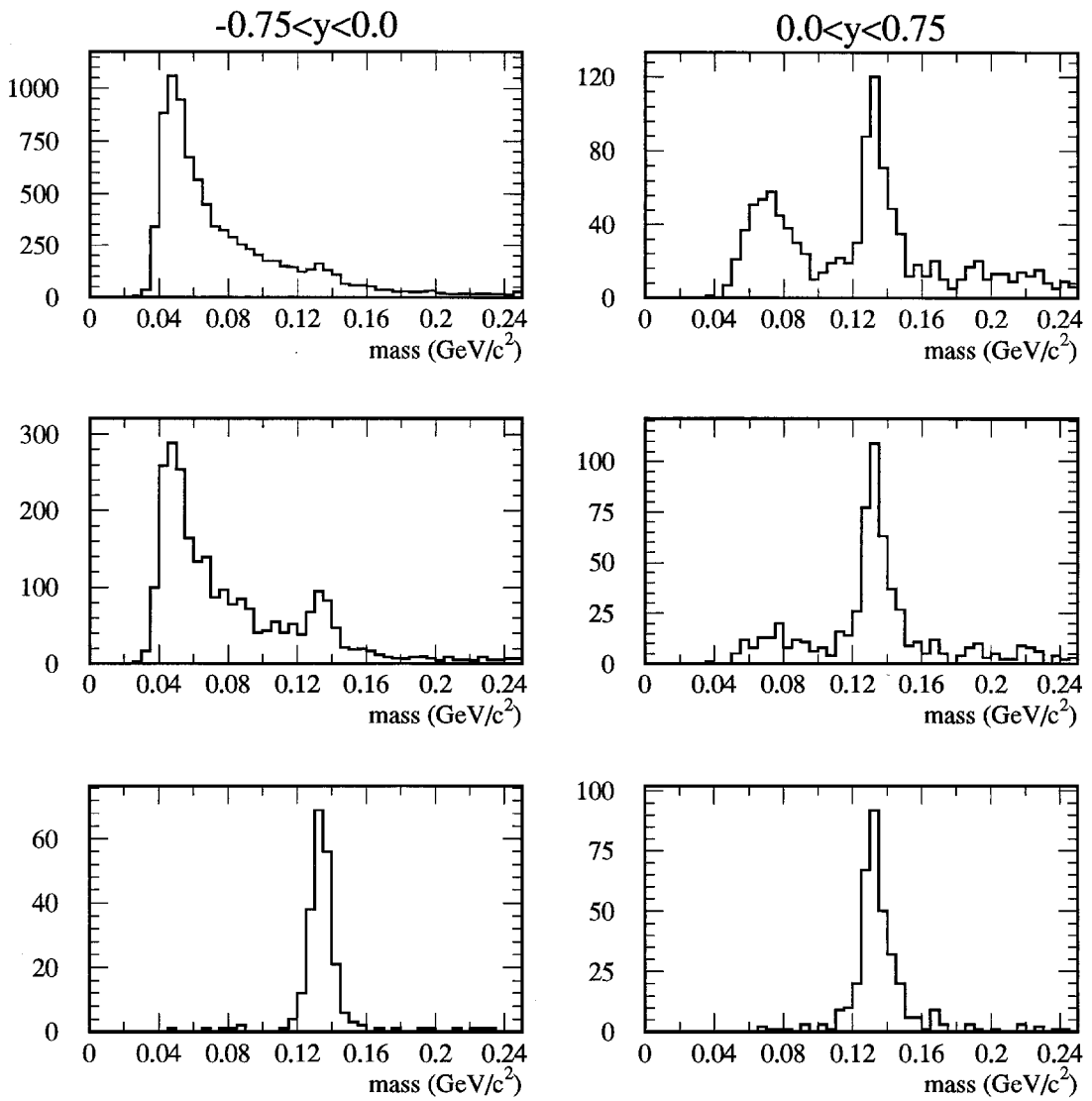

Figure 5.14 The effects of the muon bremsstrahlung rejection cuts on the 1990 $\gamma\gamma$ mass distribution in the vicinity of the π^0 peak for $\gamma\gamma$ p_T in the range 7 to 9 GeV/c in two rapidity bins. The top plots have no muon rejection criteria, the middle satisfy the offline Veto Wall cut, and the bottom plots additionally satisfy the directionality, balanced-p_T, and χ^2/E requirements.

Figure 5.15 shows the distributions of directionality for muon showers and for single photon showers.

The cut on directionality is not imposed upon showers with p_T less than 3.0 GeV/c, due to large production cross sections at these p_T's. Near the inner part of the EMLAC, the angle of incidence of particles from the target becomes more nearly perpendicular; thus, in this region, the discrimination provided by directionality is reduced. Since, in addition, the more significant halo muon population is in the outer portions of the detector, it is sufficient to use a directionality cut which depends on radius:

$$D_{cut} = 0.193 \qquad \text{for } R < 40.175 \text{ cm}$$
$$D_{cut} = 0.0048 \times R \qquad \text{for } R \geq 40.175 \text{ cm}$$

where photons with directionality greater than D_{cut} were considered likely to be muons, and thus excluded from the photon candidate pool.

$\underline{\chi^2/E}$ Cut

Further discrimination against muons was provided via the χ^2 of the fit performed by EMREC. Since the shower shape was determined for photons coming from the target, showers induced by muons travelling parallel to the beamline were not well fit by the EMREC shower shape, resulting in large fit χ^2. Since the χ^2 of the fit scales with energy, χ^2/E was chosen as a less biased variable, and Figure 5.15 demonstrates that events with $\chi^2/E > 0.1$ are predominantly associated with muons.[8] For p_T's above 3 GeV/c, this cut was therefore applied.

---

[8] This cut also excludes some hadronic showers, since they often are poorly fit by the photon shower shape.

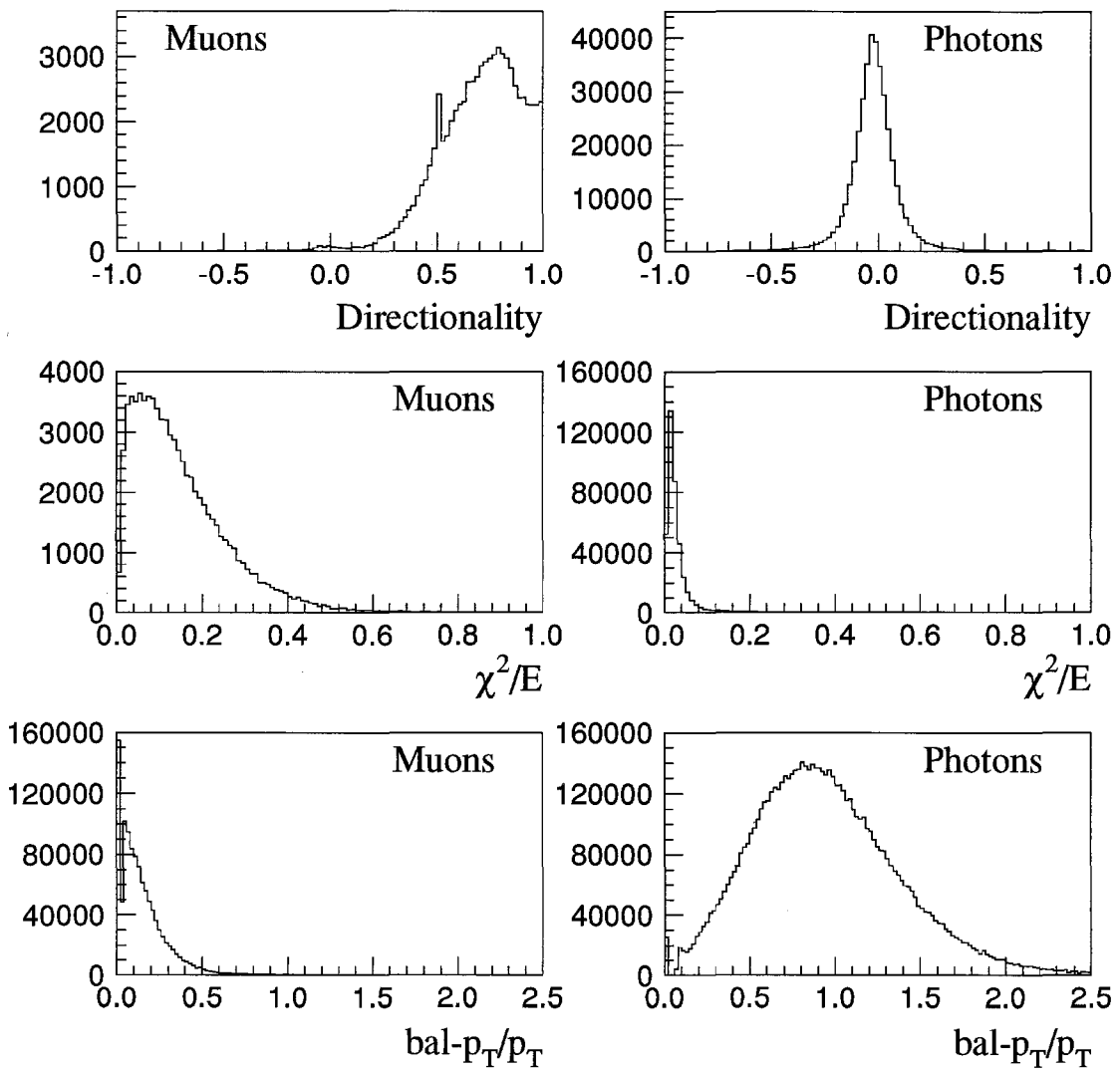

Figure 5.15 Comparisons of muon and photon distributions of directionality, χ^2/E, and balanced-p_T. The muon sample was selected by requiring veto wall hits, and the photon selection for each cut utilized a combination of the other cuts.

Balanced-p_T Cut

Given conservation of momentum, the p_T of a triggering particle should be balanced[9] by a jet of particles in the opposite direction. Since muonic showers are not strictly correlated in time and space with the rest of the recorded event, their p_T is generally *not* balanced by away-side particles. To employ this muonic signature, the p_T's of charged and neutral particles in the away-side jet were summed and this sum was divided by the p_T of the particle in question. By comparing the distribution of this variable when the veto walls indicate the presence of a muon to the same distribution in the absence of veto wall hits (Figure 5.15), the following criterion was indicated:

$$\frac{\sum_i p_T^{\,i}}{p_T^{\,\mu}} > 0.3 \tag{5.4}$$

where i labels tracks and/or showers in the 120° opposite the potential muon. For reasons stated above, this cut was also applied only for showers with $p_T > 3$ GeV/c.

Corrections for Muon Cuts

In order to correct for the improper rejection of photons by the various muon cuts, the following procedure was followed:

1) Using particularly harsh versions of the other muon-rejecting cuts, acquire a pure sample of photons containing a negligible amount of muons, which is unbiased with respect to the cut in question. (For example, reduce the coincidence requirements on the veto walls.)
2) Apply the muon rejection criterion in question to this photon sample, and calculate the correction as the fraction of photons cut.
3) Investigate the potential p_T and rapidity dependence of the cuts.

---

[9] These comments are not strictly true when k_T is considered, but the general argument remains valid.

The product of the corrections for the muon cuts is ≈5% around 4 GeV/c p_T both for π^0 and η mesons and for direct photons. The functional dependence of the corrections is the same for π^0's and η's: at p_T's above 7 GeV/c, the correction is ≈9%. The direct photon correction, instead of increasing with p_T, decreases to less than $\frac{1}{2}$% for p_T's above 7 GeV/c.

5.5.3 Energy Asymmetry Cut

The neutral meson analyses depend on the reconstruction of the two decay photons (from $\pi^0 \rightarrow \gamma\gamma$ and $\eta \rightarrow \gamma\gamma$). The energy asymmetry of the photon pair is defined as

$$A = \frac{|E_1 - E_2|}{E_1 + E_2} \tag{5.5}$$

where E_1 and E_2 are the energies of photons 1 and 2. Using the kinematics of the Lorentz boost, it can be shown that

$$A = \beta \cos\theta^* \tag{5.6}$$

where θ^* is the angle between the direction of meson propagation in the lab frame and the direction of decay photon emission in the meson center-of-mass frame, and for our purposes, $\beta \approx 1$. Since spin-0 mesons decay isotropically, the distribution of $\cos(\theta^*)$, and therefore that of energy asymmetry, is essentially flat.

Figure 5.16 shows the effect of requiring $A \leq 0.75$ on the $\gamma\gamma$ mass distribution in the π^0 and η mass regions. This energy asymmetry requirement clearly enhances the signal to background ratio. Since the correction for an asymmetry cut is trivial, and the requirement significantly improves the signal-to-noise ratios, the π^0 and η analyses included a cut of $A \leq 0.75$, and a corresponding correction factor of 1.333.

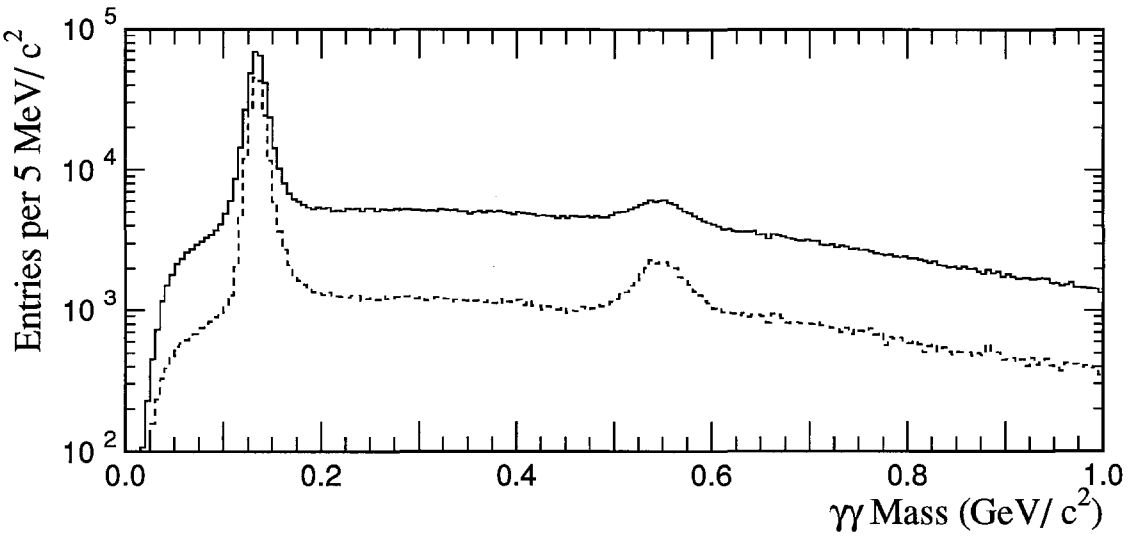

Figure 5.16 The $\gamma\gamma$ mass distribution before (solid) and after (dashed) an asymmetry cut of 0.75 from the 1991 data. The signal-to-noise ratio is significantly enhanced.

5.5.4 Longitudinal Shower Development Cut

Hadronic showers tend to develop more slowly than those precipitated by electrons and photons. More definitely, an electromagnetic shower which deposits less than 80% of its energy in the front section of the EMLAC is relatively rare, as opposed to hadronic showers which frequently have more than half of their energy in the back section, as shown in Figure 5.17. Therefore, for the purpose of hadron rejection, a requirement that

$$\frac{E_{front}}{E_{total}} > 0.2 \tag{5.7}$$

was imposed for these analyses, and the correction for this cut was a component of the reconstruction efficiency calculated from the Monte Carlo (see Section 5.4).

A further benefit of this cut was additional muon rejection; this is due to the fact that, since the back section of the EMLAC has twice as many layers as the front, showers associated with muon bremsstrahlung will frequently have small E_{front}/E_{total} ratios.

5.5.5 The Fiducial Cut and the Geometric Acceptance Correction

Showers that impinged near the edges of the live portions of the EMLAC lost a fraction of their energies to dead regions, causing both the energy and position of the reconstructed showers to be compromised. For this reason, the requirement that the shower location be at least two strips away from any octant edge was imposed. In addition, this fiducial cut rejected showers closer than two strips from the partial strips in the outer r. Figure 5.18 is a scatter plot of the positions of photons from π^0's which pass the fiducial cut.

A simple Monte Carlo was employed in order to correct for situations in which one or both of the photons from a meson decay were outside the fiducial volume of the EMLAC. π^0 and η mesons were generated, and then allowed to decay with asymmetries less than 0.75. The resulting photons were then projected to the face of the EMLAC. The ratio of the number of mesons for which both photons passed the fiducial cut and impinged on the same octant to the number of generated mesons provided the geometrical acceptance correction, which was binned in the transverse momentum, the lab-frame pseudorapidity,[10] and the longitudinal location and transverse offset (relative to the beam axis) of the vertex. The geometric acceptance correction for a given event was calculated by interpolation between the values for bins in these four input variables. Determination of the

[10] The lab-frame pseudorapidity was used to allow this calculation to be valid irrespective of the incident beam type.

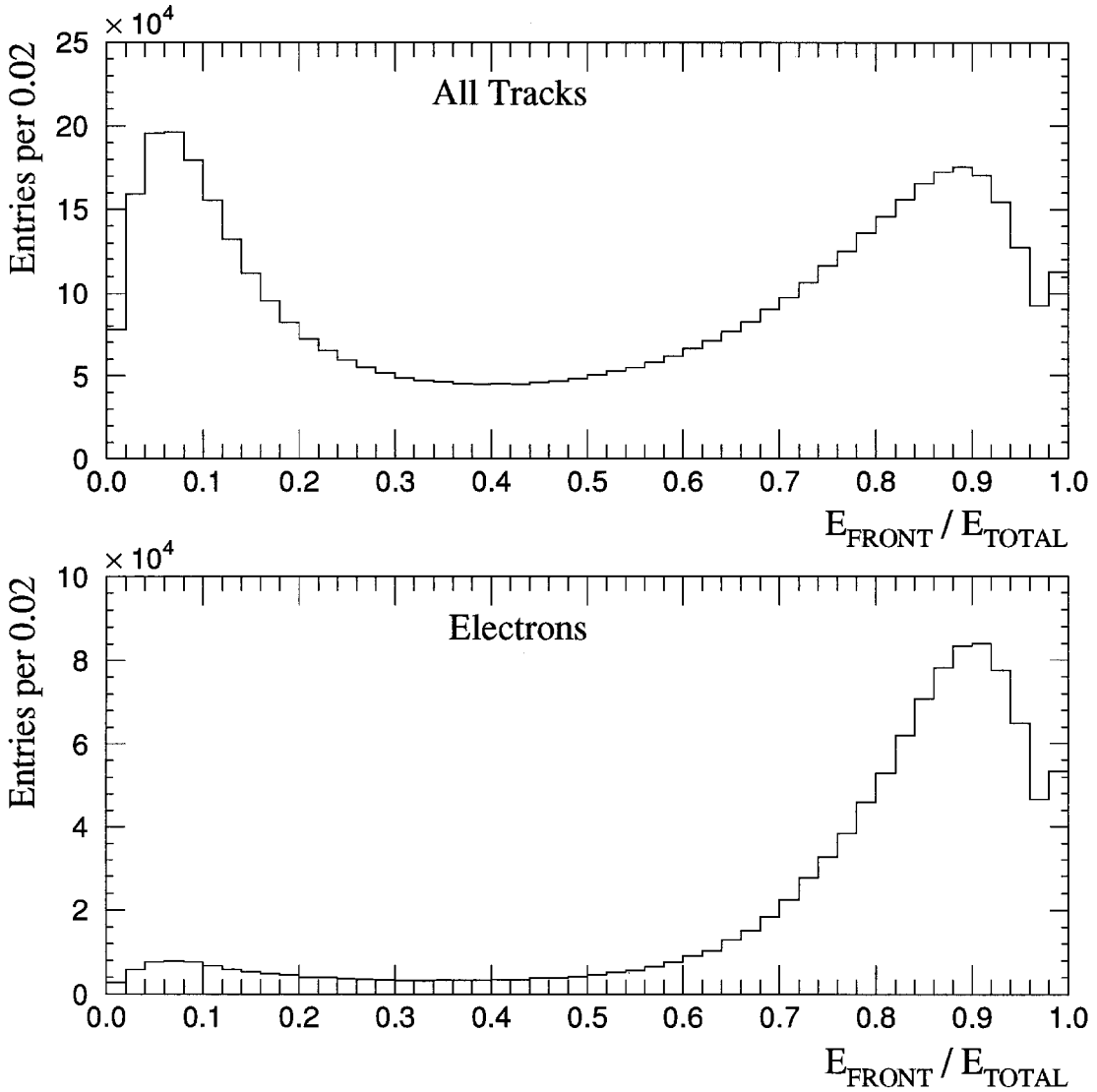

Figure 5.17 The E_{front}/E_{total} distribution for showers associated with all tracks (top) and electrons only (bottom). A shower with large E_{front}/E_{total} is likely to be of electromagnetic origin.

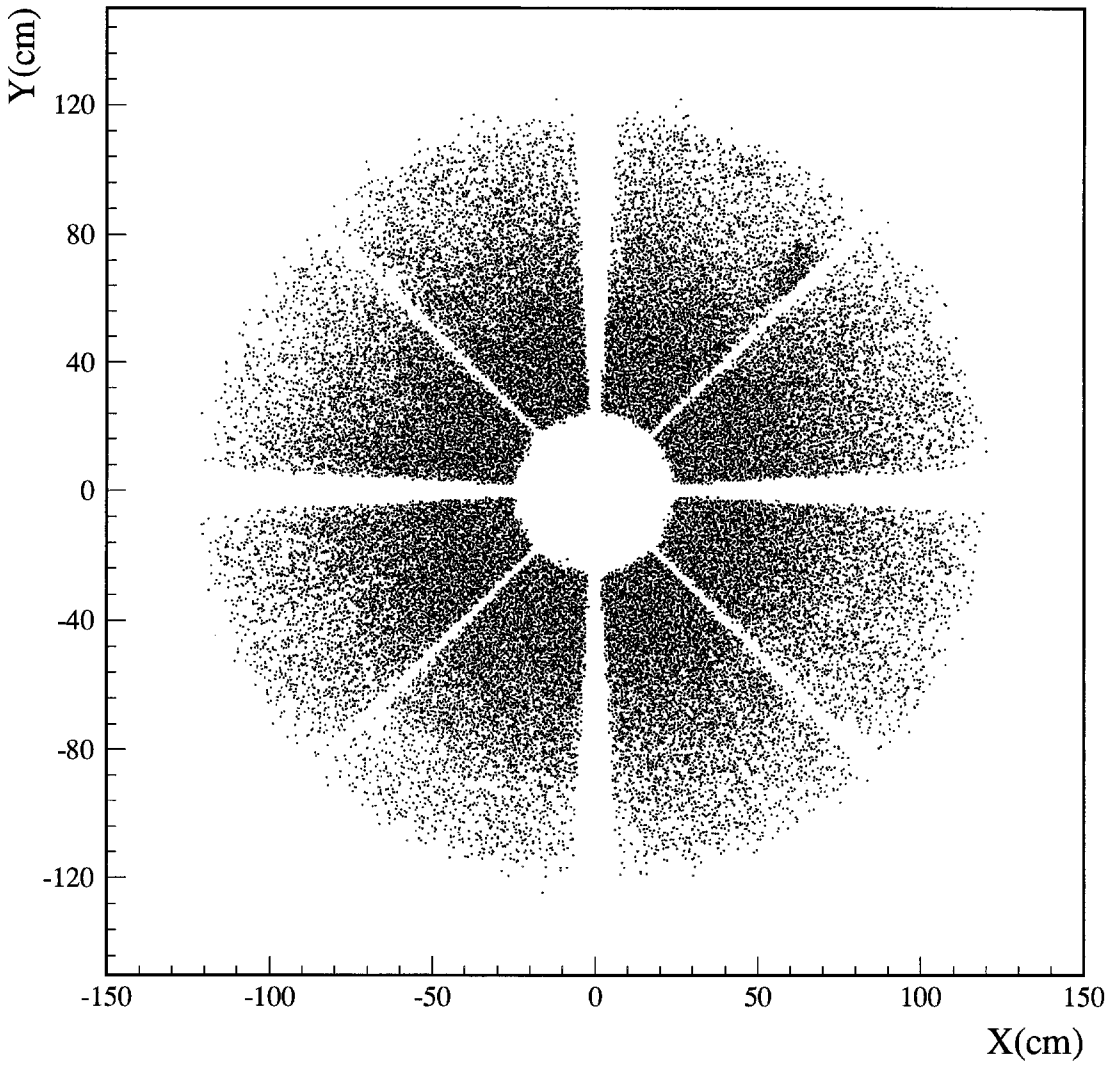

Figure 5.18 The fiducial volume of the EMLAC. Plotted here are the positions of photons from π^0's which satisfy the fiducial requirement.

geometric acceptance for single photons followed the same general procedure, with the simplification that only one photon need pass the fiducial cut. Figure 5.19 compares the π^0, η, and single photon acceptance versus rapidity, for two bins in meson transverse momentum, averaging over vertex position.

5.5.6 The Corrections for Photon Conversion and Beam Absorption

Photons originating at or near a vertex within the target region had a significant amount of material to traverse before being detected by the EMLAC. Some fraction of these photons therefore converted to e^+e^- pairs while passing through matter associated with the target or the spectrometer. If this conversion occurred before the magnet, the trajectories of the electron and positron diverged and a photon was not directly reconstructed in the EMLAC. For this reason, it was necessary[11] to correct for the fraction of mesons or direct photons lost due to the conversion of one or more photons before the downstream end of the magnet.

To this end, a comprehensive list of materials, their properties, and their positions was compiled, and each surviving photon (meson) entry in the cross section calculation was weighted to account for the fraction of entries lost due to conversion, based on the material through which the photon(s) passed.

A similar method was used to compute the correction for beam absorption. The weight applied to a cross section entry was the inverse of the calculated fraction of beam not absorbed by materials (i.e. SSD's, targets, etc.) upstream of the reconstructed vertex.

---

[11] Actually, if both the electron and positron showers were reconstructed properly, the photon could still be found. However, the conversion correction method used in this analysis had lower associated uncertainties.

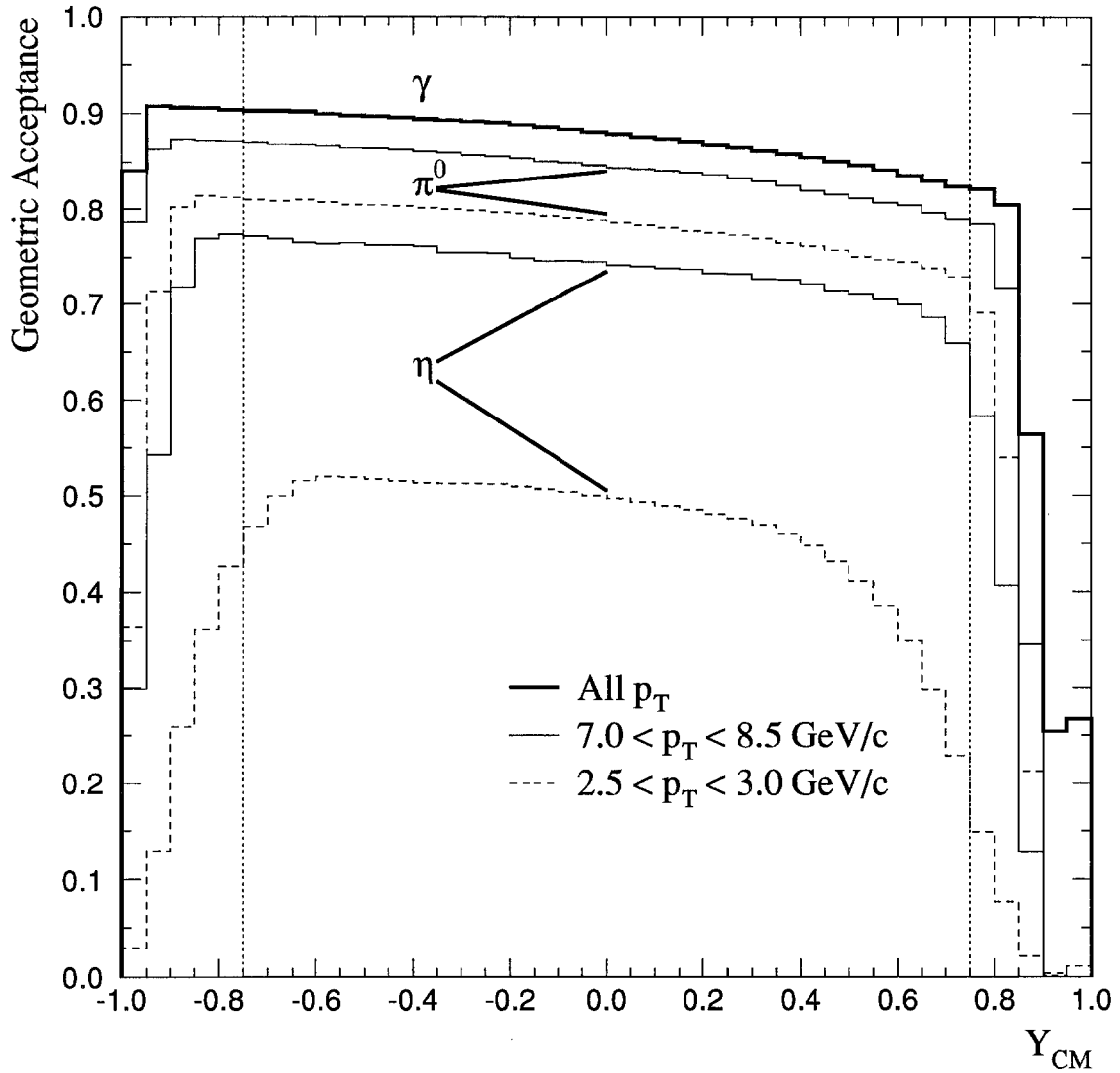

Figure 5.19 The geometric acceptance for single photons (thick histogram) and π^0 and η mesons at high and low p_T (thin solid and dashed histograms, respectively). The abscissa is the center-of-mass rapidity, and the dotted lines at $Y_{CM} = \pm 0.75$ delimit the rapidity region used in this analysis.

Target Configuration and Material		Beam Absorption	Conversion (per photon)
1990 π^-	Be	1.06	1.09
	Cu	1.02	1.19
1991 π^-	H	1.04	1.11
	Be	1.08	1.08
	Cu	1.01	1.16
1991 p	H	1.03	1.11
	Be	1.08	1.08
	Cu	1.01	1.16

Table 5.3 Average weight for beam absorption and photon conversion for the various materials in the 1990 and 1991 target configurations.

The size of each of these corrections is dependent on the reconstructed vertex position and, for conversions, the reconstructed photon position. Table 5.3 contains average weights for the various targets in the 1990 and 1991 configurations.

5.5.7 The Reconstruction Efficiency

As mentioned above, one of the primary purposes for the significant effort expended on the Monte Carlo simulation of our data was to provide a means of studying the efficiency of our reconstruction of mesons and photons. To calculate the $\pi^0/\eta/\gamma$ reconstruction efficiency, a sample of Monte Carlo $\pi^0/\eta/\gamma$ events satisfying certain criteria was assembled. These criteria included the asymmetry cut for the mesons and the requirement that decay or direct photons were within the EMLAC's fiducial volume and that they did not convert in front of the

magnet; by imposing these criteria on the sample used, double-correction for these effects was avoided. Using this sample and binning in both transverse momentum and rapidity, the reconstruction efficiency was then calculated as the ratio of the number of reconstructed $\pi^0/\eta/\gamma$'s to the number of generated $\pi^0/\eta/\gamma$'s. The reconstructed events in this ratio were required to satisfy two additional requirements. The first, which required $E_{front}/E_{tot} > 0.2$ for each photon, was included in order to correct for photons removed by this hadron-rejecting cut. The second required that the calculated trigger efficiency for the trigger octant be greater than ten percent. In order to avoid fluctuations due to excessively large trigger weights on individual events, this method corrected by an appropriate average.

As shown in Figure 5.20, the untriggered π^0 reconstruction efficiency dips both at high p_T in the forward rapidities and at low p_T in the backward rapidities. The former is due to the coalescence of the two photons. (In the inner portions of the detector, the distance between the two photons from π^0 decay is quite small, frequently causing the two photons to be reconstructed as a single photon.) The latter case is due to the fact that low-p_T objects in the outer portion of the detector have relatively low energies and are therefore more difficult to reconstruct. The "untriggered" efficiencies are those calculated without invoking the minimum trigger efficiency requirement discussed above. Of course, introduction of the 10% trigger efficiency cutoff into the calculation decreased the calculated reconstruction efficiency at p_T's at or below the trigger threshold. The π^0 reconstruction efficiency for the SINGLE LOCAL HIGH trigger is shown in Figure 5.21.

It should be stressed that the reconstruction efficiency also accounts for differences between generated and reconstructed variables. Specifically, given a sharply falling p_T spectrum and a non-negligible energy resolution, any given

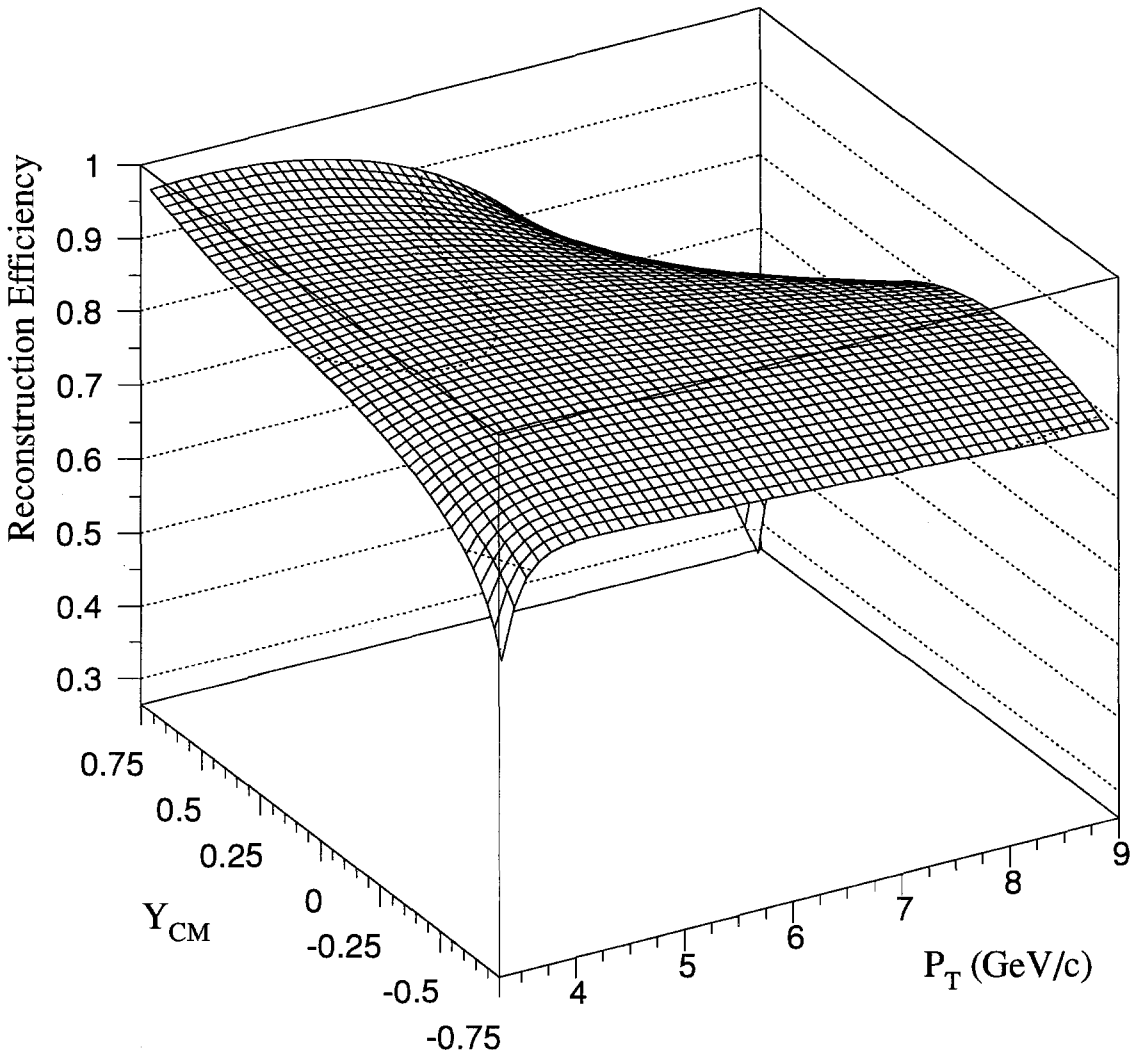

Figure 5.20 The untriggered π^0 reconstruction efficiency (and unsmearing correction) for the proton beam data as a function of transverse momentum and rapidity. Note the suppressed zero.

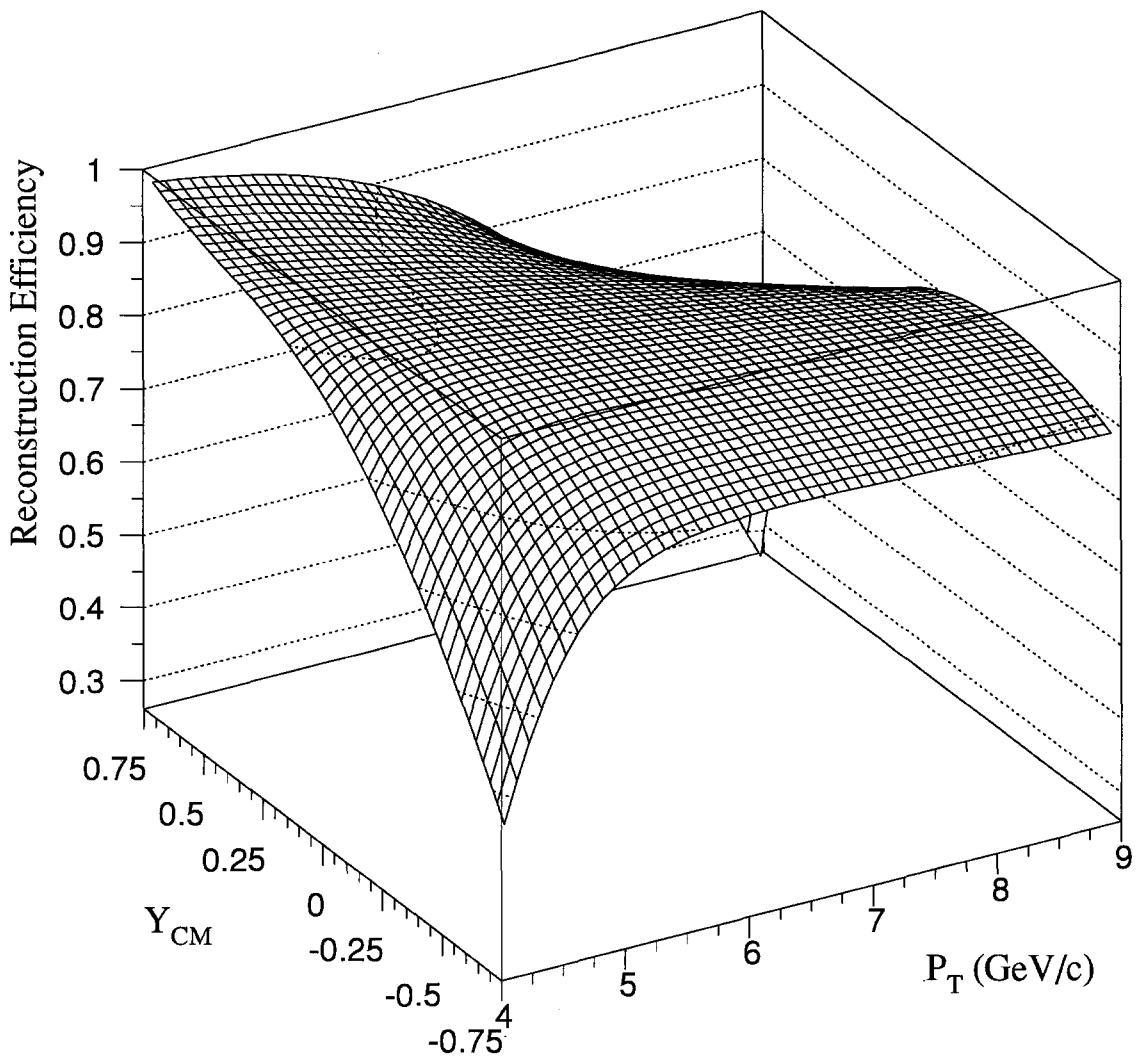

Figure 5.21 The SINGLE LOCAL HIGH trigger π^0 reconstruction (and unsmearing correction) efficiency for the proton beam data as a function of transverse momentum and rapidity. Note the suppressed zero.

reconstructed p_T corresponds more frequently to a lower generated p_T than to a higher one. Calculating the reconstruction efficiency in the method described above effectively corrects for the effects due to this sort of resolution smearing. The single photon reconstruction efficiency, shown in Figure 5.22, is dominated by this "unsmearing."

5.5.8 Selection of Valid Trigger Ranges

At sufficiently low p_T, despite all trigger corrections, any given LAC trigger becomes systematically unreliable. That point in p_T is dependent both on position (octant and rapidity) and time (run number). For this reason, it was necessary to construct a map which indicated which trigger was to be used in the cross section analysis for any given location in the detector during any given run. This map was constructed by looking at cross sections as a function of rapidity, transverse momentum, and trigger type. Where a higher-threshold trigger could be shown to be relatively free of trigger bias when compared to a lower-threshold trigger, the higher-threshold trigger, and the accompanying higher levels of statistics, was chosen. In addition, the trigger map contained information to statistically correct for "dead" regions of the EMLAC trigger, regions which were not reliable for measurements at any p_T. Thus the trigger map provided the means to keep systematics to a minimum, while maximizing the use of available statistics.

It should be noted that one may not be able to minimize the overall (statistical $\oplus$ systematic) uncertainty for all measurements using a single trigger map. Although a single trigger map is used for most calculations, rare exceptions do exist. One such example involves the η/π measurement in the 1991 data. In the 1991 data, the trigger corrections for the LOCAL GLOBAL LOW trigger have not been computed. However, the global structure of this trigger provides better acceptance for η's due to the relatively large separation of the η decay photons.

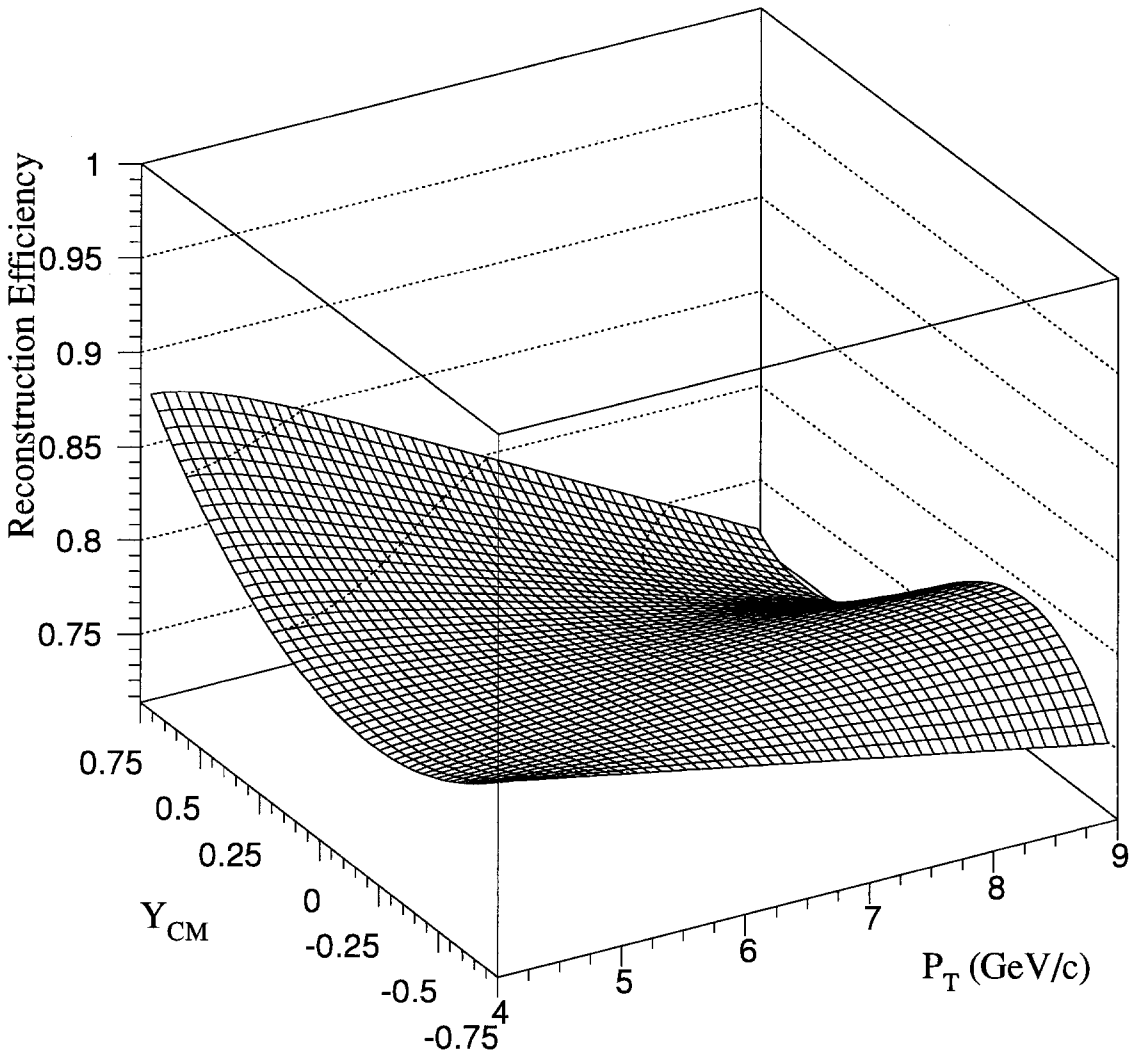

Figure 5.22 The SINGLE LOCAL LOW trigger single photon reconstruction efficiency (and unsmearing correction) for the proton beam data as a function of transverse momentum and rapidity. Note the suppressed zero.

In addition, the prescaling factor of the LOCAL GLOBAL LOW was smaller than that of the SINGLE LOCAL LOW. Since in the η/π measurement, the inefficiencies (as a function of p_T) in the LOCAL GLOBAL LOW largely cancel, use of a trigger map which included the LOCAL GLOBAL LOW trigger at low p_T reduced the overall uncertainty on the measurement of the η/π measurement.

5.5.9 The Beam Contamination Correction

The possibility of muon contamination in the secondary beams was investigated by the author [34]. The forward calorimeter was used as an instrumented beam dump during the taking of two sets of data. Running with the collimators closed provided the first data set and the second data set was acquired under normal beamline conditions. By applying appropriate cuts on the trigger scintillator signals, events used in this analysis were required to have one non-interacting beam particle. The collimator-closed sample was used to isolate and define a muon signature in the FCAL, and a search for this signature in the data acquired under normal running conditions provided an estimate of the muon contamination of the beam for both secondary beam types: for π^- data, the muon contamination level was 0.5%, and for the positive polarity secondary beam the contamination was measured to be 0.3%.

5.5.10 The Pointing-Track Cut

The EMLAC does not provide information concerning the electric charge of the particle precipitating the shower. Electrons or other charged particles from hadronic decays potentially contribute to meson and direct photon backgrounds. For the π^0 analysis, the effect of charged particles may be minimized by using the mass distribution of the signal and the background. The direct photon analysis, however, is not similarly protected. In addition, charged particles have been

shown to adversely affect the η analysis, due to the following scenario. Photons converting before the magnet produce widely separated e^+ and e^- showers. If these showers are reconstructed with the assumption that each was due to a photon originating from the vertex, the "$\gamma\gamma$ mass" tends to occur near the high-mass tail of the η signal.

For these reasons, it is beneficial to utilize the tracking system to identify showers due to charged particles. Figure 5.23 is the result of projecting reconstructed tracks to the face of the EMLAC and plotting the square of the distance between showers and the closest charged particle. For all three analyses,[12] showers having a pointing track within 1 cm were not considered photons. The occurrence of accidental overlap between photon showers and charged tracks was relatively rare. Using the π^0 signal as a gauge, a weight was applied to correct for exclusion of real photons. For the 1990 data, the correction for mesons varied slightly with pseudorapidity from 1.5% to 3.0%; in 1991, the meson corrections were in the range 1.8 to 3.9%. The corrections for photons were calculated as the square root of the corresponding meson correction.

5.5.11 Normalization

In order to calculate an absolute cross section, it is necessary to acquire a count of the beam particles impinging on the target while the experiment was "live" (ready to take data). This "Live Triggerable Beam" count, N_{LTB}, was calculated run by run using several scaled quantities.

$$N_{LTB} = f_{CLEANINT} \cdot f_{COMPUTERREADY} \cdot f_{PRETLIVE} \cdot f_{TRIGGERLIVE} \cdot N_{BEAM1 \cdot \overline{BH}} \tag{5.8}$$

---

[12] The π^0 was included for consistency.

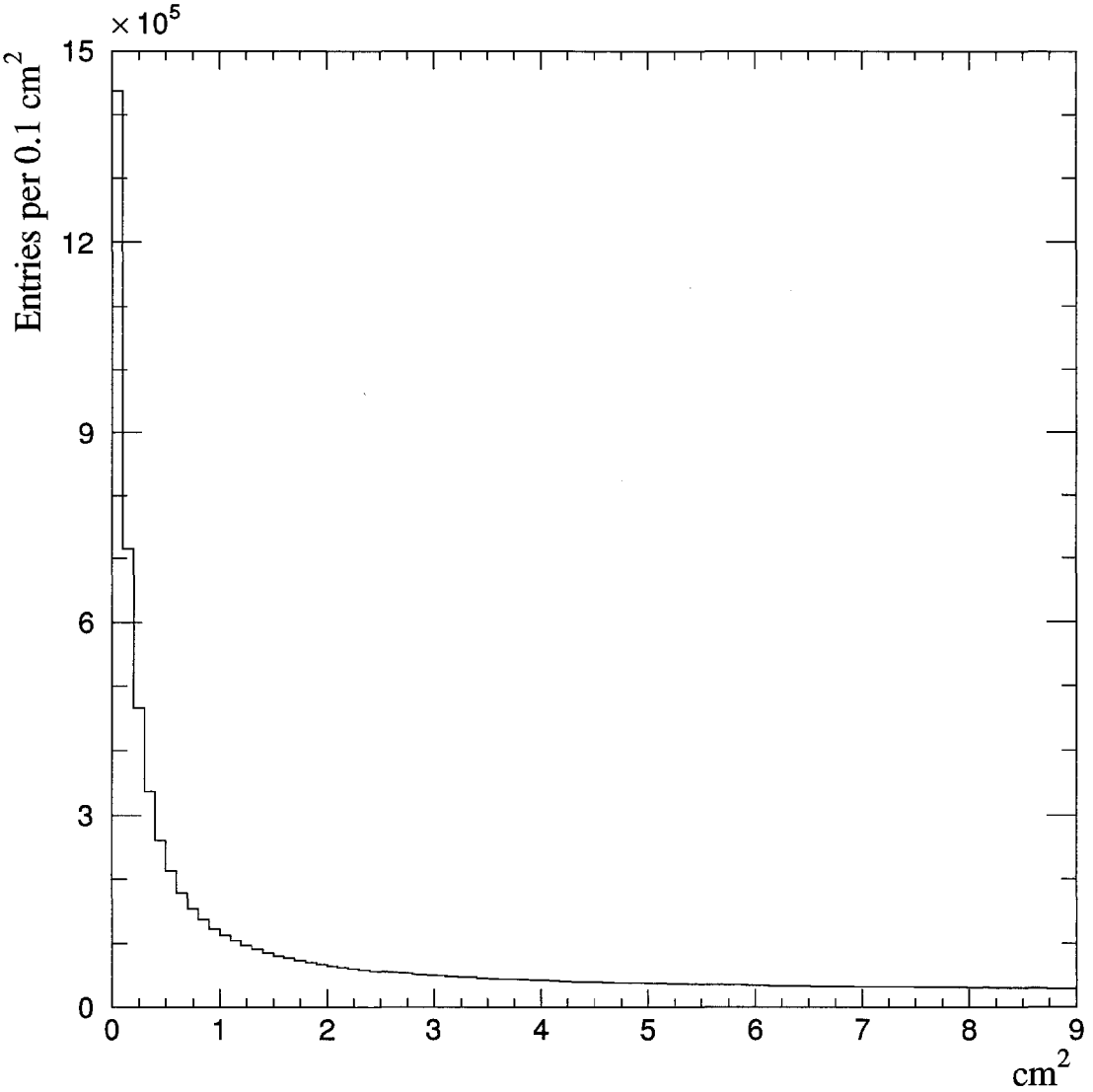

Figure 5.23 The distribution of ΔR^2, the square of the distance (at the face of the EMLAC) between a photon shower and the projected position of the nearest charged track.

- f_{CLEANINT} is the correction for the fraction of the interactions vetoed by the CLEANINT requirement.
- $f_{\text{COMPUTERREADY}}$ is the fraction of clean interactions for which the data acquisition system was ready to accept triggers.
- f_{PRETLIVE} corrects for the dead time due to occasions when a PRETRIGGER decision cannot be made because the PRETRIGGER logic is already busy evaluating a previous interaction.
- $f_{\text{TRIGGERLIVE}}$ is the fraction of interactions surviving the trigger-related vetoes such as signals from the veto walls, early p_T, or SCRKILL.
- $N_{\text{BEAM1}\cdot\overline{\text{BH}}}$ is the number of occurrences of $\text{BEAM1} \cdot \overline{\text{BH}}$, which is the fundamental count of the incident beam.

Since $f_{\text{TRIGGERLIVE}}$ has elements which vary from octant to octant, the normalization was evaluated for each octant independently.

5.5.12 Meson Signal Definition

The $\gamma\gamma$ mass distributions in the π^0 and η signal regions are shown in Figures 5.24 through 5.26, where all cuts, corrections, and weights have been applied. The method used to measure the meson signals was as follows:

1) Delineate a $\gamma\gamma$ mass band containing the meson signal.
2) Define "side-band" regions (i.e. regions to either side of the signal region) which contain background $\gamma\gamma$ combinations similar to those underneath the signal peak. The width of the sidebands (together) is chosen to match the signal band width.
3) Sum the weighted $\gamma\gamma$ combinations from the signal region and subtract from this total the weighted side-band combinations.

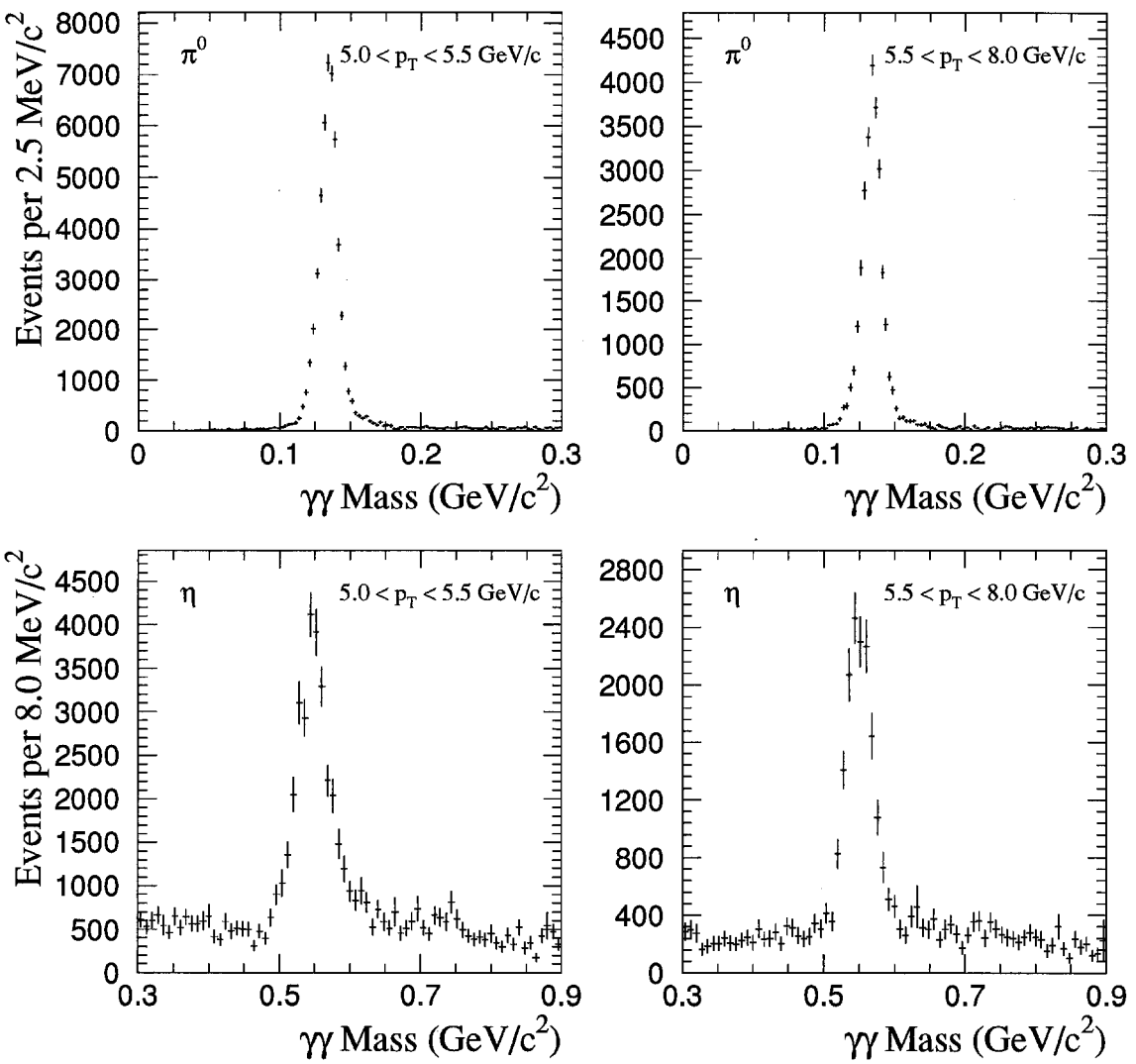

Figure 5.24 For the 1990 π^- beam data, the $\gamma\gamma$ mass distribution for two p_T ranges in the π^0 and η meson signal regions. The full set of cross-section weights have been applied to the events entered into these plots. Note that these plots are not background subtracted.

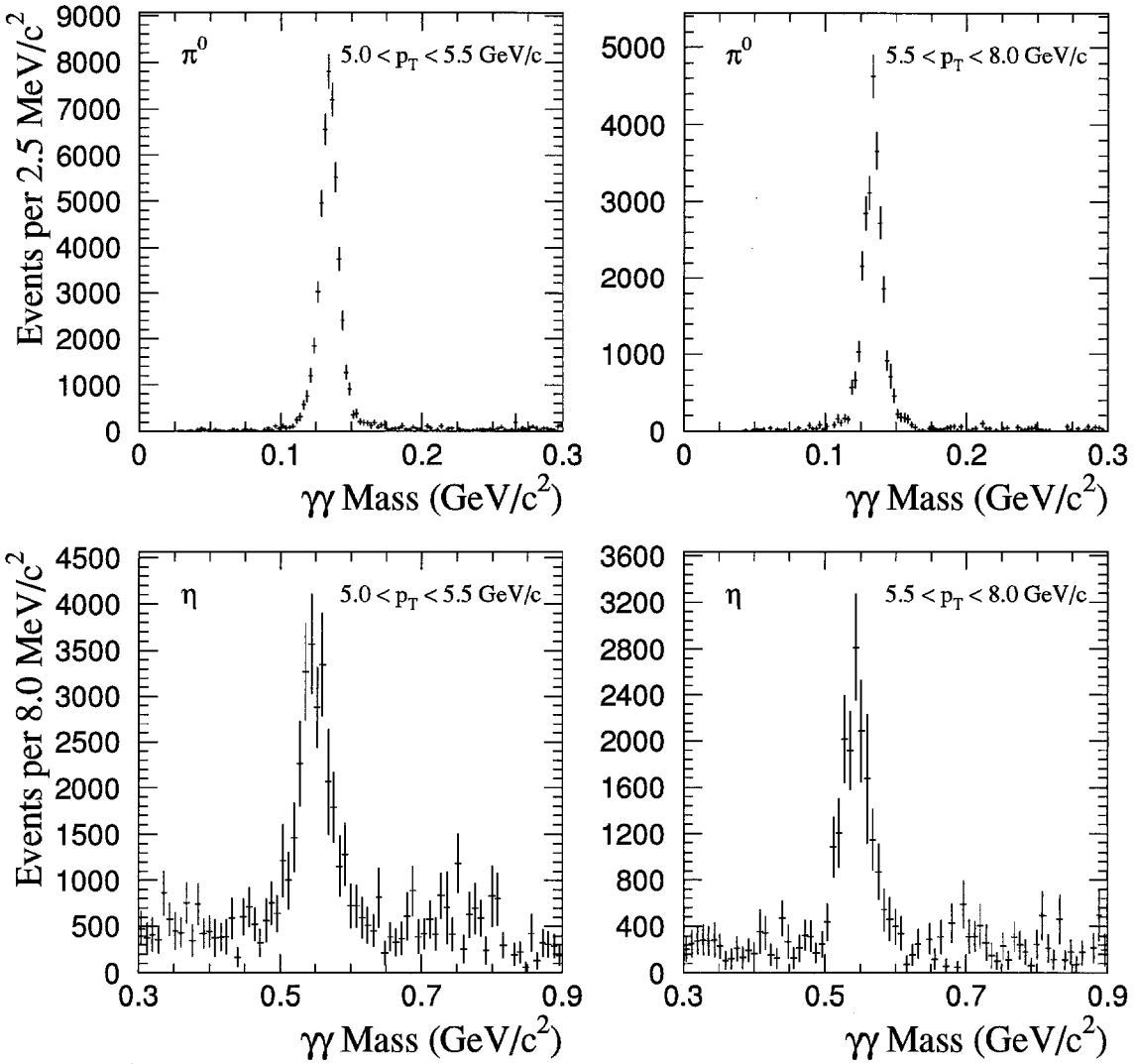

Figure 5.25 For the 1991 π^- beam data, the $\gamma\gamma$ mass distribution for two p_T ranges in the π^0 and η meson signal regions. The full set of cross-section weights have been applied to the events entered into these plots. Note that these plots are not background subtracted.

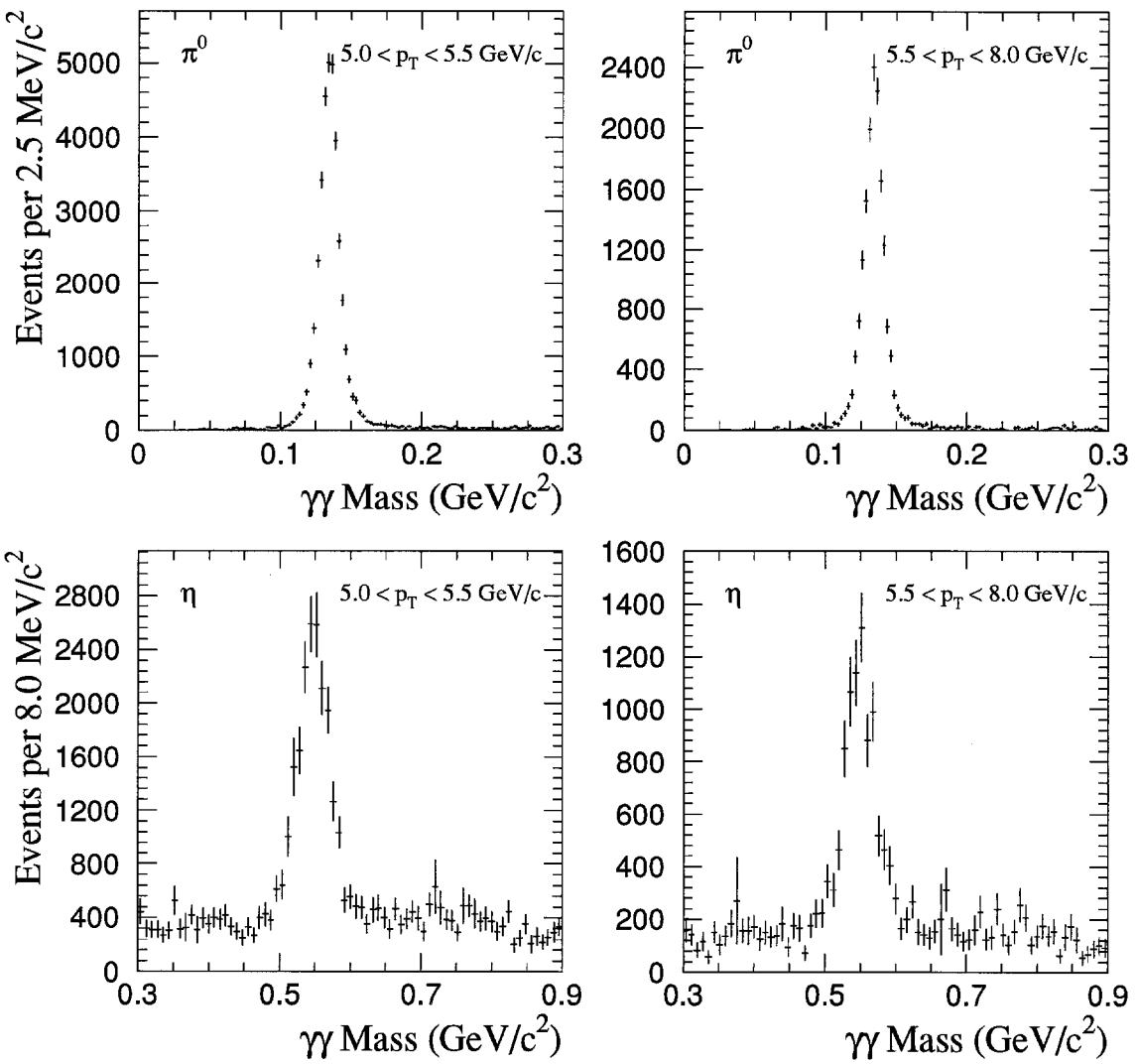

Figure 5.26 For the 1991 530 GeV/c proton beam data, the $\gamma\gamma$ mass distribution for two p_T ranges in the π^0 and η meson signal regions. The full set of cross-section weights have been applied to the events entered into these plots. Note that these plots are not background subtracted.

Meson	Signal (MeV/c^2)	Side-bands (MeV/c^2)	
		Low Mass	High Mass
π^0	100-180	70-100	190-240
η	450-650	350-450	650-750

Table 5.4 Signal and sideband mass ranges for π^0 and η meson analysis.

The use of this technique[13] effectively accounts for the uncorrelated $\gamma\gamma$ background observed under the signal peaks. The signal and sideband mass regions are displayed in Table 5.4.

5.5.13 Direct Photon Signal Definition

A direct photon candidate in the E706 data sample comes from an event satisfying all the criteria discussed in the above sections. In addition, such a photon does not combine with another photon in the octant to form a reconstructed π^0 or η with an asymmetry within a certain range. As described throughout this thesis, during all stages of this experiment, from detector design and construction to data reconstruction and analysis, significant efforts were invested to minimize the number of unreconstructed mesons resulting in background to the direct photon signal. Despite the success of these efforts, some fraction of the direct photon candidates were actually photons from the electromagnetic decay of various particles (mostly π^0's).

[13] Incidentally, the technique of fitting the signal over background has been shown to give results consistent with the above method. However, since side-band subtraction is both easily automated and generally robust, it remains the method of choice.

The Herwig Monte Carlo described earlier was used to estimate the fractional contribution from these "fake direct photons." Using the full set of reconstruction and analysis techniques described above, the direct photon candidate spectrum was measured from Monte Carlo samples containing no generated direct photons. A "γ_{fake}/π" ratio was calculated by dividing this distribution by the π^0 distribution from the same Monte Carlo events. The γ_{fake}/π was fit in p_T and rapidity, and the resulting function was multiplied by the π^0 cross section measured in the data. This product was subtracted bin by bin from the weighted direct photon candidate distribution to statistically subtract the backgrounds to the direct photon signal.

Two techniques were used to define direct photon signals in this analysis. Denoted 75S and 90N, these two techniques differed in two respects. First, the numerical portion of the labels of the two techniques refers to 100 times the π^0 asymmetry cut: a photon which, when associated with any other photon in the octant, forms a $\gamma\gamma$ pair with mass in the π^0 signal band and with asymmetry less than this cut was not considered a direct photon candidate. (For example, a photon forming a π^0 with asymmetry 0.8 would be cut from the direct photon sample in the 90N scheme; however, the 75S scheme would retain this photon as a direct photon candidate.) In both cases, the cut on η candidate asymmetry was 0.75. The second difference between the two schemes concerns the fact that by removing all direct photon candidates which form $\gamma\gamma$ mass combinations in the meson signal regions, one is ignoring the fact that some of the background underneath the signal could be due to direct photons in combination other photons in the octant. In the "S" scheme, therefore, direct photon candidates in the meson side-bands are weighted by a factor of 2 to correct for the removal of direct photons in the π^0 background under the signal. The "N" technique does not. Of course, the reconstruction efficiencies and γ_{fake}/π ratios for the two schemes are calculated

independently to properly correct for the different efficiencies and contamination rates. Although the γ_{fake}/π ratios and reconstruction efficiencies of the 75S and 90N techniques differ by as much as 30% and 10% respectively, the corrected cross sections obtained agree to within $\approx$7%, well within the quoted systematic uncertainty of $\approx 10 - 15\%$. The direct photon results presented in the following chapter were obtained using the 90N direct photon definition.

For the π^- and proton beams, respectively, Figures 5.27 and 5.28 show the unsubtracted γ/π along with the γ_{fake}/π versus p_T, for the 90N direct photon definition.

5.5.14 Cross Section Calculation

The invariant cross section per nucleon for inclusive particle production can be expressed as

$$E\frac{d^3\sigma}{dp^3} = \frac{1}{2\pi p_T \Delta p_T \Delta Y_{CM}} \frac{1}{\rho L N_A} \frac{N^X_{corr}(p_T, Y_{CM})}{N_{LTB}} \tag{5.9}$$

where

- Δp_T is the width of the transverse momentum bin
- ΔY_{CM} is the width of the center-of-mass rapidity bin
- ρ is the target density
- L is the target length
- N_A is Avogadro's Number
- N_{LTB} is the live triggerable beam defined in Section 5.5.11
- N^X_{corr} is the corrected number of occurrences of particle X in the specified p_T and Y_{CM} bin.

The corrections, excluding background subtraction, applied to acquire N^X_{corr} are listed, along with their values and the variables upon which they depend most strongly, in Table 5.5.

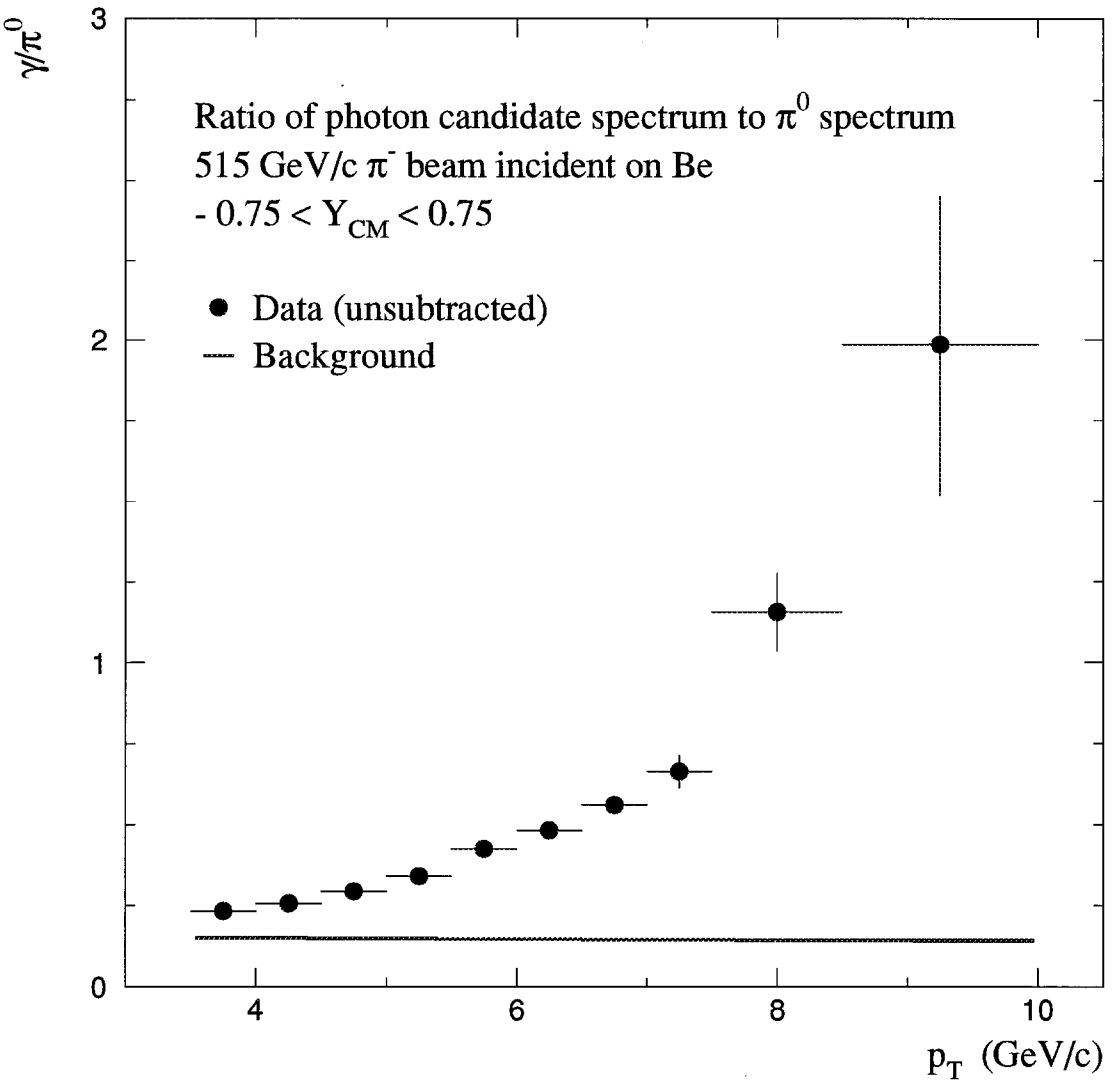

Figure 5.27 For the 515 GeV/c π^- beam incident on beryllium, the unsubtracted γ/π along with the corresponding γ_{fake}/π computed from the Monte Carlo.

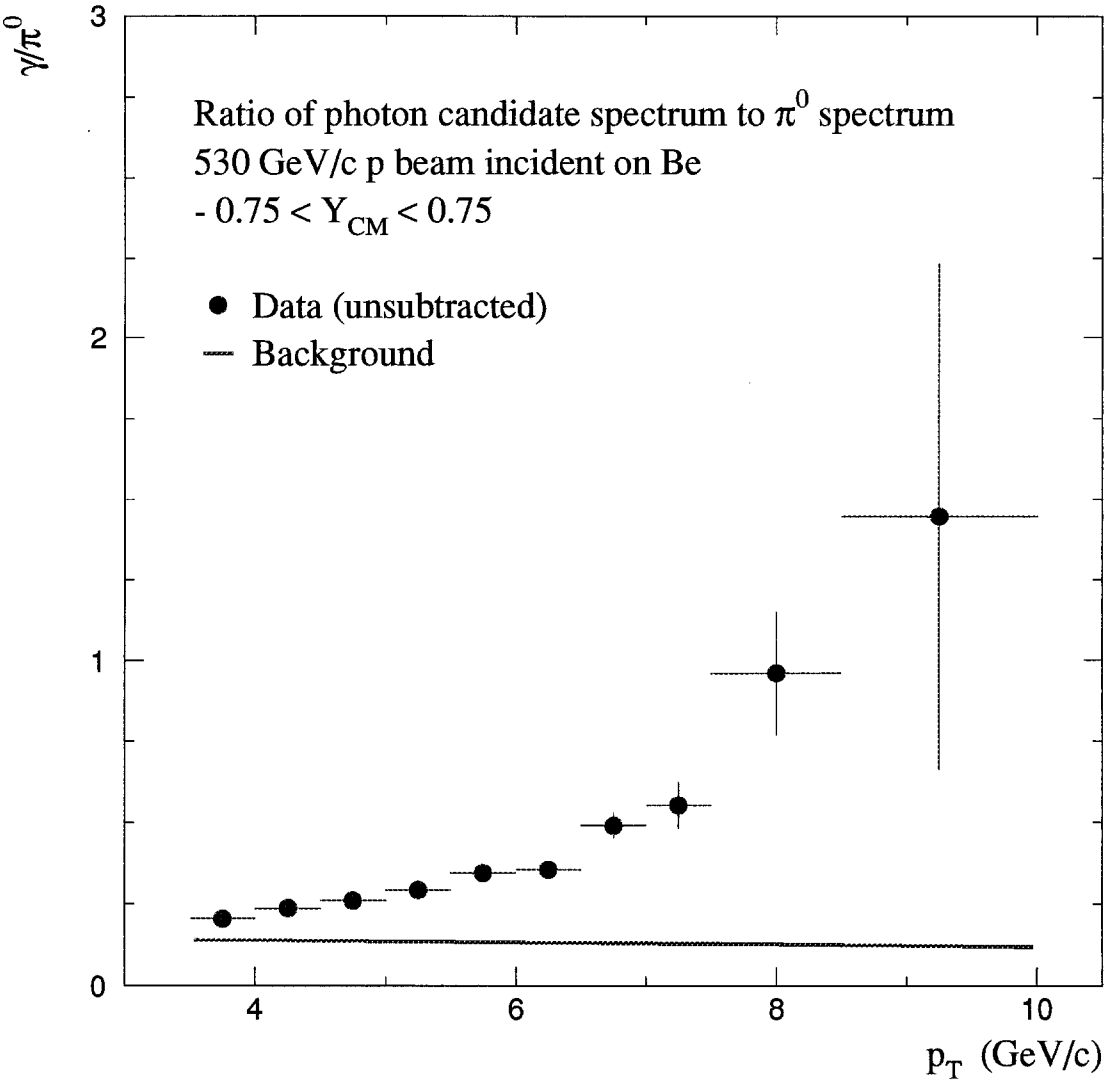

Figure 5.28 For the 530 GeV/c proton beam incident on beryllium, the unsubtracted γ/π along with the corresponding γ_{fake}/π computed from the Monte Carlo.

Correction	Range	Dependencies
Muon Bremsstrahlung	1.00 – 1.09	p_T, Y_{CM}
Pointing Track	1.01 – 1.04	Y_{CM}
Trigger Weights	1.0 – 1.5	p_T, Y_{CM}
Transverse Target	1.00 – 1.35	target, configuration
Vertex-related Weights	0.95 – 1.09	target, configuration
Muon Contamination	1.003, 1.005	p, π^- incident beam
Branching Ratio	1.012, 2.571	π^0, η production
Asymmetry	1.333	meson production
Geometric Acceptance	(See Figure 5.19)	
Reconstruction Efficiency	(See Figures 5.20 – 5.22)	
Beam Absorption	(See Table 5.3)	
Photon Conversion	(See Table 5.3)	

Table 5.5 Corrections applied to the meson and direct photon cross sections. Ranges or values of the corrections are given, along with the variables upon which the corrections depend most strongly. References are given to corrections tabulated or displayed elsewhere.

5.5.15 Combining 1990 and 1991 π^- Beam Results

As is clear from Table 5.1, 515 GeV/c π^- data were taken during both the 1990 and 1991 runs. To account for differences in the experimental apparatus, the two samples were analyzed independently. Since, however, the two samples can be used to measure the same quantities (except for the additional hydrogen-target information in 1991), statistical combination of the 1990 and 1991 π^- samples is desirable.

Many of the corrections which are expected to differ between the samples (trigger efficiencies, energy scale, etc.) were calculated independently. At this time, however, a few corrections for the 1991 π^- sample have not yet been independently evaluated. To compensate for these, corrections from samples expected to have very similar values to the 1991 π^- sample were used. The γ/π associated with the 1990 π^- sample and the efficiencies and muon corrections calculated for the 1991 proton sample were used for the 1991 π^- beam cross section measurements.

Figure 5.29 shows the ratios of cross sections measured using the 1990 and 1991 π^- data samples. The agreement in the the cross sections measured from the two samples is quite impressive, well within the quoted systematics of our measurements. Shape differences between these measurements in various projections have been taken into account in the calculation of systematic uncertainties.

The good agreement between the 1990 and 1991 result improves the confidence in our measurements and permits the combination of the two samples. In most regions in p_T and Y_{CM}, the 1990 sample, which has significantly greater sensitivity, dominates the measurement. However, in certain low-p_T regions, the

1991 analysis utilized a trigger with a smaller prescale factor; in such cases, the 1991 measurement dominates the combined result.

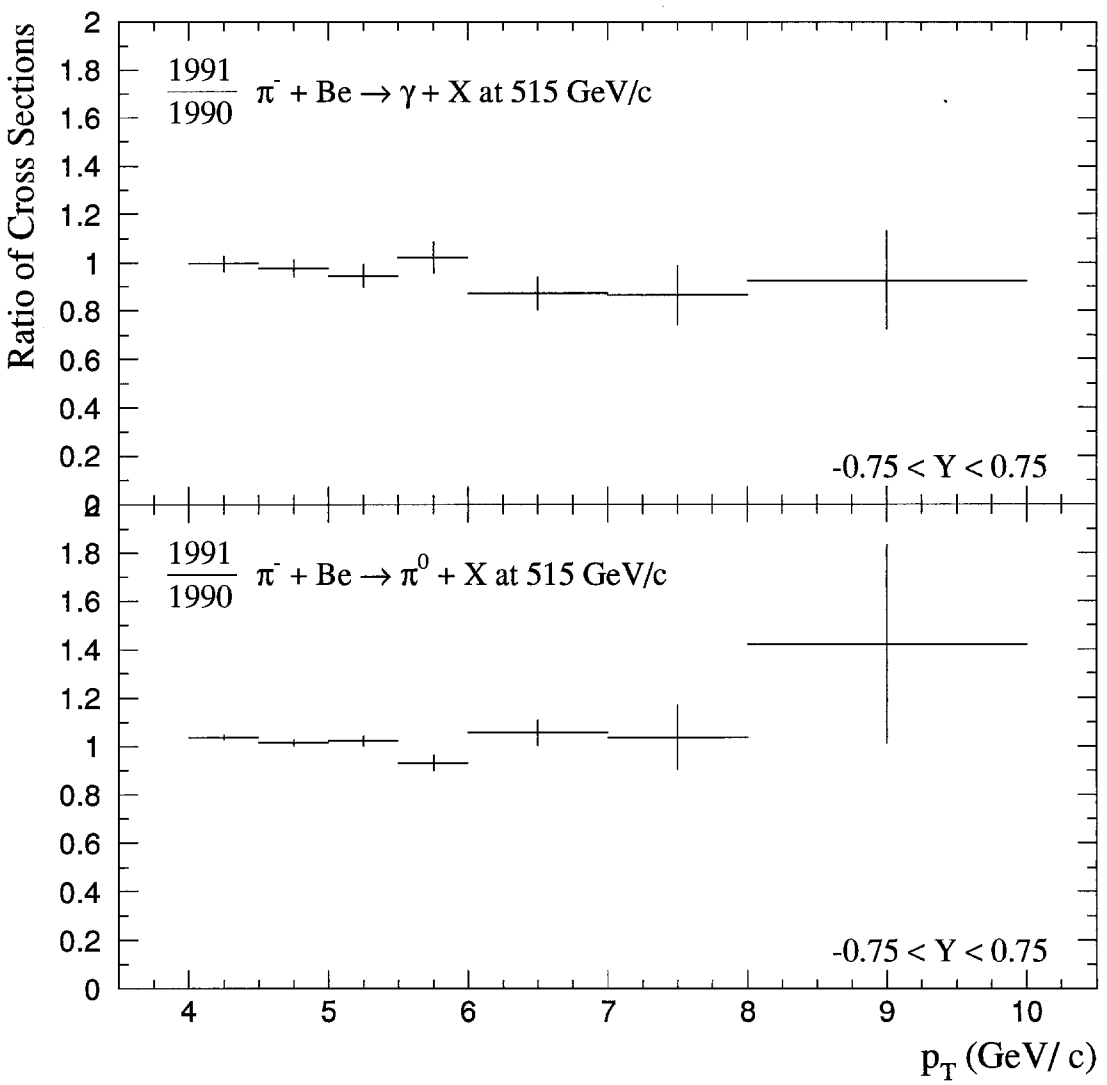

Figure 5.29 Ratios of direct photon (top) and π^0 (bottom) cross sections obtained from the 1991 (numerator) and 1990 (denominator) π^- beam incident upon beryllium, showing very good agreement between these independent measurements. Error bars represent statistical uncertainties only.

Chapter 6 Neutral Meson and Direct Photon Results

The following sections contain the results obtained via the methods described in the previous chapter. The first section presents the π^0, η, and direct photon cross sections. The next two sections show the measurement of the η/π ratio and the ratios of cross sections from the two beams. The fourth section presents an analysis of the nuclear dependence of the various production spectra. The fifth and sixth sections utilize the measured nuclear dependence in the comparison of E706 results to measurements made by other experiments and to Next to Leading Log (NLL) QCD calculations, respectively. The uncertainties quoted in the plots and tables of the first six sections are statistical only; the seventh section contains a discussion of the systematic uncertainties. The final section presents the conclusions of this analysis.

6.1 Invariant Cross Sections

This section contains graphical projections of the inclusive cross sections measured for the production of π^0's, η's, and direct photons by 515 GeV/c π^- and 530 GeV/c proton beams incident upon hydrogen, beryllium, and copper targets. (The cross-section data in these plots are presented in tabular form in the appendix.) The fractional uncertainties in the low-p_T cross-section measurements are larger than those at higher p_T because the reconstruction efficiency corrections for the low-p_T data are extrapolations. As a consequence, certain low-p_T data are shown in the cross-section plots for illustration purposes and excluded from the detailed tables.

Figures 6.1 through 6.6 display the cross sections versus transverse momentum. These measurements are averaged over the center-of-mass rapidity interval

$-0.75 < Y_{CM} < 0.75$. The abscissa value for each of the points was determined by computing the average p_T in the bin based on an exponential fit to the cross section. From these plots, a number of generalizations can be made. Each of these cross sections is a steeply falling function of p_T, with the slope becoming less extreme with increasing p_T. As one would expect, the cross section (per nucleus) at a given p_T is larger for nuclei with higher atomic mass; the shapes of the cross section as functions of p_T, however, are quite similar for data from each of the three targets. The cross sections for incident π^- are less steep than the corresponding cross sections from proton beam. For both beam types, the η production rate is roughly half that of π^0's at any given p_T, whereas the slope of the direct photon cross sections is significantly less steep than that of the corresponding π^0.

Figures 6.7 through 6.9 present the rapidity dependence of the cross section (using the high-statistics beryllium-target sample) in several p_T bins. In general, the rapidity distributions are relatively flat at the lowest p_T's. Progressively higher p_T bins show more strongly peaked rapidity distributions. The proton data is generally centered on $Y_{CM} = 0$, but the cross sections for incident π^- are significantly shifted toward forward (or positive) rapidities. This is not surprising, since partons in the π^- meson (having two valence quarks) would be expected to have a harder distribution than the partons in the target baryon (with its three valence quarks).

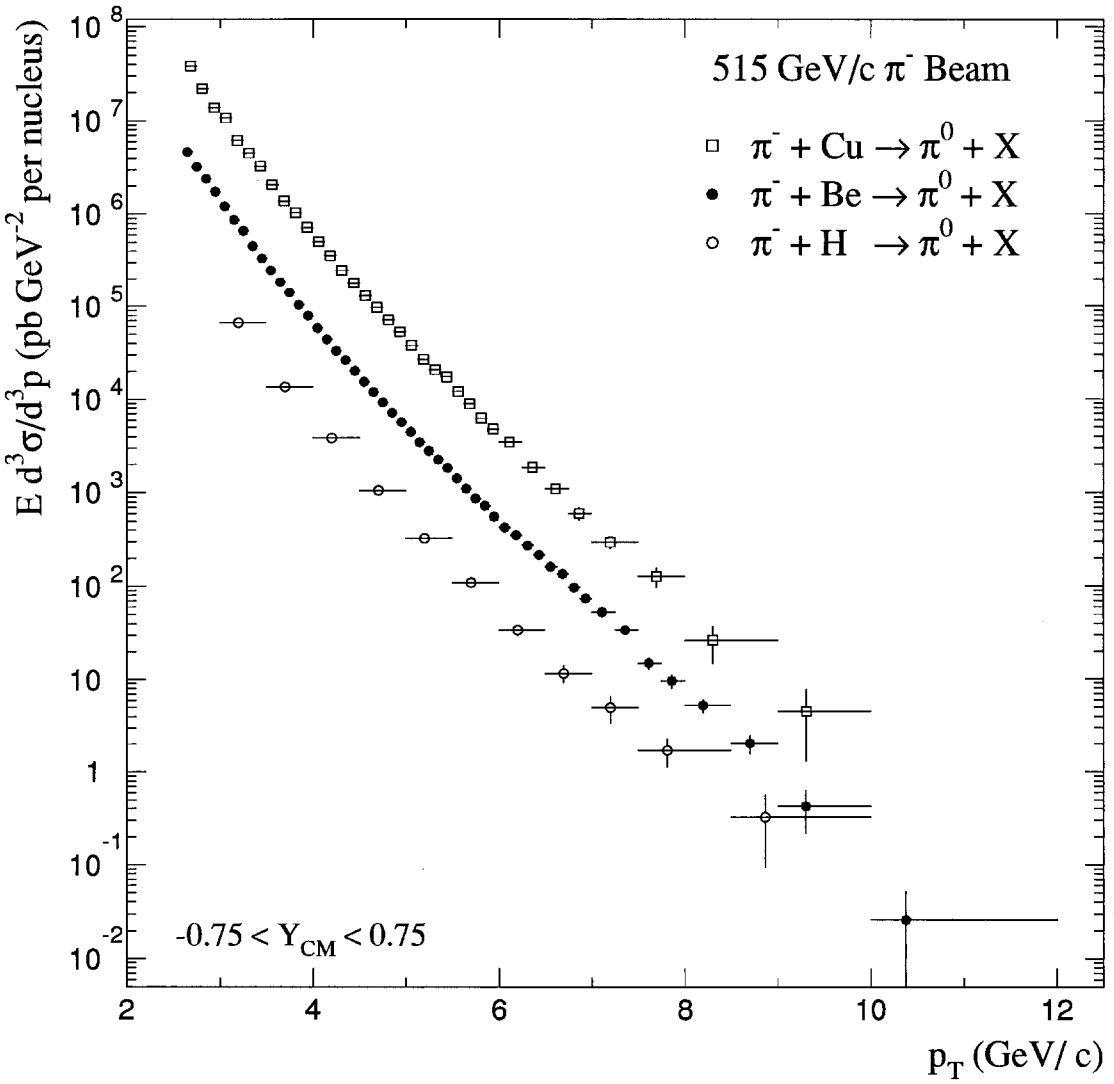

Figure 6.1 The invariant differential inclusive π^0 cross sections per nucleus as functions of the π^0 transverse momentum for 515 GeV/c π^- beam on copper, beryllium, and hydrogen targets.

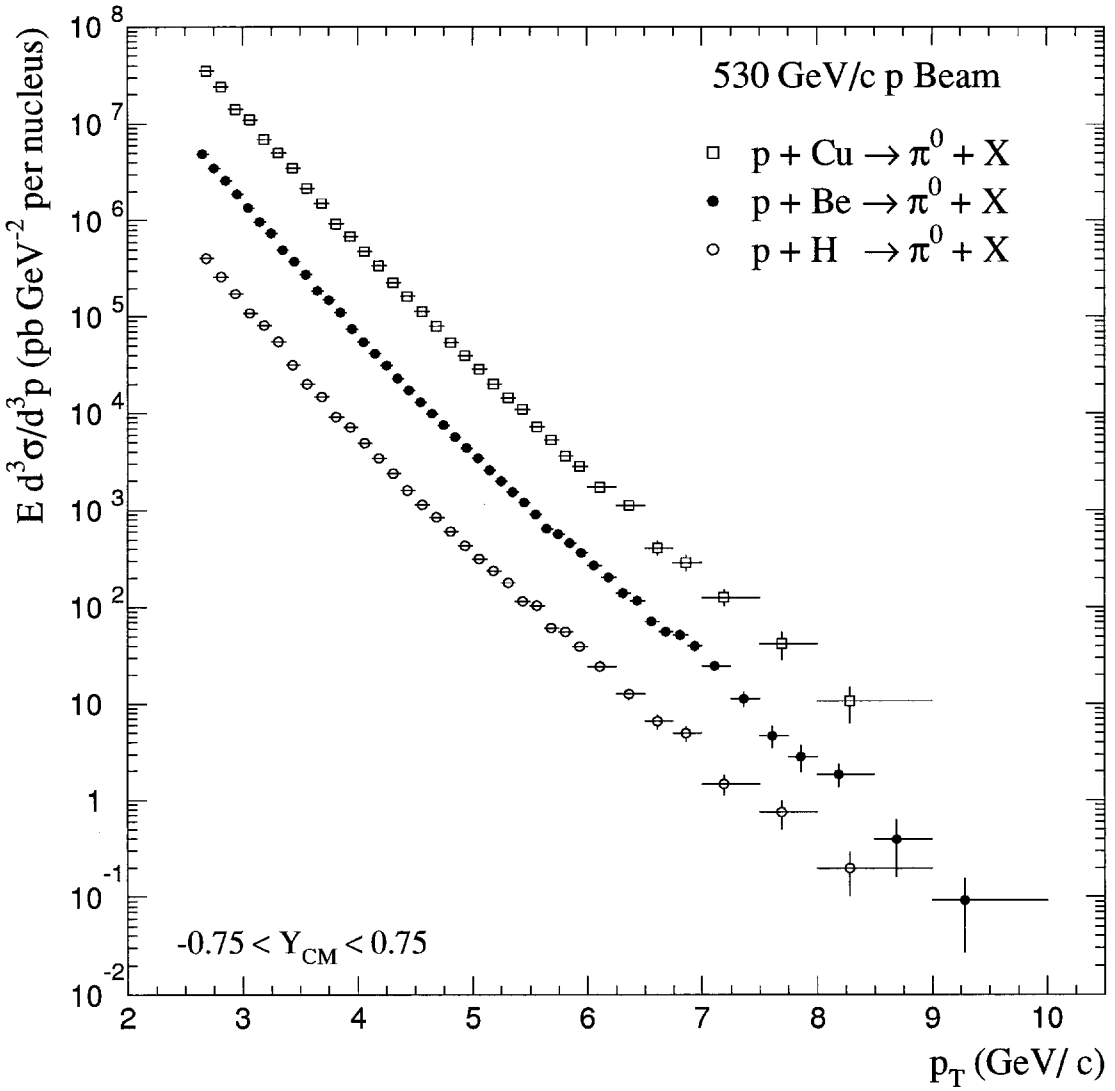

Figure 6.2 The invariant differential inclusive π^0 cross sections per nucleus as functions of the π^0 transverse momentum for 530 GeV/c p beam on copper, beryllium, and hydrogen targets.

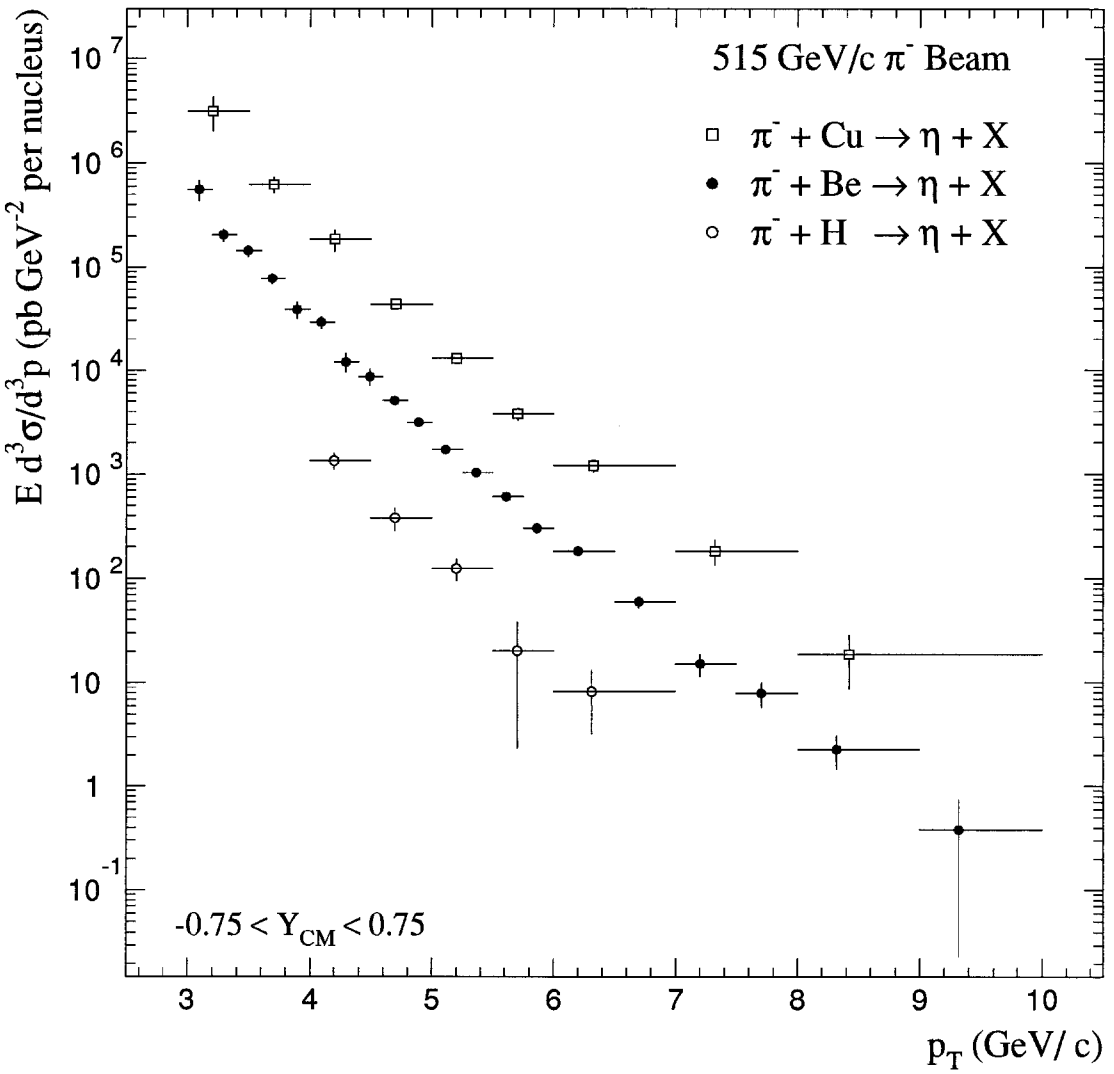

Figure 6.3 The invariant differential inclusive η cross sections per nucleus as functions of the η transverse momentum for 515 GeV/c π^- beam on copper, beryllium, and hydrogen targets.

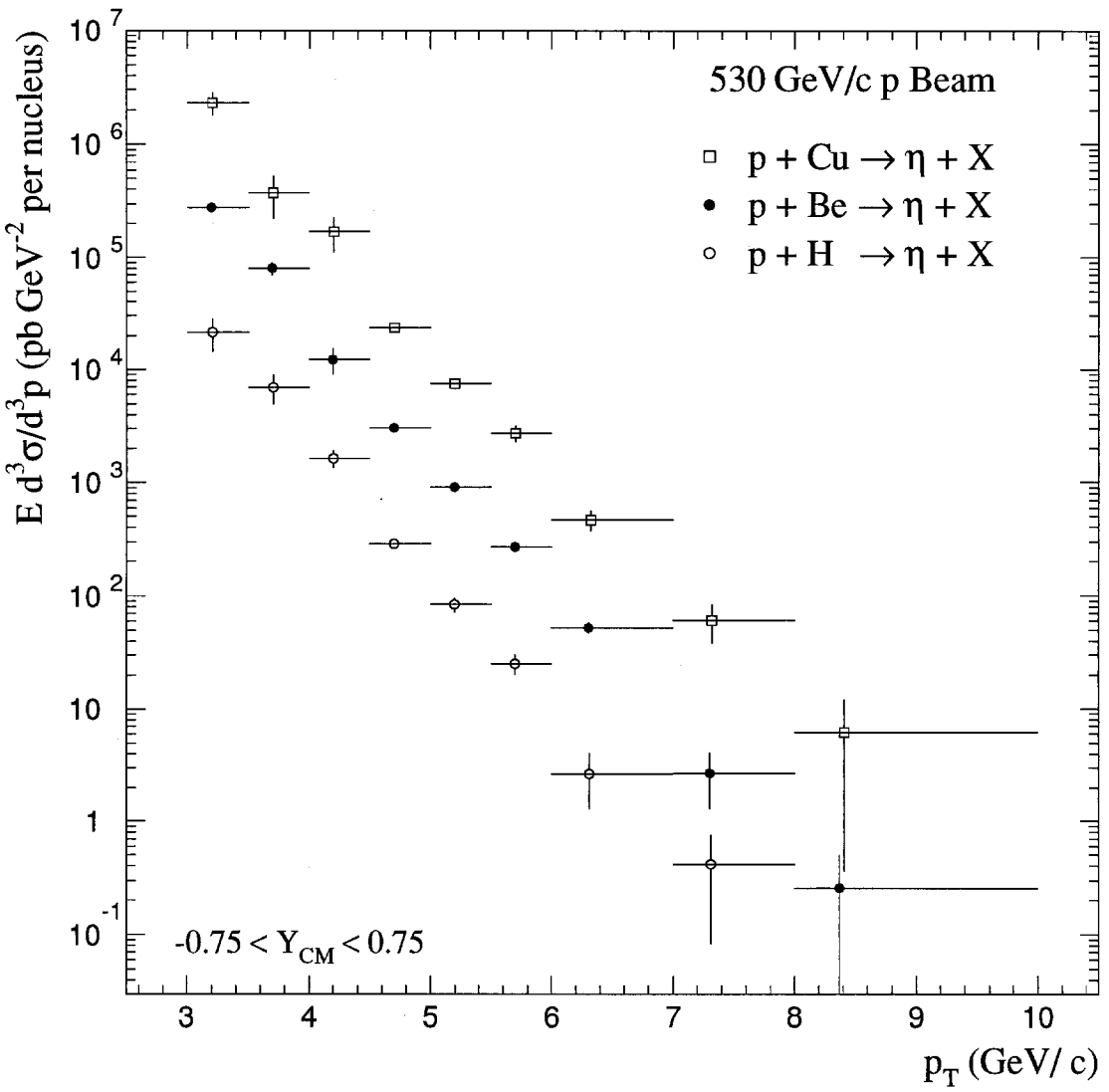

Figure 6.4 The invariant differential inclusive η cross sections per nucleus as functions of the η transverse momentum for 530 GeV/c p beam on copper, beryllium, and hydrogen targets.

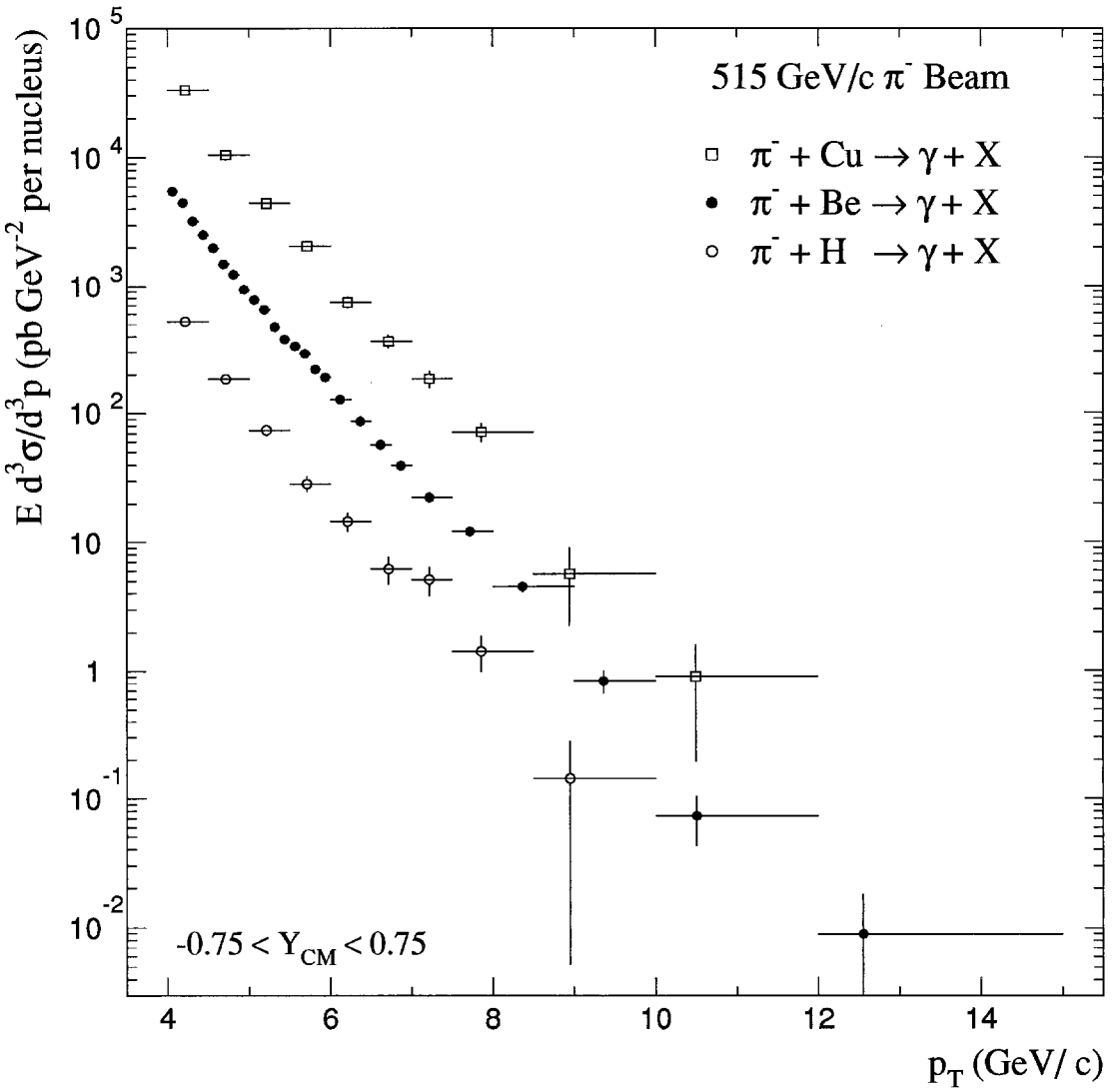

Figure 6.5 The invariant differential inclusive direct photon cross sections per nucleus as functions of the direct photon transverse momentum for 515 GeV/c π^- beam on copper, beryllium, and hydrogen targets.

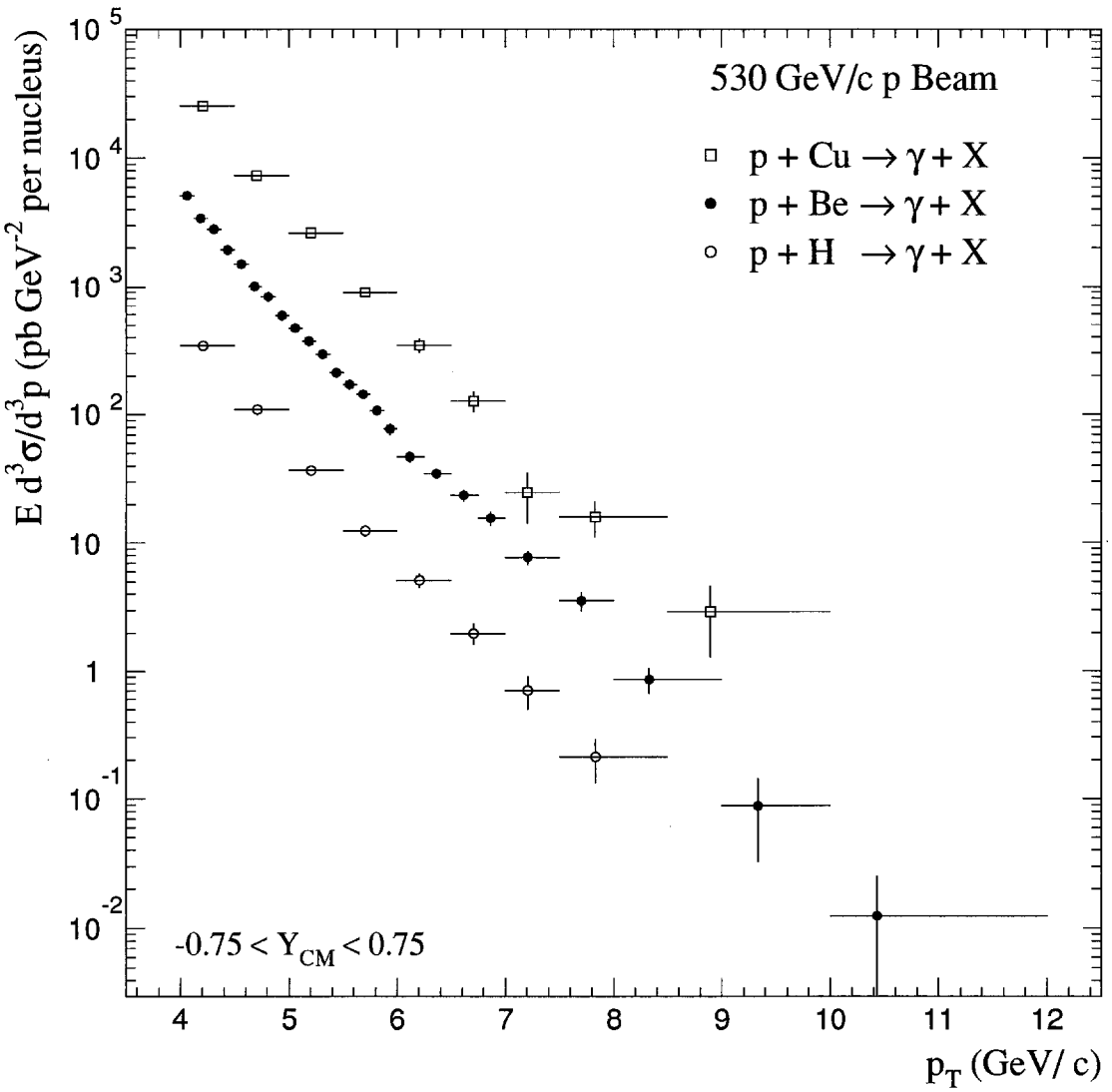

Figure 6.6 The invariant differential inclusive direct photon cross sections per nucleus as functions of the direct photon transverse momentum for 530 GeV/c p beam on copper, beryllium, and hydrogen targets.

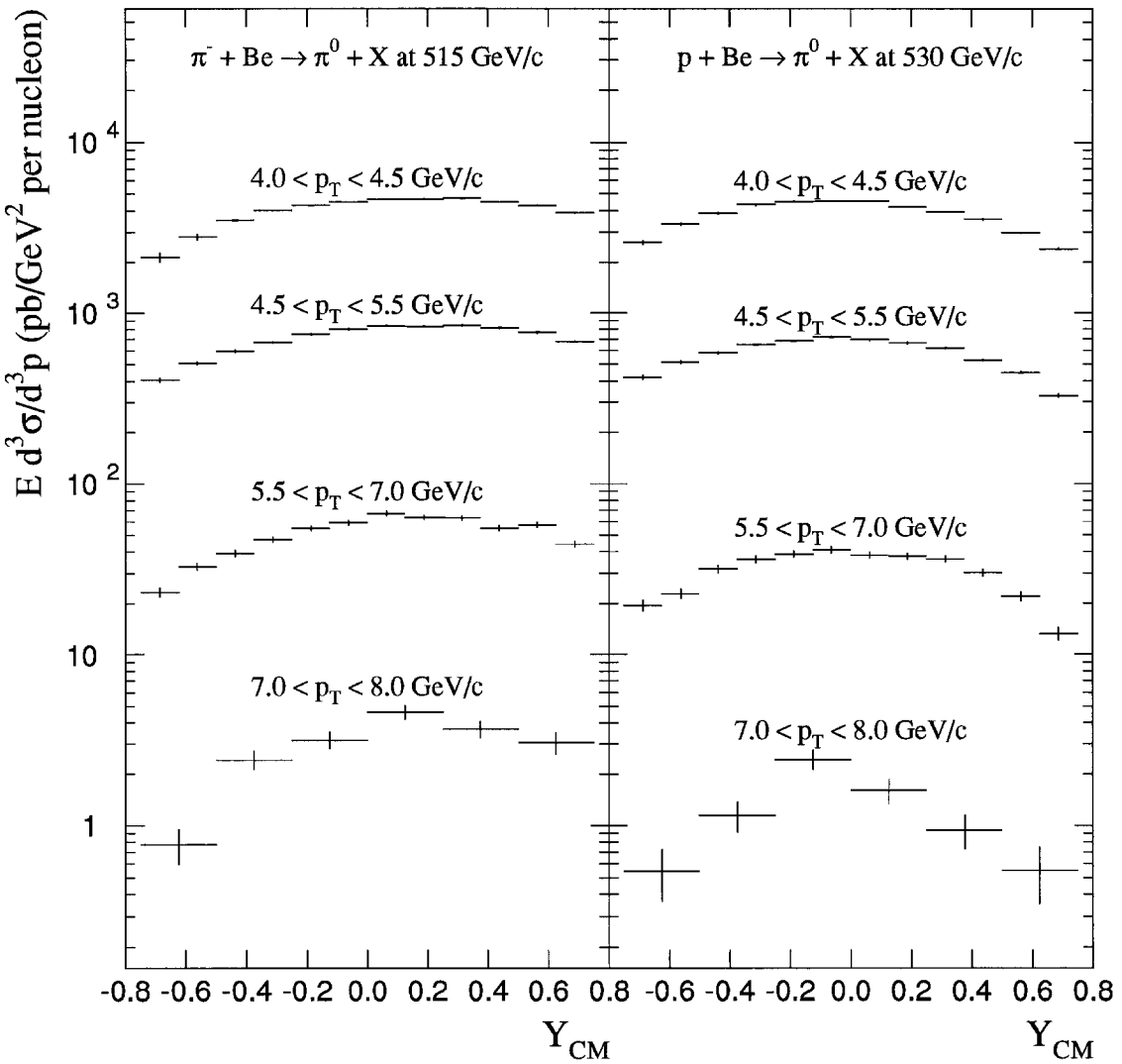

Figure 6.7 The invariant inclusive π^0 cross section per nucleon for 515 GeV/c π^- (left) and 530 GeV/c proton (right) beams incident on beryllium, as a function of Y_{CM} for several p_T intervals.

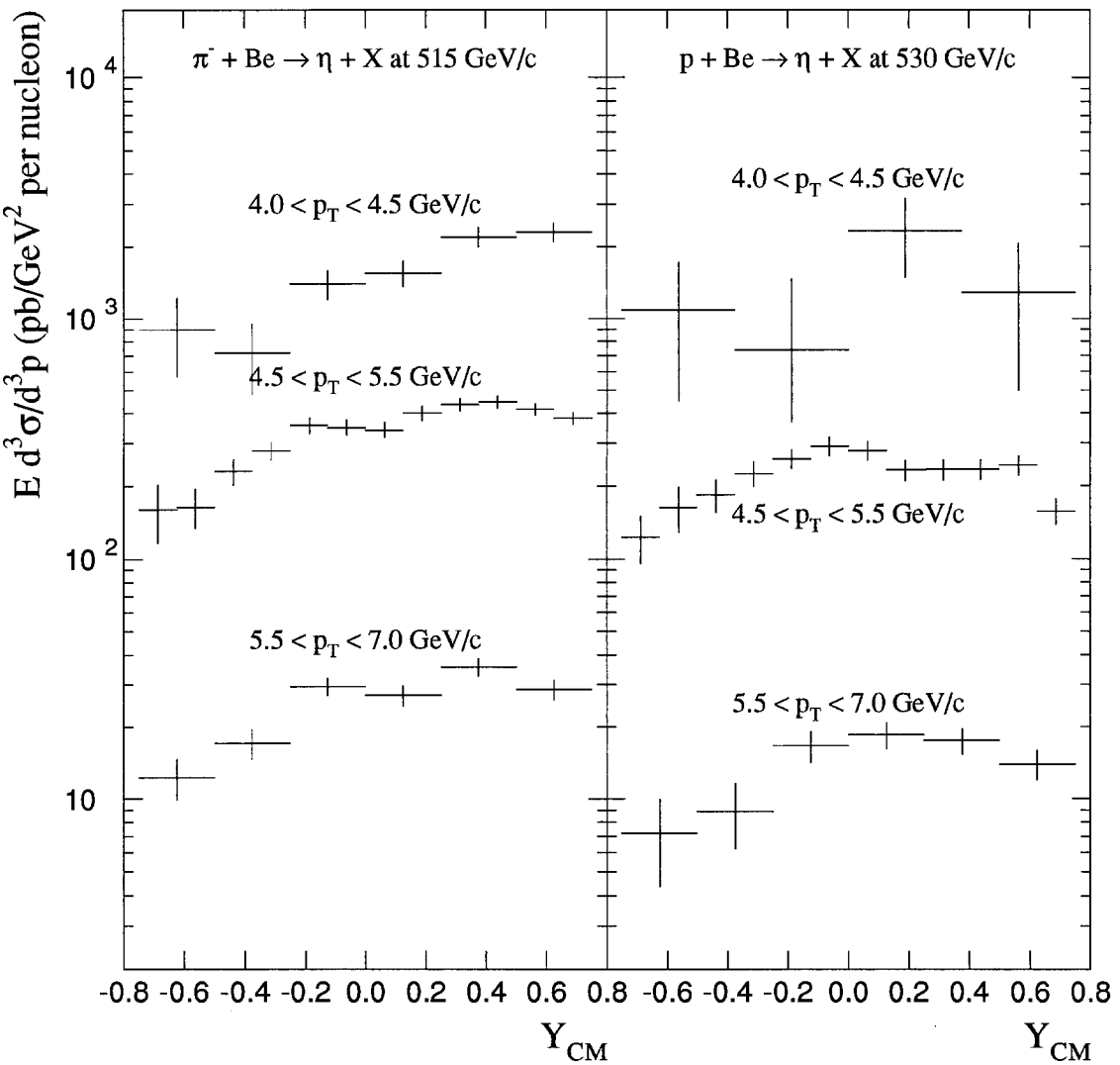

Figure 6.8 The invariant inclusive η cross section per nucleon for 515 GeV/c π^- (left) and 530 GeV/c proton (right) beams incident on beryllium, as a function of Y_{CM} for several p_T intervals.

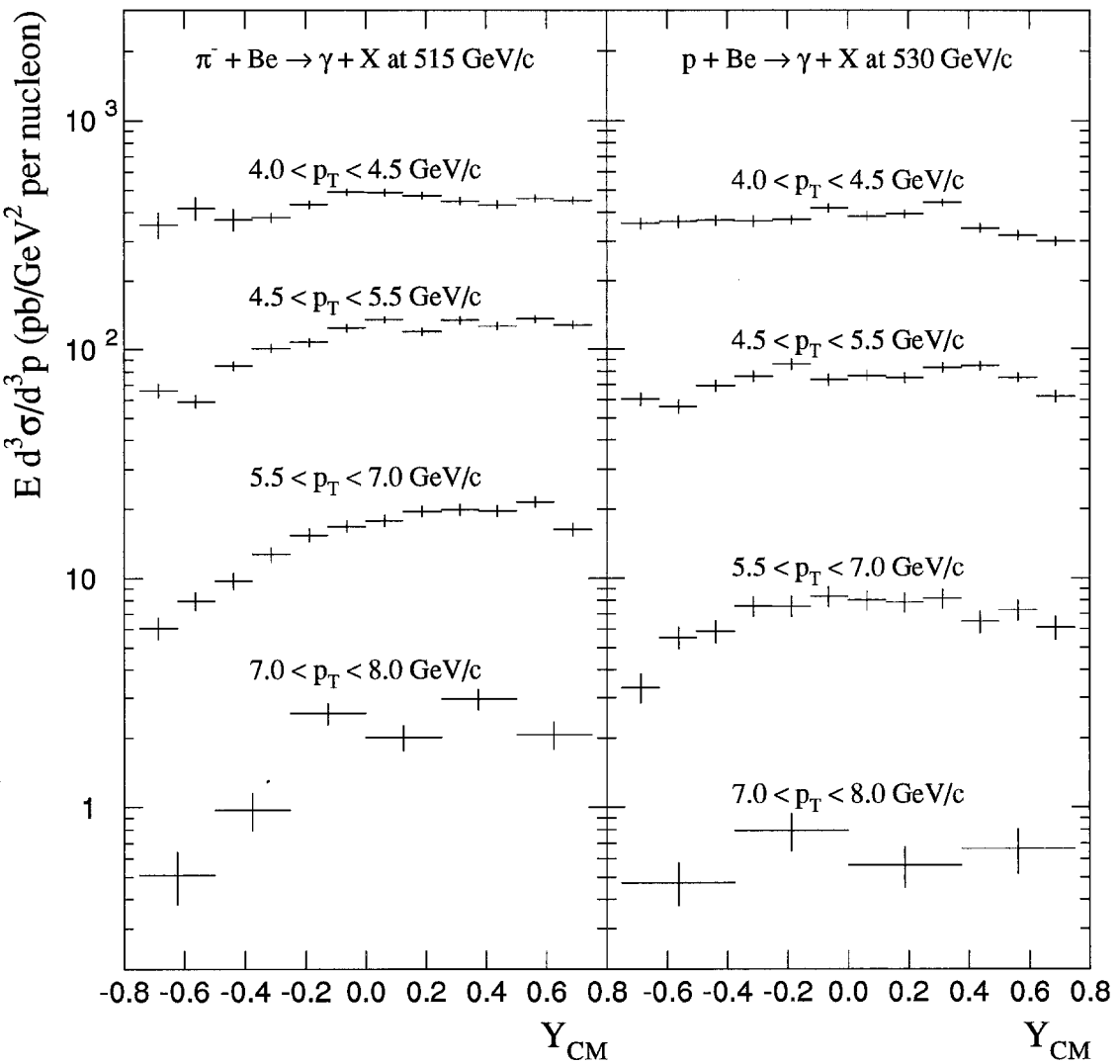

Figure 6.9 The invariant inclusive direct photon cross section per nucleon for 515 GeV/c π^- (left) and 530 GeV/c proton (right) beams incident on beryllium, as a function of Y_{CM} for several p_T intervals.

6.2 The η/π^0 Ratio

Figure 6.10 displays the ratios (as functions of p_T) of the η and π^0 cross sections for both the π^- and proton beams incident on beryllium. The measured η/π^0 ratio does not show a significant dependence on p_T; for $p_T > 3.5$ GeV/c,

$$\eta/\pi = 0.48 \pm 0.01 \quad \text{for } \pi^-\text{Be interactions}$$

$$\eta/\pi = 0.44 \pm 0.01 \quad \text{for pBe interactions}$$

as determined by the fits shown. The mean values obtained are compared to measurements by other experiments in Figure 6.11; the E706 η/π^0 ratios are consistent with the other measurements.

6.3 Beam Particle Dependence

Figure 6.12 presents ratios of direct photon (and π^0) production cross sections from the negative pion and proton beams incident on beryllium. Both the direct-photon and the π^0 cross-section ratios rise with increasing p_T; this trend is consistent with the expectation that the parton momentum distribution should be harder in the π^- than in the proton, just from considerations of the number of valence quarks.

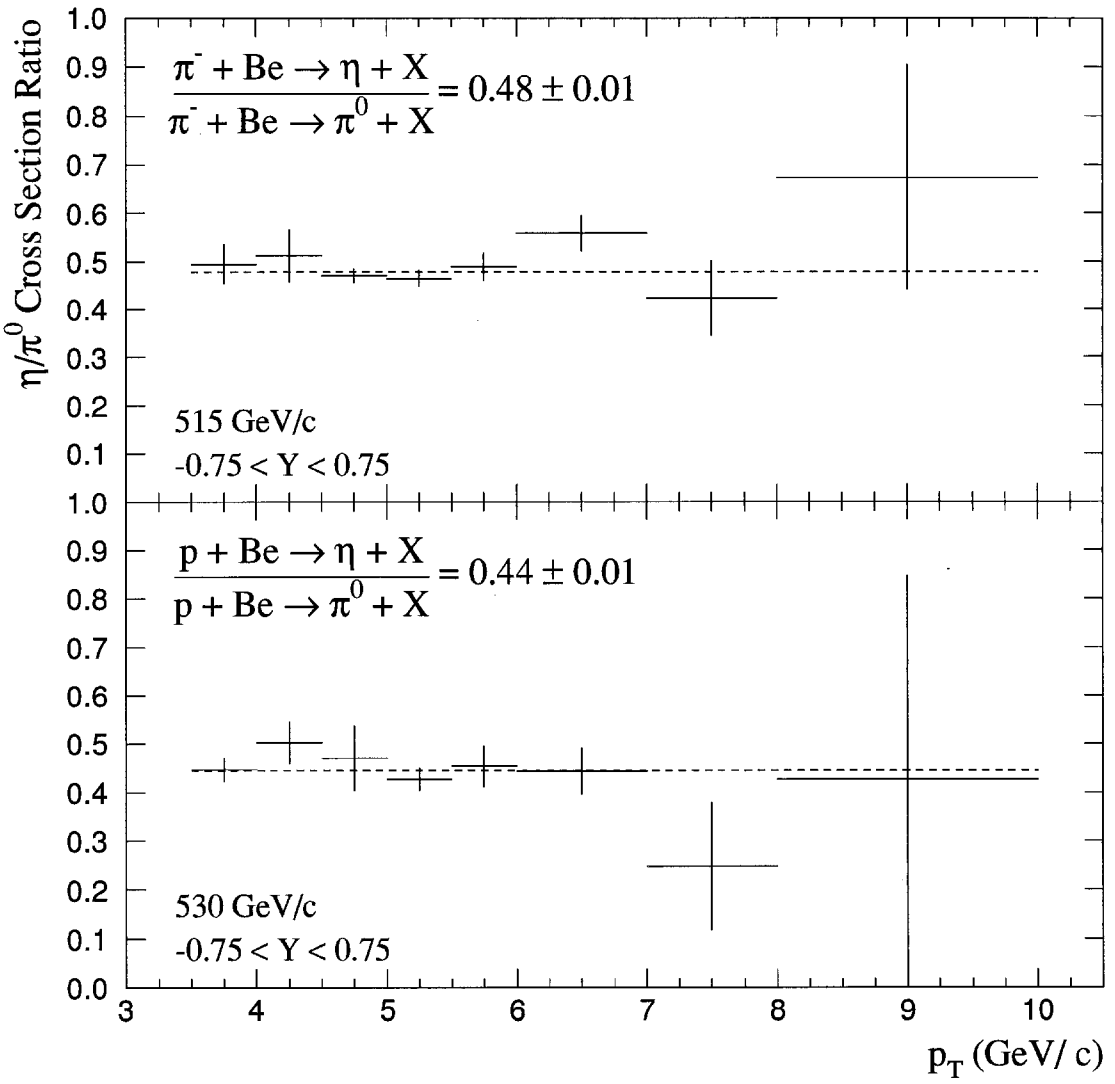

Figure 6.10 The ratio as a function of p_T of the η and π^0 cross sections for 515 GeV/c π^- beam (top) and for 530 GeV/c proton beam (bottom) on the beryllium target. The ratio is essentially independent of p_T; the dashed line indicates the measured ratio.

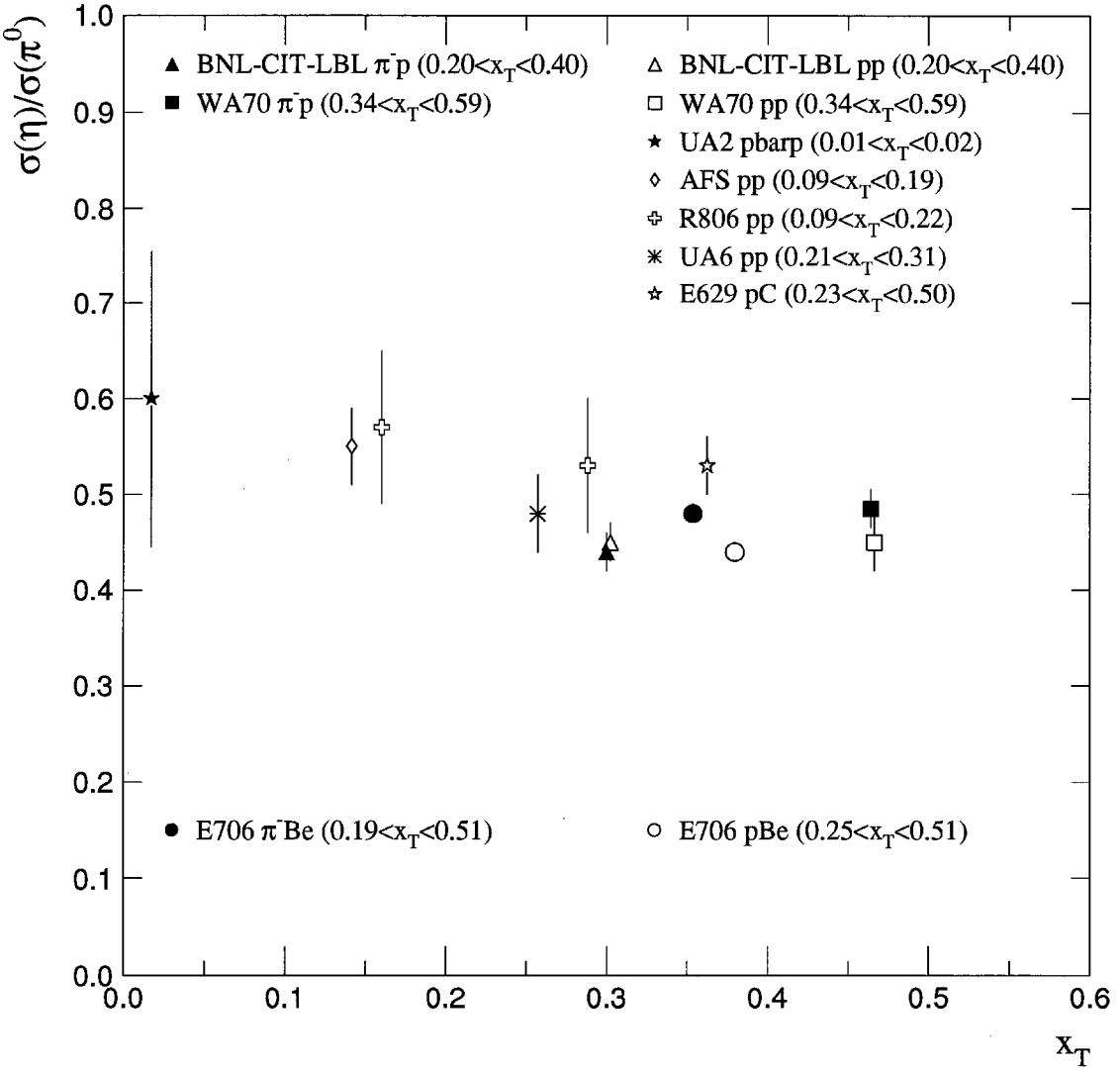

Figure 6.11 The η/π^0 ratio versus mean $x_T = 2p_T/\sqrt{s}$ for measurements made by various experiments. The overall trend is relatively flat and the E706 points are quite consistent with other measurements in our x_T region.

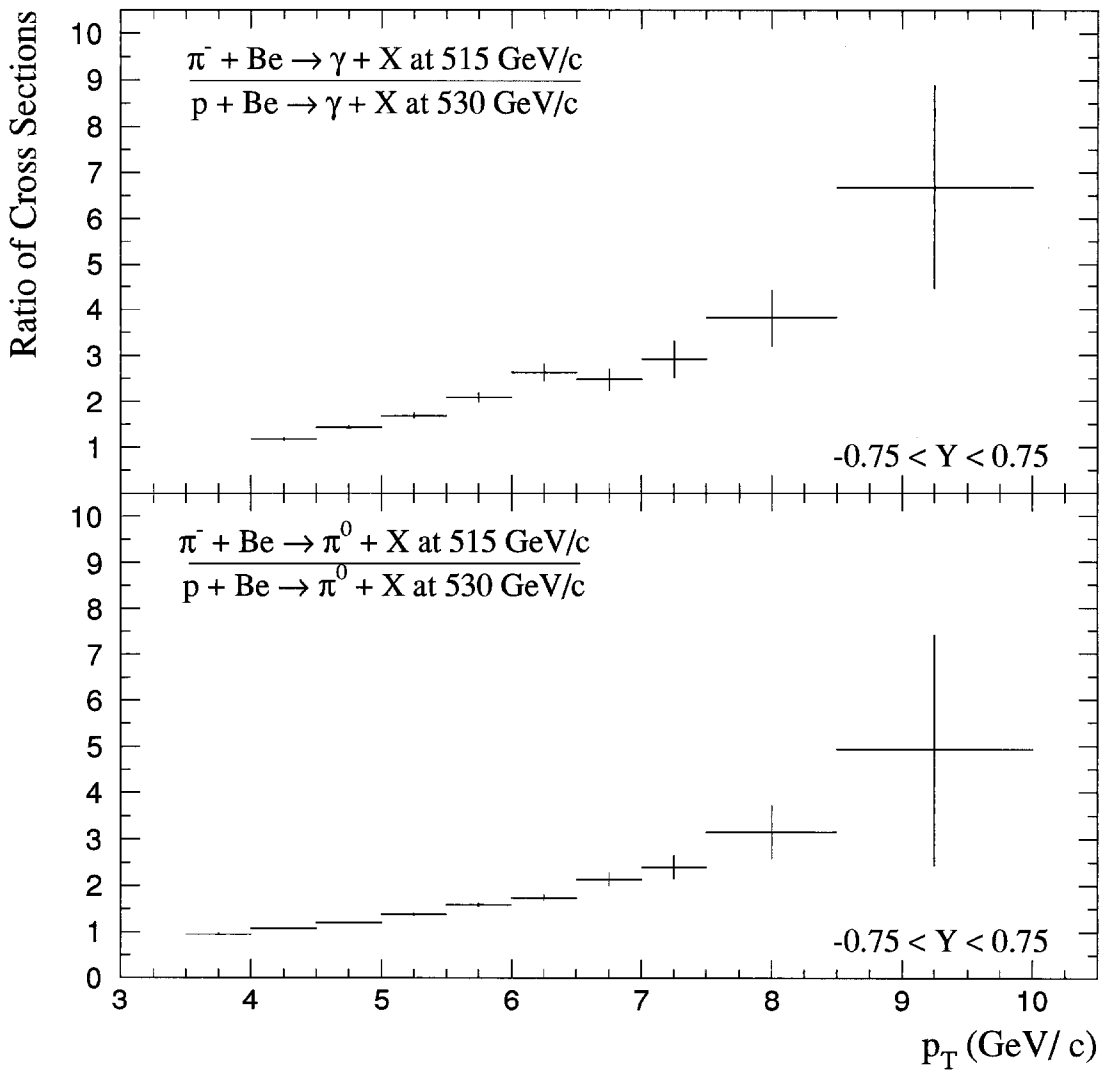

Figure 6.12 The ratio of the cross section from 515 GeV/c π^- beam and 530 GeV/c proton beam on beryllium for direct photons (top) and π^0's (bottom).

6.4 Nuclear Dependence

The cross-section measurements in the Section 6.1 were presented in units of pb/GeV^2 *per nucleus.* To first order for hard scatters, one would expect that the cross sections from a given target nucleus would scale with the number of nucleons in the target nucleus. There are, however, effects such as multiple scattering of partons within a nucleus which could alter these naive expectations. As discussed in Section 1.2.3, the nuclear dependence of a cross section may be parametrized as in Equation (1.6). Given cross-section measurements from any two targets, here labeled T1 and T2, one can rewrite the formula as

$$\alpha = 1 + \ln \frac{\sigma_{\mathrm{T1}}}{\sigma_{\mathrm{T2}}} / \ln \frac{\mathrm{A_{T1}}}{\mathrm{A_{T2}}} \tag{6.1}$$

where σ_{X} is the cross section *per nucleon* for target X.

Equation (1.6) does not necessarily hold for all nuclei. One may expect small differences in measured cross sections depending on the relative populations of protons and neutrons in the target nuclei. (For example, for both copper and beryllium, $\mathrm{Z/A} \approx 0.45$, whereas for hydrogen, $\mathrm{Z/A} = 1$.) In addition, the nucleons in copper and beryllium nuclei are constantly interacting, quite unlike the isolated proton which makes up a hydrogen atom's nucleus. Thus, it is quite reasonable to use the copper and beryllium data to determine $\alpha_{\mathrm{Be/Cu}}$, and then compare the result to the measured cross section for the hydrogen target.

Figures 6.13 and Figure 6.14 display $\alpha_{\mathrm{Be/Cu}}$ measured for π^0 production by the proton and pion beams, respectively, versus $\mathrm{p_T}$ and $\mathrm{Y_{CM}}$. Figures 6.15 through Figure 6.18 show the measured $\alpha_{\mathrm{Be/Cu}}$'s for η's and direct photons. At high $\mathrm{p_T}$, $\alpha_{\mathrm{Be/Cu}}$ exceeds one, consistent with the hypothesis of multiple scattering in the nucleus. The dashed lines are one-parameter fits to the measurements over the

Beam	Particle	$\alpha_{Be/Cu}$
π^- (515 GeV/c)	γ	1.06 $\pm$ 0.01
	π^0	1.114 $\pm$ 0.005
	η	1.16 $\pm$ 0.03
p (530 GeV/c)	γ	1.07 $\pm$ 0.01
	π^0	1.133 $\pm$ 0.004
	η	1.13 $\pm$ 0.04

Table 6.1 The nuclear-dependence parameter $\alpha_{Be/Cu}$ measured for π^0, η, and direct photon production by π^- and p beams. (Statistical uncertainties only.)

range indicated. For production of both mesons and direct photons by positive and negative beams, $\alpha_{Be/Cu}$ does not appear to depend strongly on Y_{CM}.

Table 6.1 summarizes the results of the $\alpha_{Be/Cu}$ fit values for $p_T > 4$ GeV/c. The cross-section enhancement due to nuclear effects is approximately twice as large for the mesons as it is for the direct photons. This observation is also in accord with the hypothesis that the nuclear dependence is due to multiple scattering at the parton level. Rescattering of the incident parton occurs in both meson and direct-photon production; after the interaction, however, the direct photon does not rescatter, whereas the parton which fragments to an observed meson has the potential for rescattering within the nucleus.

Figure 6.19 compares the p_T dependence of the measured $\alpha_{Be/Cu}$ for π^0 production by the 530 GeV/c π^- beam with that of the α measured by Frisch *et al.* [9] for charged pion production by 200 GeV/c π^- beam. The measurements are quite consistent at all p_T's. The lowest-p_T E706 data shown is from a separate

analysis [35]. These data show that at relatively low p_T, the measured $\alpha_{Be/Cu}$ is less than unity, as expected from nuclear shadowing.

Figure 6.20 compares the measured direct photon $\alpha_{Be/Cu}$ to calculations performed by Guo and Qiu [10]. The calculated result is consistent with the data to within the uncertainties.

Figures 6.21 and 6.22 use the model in Equation (1.6) to extrapolate from the cross sections measured on beryllium and copper targets to the cross section measured on the hydrogen target. For both beam polarities, the hydrogen-target cross section is larger than the extrapolated result but within $\approx$10% of the that result. As discussed previously, one might expect some differences, since the hydrogen nucleus does not contain any neutrons and since its lone proton is not constantly interacting with other nucleons. However, the current level of systematics[1] associated with target definition and vertex-finding (especially for the hydrogen target) do not preclude consistency.

[1] See Section 6.7.2.

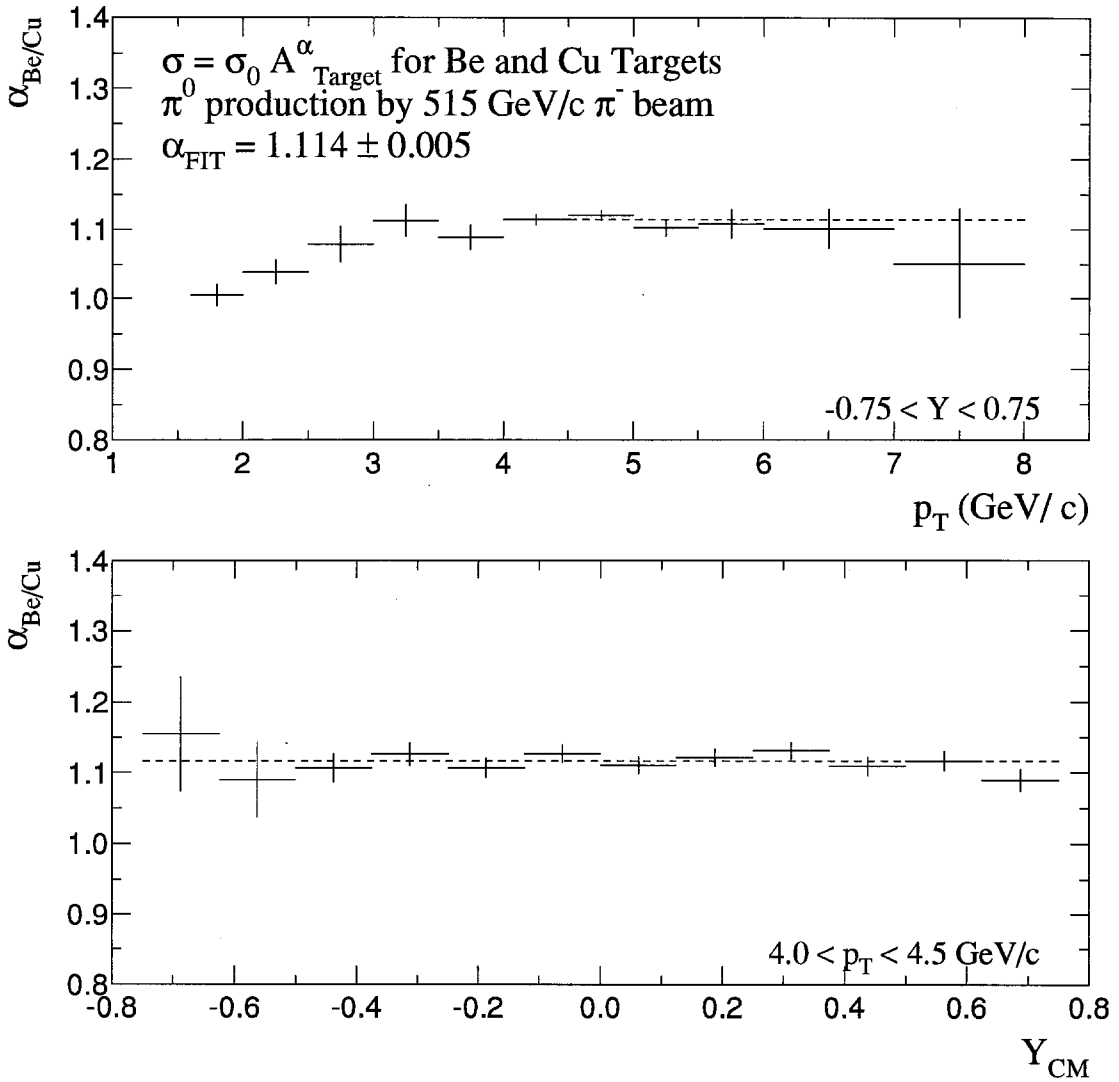

Figure 6.13 The nuclear-dependence parameter $\alpha_{Be/Cu}$ as a function of p_T and rapidity for π^0 production by 515 GeV/c π^- beam. The dashed lines represent the mean value over the range indicated. (See Table 6.1.)

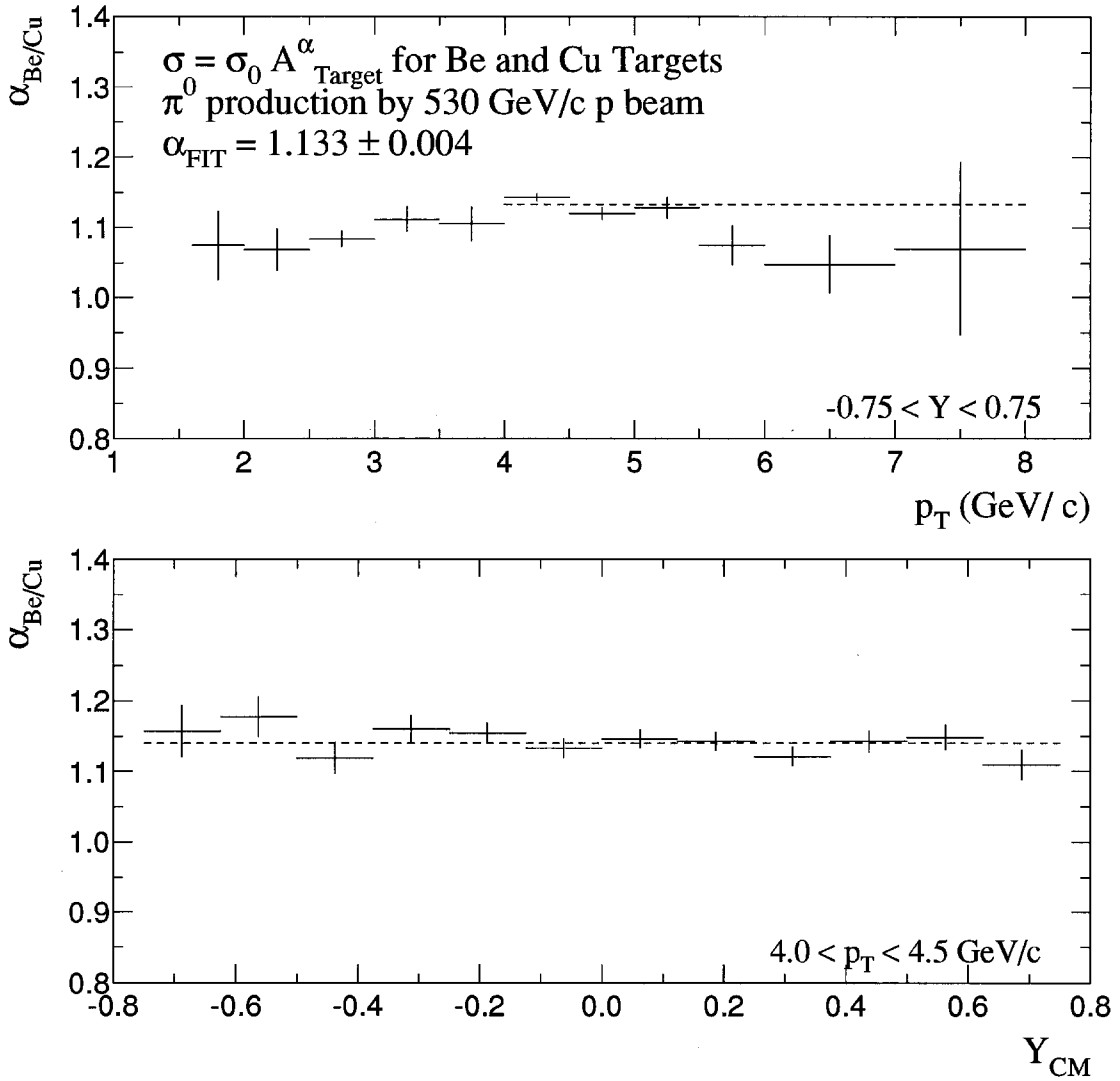

Figure 6.14 The nuclear-dependence parameter $\alpha_{Be/Cu}$ as a function of p_T and rapidity for π^0 production by 530 GeV/c proton beam. The dashed lines represent the mean value over the range indicated. (See Table 6.1.)

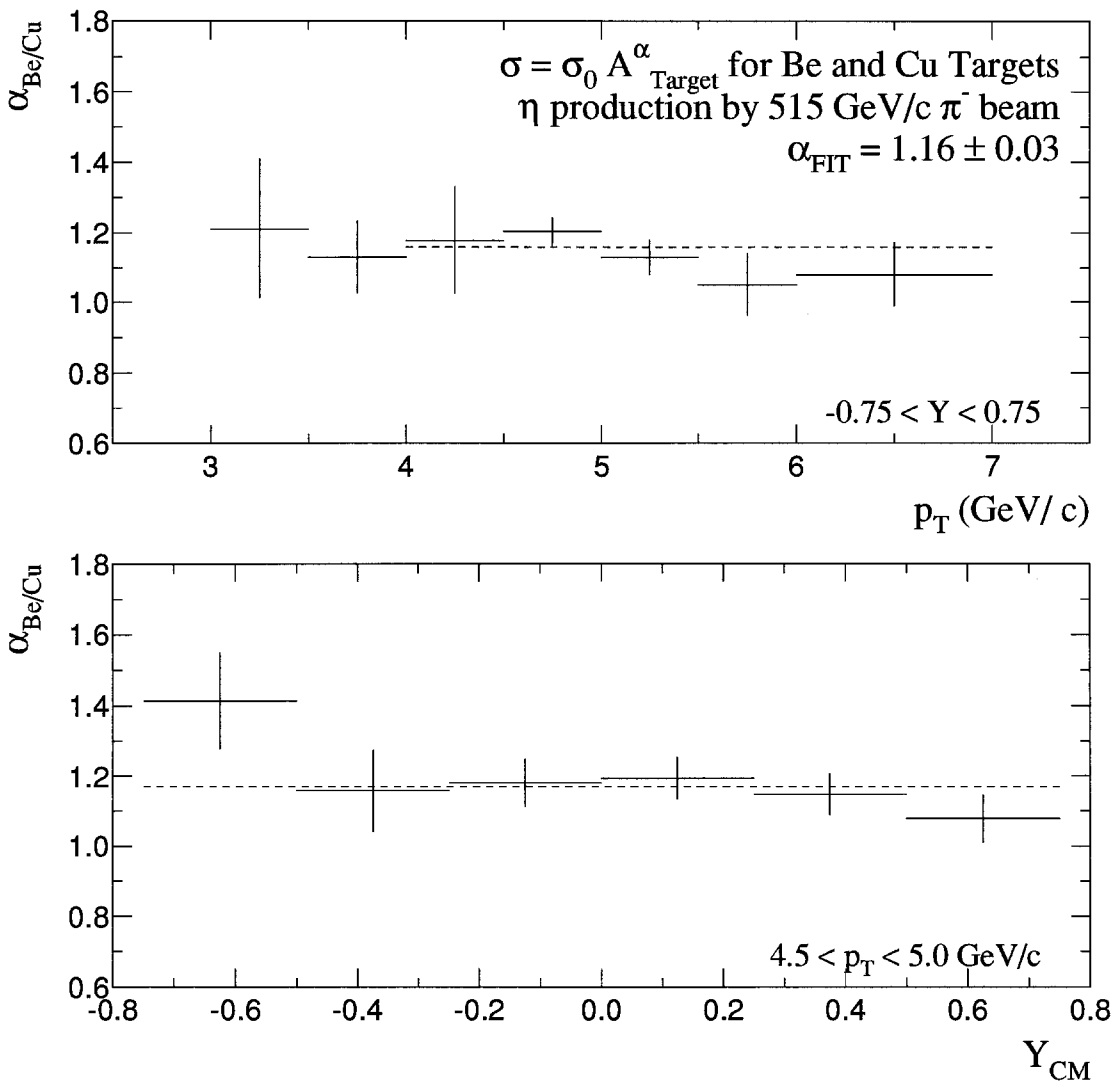

Figure 6.15 The nuclear-dependence parameter $\alpha_{Be/Cu}$ as a function of p_T and rapidity for η production by 515 GeV/c π^- beam. The dashed lines represent the mean value over the range indicated. (See Table 6.1.)

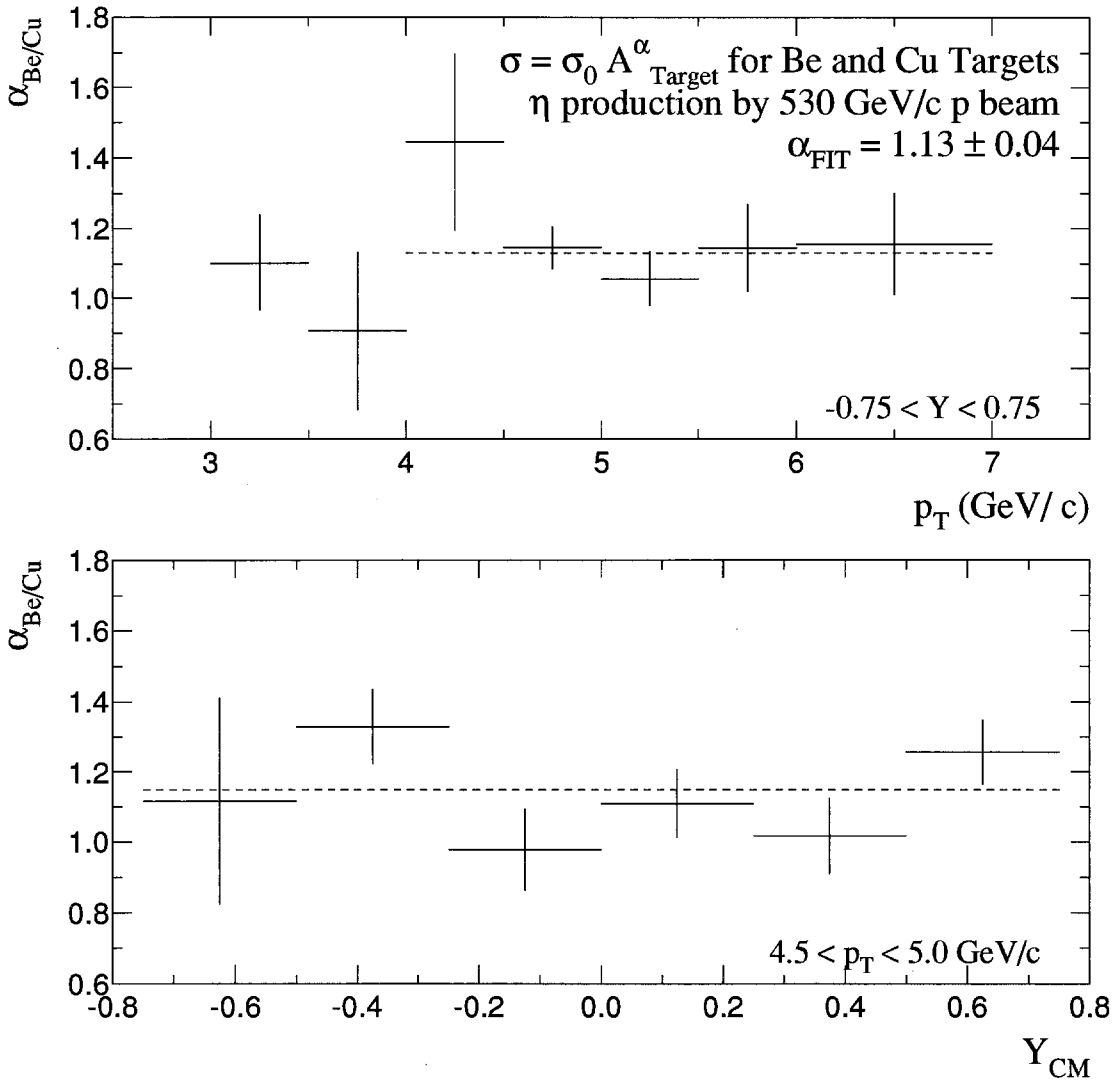

Figure 6.16 The nuclear-dependence parameter $\alpha_{Be/Cu}$ as a function of p_T and rapidity for η production by 530 GeV/c proton beam. The dashed lines represent the mean value over the range indicated. (See Table 6.1.)

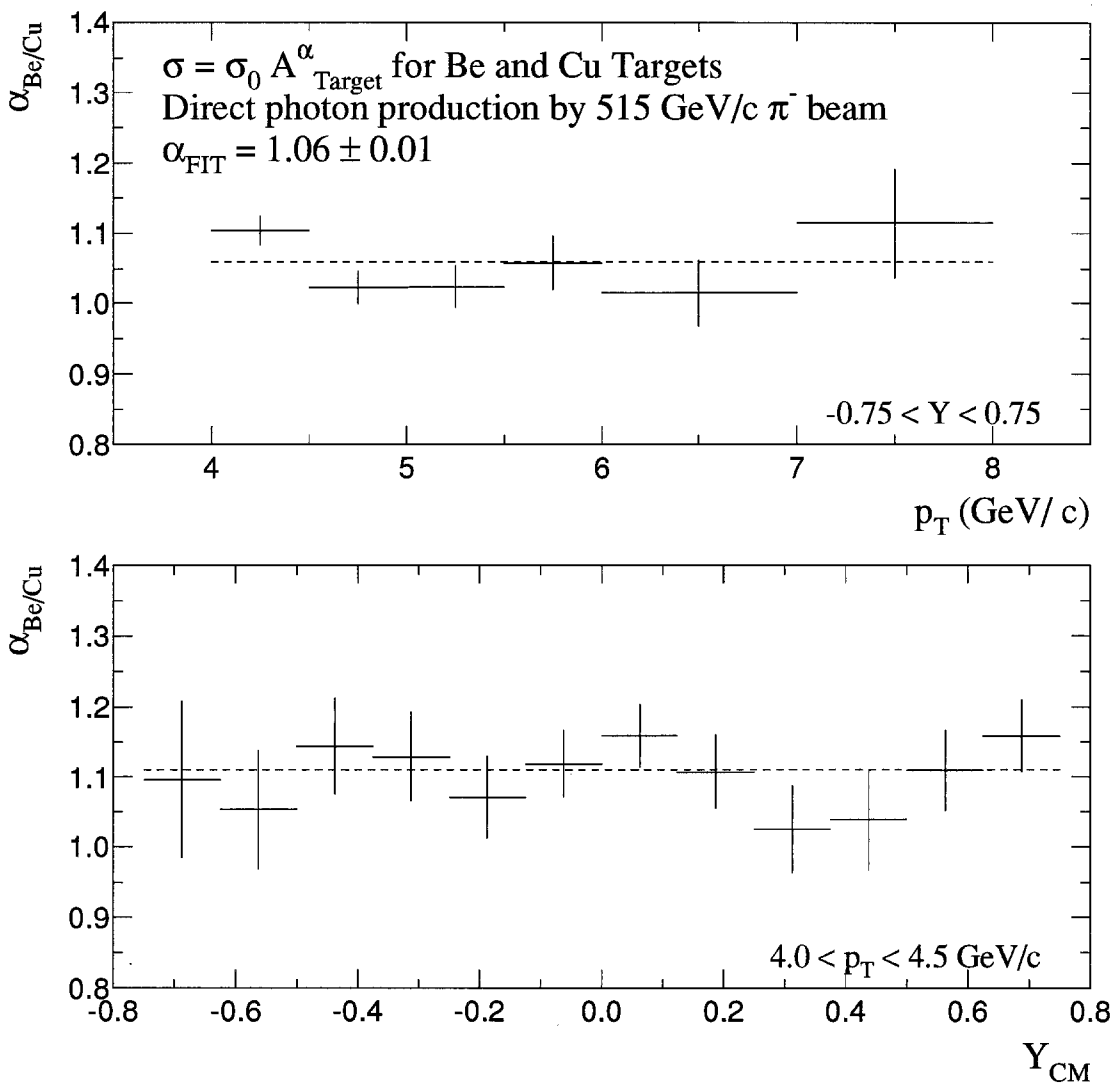

Figure 6.17 The nuclear-dependence parameter $\alpha_{Be/Cu}$ as a function of p_T and rapidity for direct photon production by 515 GeV/c π^- beam. The dashed lines represent the mean value over the range indicated. (See Table 6.1.)

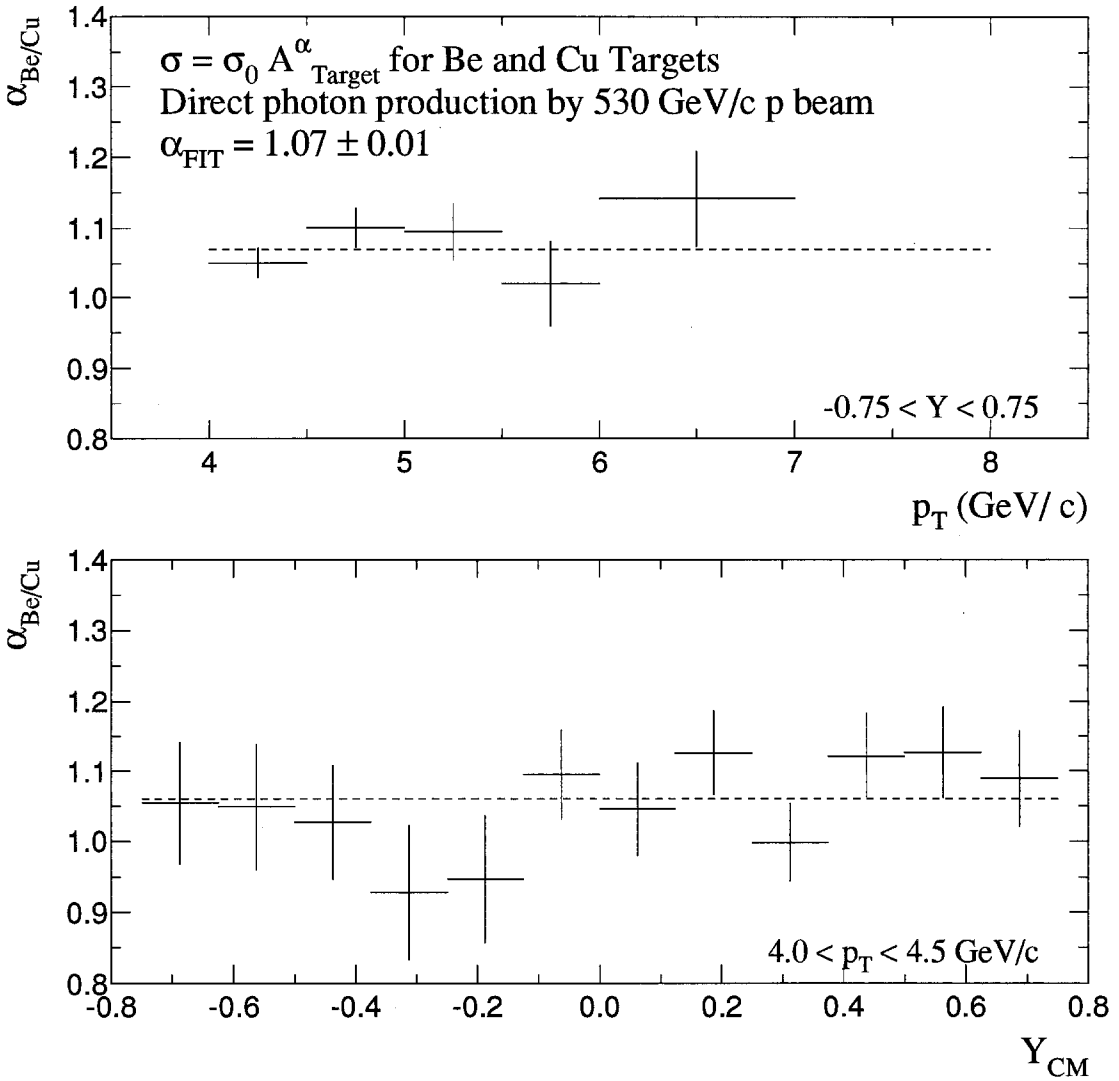

Figure 6.18 The nuclear-dependence parameter $\alpha_{Be/Cu}$ as a function of p_T and rapidity for direct photon production by 530 GeV/c proton beam. The dashed lines represent the mean value over the range indicated. (See Table 6.1.)

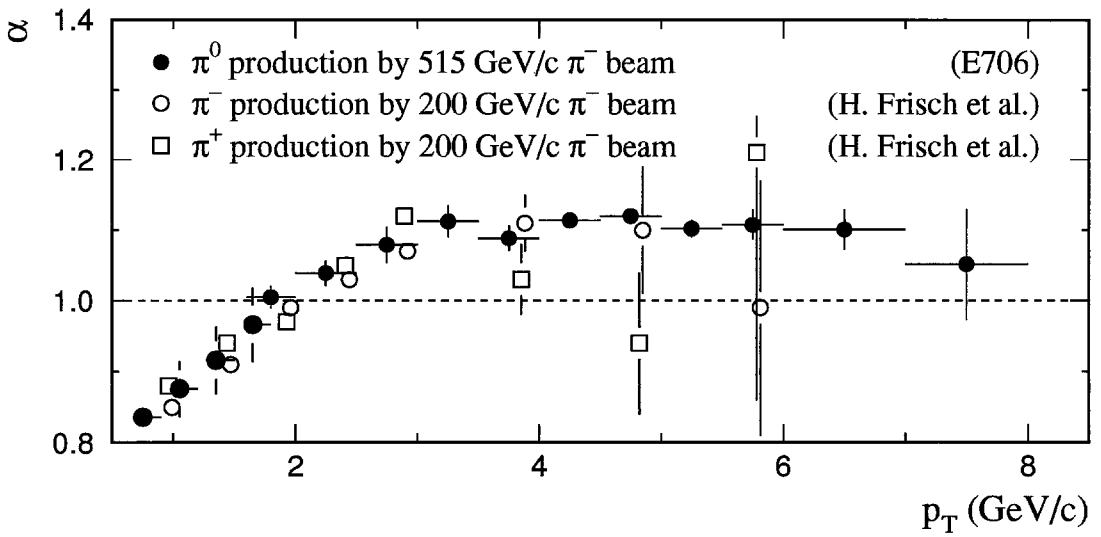

Figure 6.19 A comparison of the nuclear-dependence parameter α measured for π^0 production by a 515 GeV/c π^- beam and for charged pion production by 200 GeV/c π^- beam. The 515 GeV/c results are those measured in this thesis with additional low-p_T points from the low-bias trigger analysis by Kuehler [35], and the 200 GeV/c results were measured by Frisch *et al.* [9].

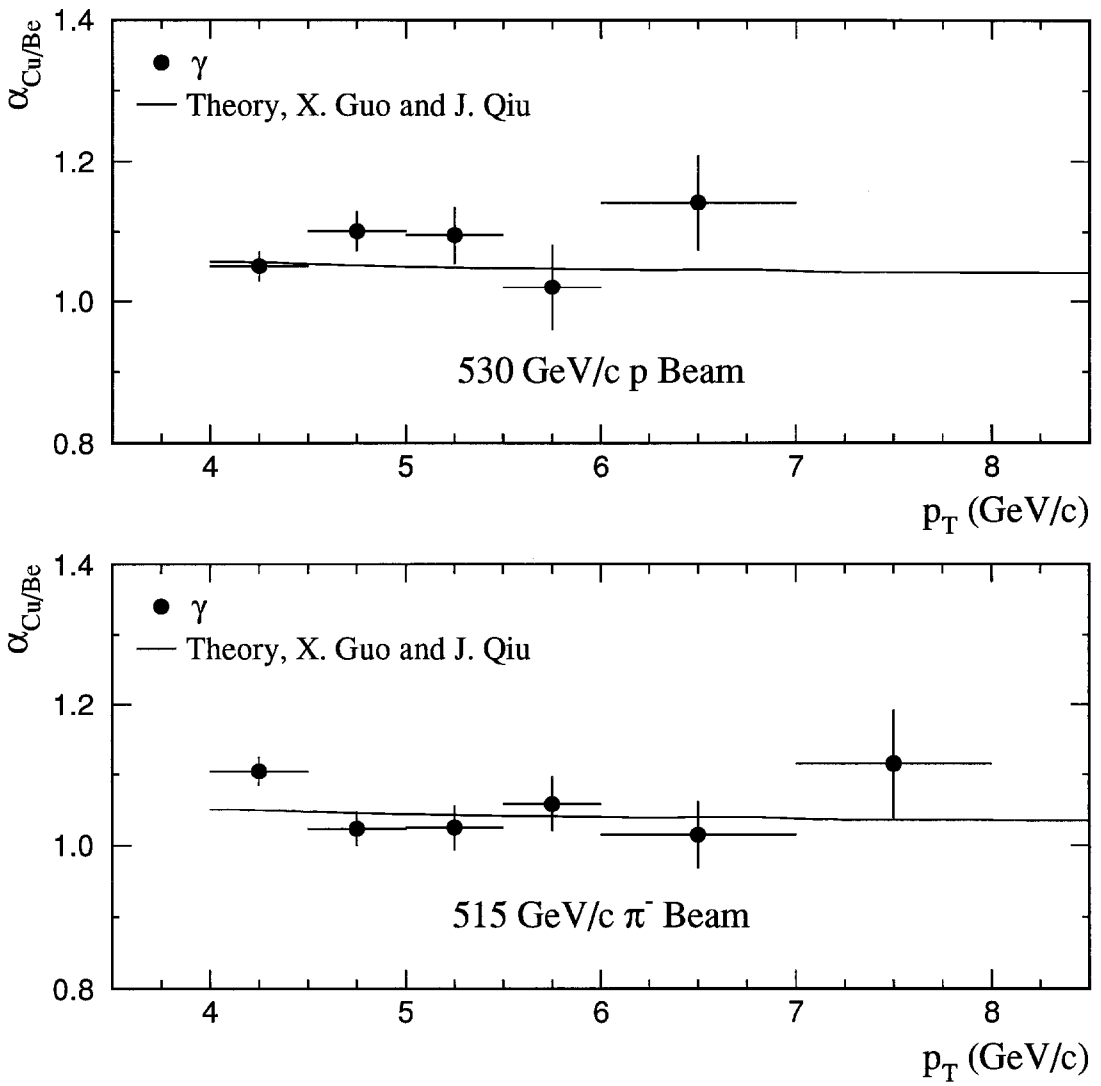

Figure 6.20 $\alpha_{Be/Cu}$ measured for direct-photon production by 515 GeV/c π^- beam (top) and by 530 GeV/c proton beam (bottom), compared to theoretical expectations [10].

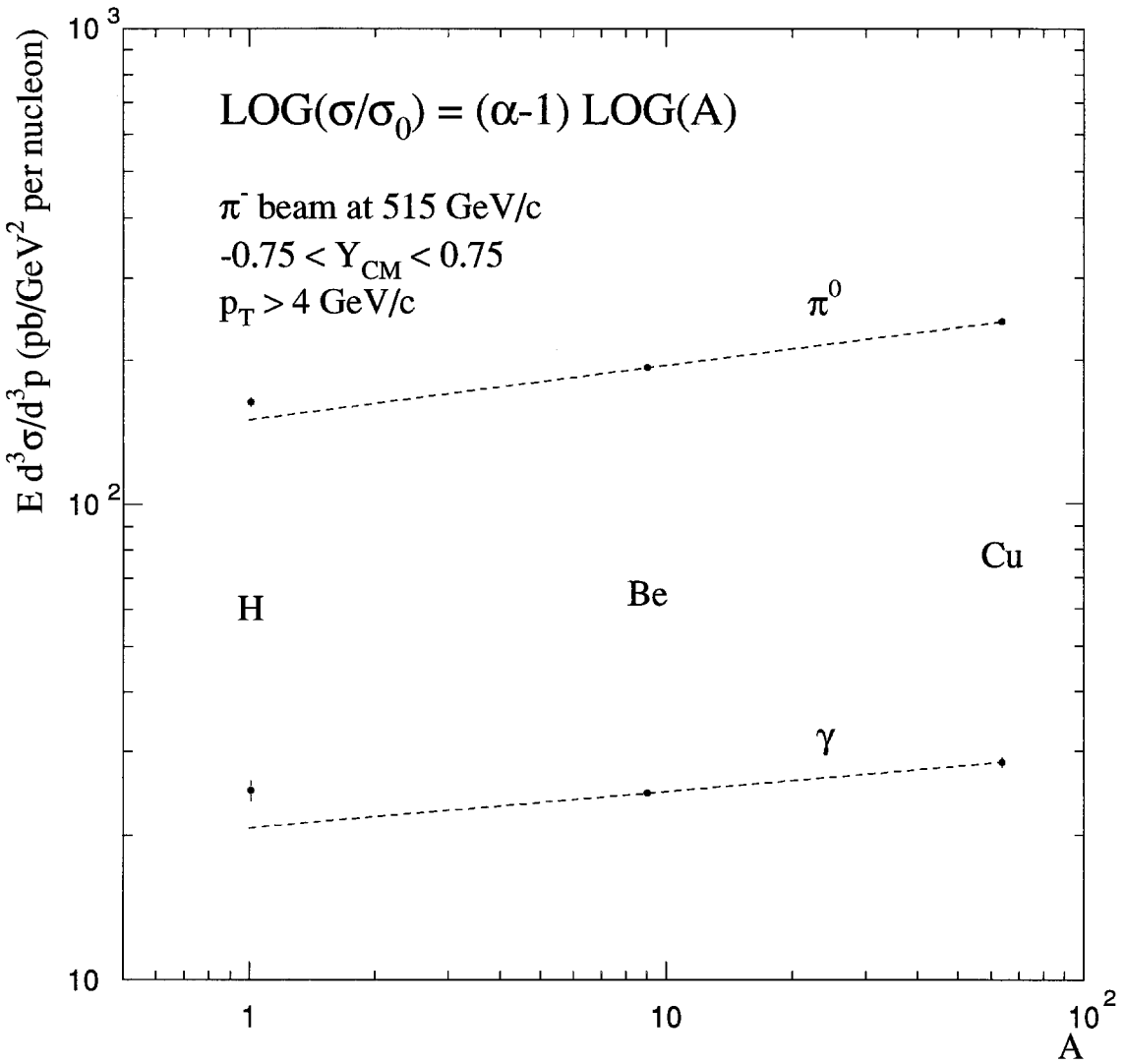

Figure 6.21 The hydrogen-, beryllium-, and copper-target cross sections per nucleon for π^0 and direct-photon production by 515 GeV/c π^- beam averaged over $-0.75 < Y_{CM} < 0.75$ and $p_T > 4$ GeV/c. The dashed lines are fits to the copper and beryllium data; the slope of the line is $\alpha_{Be/Cu} - 1$.

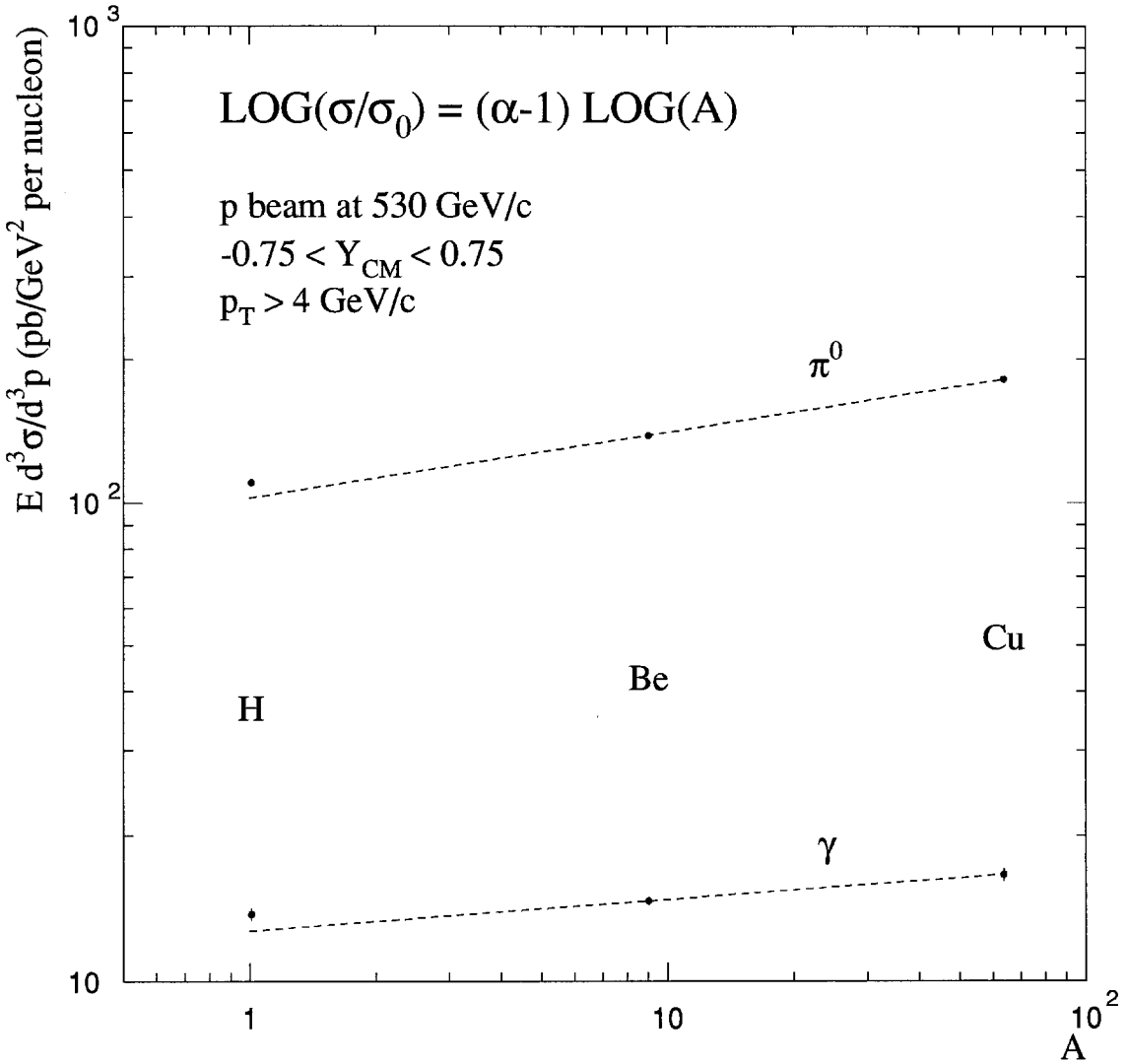

Figure 6.22 The hydrogen-, beryllium-, and copper-target cross sections per nucleon for π^0 and direct-photon production by 530 GeV/c proton beam averaged over $-0.75 < Y_{CM} < 0.75$ and $p_T > 4$ GeV/c. The dashed line are fits to the copper and beryllium data; the slope of the line is $\alpha_{Be/Cu} - 1$.

6.5 Cross Section Comparisons to other Experiments

In Figure 6.23, the π^0 cross section from the 515 GeV/c π^-Be interactions is compared to π^0 production by π^- beams at similar momenta as measured by other experiments. The cross sections are presented *per nucleon* and corrections for the nuclear dependence have been applied to results obtained using nuclear targets. The E706 measurement, which is the highest $\sqrt{s}$ incident π^- beam measurement to date, clearly has exceptional statistical precision and p_T range. Taking all of the data together, a trend toward larger cross sections at larger $\sqrt{s}$ is observed.

Figure 6.24 similarly compares the π^0 cross section from the 530 GeV/c proton beam incident on the beryllium target to measurements published by various other experiments with similar beam momenta. For comparison purposes, the E706 cross section was measured for the range $-0.5 < Y_{CM} < 0.5$. The E706 result was also corrected by a factor of $1/9^{\alpha-1}$ so that direct comparison can be made with the proton-on-proton results. Once again, a larger $\sqrt{s}$ generally corresponds to larger cross sections.

Figures 6.25 and 6.26 display the measured direct photon cross sections as functions of p_T in comparison with direct photon cross sections published by other experiments. The E706 515 GeV/c π^- beam measurement is the highest $\sqrt{s}$ meson-induced direct photon measurement to date. Once again, the E706 data has impressive range in p_T and relatively high statistics. Although these data are integrated over different rapidity intervals, the expected trend toward larger cross sections at higher $\sqrt{s}$ is observed in the direct photon data as well.

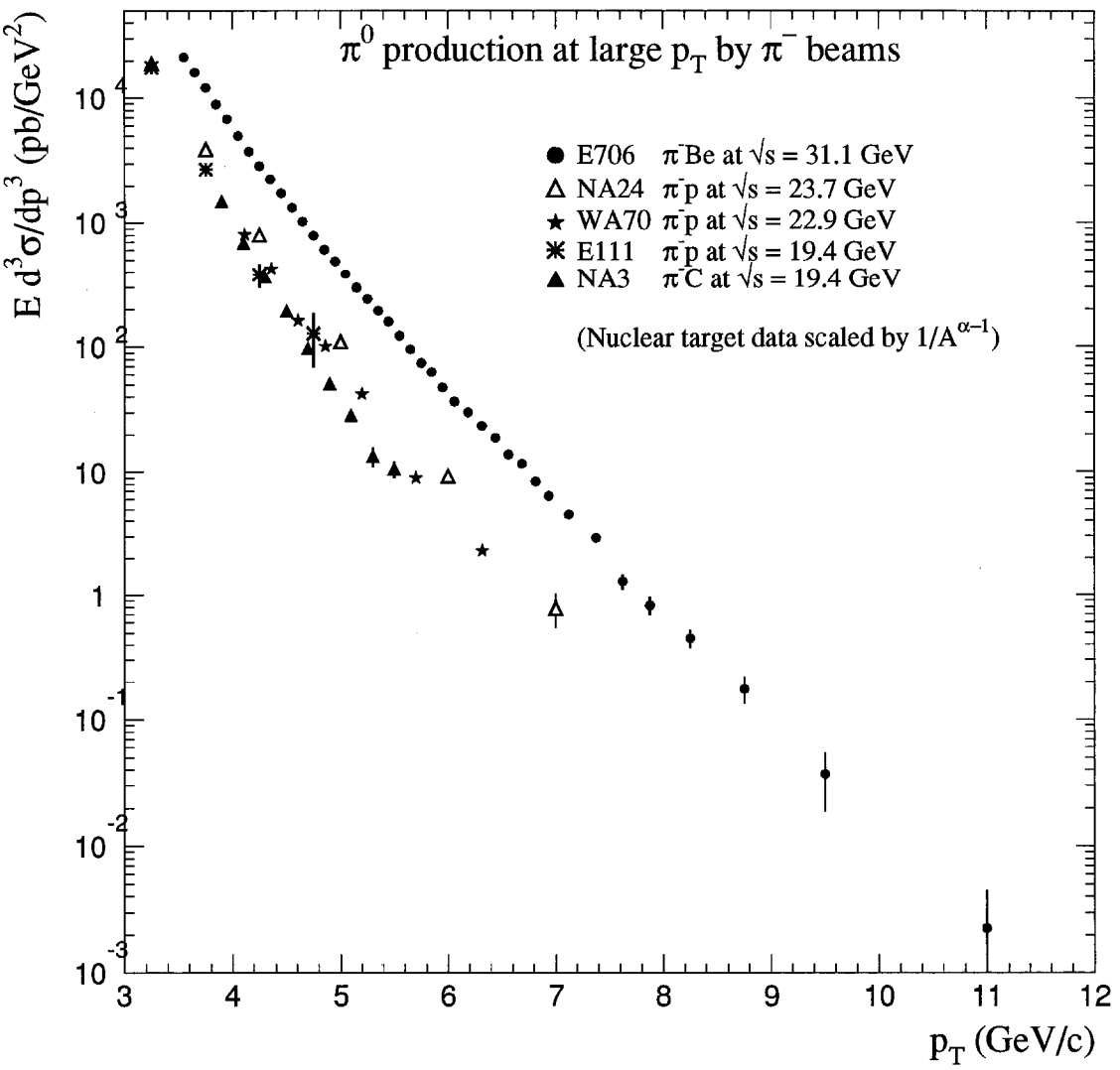

Figure 6.23 π^0 production by π^- beams at various values of $\sqrt{s}$. Cross sections measured by NA24 [36], WA70 [37], E111 [38], and NA3 [39] are compared to the E706 results. The uncertainties shown are statistical only, and nuclear dependence (where applicable) has been taken into account, using the α measured in this analysis.

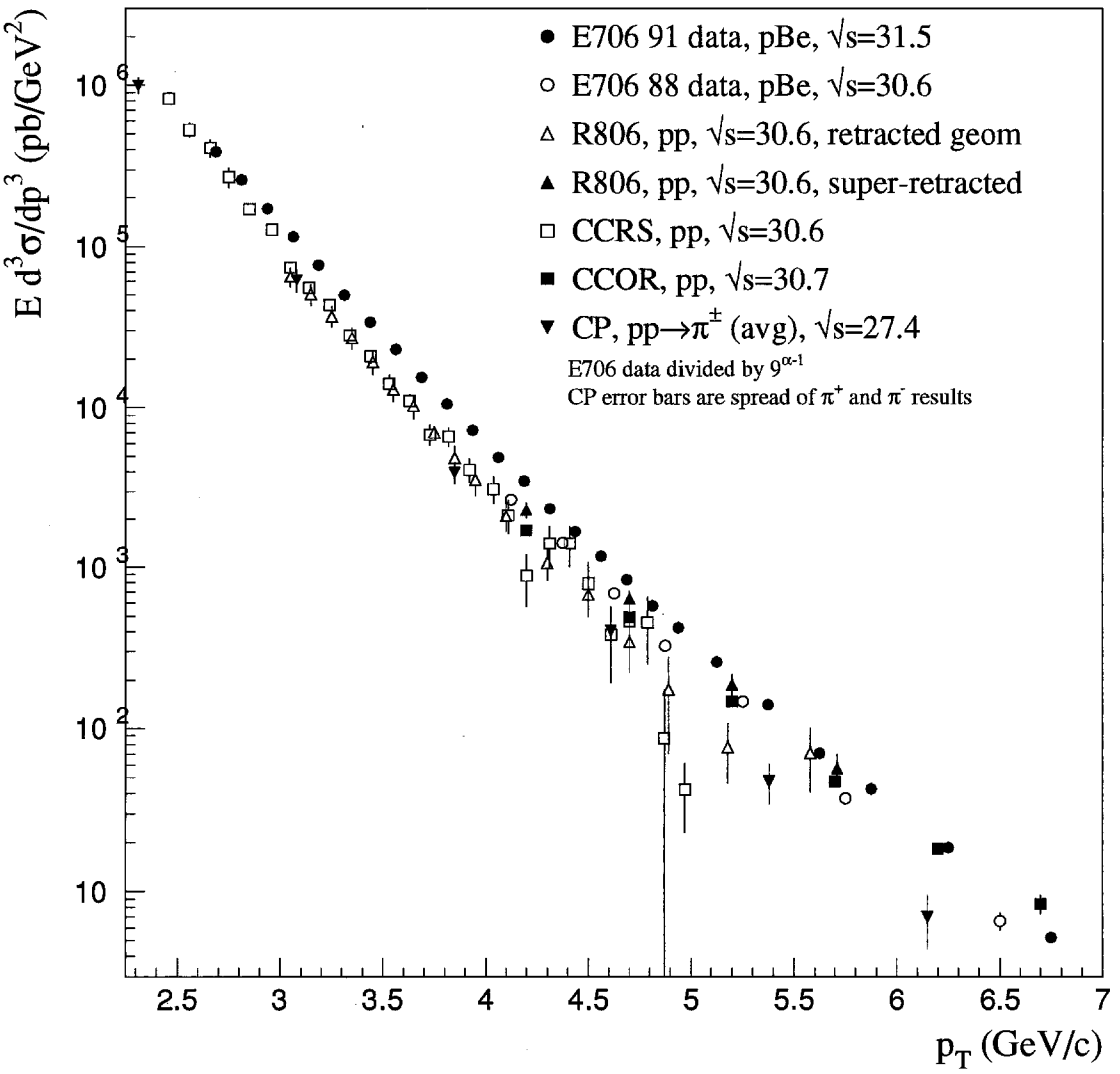

Figure 6.24 Pion production by proton beams at nearby values of $\sqrt{s}$. Cross sections measured by R806 [40], CCRS [41], CCOR [42], and CP [43] are compared to the E706 results. The uncertainties shown are statistical only; in the case of the Chicago-Princeton result, the uncertainties shown are the spread in the $\pi^{\pm}$ results. Nuclear dependence has been taken into account for the E706 data.

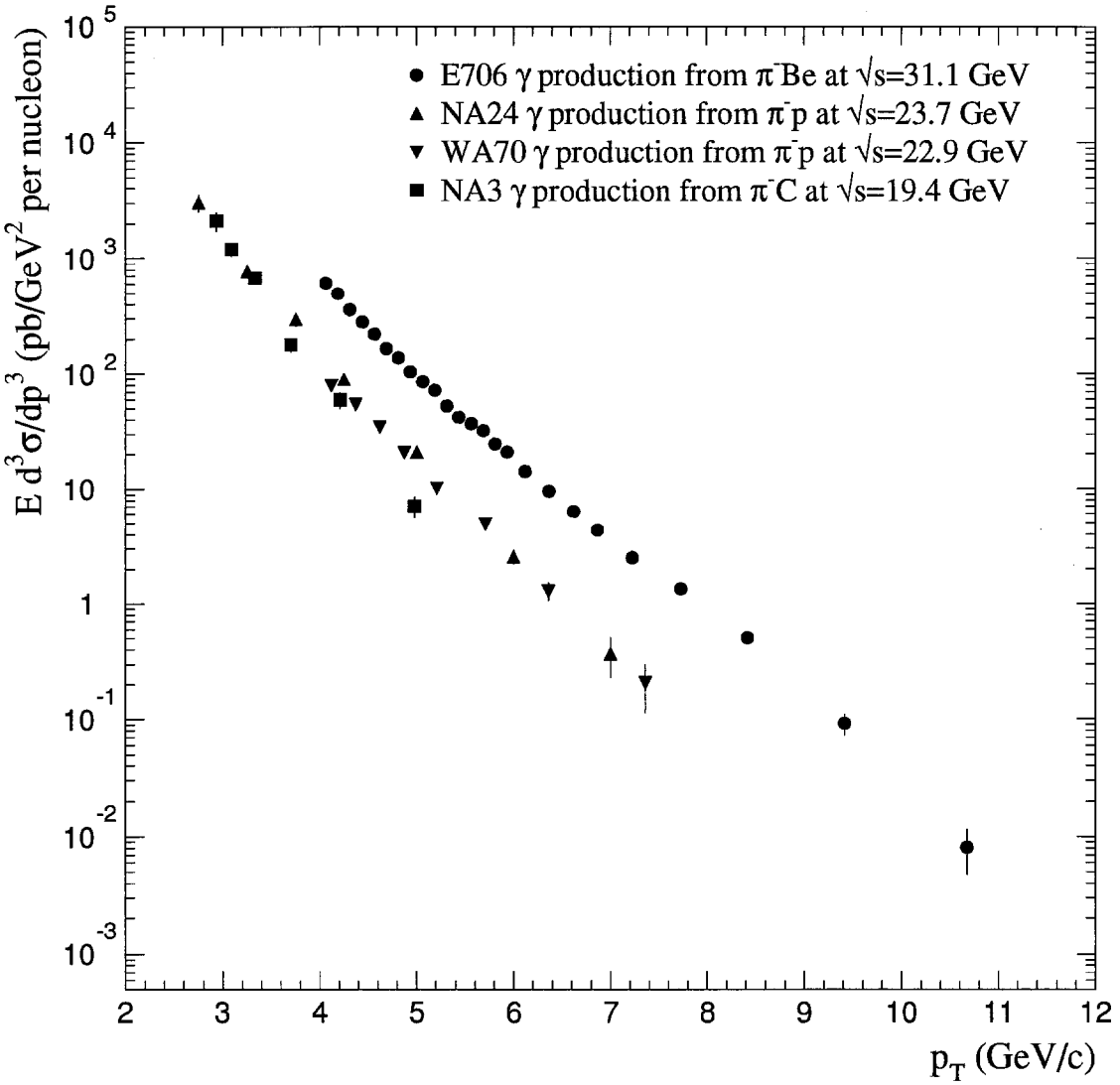

Figure 6.25 Direct-photon production by π^- beams at various values of $\sqrt{s}$. Cross sections measured by NA24 [44], NA3 [45], and WA70 [46] are compared to the E706 results. The uncertainties shown are statistical only, and nuclear dependence (where applicable) has been taken into account, using the α measured in this analysis.

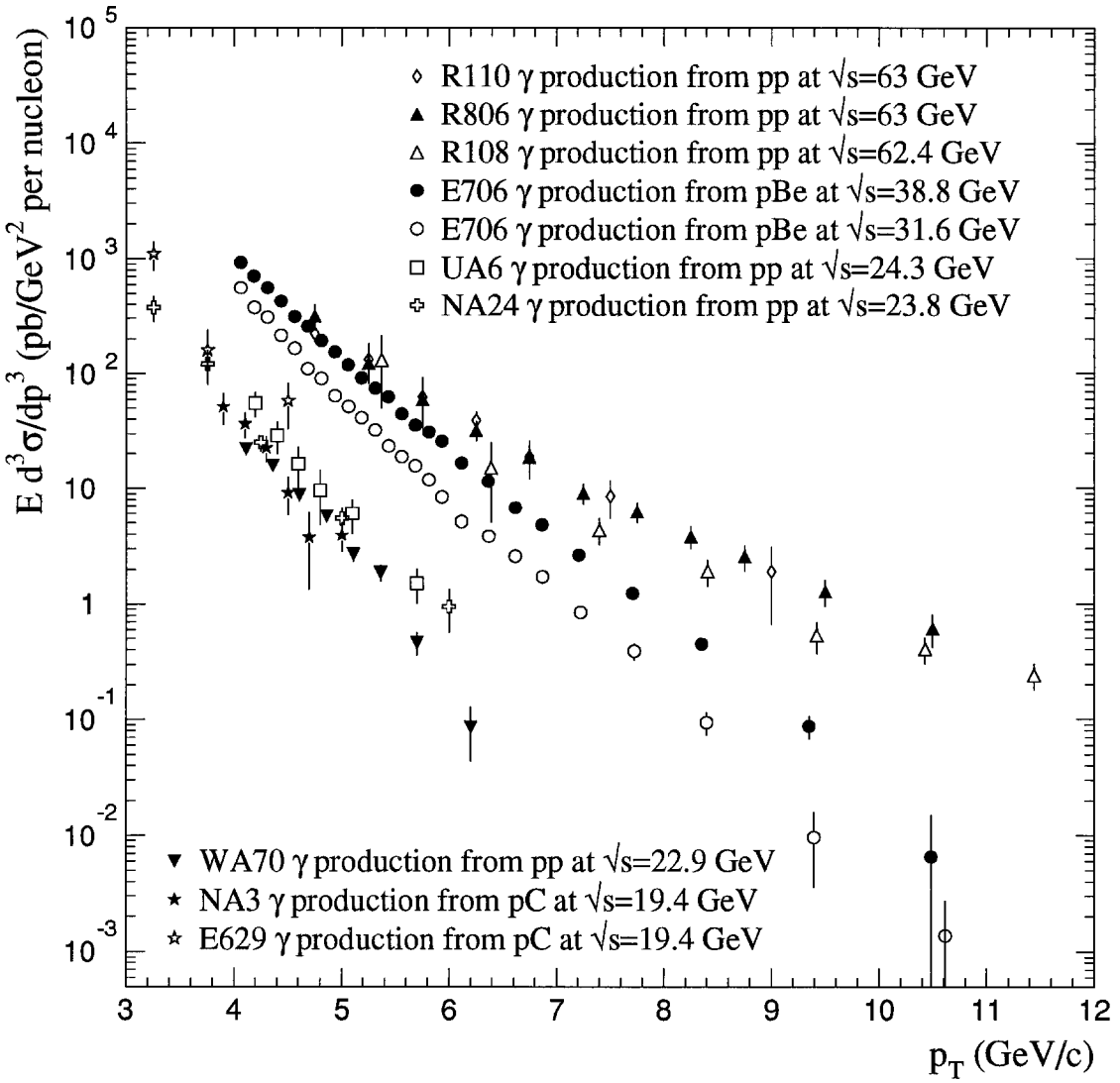

Figure 6.26 Direct-photon production by proton beams at various values of $\sqrt{s}$. Cross sections measured by R110 [47], R806 [48], R108 [49], UA6 [50], NA24 [44], WA70 [51], NA3 [45], and E629 [52] are compared to the E706 results (including preliminary 800 GeV/c results). The uncertainties shown are statistical only, and an adjustment for nuclear dependence (where applicable) has been made.

6.6 Comparison of Cross Sections to NLL QCD Calculations

Next to Leading Log (NLL) calculations have been performed for π^0, η, and direct photon cross sections for comparison to our data. The theoretical calculations for inclusive direct photon cross sections shown in this section were performed using a package developed by Qiu (unpublished) which was based on an earlier package by Aurenche, *et al.* [53]. The meson cross-section calculations were performed using code due to Aversa, *et al.* [54]. For both the direct photon code and the meson code, the QCD calculations model the beryllium target by initiating the hard scatter on a proton $\frac{4}{9}$ of the time and on a neutron $\frac{5}{9}$ of the time. Since this model does not include nuclear effects, the QCD calculations have been adjusted for these effects using the measured results reported in Section 6.4.

Inputs to these calculations include not only the appropriate $\sqrt{s}$ and p_T and Y_{CM} ranges for our data, but also a choice of parton distribution functions (PDF's), renormalization scales (μ_R), factorization scales (m_F), and, for meson production, fragmentation functions (FF's) and fragmentation scales (μ_F). In principle, were the perturbative calculation performed to all orders, the resulting predictions should not depend on the choice of scale. One method of measuring the sensitivity of the predictions to the various inputs is to perform two calculations, holding most inputs constant and using two reasonable choices of scale[2] and computing the fractional difference in the resulting predictions. Figures 6.27 and 6.28 use this method to illustrate the sensitivity of the calculated cross sections to these scales (top two plots) by holding one or two scales constant and varying the other(s) by factors of 2. The bottom plots compare the cross sections obtained

[2] $Q = \mu_R = m_F = \mu_F = p_T$ is typically considered the "natural" scale, although since measurements by many experiments prefer low scales, the choice of $Q = \frac{1}{2}p_T$ is not considered unreasonable.

using several PDF's, namely ABFOW [55], MRSG [56], and CTEQ3M [57]. The dependence of the calculated cross section on the various scales is significant, with smaller scales producing larger cross section expectations. The dependence on choice of PDF is less significant, with typical variations less than 20%; this is not necessarily surprising since the determinations of the various PDF's are based on very similar data sets. Nevertheless, the combined variation in the calculations associated with reasonable choices is quite large; thus, to fully realize the potential of the data to constrain the theory will require additional efforts in reducing the uncertainties associated with the theory and its use.

In spite of significant variations in the calculations due to moderate changes in these inputs, if the scales are constrained to reasonable ranges, the calculations are not in good agreement with the direct photon cross sections. Due to the existence of additional degrees of freedom associated with the choice of fragmentation functions, fragmentation scales, or other fragmentation-related inputs, QCD calculations for meson production can be made to match the data. The discrepancies between the direct photon data and the corresponding calculations can be parametrized using k_T smearing. (k_T is the intrinsic transverse momentum of the scattering partons. By estimating the impact of k_T on the theory, one may be able to account for some of the higher-order effects that NLL QCD theory does not address.) Plots are included which show that good agreement between theory and data can be obtained for both direct photons and π^0's with a choice of relatively small scales, a sensible π^0 fragmentation function, and $k_T \approx 1.4$ GeV/c. (Values of k_T in this range are similar to direct measurements of k_T in our experiment, which yield values in the range between 1.0 and 1.6 [58].)

One variation not addressed by Figure 6.27 concerns the choice of fragmentation function. Figure 6.29 compares two NLL calculations (using ABFOW and

ABFKW [59] PDF's) with the π^0 cross section for incident 515 GeV/c π^- beam. One calculation employs the BKK [60] FF and the other uses the CGGRW [61] FF. It should be noted that the scales $Q \equiv \mu_F = \mu_R = m_F = \frac{1}{2}p_T$ have been chosen, since otherwise the predictions would be significantly ($\approx \times 2$) lower. Given these low scales, the calculated result using the CGGRW fragmentation function matches well with the data. However, the same cannot be said for the π^0 cross section calculations for incident 530 GeV/c protons, as can be seen in Figure 6.30. An even lower scale would have to be used to cause the calculation to match the data.

As in the case of the π^0, the η calculations have a number of fragmentation-related input parameters, and judicious choices among these and the various scales allow one to find a calculation which agrees with the measured cross section. Figures 6.31 and 6.32 compare the η cross sections (for pion and proton beam, respectively) with NLL QCD calculations using $Q = \frac{1}{2}p_T$, ABFOW/ABFKW PDF's, and CGGRW FF's [62] with two choices of the parameter δ. (δ is the cone size used in assigning final state η's to fragmenting partons.) The theory and the data agree quite well, but the multiplicity of adjustable calculational inputs reduces the significance of the agreement.

NLL calculations for direct photon production do not have fragmentation-related input parameters; thus, comparison of calculations with measured direct photon cross sections is a more direct test of the theory. Figure 6.33 demonstrates that even with the both scales set to $\frac{1}{2}p_T$, the NLL prediction for direct-photon production by 515 GeV/c π^- beam on beryllium falls significantly short of the data. A similar discrepancy also occurs in the comparison of the direct photon cross section from the proton beam data and the corresponding theory (see Figure 6.34). Since calculations beyond NLL order are not currently available and

one of the effects of higher-order terms is to give partons transverse momentum (through gluon radiation), one could parametrize the higher-order effects by adding an effective k_T smearing to the NLL calculation. Allowing the colliding partons to have intrinsic transverse momentum (or k_T) for the purposes of the calculation causes the calculated cross section to be increased since the production cross section is steeply falling and thus k_T predominantly smears low-p_T production to higher p_T's. Figure 6.35 (for the π^- data) and Figure 6.36 (for the proton data) demonstrate that with reasonable choices of scales, FF's, and PDF's, along with $k_T \approx 1.4$ GeV/c, the calculations are consistent with the measured π^0 and direct photon cross sections for both beam types.

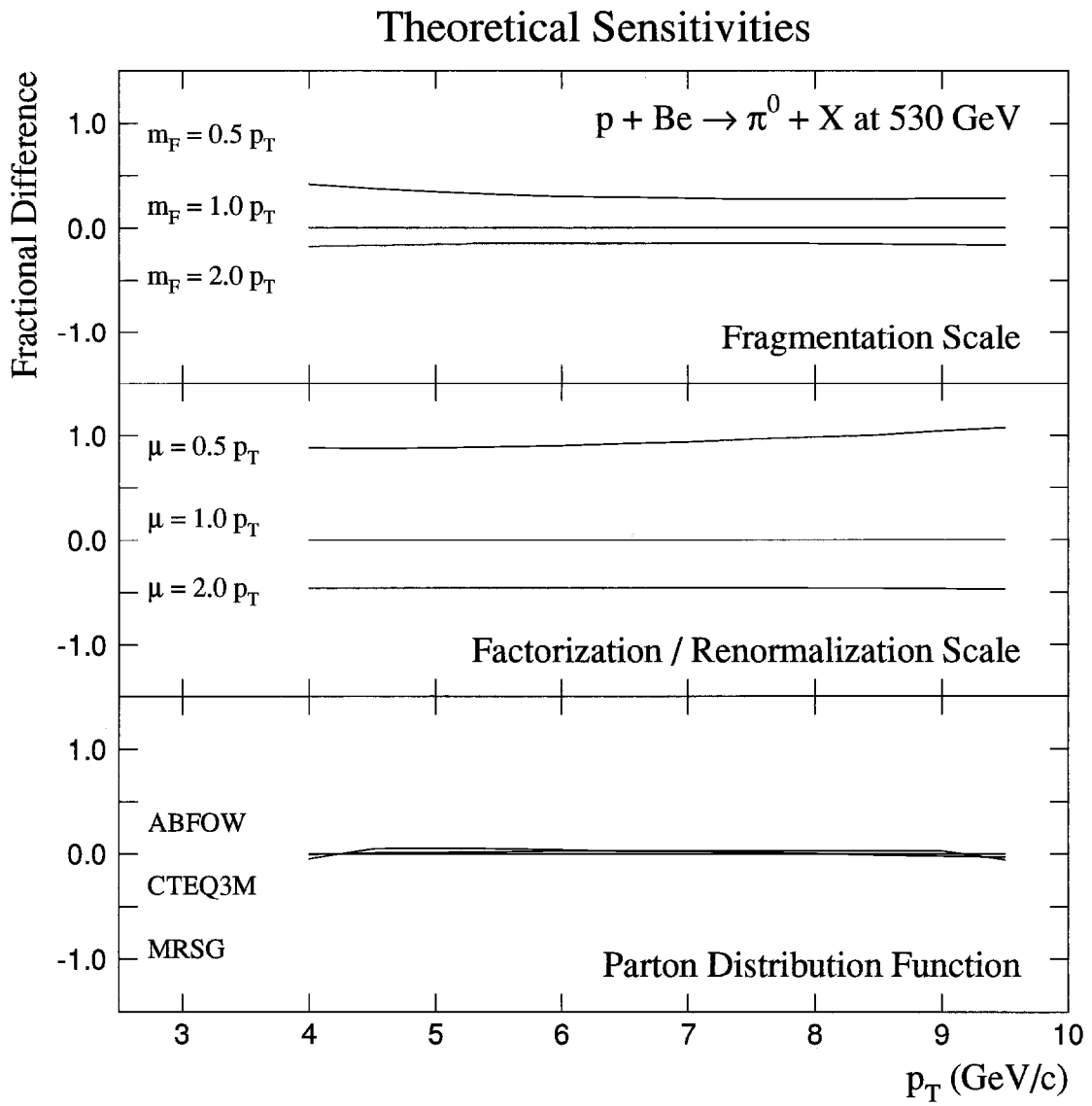

Figure 6.27 The fractional difference between π^0 cross-section calculations, illustrating the calculations' sensitivity to choice of fragmentation scale (top), factorization and renormalization scales (middle), and choices of a few recent PDF's (bottom).

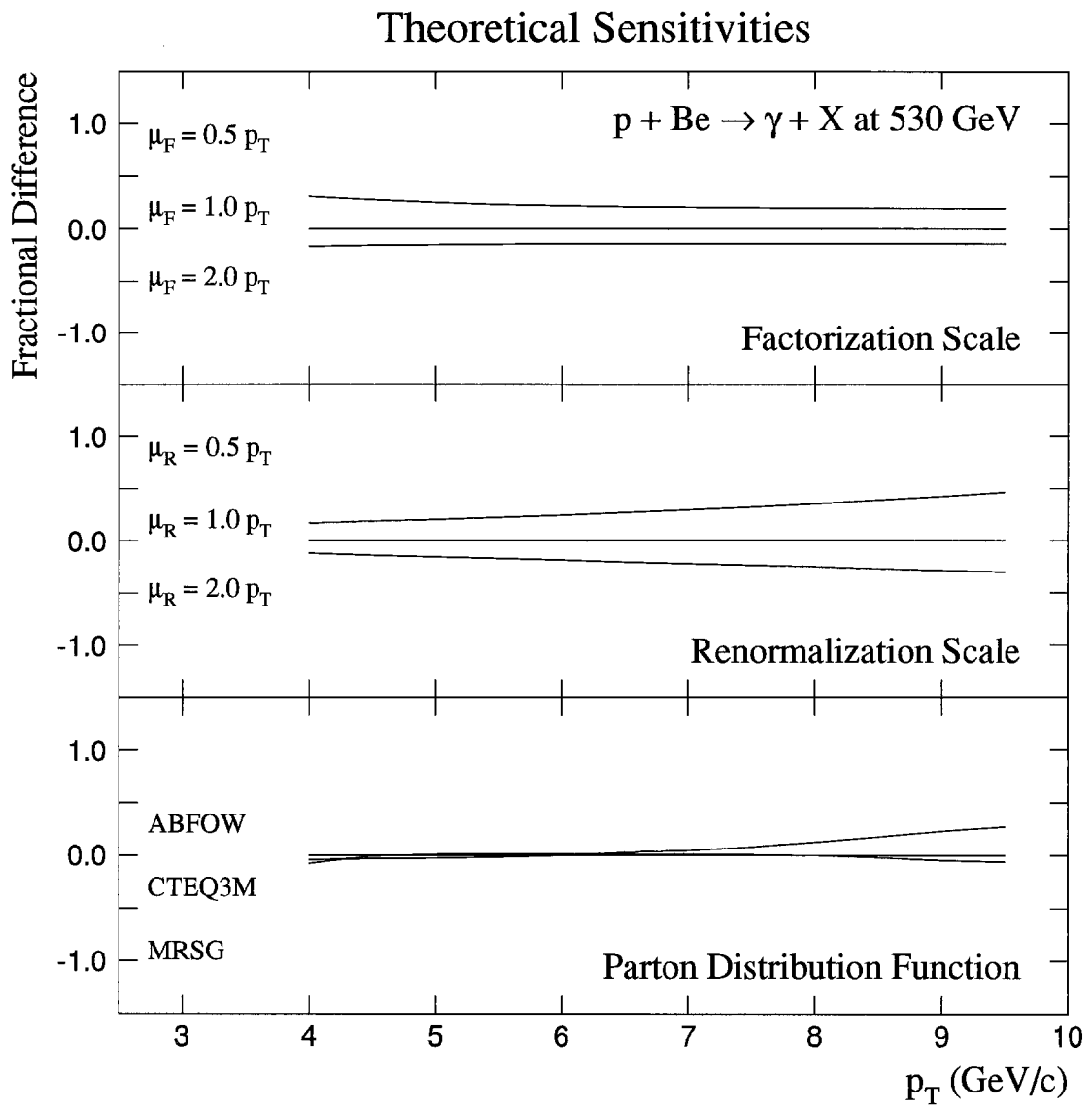

Figure 6.28 The fractional difference between direct photon cross-section calculations, illustrating the calculations' sensitivity to choice of factorization scale (top), renormalization scale (middle), and choices of a few recent PDF's (bottom).

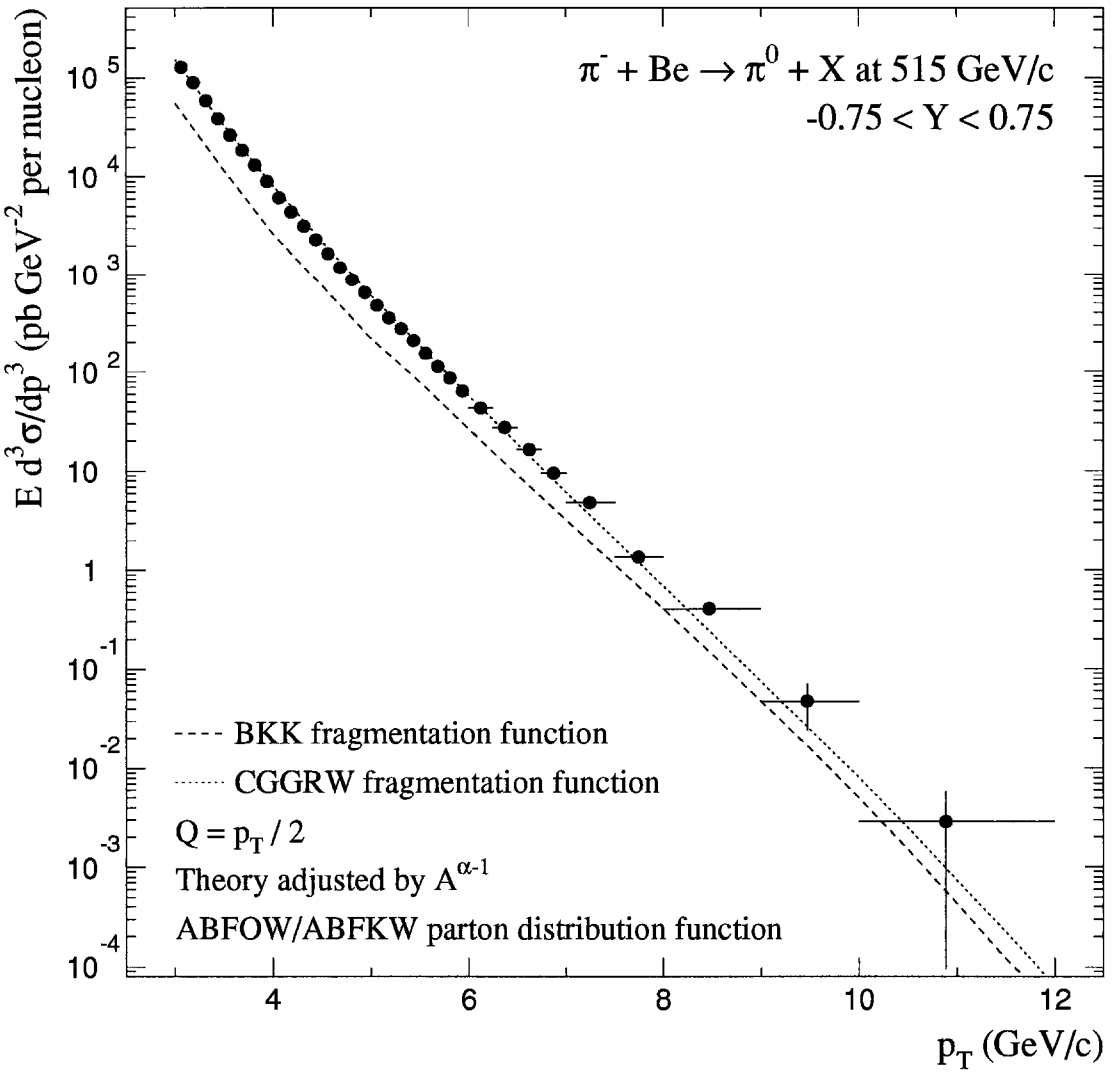

Figure 6.29 Comparison of the invariant π^0 cross section for 515 GeV/c π^- beam on beryllium to calculations employing BKK (dashed) and CGGRW (dotted) fragmentation functions. Both calculations were performed with ABFOW/ABFKW parton distribution functions and with $Q = p_T/2$, and both were corrected for the observed nuclear dependence.

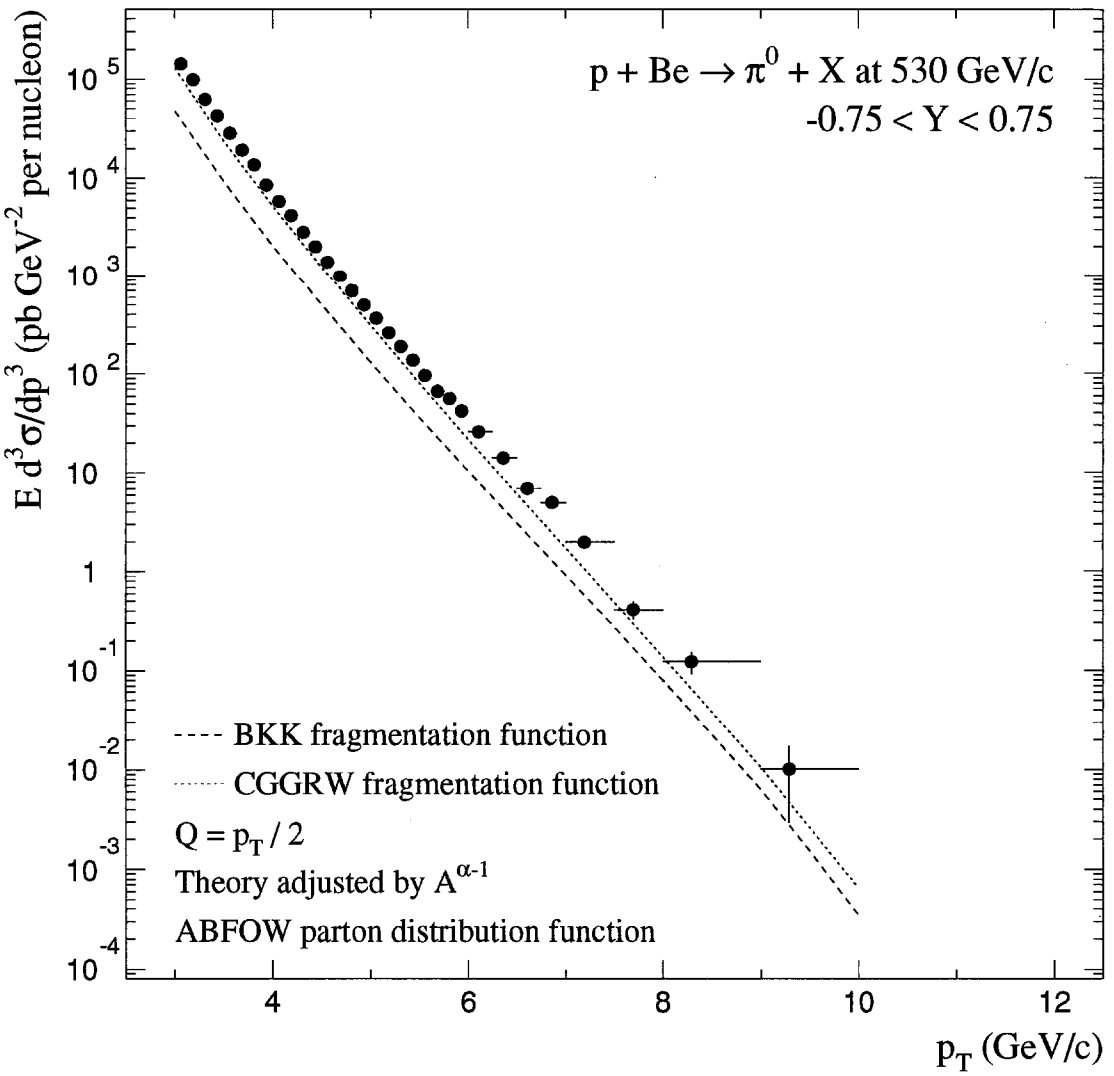

Figure 6.30 Comparison of the invariant π^0 cross section for 530 GeV/c proton beam on beryllium to calculations employing BKK (dashed) and CGGRW (dotted) fragmentation functions. Both calculations were performed with ABFOW parton distribution functions and with $Q = p_T/2$, and both were corrected for the observed nuclear dependence.

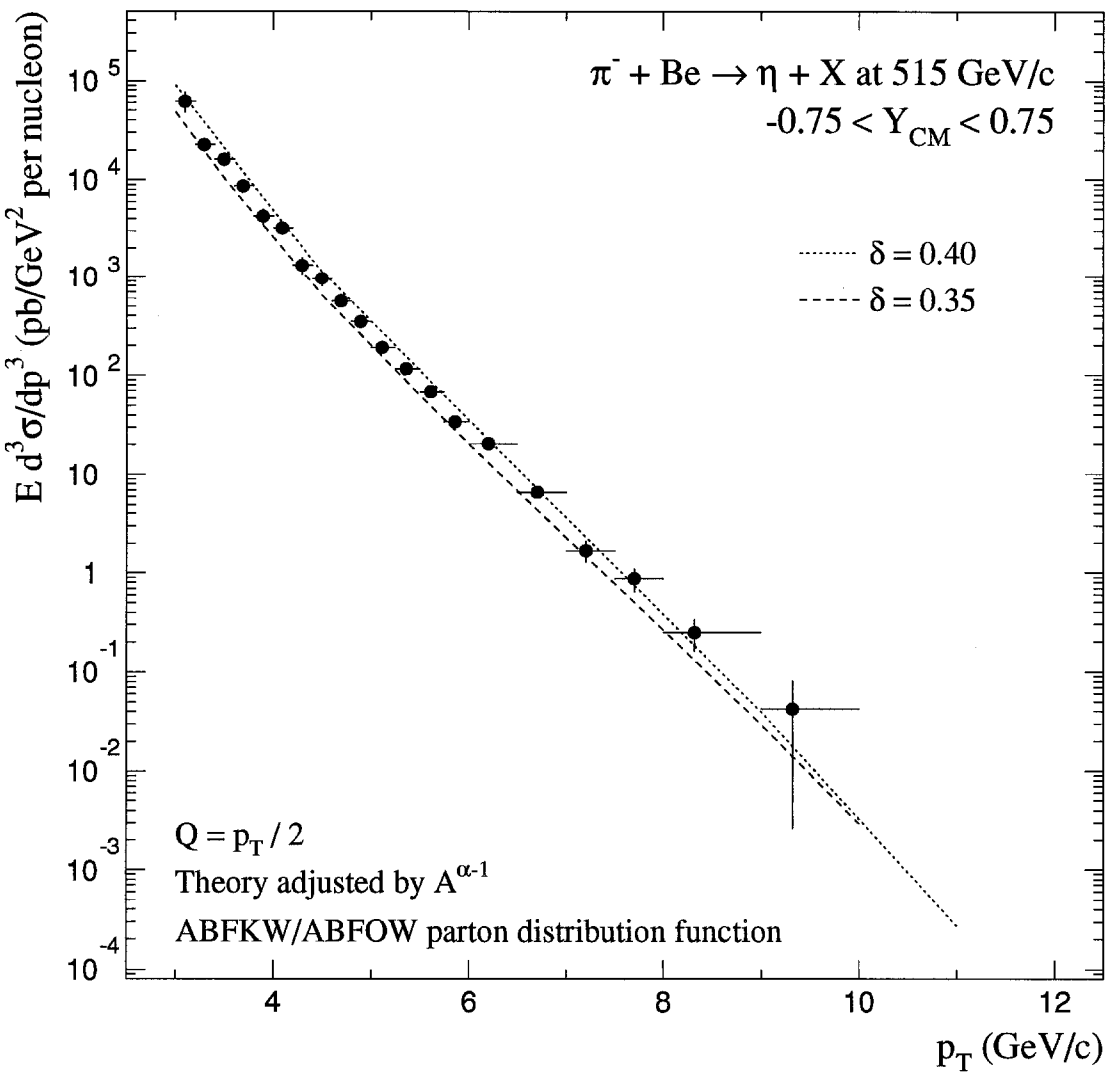

Figure 6.31 QCD calculations with $Q^2 = \frac{1}{2}p_T$ compared to the measured η cross section for 515 GeV/c π^- beam incident on beryllium. The CGGRW [62] fragmentation function depends on the parameter δ, which corresponds to a cone size used in assigning final state η's to fragmenting partons.

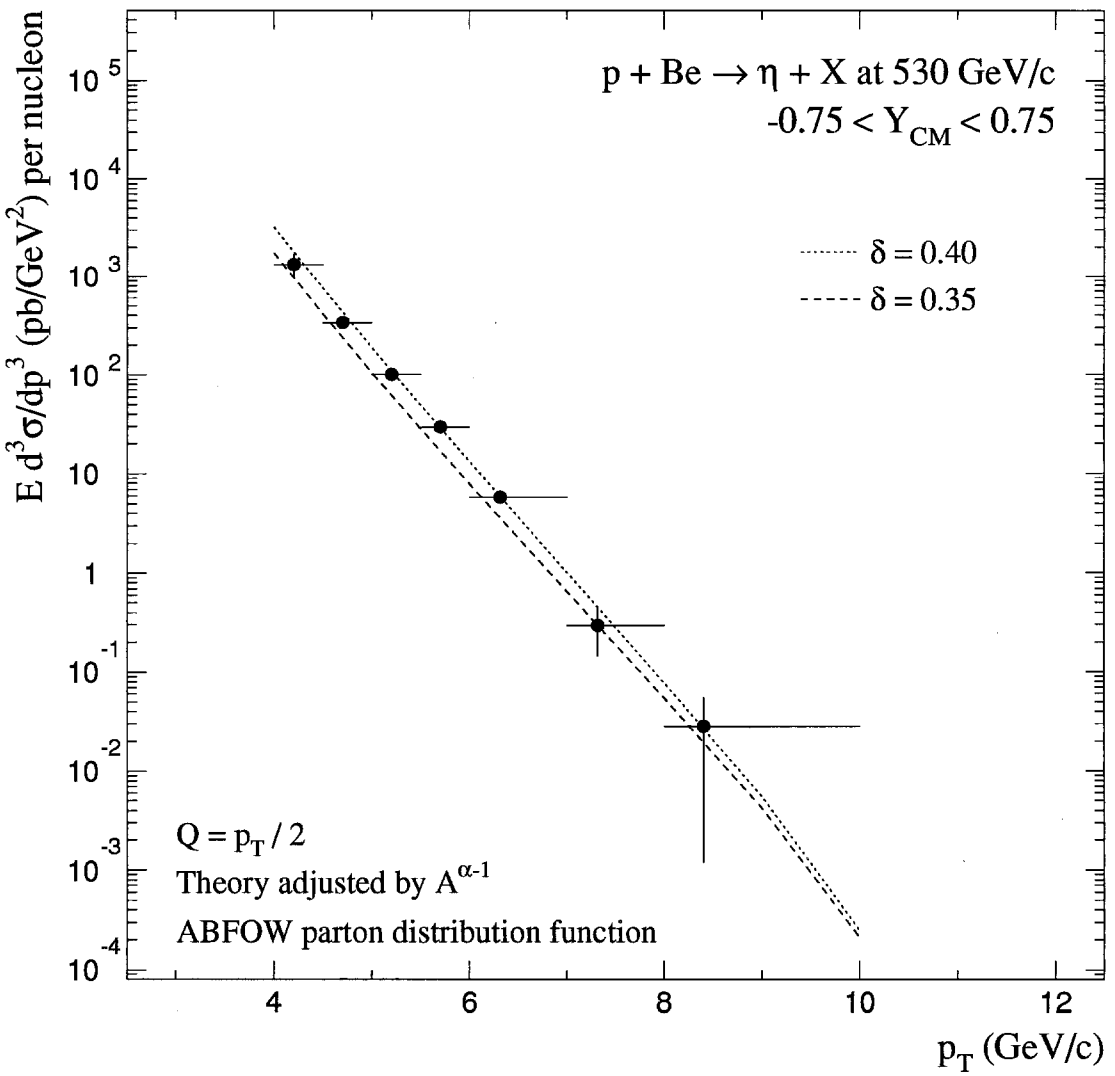

Figure 6.32 QCD calculations with $Q^2 = \frac{1}{2}p_T$ compared to the measured η cross section for 530 GeV/c proton beam incident on beryllium. The CGGRW [62] fragmentation function depends on the parameter δ, which corresponds to a cone size used in assigning final state η's to fragmenting partons.

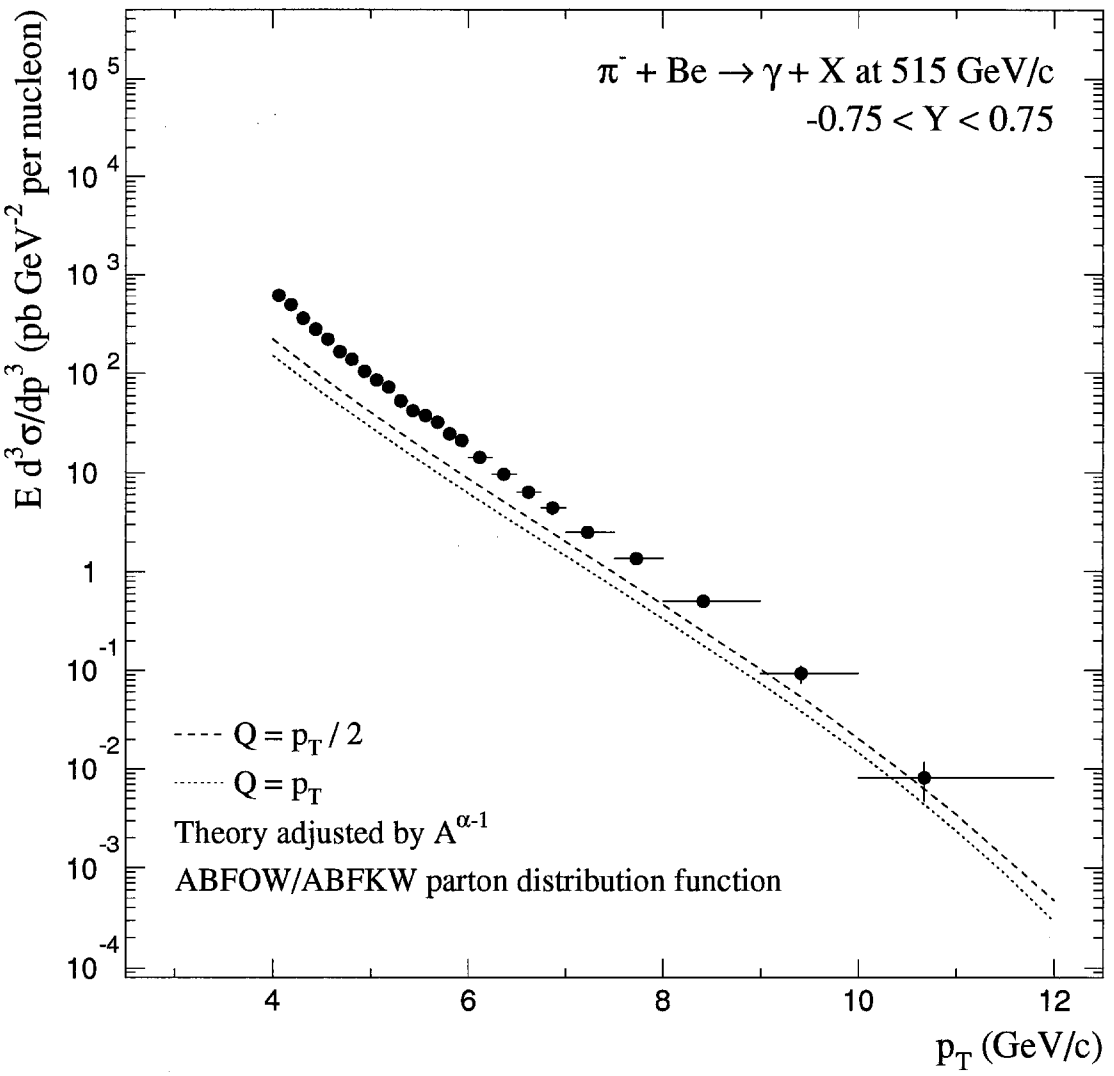

Figure 6.33 Comparison of the invariant direct photon cross section for 515 GeV/c π^- beam on beryllium to calculations employing ABFOW/ABFKW parton distribution functions with $Q = p_T$ (dotted) and $Q = p_T/2$ (dashed).

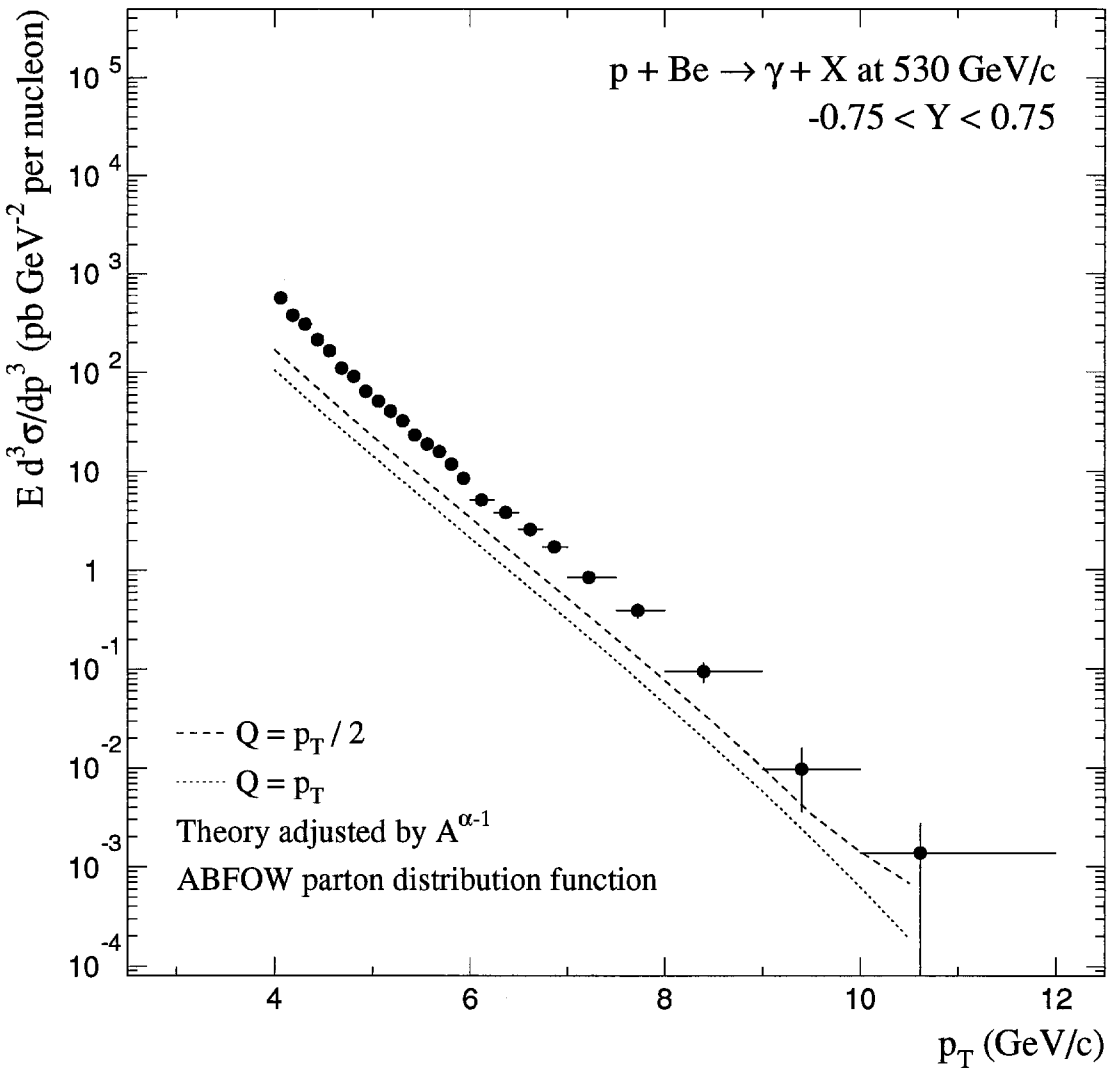

Figure 6.34 Comparison of the invariant direct photon cross section for 530 GeV/c proton beam on beryllium to calculations employing the ABFOW parton distribution function with $Q = p_T$ (dotted) and $Q = p_T/2$ (dashed).

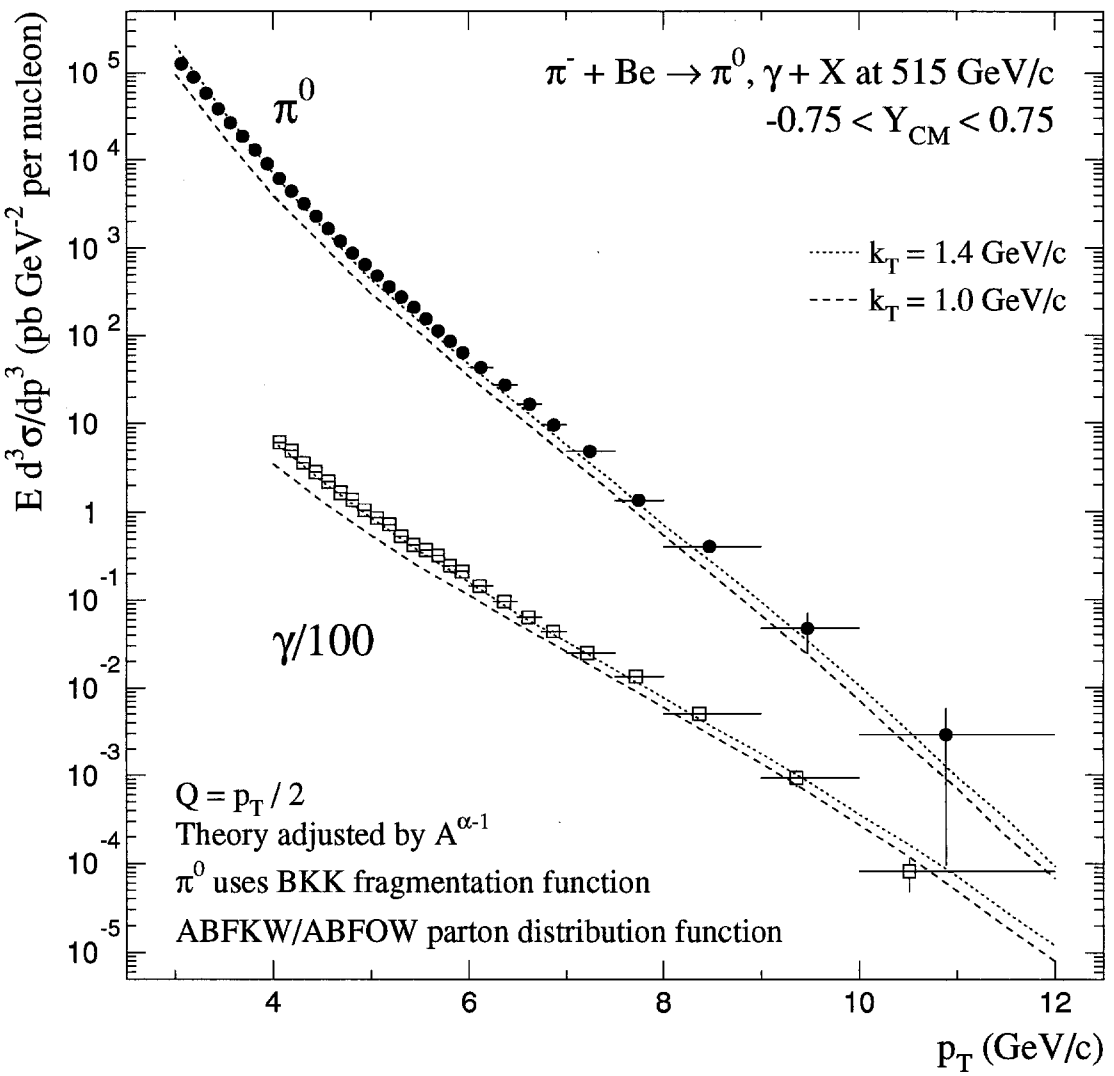

Figure 6.35 The π^0 and direct photon cross sections for 515 GeV/c π^- beam on beryllium compared to calculations which included k_T's of 1.0 (dashed) and 1.4 GeV/c (dotted).

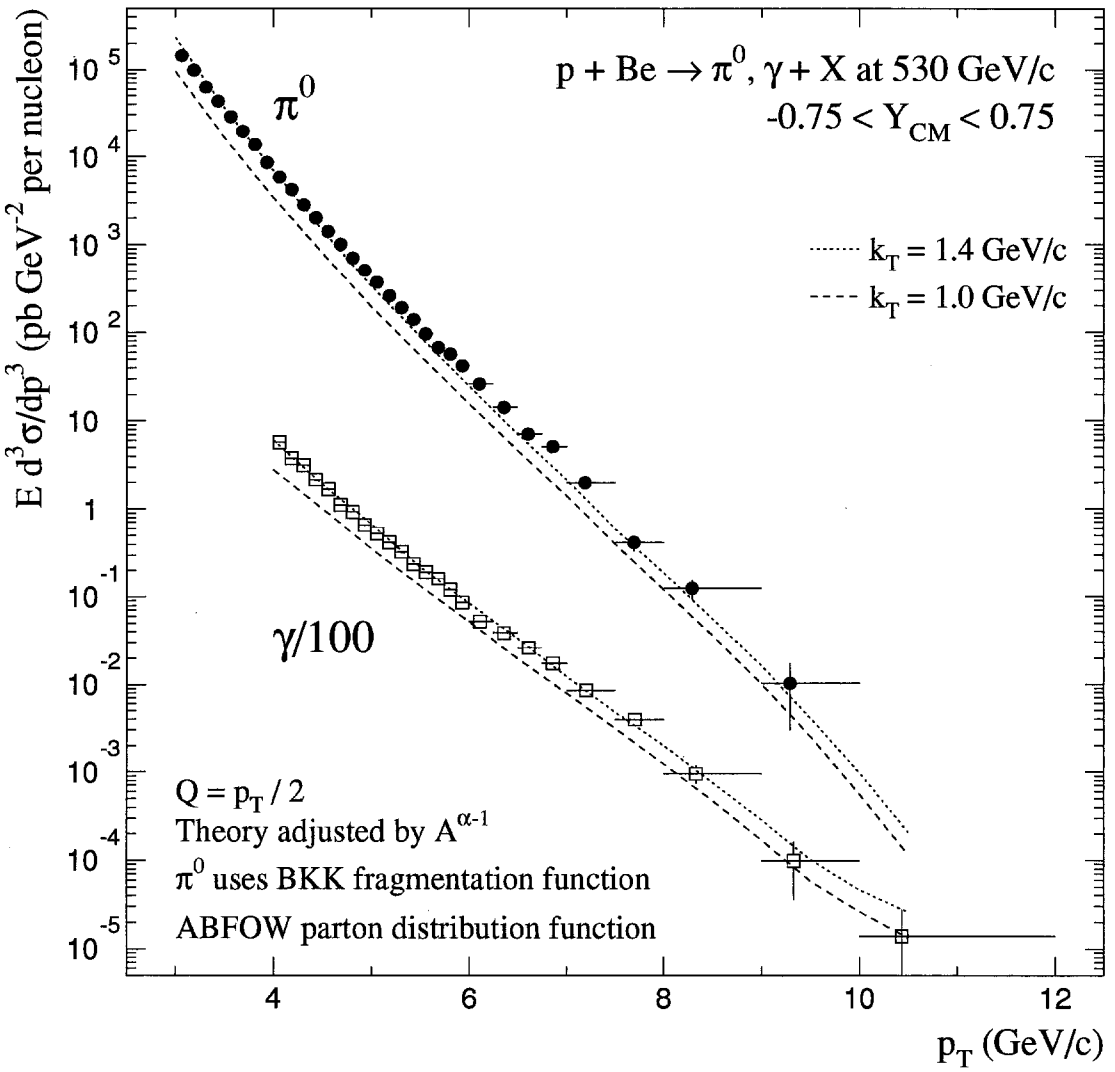

Figure 6.36 The π^0 and direct photon cross sections for 530 GeV/c proton beam on beryllium compared to calculations which included k_T's of 1.0 (dashed) and 1.4 GeV/c (dotted).

6.7 Systematic Uncertainties

As previously stated, the uncertainties shown in all data plots in this thesis reflect statistical uncertainties only. This section contains a discussion of the important sources of systematic uncertainty and provides estimates of their contributions. It should be noted that the various measurements presented in this thesis do not all share the same sensitivity to a given systematic uncertainty. For example, the uncertainty in the normalization contributes directly to the uncertainty in a cross-section measurement, whereas it is frequently insignificant in ratio measurements such as the nuclear dependence.

6.7.1 Uncertainties in the Cross Sections

The largest components of the systematic uncertainty in our cross-section measurements are due to energy scale calibration, normalization, signal definition/background subtraction, reconstruction efficiency, and the trigger. By comparing results of various scalers and cross-checking samples in which the normalizations are calculated independently, the uncertainty in the normalization procedure is conservatively estimated to be $\pm 10\%$. The systematic uncertainty due to uncertainties in the calibration of the energy response depends on p_T: for neutral meson cross sections the associated contribution is $\approx \pm 6\%$ for p_T's around 4 GeV/c and $\approx \pm 9\%$ for p_T's around 8 GeV/c, whereas for the direct photons, the contribution is $\approx \pm 5\%$ for p_T's around 4 GeV/c and $\approx \pm 7\%$ for p_T's around 8 GeV/c. The uncertainty associated with the reconstruction efficiency (which includes the unsmearing function) is $\approx \pm 11\%$ for the π^0 and direct photon cross sections and $\approx \pm 15\%$ for the η. Uncertainties due to the trigger map add an additional $\approx \pm 5\%$ uncertainty for the π^0 and direct photon cross sections at low p_T's; the η, due to the wider average separation of its photons, has a local-trigger-related uncertainty

Cross Section	$p_T \approx 4$ GeV/c	$p_T \approx 8$ GeV/c
γ	23%	21%
π^0	18%	18%
η	22%	21%

Table 6.2 Combined systematic uncertainty contributions (added in quadrature) for the direct photon, π^0, and η inclusive cross sections.

of $\approx$10% at low p_T. For direct photon cross-section measurements, the uncertainty in the γ/π background contributes uncertainties of order $\approx \pm 15\%$ for p_T's around 4 GeV/c and $\approx \pm 10\%$for p_T's around 8 GeV/c. Sideband subtraction in the π^0 and η cross sections is relatively robust except in regions of extremely low statistics; the associated systematic uncertainty is estimated to be $\approx \pm 3\%$.

There are several sources which contribute somewhat smaller systematic uncertainties (up to $\approx$3%). These include the systematics associated with the corrections for the muon cuts, beam absorption, acceptance, photon conversions, transverse target acceptance, and vertex reconstruction efficiency. In addition, the Monte-Carlo-to-data surfaces, the vertex resolution (i.e. target material definition), and the existence of minority particles in the beam contribute systematics of this order.

Table 6.2 shows the approximate size and p_T-dependence of the systematic uncertainty in the direct photon, π^0, and η inclusive cross sections. The systematics do not differ significantly between 1990 and 1991 or between π^- and proton data.

6.7.2 Uncertainties in Various Cross-Section Ratios

The largest of the systematic uncertainties in the cross sections, namely energy scale and normalization uncertainties, are generally negligible in measurements based on ratios, such as the nuclear dependence, the η/π^0, and the beam dependence measurements. Systematics associated with these measurements are therefore dominated by the largest uncertainties which are not equal in the numerator and the denominator.

For the measurement of the nuclear dependence, the systematic uncertainty in the measurement of $\alpha_{\mathrm{Be/Cu}}$ is estimated to be $\approx \pm 2\%$. This uncertainty is dominated by contributions from the longitudinal target definitions and associated corrections for the tails and the longitudinal dependence of the vertex-finding efficiency and background. The longitudinal dependence of beam absorption and photon conversion corrections, target material specifications, and the transverse target fiducial cut and correction all contribute less significantly to the systematics of this measurement. It should be noted that since the largest contributors to the systematics of this measurement effect the mesons and the direct photons in the same way, the difference between the α's measured for mesons and direct photons has somewhat less uncertainty, of order 0.01.

Since the hydrogen target is the least dense of the three targets employed in this experiment, vertex-related backgrounds are likely to affect the hydrogen cross-section measurement more than the others. For this reason, the systematic uncertainty on the hydrogen measurement relative to the projection from the $\alpha_{\mathrm{Be/Cu}}$ is approximately 5%. Projection errors due to uncertainty in the beryllium-copper fit comprise an additional 2% for the π^0 comparison and 4% for the direct photon comparison.

The systematic uncertainty associated with the η/π^0 measurement is estimated to be $\pm 10\%$. This number is dominated by uncertainties associated with the trigger and the reconstruction efficiency.

Since the normalization and energy scale of the two samples used to measure the beam dependence are not identical, there is no exact cancellation of uncertainties in a ratio of cross sections from different beams. However, since the methods used for the analyses were the same in both cases, some of the uncertainties are correlated between the two samples; thus, this measurement is assigned a systematic uncertainty of $\approx 15\%$.

6.8 Conclusions

This thesis presents the results of studies of high-p_T π^0, η, and direct photon production by 515 GeV/c π^- and 530 GeV/c proton beams incident on hydrogen, beryllium, and copper targets. The inclusive cross sections were measured for p_T's above 3.0 GeV/c in the center-of-mass rapidity interval $-0.75 < Y_{CM} < 0.75$. These data were collected by experiment E706 at Fermilab, a second-generation direct photon experiment which used a finely-segmented lead–liquid argon electromagnetic calorimeter for detection of photons and a precision tracking system for the detection of charged particles.

The ratio of η to π^0 production (for meson p_T's greater than 3.5 GeV/c) was measured to be $0.48 \pm 0.01 \pm 0.05$ and $0.44 \pm 0.01 \pm 0.05$ for the π^- and p beams, respectively, incident on the beryllium target. These findings are consistent with similar measurements performed by other experiments. The ratio of cross sections produced by the proton and negative pion beams were also presented for π^0 and direct photon production. The trends versus p_T are consistent with expectations from simple arguments based on leading-order parton-interaction diagrams.

The nuclear dependences of the measured cross sections were parametrized in the form A^{α}. E706 is the first experiment capable of measuring the nuclear dependence of direct photon production. This measurement provides unique insights into the mechanisms responsible for the nuclear enhancement of high-p_T particle production. α was measured using the beryllium and copper data for high-p_T η, π^0, and direct photon production by both the proton and the negative pion beams. For direct photons, the average α for $p_T >$ 4.0 GeV/c was measured to be $1.06 \pm 0.01 \pm 0.02$ for the π^- beam and $1.07 \pm 0.01 \pm 0.02$ for the proton beam. The α measurements for the π^0 and η meson production by both beams were quite similar to each other; the average for $p_T >$ 4.0 GeV/c was $\approx 1.13 \pm 0.02$(systematic). These measurements indicate approximately twice the nuclear enhancement in meson production as in direct-photon production, an observation which is consistent with the multiple-scattering model of nuclear dependence. Using the beryllium and copper data, a simple extrapolation to the hydrogen cross section was made. This extrapolation did not take into account differences in Z/A ratios or modifications of the nucleon parton distribution functions due to the interactions among the nucleons within a nucleus. The measured hydrogen cross sections are within $\approx$10% of these extrapolated values.

NLL QCD calculations were compared to the measured π^0, η, and direct photon cross sections. The calculations are quite sensitive to choice of scales and, in the case of the mesons, choice of fragmentation-related parameters. By making full use of the flexibility in the calculations due to variations in the inputs, one can tune the NLL QCD calculations for neutral mesons to the measured neutral meson cross sections using scales of order $\frac{1}{2}p_T$. The direct photon calculations have fewer tunable inputs, and thus comparisons with direct photon cross sections are more significant probes of the status of these NLL QCD calculations. The measured direct photon cross sections are poorly matched by the corresponding

NLL QCD calculations even with scales significantly lower than $\frac{1}{2}p_T$, indicating the need for further theoretical efforts in the evaluation of direct photon production, perhaps incorporating higher-order terms in the calculations. The effect of these higher-order terms may be roughly parametrized through the introduction of a k_T smearing; using $k_T \approx 1.4$ GeV/c and scales of order $\frac{1}{2}p_T$ results in agreement between the calculation (with the k_T enhancement) and our measured inclusive π^0 and direct photon cross sections for incident π^- and proton beams at 0.5 TeV/c.

References

[1] G. Alverson *et al.*, Direct Photon Production at High p_T in π^-Be and pBe collisions at 500 GeV/c, Phys. Rev. Lett. **68**, 2584 (1992).

[2] G. Alverson *et al.*, Production of π^0 mesons at high p_T in π^-Be and pBe collisions at 500 GeV/c, Phys. Rev. D **45**, 3899 (1992).

[3] G. Alverson *et al.*, Production of direct photons and neutral mesons at large transverse momenta by π^- and p beams at 500 GeV/c, Phys. Rev. D **48**, 5 (1993).

[4] G. Alverson *et al.*, Structure of the recoiling system in direct–photon and π^0 production by π^- and p beams at 500 GeV/c, Phys. Rev. D **49**, 3106 (1994).

[5] Particle Data Group, Review of Particle Properties, Phys. Rev. D **54**, (1996).

[6] J. F. Owens, Rev. Mod. Phys. **59**, 465 (1987).

[7] D. Striley, Large Transverse Momentum π^0 Meson Production by 0.5 TeV/c p, π^+, and K^+ Incident on Beryllium, Ph.D. thesis, University of Missouri at Columbia, 1996.

[8] J. W. Cronin *et al.*, Phys. Rev. D **11**, 3105 (1975).

[9] H. Frisch *et al.*, Phys. Rev. D **27**, 1001 (1983).

[10] X. Guo and J. Qiu, Nuclear dependence in direct photon production, Phys. Rev. D **53**, 6144 (1996).

[11] P. Aurenche and M. Whalley, RAL-89-106 preprint, 1989.

[12] P. D. D. S. Weerasundara, A Study of Large Transverse Momentum Direct Photon plus Away-Side Jet Production using 500 GeV/c proton and π^- Beams Incident on a Beryllium Target, Ph.D. thesis, University of Pittsburgh, 1993.

[13] W. Chung, A Study of the Event Structure in High P_t Direct Photon and π^0 Production by 515 GeV/c π^- and 800 GeV/c Proton Beams Incident on Nuclear Targets, Ph.D. thesis, University of Pittsburgh, 1995.

[14] E. Engels *et al.*, A Silicon Microstrip Vertex Detector for Direct Photon Physics, Nucl. Instrum. Meth. **A253**, 523 (1987).

[15] E. Engels *et al.*, Performance Characteristics and Radiation Damage Results from the Fermilab E706 Silicon Microstrip Detector System, Nucl. Instrum. Meth. **A279**, 272 (1989).

[16] K. Hartman, Hadronic Production of π^0 Pairs and Associated Event Structure at 530 GeV, Ph.D. thesis, Pennsylvania State University, 1990.

[17] C. Bromberg *et al.*, Design and operation of large straw–tube drift chamber planes, Nucl. Instrum. Meth. **A307**, 292 (1991).

[18] D. Skow, A Study of High Momentum Eta Meson Production, Ph.D. thesis, University of Rochester, 1990.

[19] G. Drake *et al.*, CDF Front End Electronics: The Rabbit System, Nucl. Instrum. Meth. **A269**, 68 (1988).

[20] L. Sorrell, Measurement of the Nuclear Dependence of Direct Photon and Neutral Meson Production at High Transverse Momentum by Negative 515 GeV/c Pions Incident on Beryllium and Copper Targets, Ph.D. thesis, Michigan State University, 1995.

[21] L. Sorrell, The E706 Trigger System, E706 Note 201.

[22] R. Roser, Eta Production at High Transverse Momentum by Negative 520 GeV/c Pions Incident on Beryllium and Copper Targets, Ph.D. thesis, University of Rochester, 1994.

[23] *VAXONLINE Users Guide*, FNAL Computer Department, Fermilab, Batavia, Ill., pN-252.

[24] C. Lirakis, E706 Data Acquisition System, Proceedings of the First Annual Conference on Electronics for Future Colliders, LeCroy Corporation, 1991.

[25] N. Varelas, π^0 Production at High Transverse Momenta from π^- Collisions at 520 GeV/c on Be and Cu Targets, Ph.D. thesis, University of Rochester, 1994.

[26] R. Benson, Characteristics of Forward Energy Production in Proton-Nucleus and Pion-Nucleus Collisions at 530 GeV/c, Ph.D. thesis, University of Minnesota, 1989.

[27] P. Chang, Massive $\pi^0\pi^0$,$\pi^0\pi^-$ and $\pi^0\pi^+$ Production from 515 GeV/c π^- Collisions with Beryllium and Copper Targets, Ph.D. thesis, Northeastern University, 1994.

[28] S. Blusk, Measurement of the Production Cross Section of Charm Mesons at High Transverse Momentum in 515 GeV/c π^--Nucleon Collisions, Ph.D. thesis, University of Pittsburgh, 1995.

[29] M. Begel, Ph.D. thesis, University of Rochester, 1996.

[30] N. Varelas, Calibration of the Fermilab E706 Liquid Argon Electromagnetic Calorimeter, Nucl. Phys. B. (Proc. Suppl.) **44**, 153 (1995).

[31] L. de Barbaro *et al.*, Calibration and Performance of E706 Liquid Argon Electromagnetic Calorimeter, to be submitted to Nucl. Instrum. Meth. , (in preparation).

[32] G. Marchesini *et al.*, *HERWIG Reference Manual*, v5.7 ed.

[33] F. Carminati, *GEANT, Detector Description and Simulation Tool*, 1993.

[34] G. Osborne, A Measurement of the Muon Content of the 1991 MWest Beam, E706 Note 197.

[35] J. Kuehler, An Analysis of π^0 Mesons Produced in Minimum Bias 515 GeV/c π^- Nuclear Collisions, Ph.D. thesis, University of Oklahoma, 1995.

[36] C. D. Marzo *et al.*, Measurement of π^0 production at large transverse momentum in pi$^-$p, pi$^+$p, and pp collisions at 300 GeV/c, Phys. Rev. D **36**, 16 (1987).

[37] M. Bonesini *et al.*, High transverse momentum π^0 production by π^- and π^+ on protons at 280 GeV/c, Z. Phys. **C42**, 527 (1989).

[38] G. Donaldson *et al.*, Inclusive π^0 production at large transverse momentum from $\pi^\pm$p and pp interactions at 100-GeV/c and 200-GeV/c, Phys. Rev. Lett. **36**, 1110 (1976).

[39] J. Badier *et al.*, Inclusive high p_T π^0 production from $\pi^\pm$ and protons at 200 GeV/c, Z. Phys. **C30**, 45 (1986).

[40] C. Kourkoumelis *et al.*, A Study of the Production of High-p_T π^0's at the CERN Intersecting Storage Rings, Z. Phys. **C5**, 95 (1980).

[41] F. Bŭsser *et al.*, A study of inclusive spectra and two-particle correlations at large transverse momentum, Nucl. Phys. **B106**, 1 (1976).

[42] A. L. S. Angelis *et al.*, A measurement of inclusive π^0 production at large p_T from p–p collisions at the CERN ISR, Phys. Lett. **B79**, 505 (1978).

[43] D. Antreasyan *et al.*, Production of hadrons at large transverse momentum in 200-, 300-, and 400-GeV p-p and p-nucleus collisions, Phys. Rev. D **19**, 764 (1979).

[44] C. D. Marzo *et al.*, Measurement of direct photon production at large transverse momentum in π^-p, π^+p, and pp collisions at 300 GeV/c, Phys. Rev. D **36**, 8 (1987).

[45] J. Badier *et al.*, Direct Photon Production from Pions and Protons at 200–GeV/c, Z. Phys. **C31**, 341 (1986).

[46] M. Bonesini *et al.*, High transverse momentum prompt photon production by π^- and π^+ on protons at 280 GeV/c, Z. Phys. **C37**, 535 (1988).

[47] A. L. S. Angelis *et al.*, Direct photon production at the CERN ISR, Nucl. Phys. **B327**, 541 (1989).

[48] E. Anassontzis *et al.*, High-p_T Direct Photon Production in pp Collisions, Z. Phys. **C13**, 277 (1982).

[49] A. L. S. Angelis *et al.*, Search for direct single–photon production at large p_T in proton–proton collisions at $\sqrt{s} = 62.4$ GeV, Phys. Lett. **B94**, 106 (1980).

[50] G. Sozzi *et al.*, Direct photon production in $\bar{p}$p and pp interactions at $\sqrt{s} = 24.3$ GeV/c, Phys. Lett. **B317**, 243 (1993).

[51] M. Bonesini *et al.*, Production of high transverse momentum prompt photons and neutral pions in proton–proton interactions at 280 GeV/c, Z. Phys. **C38**, 371 (1988).

[52] M. McLaughlin *et al.*, Inclusive Production of Direct Photons in 200–GeV/c Collisions, Phys. Rev. Lett. **51**, 971 (1983).

[53] P. Aurenche *et al.*, Prompt photon production at large p_T in QCD beyond the leading order, Phys. Lett. **B140**, 87 (1984).

[54] F. Aversa *et al.*, Nucl. Phys. **B327**, 105 (1989).

[55] P. Aurenche *et al.*, Gluon content of the nucleon probed with real and virtual photons, Phys. Rev. D **39**, 3275 (1989).

[56] A. D. Martin, W. J. Stirling, and R. G. Roberts, Phys. Lett. **B354**, 155 (1995).

[57] M. Gluck, E. Reya, and A. Vogt, Phys. Lett. **B306**, 391 (1993).

[58] M. Zielinski, On High p_T Direct Photons, Mesons and pQCD, Proceedings of the 3rd International Symposium on Radiative Corrections, Cracow, Poland, 1–5 August 1996.

[59] P. Aurenche *et al.*, The gluon content of the pion from high-p_T direct photon production, Phys. Lett. **B233**, 517 (1989).

[60] J. Binnewies, B. A. Kniehl, and G. Kramer, Pion and kaon production in e^+e^- and ep collisions at next-to-leading order, Phys. Rev. D **52**, 4947 (1995).

[61] P. Chiappetta *et al.*, Next-to-leading-order determination of pion fragmentation functions, Nucl. Phys. B **412**, 3 (1994).

[62] M. Greco and S. Rolli, Next to leading order eta production at hadron colliders, Z. Phys. C **60**, 169 (1993).

Appendix: Measured Cross Sections

This appendix contains the measured cross sections in tabular form. (See Figure 6.1 and following for a graphical representation of this data). Errors given are statistical only; for systematics, consult Table 6.2.

p_T Range (GeV/c)	$Ed^3\sigma/dp^3$(Be) (pb/GeV^2)
3.000 - 3.100	134300 ± 4900
3.100 - 3.200	96100 ± 2200
3.200 - 3.300	73000 ± 1900
3.300 - 3.400	50400 ± 1400
3.400 - 3.500	36700 ± 1100
3.500 - 3.600	27320 ± 730
3.600 - 3.700	20520 ± 490
3.700 - 3.800	15620 ± 320
3.800 - 3.900	11420 ± 280
3.900 - 4.000	8740 ± 190
4.000 - 4.100	6384 ± 71
4.100 - 4.200	4824 ± 56
4.200 - 4.300	3678 ± 27
4.300 - 4.400	2889 ± 23
4.400 - 4.500	2219 ± 19
4.500 - 4.600	1701 ± 16
4.600 - 4.700	1310 ± 14
4.700 - 4.800	1018 ± 11
4.800 - 4.900	786.1 ± 9.9
4.900 - 5.000	628.8 ± 8.8
5.000 - 5.100	496.1 ± 7.5
5.100 - 5.200	383.6 ± 6.4
5.200 - 5.300	309.4 ± 5.7
5.300 - 5.400	248.6 ± 5.1
5.400 - 5.500	203.1 ± 4.5
5.500 - 5.600	157.4 ± 3.9
5.600 - 5.700	122.7 ± 3.4
5.700 - 5.800	95.4 ± 3.0
5.800 - 5.900	80.3 ± 2.7
5.900 - 6.000	61.3 ± 2.4
6.000 - 6.125	47.0 ± 1.9
6.125 - 6.250	38.7 ± 1.6
6.250 - 6.375	30.1 ± 1.4
6.375 - 6.500	24.1 ± 1.3
6.500 - 6.625	17.7 ± 1.1
6.625 - 6.750	14.93 ± 0.96
6.750 - 6.875	10.78 ± 0.81
6.875 - 7.000	8.2 ± 0.71
7.000 - 7.250	5.82 ± 0.42
7.250 - 7.500	3.76 ± 0.35
7.500 - 7.750	1.65 ± 0.22
7.750 - 8.000	1.06 ± 0.17
8.000 - 8.500	0.576 ± 0.094
8.500 - 9.000	0.226 ± 0.052
9.000 - 10.000	0.047 ± 0.023
10.000 - 12.000	0.0029 ± 0.0029

p_T Range (GeV/c)	$Ed^3\sigma/dp^3$(Cu) (pb/GeV^2)
3.000 - 3.125	168000 ± 13000
3.125 - 3.250	97200 ± 4700
3.250 - 3.375	70800 ± 3700
3.375 - 3.500	51600 ± 3600
3.500 - 3.625	32500 ± 1900
3.625 - 3.750	21700 ± 1100
3.750 - 3.875	16260 ± 590
3.875 - 4.000	11320 ± 440
4.000 - 4.125	7950 ± 150
4.125 - 4.250	5630 ± 140
4.250 - 4.375	3912 ± 64
4.375 - 4.500	2836 ± 52
4.500 - 4.625	2051 ± 39
4.625 - 4.750	1509 ± 32
4.750 - 4.875	1113 ± 27
4.875 - 5.000	831 ± 23
5.000 - 5.125	596 ± 19
5.125 - 5.250	419 ± 16
5.250 - 5.375	325 ± 13
5.375 - 5.500	270 ± 12
5.500 - 5.625	190 ± 10
5.625 - 5.750	139.5 ± 9.3
5.750 - 5.875	98.4 ± 6.7
5.875 - 6.000	75.0 ± 6.1
6.000 - 6.250	54.3 ± 3.5
6.250 - 6.500	29.2 ± 2.5
6.500 - 6.750	17.3 ± 1.9
6.750 - 7.000	9.5 ± 1.5
7.000 - 7.500	4.63 ± 0.67
7.500 - 8.000	1.99 ± 0.48
8.000 - 9.000	0.41 ± 0.18
9.000 - 10.000	0.071 ± 0.050

p_T Range (GeV/c)	$Ed^3\sigma/dp^3$(H) (pb/GeV^2)
3.5 - 4.0	13500 ± 1700
4.0 - 4.5	3814 ± 80
4.5 - 5.0	1042 ± 30
5.0 - 5.5	319 ± 15
5.5 - 6.0	107.6 ± 8.3
6.0 - 6.5	33.5 ± 4.3
6.5 - 7.0	11.4 ± 2.3
7.0 - 7.5	4.9 ± 1.5
7.5 - 8.5	1.69 ± 0.57
8.5 - 10.0	0.32 ± 0.23

Table 6.3 Invariant differential cross sections per nucleon as functions of p_T for inclusive π^0 production in the range $-0.75 < Y_{CM} < 0.75$ by 515 GeV/c π^- beam incident upon hydrogen, beryllium, and copper targets.

p_T Range (GeV/c)	$Ed^3\sigma/dp^3$(Be) (pb/GeV^2)
3.500 - 3.600	30600 ± 1100
3.600 - 3.700	20690 ± 770
3.700 - 3.800	16360 ± 630
3.800 - 3.900	12150 ± 420
3.900 - 4.000	8259 ± 85
4.000 - 4.100	6092 ± 45
4.100 - 4.200	4612 ± 37
4.200 - 4.300	3467 ± 29
4.300 - 4.400	2546 ± 24
4.400 - 4.500	1926 ± 19
4.500 - 4.600	1446 ± 16
4.600 - 4.700	1104 ± 13
4.700 - 4.800	833 ± 11
4.800 - 4.900	633.0 ± 9.4
4.900 - 5.000	483.7 ± 8.0
5.000 - 5.100	379.7 ± 7.0
5.100 - 5.200	285.5 ± 5.8
5.200 - 5.300	221.1 ± 5.3
5.300 - 5.400	170.2 ± 4.3
5.400 - 5.500	133.2 ± 3.9
5.500 - 5.600	100.6 ± 3.3
5.600 - 5.700	71.7 ± 2.9
5.700 - 5.800	62.6 ± 2.6
5.800 - 5.900	51.1 ± 2.3
5.900 - 6.000	40.6 ± 2.0
6.000 - 6.125	30.0 ± 1.5
6.125 - 6.250	22.4 ± 1.3
6.250 - 6.375	15.5 ± 1.1
6.375 - 6.500	12.99 ± 0.97
6.500 - 6.625	7.87 ± 0.72
6.625 - 6.750	6.15 ± 0.65
6.750 - 6.875	5.71 ± 0.62
6.875 - 7.000	4.39 ± 0.53
7.000 - 7.250	2.74 ± 0.30
7.250 - 7.500	1.25 ± 0.20
7.500 - 7.750	0.51 ± 0.13
7.750 - 8.000	0.312 ± 0.099
8.000 - 8.500	0.204 ± 0.054
8.500 - 9.000	0.043 ± 0.025
9.000 - 10.000	0.0102 ± 0.0072

p_T Range (GeV/c)	$Ed^3\sigma/dp^3$(Cu) (pb/GeV^2)	$Ed^3\sigma/dp^3$(H) (pb/GeV^2)
3.500 - 3.625	31800 ± 2000	22800 ± 2000
3.625 - 3.750	22200 ± 1500	16700 ± 1400
3.750 - 3.875	13500 ± 780	10280 ± 750
3.875 - 4.000	10010 ± 370	8120 ± 280
4.000 - 4.125	6943 ± 88	5520 ± 92
4.125 - 4.250	4986 ± 70	3875 ± 73
4.250 - 4.375	3326 ± 51	2675 ± 54
4.375 - 4.500	2373 ± 41	1806 ± 43
4.500 - 4.625	1650 ± 32	1279 ± 37
4.625 - 4.750	1166 ± 26	947 ± 26
4.750 - 4.875	792 ± 20	684 ± 22
4.875 - 5.000	581 ± 17	489 ± 18
5.000 - 5.125	419 ± 14	358 ± 15
5.125 - 5.250	295 ± 11	268 ± 12
5.250 - 5.375	212.2 ± 9.4	201 ± 12
5.375 - 5.500	161.3 ± 8.3	129.3 ± 8.1
5.500 - 5.625	107.3 ± 6.5	116.3 ± 8.0
5.625 - 5.750	78.2 ± 5.5	68.7 ± 5.8
5.750 - 5.875	52.7 ± 4.6	62.4 ± 5.4
5.875 - 6.000	41.2 ± 3.8	44.5 ± 4.9
6.000 - 6.250	25.4 ± 2.0	27.6 ± 2.5
6.250 - 6.500	16.4 ± 1.7	14.1 ± 1.9
6.500 - 6.750	6.1 ± 1.0	7.4 ± 1.2
6.750 - 7.000	4.23 ± 0.76	5.6 ± 1.0
7.000 - 7.500	1.86 ± 0.36	1.64 ± 0.38
7.500 - 8.000	0.61 ± 0.20	0.84 ± 0.27
8.000 - 9.000	0.156 ± 0.064	0.22 ± 0.11

Table 6.4 Invariant differential cross sections per nucleon as functions of p_T for inclusive π^0 production in the range $-0.75 < Y_{CM} < 0.75$ by 530 GeV/c p beam incident upon hydrogen, beryllium, and copper targets.

p_T Range (GeV/c)	$Ed^3\sigma/dp^3$(Be) (pb/GeV^2)
3.000 - 3.200	62000 ± 14000
3.200 - 3.400	22600 ± 3100
3.400 - 3.600	15900 ± 1900
3.600 - 3.800	8570 ± 980
3.800 - 4.000	4240 ± 780
4.000 - 4.200	3220 ± 430
4.200 - 4.400	1320 ± 270
4.400 - 4.600	960 ± 170
4.600 - 4.800	562 ± 26
4.800 - 5.000	348 ± 16
5.000 - 5.250	190.3 ± 9.4
5.250 - 5.500	114.8 ± 6.5
5.500 - 5.750	67.7 ± 4.7
5.750 - 6.000	33.6 ± 3.1
6.000 - 6.500	20.3 ± 1.5
6.500 - 7.000	6.59 ± 0.76
7.000 - 7.500	1.68 ± 0.40
7.500 - 8.000	0.87 ± 0.23
8.000 - 9.000	0.250 ± 0.087
9.000 - 10.000	0.042 ± 0.040

p_T Range (GeV/c)	$Ed^3\sigma/dp^3$(Cu) (pb/GeV^2)	$Ed^3\sigma/dp^3$(H) (pb/GeV^2)
3.0 - 3.5	49000 ± 18000	—
3.5 - 4.0	9800 ± 1700	—
4.0 - 4.5	2910 ± 700	1340 ± 230
4.5 - 5.0	677 ± 47	376 ± 95
5.0 - 5.5	204 ± 16	124 ± 30
5.5 - 6.0	59.6 ± 8.1	20 ± 18
6.0 - 7.0	18.9 ± 2.4	8.1 ± 5.0
7.0 - 8.0	2.87 ± 0.77	—
8.0 - 10.0	0.29 ± 0.16	—

Table 6.5 Invariant differential cross sections per nucleon as functions of p_T for inclusive η production in the range $-0.75 < Y_{CM} < 0.75$ by 515 GeV/c π^- beam incident upon hydrogen, beryllium, and copper targets.

p_T Range (GeV/c)	$Ed^3\sigma/dp^3$(Be) (pb/GeV^2)	$Ed^3\sigma/dp^3$(Cu) (pb/GeV^2)	$Ed^3\sigma/dp^3$(H) (pb/GeV^2)
4.0 - 4.5	1360 ± 350	2640 ± 900	—
4.5 - 5.0	336 ± 14	366 ± 34	282 ± 27
5.0 - 5.5	101.4 ± 5.4	118 ± 12	83 ± 11
5.5 - 6.0	29.6 ± 2.7	42.5 ± 6.8	25.1 ± 4.9
6.0 - 7.0	5.82 ± 0.62	7.3 ± 1.5	2.6 ± 1.4
7.0 - 8.0	0.30 ± 0.15	0.96 ± 0.36	0.41 ± 0.33
8.0 - 10.0	0.029 ± 0.027	0.098 ± 0.092	—

Table 6.6 Invariant differential cross sections per nucleon as functions of p_T for inclusive η production in the range $-0.75 < Y_{CM} < 0.75$ by 530 GeV/c p beam incident upon hydrogen, beryllium, and copper targets.

p_T Range (GeV/c)	$Ed^3\sigma/dp^3$(Be) (pb/GeV^2)
4.000 - 4.125	611 ± 15
4.125 - 4.250	493 ± 12
4.250 - 4.375	356.9 ± 8.7
4.375 - 4.500	278.0 ± 7.2
4.500 - 4.625	220.5 ± 5.7
4.625 - 4.750	165.0 ± 4.7
4.750 - 4.875	137.3 ± 4.1
4.875 - 5.000	104.0 ± 3.5
5.000 - 5.125	85.7 ± 3.0
5.125 - 5.250	72.1 ± 2.6
5.250 - 5.375	52.7 ± 2.2
5.375 - 5.500	41.9 ± 1.9
5.500 - 5.625	37.2 ± 1.7
5.625 - 5.750	32.2 ± 1.5
5.750 - 5.875	24.5 ± 1.3
5.875 - 6.000	21.0 ± 1.2
6.000 - 6.250	14.16 ± 0.66
6.250 - 6.500	9.56 ± 0.53
6.500 - 6.750	6.32 ± 0.41
6.750 - 7.000	4.37 ± 0.33
7.000 - 7.500	2.48 ± 0.17
7.500 - 8.000	1.34 ± 0.11
8.000 - 9.000	0.503 ± 0.046
9.000 - 10.000	0.092 ± 0.019
10.000 - 12.000	0.0081 ± 0.0034
12.000 - 15.000	0.0010 ± 0.0010

p_T Range (GeV/c)	$Ed^3\sigma/dp^3$(Cu) (pb/GeV^2)	$Ed^3\sigma/dp^3$(H) (pb/GeV^2)
4.0 - 4.5	525 ± 16	519 ± 31
4.5 - 5.0	166.1 ± 6.3	184 ± 12
5.0 - 5.5	69.5 ± 3.3	73.1 ± 6.8
5.5 - 6.0	32.2 ± 1.9	28.4 ± 3.9
6.0 - 6.5	11.6 ± 1.1	14.4 ± 2.4
6.5 - 7.0	5.77 ± 0.68	6.1 ± 1.5
7.0 - 7.5	2.91 ± 0.44	5.1 ± 1.3
7.5 - 8.5	1.12 ± 0.18	1.41 ± 0.44
8.5 - 10.0	0.089 ± 0.054	0.14 ± 0.14
10.0 - 12.0	0.014 ± 0.011	—

Table 6.7 Invariant differential cross sections per nucleon as functions of p_T for inclusive γ production in the range $-0.75 < Y_{CM} < 0.75$ by 515 GeV/c π^- beam incident upon hydrogen, beryllium, and copper targets.

p_T Range (GeV/c)	$Ed^3\sigma/dp^3$(Be) (pb/GeV^2)
4.000 - 4.125	567 ± 13
4.125 - 4.250	379 ± 10
4.250 - 4.375	311.3 ± 8.0
4.375 - 4.500	215.2 ± 6.3
4.500 - 4.625	167.1 ± 5.2
4.625 - 4.750	111.1 ± 4.1
4.750 - 4.875	91.6 ± 3.5
4.875 - 5.000	65.0 ± 2.9
5.000 - 5.125	52.0 ± 2.4
5.125 - 5.250	41.4 ± 2.1
5.250 - 5.375	32.7 ± 1.8
5.375 - 5.500	23.5 ± 1.6
5.500 - 5.625	18.9 ± 1.3
5.625 - 5.750	15.9 ± 1.1
5.750 - 5.875	11.93 ± 0.97
5.875 - 6.000	8.51 ± 0.82
6.000 - 6.250	5.17 ± 0.45
6.250 - 6.500	3.85 ± 0.35
6.500 - 6.750	2.6 ± 0.27
6.750 - 7.000	1.72 ± 0.22
7.000 - 7.500	0.85 ± 0.10
7.500 - 8.000	0.391 ± 0.064
8.000 - 9.000	0.095 ± 0.021
9.000 - 10.000	0.0098 ± 0.0062
10.000 - 12.000	0.0014 ± 0.0014

p_T Range (GeV/c)	$Ed^3\sigma/dp^3$(Cu) (pb/GeV^2)	$Ed^3\sigma/dp^3$(H) (pb/GeV^2)
4.0 - 4.5	374 ± 11	387 ± 12
4.5 - 5.0	108.4 ± 4.4	122.6 ± 5.1
5.0 - 5.5	38.6 ± 2.1	41.5 ± 2.5
5.5 - 6.0	13.2 ± 1.1	14.1 ± 1.3
6.0 - 6.5	5.06 ± 0.61	5.78 ± 0.75
6.5 - 7.0	1.87 ± 0.33	2.23 ± 0.43
7.0 - 7.5	0.36 ± 0.15	0.79 ± 0.23
7.5 - 8.5	0.234 ± 0.071	0.239 ± 0.089
8.5 - 10.0	0.043 ± 0.024	—

Table 6.8 Invariant differential cross sections per nucleon as functions of p_T for inclusive γ production in the range $-0.75 < Y_{CM} < 0.75$ by 530 GeV/c p beam incident upon hydrogen, beryllium, and copper targets.

γ Production	$Ed^3\sigma/dp^3$ (pb/GeV^2) vs. Y_{CM} and p_T (GeV/c)			
Y_{CM} Range	$4.0 < p_T < 4.5$	$4.5 < p_T < 5.0$	$5.0 < p_T < 7.0$	$7.0 < p_T < 8.0$
-0.750 – -0.625	353 ± 46	66.1 ± 4.5	6.07 ± 0.66	0.51 ± 0.13
-0.625 – -0.500	417 ± 48	59.3 ± 3.7	7.97 ± 0.73	
-0.500 – -0.375	372 ± 40	84.4 ± 3.9	9.73 ± 0.83	0.97 ± 0.18
-0.375 – -0.250	379 ± 17	100.8 ± 4.3	12.71 ± 0.92	
-0.250 – -0.125	431 ± 16	107.1 ± 4.5	15.4 ± 1.0	2.57 ± 0.28
-0.125 – 0.000	490 ± 16	124.3 ± 4.6	16.9 ± 1.1	
0.000 – 0.125	486 ± 16	134.7 ± 4.6	17.8 ± 1.1	2.01 ± 0.26
0.125 – 0.250	472 ± 16	119.7 ± 4.6	19.7 ± 1.1	
0.250 – 0.375	447 ± 17	133.5 ± 4.8	19.9 ± 1.1	2.98 ± 0.30
0.375 – 0.500	431 ± 18	126.4 ± 4.8	19.7 ± 1.1	
0.500 – 0.625	460 ± 18	135.1 ± 4.8	21.5 ± 1.2	2.07 ± 0.29
0.625 – 0.750	450 ± 17	127.4 ± 4.7	16.3 ± 1.1	

π^0 Production	$Ed^3\sigma/dp^3$ (pb/GeV^2) vs. Y_{CM} and p_T (GeV/c)			
Y_{CM} Range	$4.0 < p_T < 4.5$	$4.5 < p_T < 5.0$	$5.0 < p_T < 7.0$	$7.0 < p_T < 8.0$
-0.750 – -0.625	2140 ± 130	404 ± 12	23.2 ± 1.5	0.77 ± 0.18
-0.625 – -0.500	2820 ± 110	506 ± 11	32.9 ± 1.5	
-0.500 – -0.375	3523 ± 46	596 ± 10	39.2 ± 1.7	2.42 ± 0.31
-0.375 – -0.250	4027 ± 45	672 ± 10	47.2 ± 1.8	
-0.250 – -0.125	4298 ± 40	749 ± 10	54.9 ± 2.0	3.17 ± 0.37
-0.125 – 0.000	4502 ± 40	803 ± 10	59.1 ± 2.0	
0.000 – 0.125	4668 ± 38	838 ± 10	67.1 ± 2.1	4.61 ± 0.42
0.125 – 0.250	4678 ± 39	833 ± 10	63.7 ± 2.0	
0.250 – 0.375	4719 ± 40	841 ± 10	63.1 ± 2.0	3.67 ± 0.41
0.375 – 0.500	4500 ± 41	816 ± 11	54.9 ± 2.1	
0.500 – 0.625	4281 ± 41	766 ± 11	57.6 ± 2.1	3.06 ± 0.43
0.625 – 0.750	3882 ± 40	677 ± 10	44.4 ± 1.9	

η Production	$Ed^3\sigma/dp^3$ (pb/GeV^2) vs. Y_{CM} and p_T (GeV/c)		
Y_{CM} Range	$4.0 < p_T < 4.5$	$4.5 < p_T < 5.0$	$5.0 < p_T < 7.0$
-0.750 – -0.625	890 ± 320	160 ± 43	12.3 ± 2.4
-0.625 – -0.500		165 ± 30	
-0.500 – -0.375	720 ± 230	231 ± 28	17.1 ± 2.4
-0.375 – -0.250		280 ± 23	
-0.250 – -0.125	1390 ± 200	357 ± 27	29.5 ± 2.5
-0.125 – 0.000		351 ± 25	
0.000 – 0.125	1550 ± 190	343 ± 24	27.1 ± 2.6
0.125 – 0.250		402 ± 28	
0.250 – 0.375	2190 ± 200	436 ± 27	35.5 ± 3.0
0.375 – 0.500		447 ± 28	
0.500 – 0.625	2280 ± 210	417 ± 25	28.5 ± 2.8
0.625 – 0.750		382 ± 23	

Table 6.9 For several p_T bins, the invariant differential cross sections per nucleon as functions Y_{CM} for inclusive direct photon, π^0, and η production by 515 GeV/c π^- beam incident upon beryllium.

γ Production	$Ed^3\sigma/dp^3$ (pb/GeV^2) vs. Y_{CM} and p_T (GeV/c)			
Y_{CM} Range	$4.0 < p_T < 4.5$	$4.5 < p_T < 5.0$	$5.0 < p_T < 7.0$	$7.0 < p_T < 8.0$
-0.750 – -0.625	358 ± 20	60.5 ± 3.8	3.34 ± 0.50	
-0.625 – -0.500	363 ± 22	56.0 ± 3.6	5.5 ± 0.59	0.47 ± 0.10
-0.500 – -0.375	369 ± 19	69.1 ± 3.8	5.88 ± 0.65	
-0.375 – -0.250	366 ± 19	75.9 ± 4.0	7.56 ± 0.75	
-0.250 – -0.125	371 ± 17	85.8 ± 4.3	7.55 ± 0.79	0.79 ± 0.14
-0.125 – 0.000	416 ± 17	73.3 ± 4.2	8.32 ± 0.83	
0.000 – 0.125	384 ± 16	76.4 ± 4.0	8.01 ± 0.78	
0.125 – 0.250	392 ± 15	74.9 ± 3.9	7.85 ± 0.78	0.56 ± 0.11
0.250 – 0.375	440 ± 15	83.2 ± 3.8	8.13 ± 0.78	
0.375 – 0.500	341 ± 14	84.4 ± 3.8	6.47 ± 0.72	
0.500 – 0.625	318 ± 14	75.0 ± 3.7	7.24 ± 0.74	0.66 ± 0.14
0.625 – 0.750	299 ± 14	62.2 ± 3.6	6.09 ± 0.70	

π^0 Production	$Ed^3\sigma/dp^3$ (pb/GeV^2) vs. Y_{CM} and p_T (GeV/c)			
Y_{CM} Range	$4.0 < p_T < 4.5$	$4.5 < p_T < 5.0$	$5.0 < p_T < 7.0$	$7.0 < p_T < 8.0$
-0.750 – -0.625	2611 ± 66	421 ± 13	19.4 ± 1.5	0.54 ± 0.18
-0.625 – -0.500	3329 ± 71	514 ± 12	22.8 ± 1.4	
-0.500 – -0.375	3860 ± 62	581 ± 11	31.6 ± 1.6	1.15 ± 0.23
-0.375 – -0.250	4324 ± 60	648 ± 11	36.0 ± 1.7	
-0.250 – -0.125	4510 ± 49	681 ± 10	38.6 ± 1.7	2.44 ± 0.33
-0.125 – 0.000	4532 ± 45	716 ± 10	40.8 ± 1.8	
0.000 – 0.125	4528 ± 43	690.3 ± 9.8	38.1 ± 1.6	1.60 ± 0.26
0.125 – 0.250	4218 ± 40	663.3 ± 9.5	37.6 ± 1.7	
0.250 – 0.375	3914 ± 37	617.5 ± 9.2	36.2 ± 1.6	0.94 ± 0.22
0.375 – 0.500	3557 ± 38	524.9 ± 8.9	30.1 ± 1.5	
0.500 – 0.625	2966 ± 36	445.5 ± 8.6	21.9 ± 1.5	0.55 ± 0.20
0.625 – 0.750	2395 ± 34	326.6 ± 7.8	13.2 ± 1.2	

η Production	$Ed^3\sigma/dp^3$ (pb/GeV^2) vs. Y_{CM} and p_T (GeV/c)		
Y_{CM} Range	$4.0 < p_T < 4.5$	$4.5 < p_T < 5.0$	$5.0 < p_T < 7.0$
-0.750 – -0.625		123 ± 28	7.2 ± 2.8
-0.625 – -0.500	1080 ± 630	164 ± 35	
-0.500 – -0.375		184 ± 28	8.9 ± 2.7
-0.375 – -0.250		226 ± 26	
-0.250 – -0.125	740 ± 730	259 ± 24	16.6 ± 2.5
-0.125 – 0.000		292 ± 26	
0.000 – 0.125		280 ± 25	18.4 ± 2.3
0.125 – 0.250	2320 ± 850	232 ± 22	
0.250 – 0.375		233 ± 23	17.5 ± 2.2
0.375 – 0.500		234 ± 22	
0.500 – 0.625	1280 ± 780	244 ± 23	13.9 ± 2.0
0.625 – 0.750		157 ± 20	

Table 6.10 For several p_T bins, the invariant differential cross sections per nucleon as functions Y_{CM} for inclusive direct photon, π^0, and η production by 530 GeV/c proton beam incident upon beryllium.